CRANFIELD UNIVERSITY

ZAHARADDEEN ALI HUSSAINI

NUMERICAL DESIGN AND SIMULATION OF CSP MULTI-TOWER SOLAR HELIOSTAT FIELD

SCHOOL OF WATER, ENERGY AND ENVIRONMENT

PhD Thesis
Academic Year: 2016 - 2020

Supervisors:
Dr Peter King
Professor Chris Sansom

May 2020

CRANFIELD UNIVERSITY

SCHOOL OF WATER, ENERGY AND ENVIRONMENT

PhD Thesis

Academic Year 2016 - 2020

ZAHARADDEEN ALI HUSSAINI

Numerical Design and Simulation of CSP Multi-Tower Solar Heliostat Field

Supervisors:
Dr Peter King
Professor Chris Sansom

May 2020

ABSTRACT

In power tower systems, the heliostat field is one of the essential subsystems in the plant due to its significant contribution to the plant's overall power losses and total plant investment cost. The design and optimisation of the heliostat field is hence an active area of research, with new field improvement processes and configurations being actively investigated. In this thesis, a different configuration of a multi-tower field is explored. This involves adding an auxiliary tower to the field of a conventional power tower Concentrated Solar Power (CSP) system.

The methodology for the auxiliary towers positioning were based on the region in the field which has the least effective reflecting heliostats. The multi-tower configuration was initially applied to a 50MWth conventional field in the case study region of Nigeria. The results from an optimised multi-tower field, achieved through MATLAB Genetic Optimisation, show a marked increase in the annual thermal energy output and mean annual efficiency of the field over a typical conventional field. The efficiency and thermal energy output become even more pronounced in optimised multi-tower fields with two auxiliary towers. For the given thermal field power, the gain recorded in the thermal energy output could not offset the additional costs from the presence of additional towers and receivers in the field. However, in much larger fields a higher number of weaker heliostats were witnessed in the field. The auxiliary towers in the field thus provides an alternate aim point for the weaker heliostat, thereby considerably cutting down on some optical losses, which in turn gives rise to higher energy output. At 400MWth, the one auxiliary tower multi-tower field configuration provides both a lower LCOH and a higher field efficiency over a single conventional power tower field with similar thermal field output power.

The thesis goes further to explore and develop methods in which the field layout generation methodologies in multi-tower fields can be improved. The Auxiliary Tower with Subfield Configuration (ATS) and Heliostat Repositioning Configuration (HRC). The addition of auxiliary tower has already shown to hold much potential in large plants. ATS and HRC further show that the same intended field thermal power output can be reached with a lesser LCOH and a higher field efficiency when compared to both conventional fields and optimised multi-tower fields of similar thermal ratings. These field improvement strategies were then applied to an existing field, the Gemasolar plant in Sevilla Spain, as a case study in order to further highlight their applications.

In this work, multi-towers have shown that in large solar fields, a clear advantage over the conventional fields exists by proving a higher field efficiency and thermal energy output. Multi-tower fields have thus shown to provide a viable alternative to conventional fields and equally provide the potential to change the way power tower fields are being built in the future.

Keywords:

Solar Field Optimisation, Multiple Towers, Power Tower, Central Receiver

ACKNOWLEDGEMENTS

I would first like to thank my supervisors, Dr Peter King and Professor Chris Sansom for their tremendous support, guidance and patience through this project. It has been a long journey and it was certainly reassuring knowing they were there through every turn.

I would like to thank dear folks from the precision engineering office; Talib Kayani, Bernadin Namoano, Mohammed Bahrammi, Peter Xia, Adam Bennet and Katherin Goby for taking in all the complaints, the relentless help, and the listening ear. It has been a fun journey. Special thanks to Bernadine Namoano for providing an entire new dimension in the work and late-night company in the office.

I am grateful to Petroleum Trust Development Fund (PTDF) in Nigeria for funding through this project.

Finally, I would like to thank my entire family. My ever-supportive parents, for their moral and spiritual support. To my sisters and brothers, I am grateful for your presence despite being miles away. Special thanks to my wife for her support, patience and bearing with me as I battled through the PhD.

TABLE OF CONTENTS

LIST OF FIGURES

LIST OF TABLES

LIST OF ABBREVIATIONS

Annually Equivalent Efficiency Distribution (AEED)

Auxiliary Tower with Subfield configuration (ATS)

Capital Recovery Factor (CRF)

carbon dioxide (CO_2)

Compound Parabolic Collector (CPC)

Concatenated Micro-Tower (CMT)

Concentrated Solar Power (CSP)

Conference of Parties (COP21)

Convention on Climate Change (UNFCCC)

Cumulative Density Function (CDF)

Department of Energy (DOE),

Direct Normal Irradiance (DNI)

Energy Commission of Nigeria (ECN)

Genetic Algorithm (GA)

German Aerospace Centre (DLR)

Graphics Processing Unit (GPU)

Gross Domestic Product (GDP).

Gross National Income (GNI)

Heat Transfer Fluid (HTF)

Heliostat Field Layout Design (HFLD)

Heliostat Repositioning Configuration (HRC)

Heliostats Field Layout Calculations (HFLCAL)

Human Development Index

kilometre (KM)

Levelized Cost of Electricity (LCOE)

Levelized Cost of Heat (LCOH)

Life Cycle Assessment (LCA)

Modular Integrated Utility Systems (MIUS)

Multi Tower Solar Array (MTSA)

National Adaptation Strategy and Plan of Action on Climate Change for Nigeria (NASPA-CCN)

National Renewable Energy Laboratory (NREL)

National Solar Thermal Test Facility (NSTTF)

NiMet (Nigerian Metrological Agency)

Particle Swarm Optimisation (PSO)

Phase Change Material (PCM)

Power Conversion Unit (PCU)

Renewable Energy Master Plan (REMP)

Solar Electric Generating Systems' (SEGs)

Sustainable Development Goals (SDGs)

System Advisor Model (SAM)

Thermal Energy Storage (TES)

Typical Meteorological Year (TMY)

United Nations Development Program (UNDP)

University of Zaragoza (UNIZAR

Wind Information System (WIS)

1 INTRODUCTION

At the 21st Conference of Parties (COP21) climate conference in Paris by the United Nations Framework Convention on Climate Change (UNFCCC) in the month of December 2015, a momentous agreement was reached by several countries to intensify the efforts towards combating climate change by keeping the unprecedented increase in temperature rise to below 2°C and to further limiting it to 1.5 °C in the long run [1].

Efforts must be made in increasing the renewable energy penetration index in the energy mix in order to achieve the target of limiting the global temperature increase. Due to the declining patronage on nuclear energy and volatile petroleum and natural gas prices, coupled with the rising global temperature predominately due to the atmospheric build-up of carbon dioxide (CO_2), nations at large are opting and considering renewable energy technologies for their power generation. Solar energy, in particular, is seen as an extremely viable option, especially in areas with good solar insolation [2].

Solar thermal energy can be defined as a form of energy; thermal or electrical harnessed through the utilization of some medium or technology. Solar thermal energy for electricity generation is typically referred to as Concentrated Solar Power (CSP) [3]. In this paper, the emphasis is given to solar thermal electricity. CSP can be a driving force in the cause of reducing CO_2 emission, thereby contributing to reducing and limiting the global temperature increase.

1.1 Concentrating Solar Power Systems

Concentrated Solar Power systems utilizes mirrors to concentrate the beam radiation from the sun onto an absorber or receiver which hold and heats up the solid, liquid or gas that is subsequently used directly or indirectly to power turbines for electricity generation [3]. Figure 1-1 shows the basic operational principle of CSP systems.

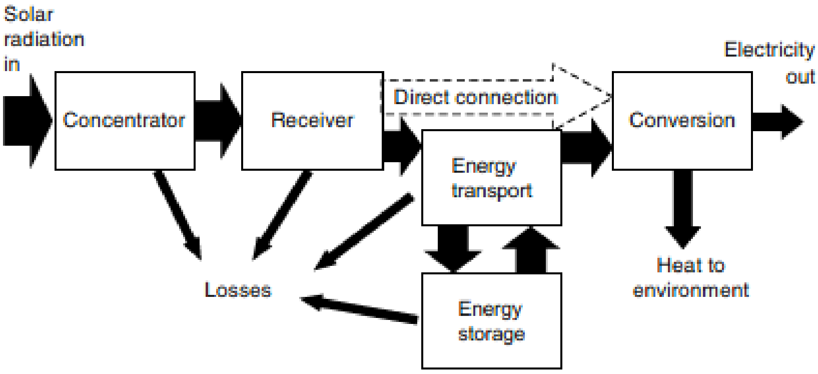

Figure 1-1 Basic operational principles of the Concentrated Solar Power systems

The operational principles of concentrating power have been known for well over a century [4]. However, commercial production only began in the 1980s in California with the installed capacity 354 MWe Solar Electric Generating Systems' (SEGs) plant [5]. The SEGs plant proved the commercial viability of the system as they have been operating under utility ownership since 1984. The growth and development of CSP suffered a significant setback for about 15 years, between 1991 and 2005, as no new CSP plants were built anywhere in the world [6]. During that time, installed photovoltaics (PV) capacity grew to be some ten times greater than CSP. This resulted in a significant cost reduction of the technology over the recent years, leaving behind the CSPs path to cost reduction [4]. By the year 2012, the cost of installing PV for non-dispatchable electricity production was cheaper than CSP. This prompted the need to harness the CSPs potential of built-in thermal energy storage [4].

Several technologies are used to concentrate and collect sunlight and to turn it into medium to high-temperature heat which could be subsequently converted into electricity. The heat can also be stored, which could be extracted at night from the storage medium to drive the turbine when there is not any sunshine. Concentrating solar power technologies continue to mature and are being deployed worldwide [4,6].

1.2 Types of CSP Plants

Generally, CSPs can be broken down into two categories; point and line focusing CSP systems. Line focusing systems include; linear Fresnel and parabolic trough system. Point focusing systems include; power tower system and the parabolic dish system [2]. A depiction of the types of CSP systems is shown in Figure 1-2 [7].

1.2.1 Dish/Engine Systems

Dish/Engine systems are small units that produce electricity typically in a small range of ten of kW or even smaller. The dish system offers the highest transformation of any CSP system [8]. The system utilizes dishes of mirrors that reflect sunlight onto a thermal receiver and a central engine which produces electricity. Dish engine systems can track the sun in two-axes. The engine placed at the focal point is typically stirling or a small gas turbine [9].

1.2.2 Linear Concentrating Systems-Parabolic trough

Linear concentrating collectors capture the sun's energy with parabolic shaped mirrors that reflect and focus the sunlight onto an absorber tube placed along the focal line of the parabolic reflective material. The receiver contains a Heat Transfer Fluid (HTF) that is heated by the sunlight and transfers energy to conventional steam cycle to produce superheated steam which powers a turbine that drives a generator to produce electricity. The field typically consists of many collectors in parallel rows that are aligned to track the sun in one axis to optimise energy collection.

1.2.3 Power Tower Systems

Power tower systems use large distributed tracking mirrors (heliostats) that concentrate the beam radiation onto a receiver atop a centrally located tower. A very high temperature of up to 1000˚C is achievable in this kind of system [10]. The concentrated solar energy is absorbed by the working fluid, which produces the steam used in powering a turbine to produce electricity [5,11].

1.2.4 Linear Fresnel System

Linear Fresnel system is very much alike to the parabolic trough system. However, in place of the parabolic reflector, almost flat linear mirror strips are being utilized which reflect radiation onto a fixed receiver mounted over on top of the mirrors [5]. The nature of the mirrors utilized here makes it considerably cheaper than other technologies to make and the fact that they do not need much structural support as they are mounted close to the ground [3].

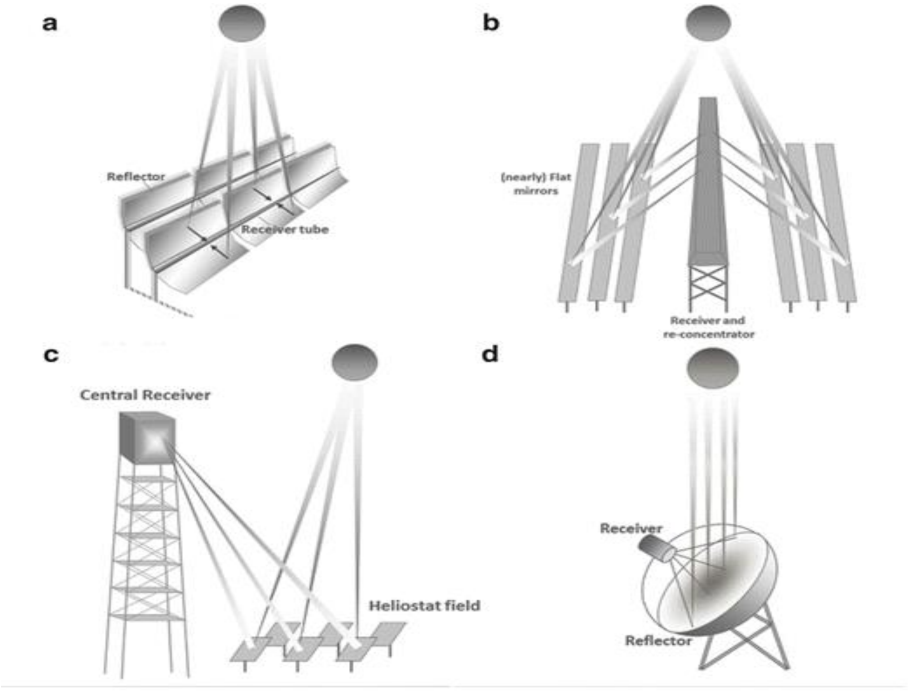

Figure 1-2 Concentrated Solar Power Types a) Parabolic Dish b) Linear Fresnel c) Power Tower d) Dish System [7]

1.2.5 Context and Gap of Knowledge

Due to the declining patronage of nuclear energy and volatile petroleum and natural gas prices, coupled with the rising global temperature, predominately due to the atmospheric build-up of CO_2, nations at large are opting for and considering renewable energy technologies for their power generation. Solar energy is seen as an extremely viable option, especially in areas with good solar insolation. Solar thermal energy for electricity generation is typically referred to as Concentrated Solar Power. Concentrated Solar Power can be a driving force in the cause of reducing CO_2 emission, thereby contributing to reducing and limiting the global temperature increase. Of the existing types of CSP systems, power tower systems are one of the most promising solar thermal technologies. This is mainly due to the power tower system's ability to offer high operating temperature upto 1,000 °C and, thus, a high annual efficiency [12].

The heliostat field in power tower systems is one of the essential subsystems due to its significant contribution to the plant's total investment cost. About 40-50% of the plant's cost is attributed to the heliostat field [13–17]. The field equally amounts to the overall plant's power loses of about 40% [13,18–21]. It has hence become essential to ensure that the field layout is the most optimal at collecting energy from the sun. The design and optimisation of the heliostat field is hence an active area of research with new field improvement processes being actively investigated. Several methods have been proposed in the literature to improve heliostat field efficiencies and reduce losses either by improving through optimisation and suggesting new heliostat field layout patterns or configurations entirely. One such method is the multi-tower system. In multi-tower systems, certain number of towers are introduced in the field and hence deviating away from the conventional setup of a single tower dedicated to a field.

Although it is only recently that multi-tower setup has attracted much interest in the research community, the configuration has been explored in the past, as shown in the literature. Some clear advantages over the single tower concept have been highlighted in terms of flexibility in providing power and reduced risks associated with the take-off of sizeable commercial project plants. Multi-tower systems have the potential to reduce some of the optical losses such as blockage, attenuation and spillage losses generally associated with the single tower system mainly due to the increasing distance of the heliostats from the tower. However, the possible increase in the plant cost, due to the increase in the number of towers, receivers and piping, must be offset by the reduction in optical losses of the field. Therefore, choosing the number of towers remains a critical issue in the optimisation process, and the optimum transition size from single to multi-tower must equally be thoroughly investigated.

In all the multi-tower configurations reviewed, each tower has its own heliostat field by way of replicating an entire field with surrounding heliostats in smaller units until the capacity required is met. In this work, a different architecture of the multi-tower configuration is investigated. The configuration explored, which provides an alternate viewpoint to the usual mainstream multi-tower configuration, involves adding auxiliary towers to an existing surrounding field. A paper in [22], produced by the author, has been published in this regard.

Furthermore, when compared to the numerous field layout optimisation and improvement techniques seen in conventional tower systems, no record in the literature of field improvement strategies is seen for multi-tower power tower systems. The thesis hence goes further to explore and develop methods in which the field layout generation methodologies in multi-tower systems can be improved.

1.3 Aim

This research aims to investigate, through numerical simulation, the design, development and evaluation of a 50MWth multi-tower solar field layout in Nigeria.

1.4 Objectives

The following objectives must be met in realizing the aim.

a. Review of single conventional power tower heliostat field layout and optimisation methodologies.
b. Evaluate the potential of power tower systems in Nigeria and establish the environmental factors entailed in the site selection process.
c. Generate the heliostat field layout and implement design, modelling and optimisation for a 50MWth conventional Power tower field.
d. Develop a method for the design and modelling of a 50MWth multi-tower power tower heliostat field.
e. Examine the optimum transition size from a single to a multi-tower field.
f. Develop field layout generation methodologies specific to a multi-tower field setup.
g. Develop a model for multi-tower system configuration applicable to different locations.

1.5 Methodology

The following methodological approaches were taken to achieve the stated objectives.

1. As the research is mainly focused on the heliostat field of a multi-tower system, the emphasis was given to the review of existing field layout generation and optimisation methodologies of conventional solar power tower fields. One of such methodologies of field layout was adopted for the design of a conventional system. Validation of the methodology chosen with existing literature was equally implemented.
2. Evaluated the potential of a solar power tower plant at a location in Nigeria by establishing the environmental factors at the selected location (including solar radiation, solar position time and other relevant meteorological factors). Factors that define the prospect of a concentrated solar plant in each location were also assessed to establish the viability of such a system at an identified site.
3. Determined and selected the design point operating period and design point Direct Normal Irradiance (DNI) for a 50MWth power tower system. This was done by establishing the sun radiation utilization efficiency.
4. Implemented performance modelling and energy collection optimisation in the generated field of a conventional system by applying the different models of heliostat field losses in the design of the 50MWth. Field layout generation methodology and the optical losses model adopted from the literature review, as mentioned above, was initially equally validated. The optimisation procedure was simulated over specific days throughout the year in order to establish total annual intercepted energy at the receiver aperture.
5. Established the plant economic performance of all combination of towers considered in order to provide an insight into the viability of possible advantages a multi-tower field and determine the optimum transition size from a single conventional field to multiple tower field.
6. Developed a methodology for field layout and aiming strategy for each heliostat in a multi-tower field setup. Field layout and aiming strategy will initially be done for a maximum of two-towers all within the scope of 50MWth field. Placement location for the additional towers was also determined.
7. Implemented performance modelling and energy collection optimisation in the new multi-tower field by equally applying optical loss models in the generated multi-tower field. Factors such as additional tower location, tower height and receiver dimensions will have to be considered in the optimisation process.
8. Developed two new models in the multi-tower configurations capable of producing a field that is more suited to a multi-tower field setup.

1.6 Thesis Structure

The nature of the study necessities the need to break up the dissertation into different segments in order to aid comprehension of the entire project. The study initially develops the configuration of a conventional field before developing the multi-tower field. The project is thus presented in blocks, each clearly defining an aspect of the methodology.

Chapter 1 - The Chapter introduces CSP, presents the objectives, methodology and gap of knowledge.

Chapter 2 - This chapter forms part of the literature review. Power tower systems were discussed with emphasis made on the heliostat field. The gap of knowledge of the study was also defined and brought forward here.

Chapter 3 - Site selection criteria for the identified location where the system was sited, and the strategies that guide the development of CSP systems were highlighted in this chapter. The environmental setup and design parameters for the establishment of the system were also outlined.

Chapter 4 - The chapter describes the methodology for the development of a conventional power tower field. The results and discussion of the result were also highlighted.

Chapter 5 – This chapter defines the core aspect of the study. The chapter follows a similar procedure to Chapter 4. The methodology for multi-tower field development was highlighted. Multi-tower field improvement studies were also discussed and analysed in the Chapter.

Chapter 6 - In this chapter, an existing field, the Gemasolar field in Sevilla, Spain, was used as a case study to apply the multi-tower field models developed. The results were highlighted and discussed, as well.

Chapter 7 – Discussion and conclusion Chapter. Further possible work on the study was also outlined.

2 POWER TOWER SYSTEMS

This chapter provides a substantial and critical discussion of power tower systems as a type of CSP system. Emphasis is given to the collector field and plant configurations in order to highlight the relevance and originality of the research problems and knowledge gap earlier stated.

2.1 History

Amongst all the technologies, power tower systems are one of the most promising. Power towers can readily integrate thermal energy storage into their operation, providing higher capacity factors, which can potentially provide for cost-effective, dispatchable electricity capable of serving immediate and base-load power markets [3,10,22–25].

The power tower system costs are dominated by the tower (accounts for one-fifth of the total cost), and the receiver (around 60% of the cost [26]). The Power tower technology can be considered as sufficiently mature after the pioneering experience of several 0.5– 10MWe pilot plants in the early 1980s, [27–29]. A brief insight into the historical landmark Power tower systems is made in the following subsections.

Table 2-1 highlights some of the demonstration plants that have been developed over the years.

Table 2-1- Demonstration plants

	Eurelios (Italy)	Sunshine (Japan)	IEA-CRS (Spain)	Solar One (USA)	Solar Two (USA)	CESA 1 (Spain)	Themis (France)	MSEE (USA)	SES 5 (CIS-USSR)	Weizmann (Israel)
Net turbine rating (MWe)	1	1	0.5	10	10	1.2	2.5	0.75	-	-
Thermal power (MWth)	-	5.95	7.7	43.4	56	7.7	8.9	5.5	5	0.5
Irradiance (W/m²)	850	750	7,920	950	950	700	1,040	~1,000	800	-
Reflector area (m²)	6,260	12,912	3,655	71,095	81,344	11,880	10,740	7,845	40,584	3,500
Field area (m²)	3.5	~2	~2	29.1	35	7.7	~2	-	-	-
Target height (m)	55	69	43	80	80	60	106	61	80	80
Receiver	Cavity	Cone/Cavity	Cavity	External cylinder	External cylinder	Cavity	Cavity	Cavity	External	CPC + cavity 'porcupine'
Heat transfer fluid	Water/ steam	Water/ steam	Liquid Sodium	Water/ steam	Molten salt	Water/ steam	Molten salt	Molten salt	Water/ steam	Beam down air
Storage media	Nitrate Salt/Water	Nitrate Salt/Water	Sodium	Oil/Rock	Nitrate Salt	Nitrate Salt	Hitech Salt	Nitrate Salt	Water/ steam	Fossil Hybrid
Storage capacity (MWth)	0.036	-	-	-	107	-	-	-	-	-
Thermal Power (MWht)	-	3.0	1.0	28.0	-	3.5	12.5	2.5	1.5	-

CPC here refers to Compound Parabolic Collector

2.1.1 Solar One and Solar Two

Solar one represented a significant milestone as the first system in the world configured as a mature pre-commercial pilot plant and deemed as worthy of mention in the history of the technology. The lessons from the system are central to and are still being utilized by the present commercial activity with tower systems [28].

The work on Solar One began in 1973 when engineers at Sandia National Laboratories in Albuquerque, New Mexico, and Livermore, California, studied the feasibility of the power tower concept and determined that the system held promise to generate electricity on a large scale. The study led to the establishment of the National Solar Thermal Test Facility (NSTTF) in Albuquerque in 1976 and the development of the 10 MWe Solar One pilot plant around Barstow, California which began operation in 1982.

The plant has a 45MWth large cylindrical type receiver sitting atop a 90 meters tower of surround field configuration having 1,818 heliostats with an area of 39 m^2 [30]. The HTF used here was water which was heated by the receiver to produce steam which could directly be sent to the power conversion unit to produce electricity or to thermally charge an enormous single rock- sand- and oil- thermocline tank sized for 4 hours of turbine operation at 7 MWe [28].

Solar One did have some deficiencies including inefficiencies in its storage system and difficulties operating under intermittent cloud cover which further lead to the realization that single-phase medium HTF like motlen salts could a be used in the receiver and directly for the storage [31]

2.1.2 Solar Two

Solar Two was constructed by making slight changes to the Solar One project. A minimal modification was made to the field and Power Conversion Unit (PCU) and tower. The primary modification was made by introducing the molten technology heat transfer system to the plant [32], see Figure 2-1.

Retrofitting Solar One to Solar Two lasted from 1992 into 1995. Operation of Solar Two lasted three years from April 1996 to April 1999 and during that time the goal to gauge the molten salt technology in the receiver and storage has been proven. The storage capability allowed solar energy to be collected and stored for dispatch when required or during periods of low or no insolation [28]. Another goal met by the Solar Two plant was generating information to promote interest in the commercial take-off of the power tower technology by demonstration and increasing database of system performance and operating costs [33,34].

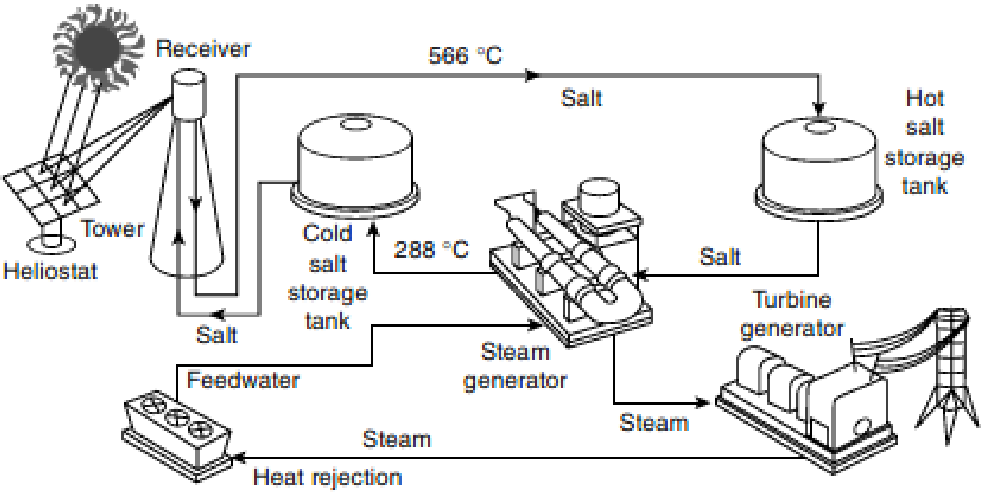

Figure 2-1 - Solar Two plant configuration [32]

By 2010 as many as seven solar power plants have sprung up in various parts of the world and each with its own concept and configuration. Table 2-2 below shows a summary of some of the existing commercial power tower systems as of November 2019 and their features as extracted from numerous sources [28,30,35–37].

Table 2-2 Commercial and operational solar power towers (updated to November 2019)

Plant	Net (electric) power (MWe)	Reflecting area (m^2)	Field area (ha)	Target height (m)	Receiver	Heat transfer fluid	Storage capacity	Storage media	First operation
PS10, Spain	11	75,216	55	100	Hemi-cylindrical Cavity (4-panel)	Saturated steam	50 minutes at 50% load	Saturated steam	2006
PS20, Spain	20	150,000	80	165	Hemi-cylindrical cavity	Saturated steam	1 hour	Saturated Steam	2009
Sierra Sun Tower, USA	5	-	8	65	Dual cavity external 4-panel	Superheated steam	None	-	2010
Gemasolar, Spain	19.9	304,750	195	140	External cylinder	Molten salt	278MWht (15hrs)	Molten Salt	2011
Chevron, USA	Steam: 29MWth	194,000	40	100	Flat panel	Saturated steam	None	-	2010
Ivanpah Solar Electric Generating System, USA	377	2,600,000	1,416	137	External 4-panels N, S, E, W	Saturated steam	None	-	2014
Crescent Dunes, USA	110	1,071,361	540	164	External cylinder	Molten salt	3,000MWht (10hrs)	Molten Salt	2013
ACME Solar Tower Bikaner, India	2.5 W	16,222		-	-	Molten salt	None	-	2012
SUPCON Deling 10 W Tower, China	10	63,000	25	-	External cylinder	Molten Salt	2hrs	Molten Salt	2013

SUPCON Deling 50 W Tower, China	50	542,700	330	200	External cylinder	Molten Salt	7hrs	Molten Salt	2017
Luneng ixi 50MW molten Salt Tower, China	50	607,200		188	External cylinder	Molten Salt	12 hrs	Molten Salt	2019
Khi Solar one, South Africa	50	576,800	140	200	Three cavity receiver	Water	2 hrs	Superheated Steam	2016
As lim Plot B, Israel	121	1,052,480	-	240	External cylinder	Water	None	Steam	2019
Noor 3, Morocco	150	1,320,900	550	250	External cylinder	Molten Salt	7.5 hrs	Molten Salt	2018
Sundrop CSP Project, Australia	Heat Generation 39 W & Electricity 1.5,	51,505		127	-	Water	None	-	2016
Shoung Dunhuang 100 W P se II, China	100	1,380,000	-	220	External cylinder	Molten Salt	11 hrs	Molten Salt	2018
Qing i Gonghe 50 W CSP Plant, China	50	515,900	-	171	External cylinder	Molten Salt	6 hrs	Molten Salt	2019
Shoung Dunhuang 10 W P se I	10	175,375	-	138	External cylinder	Molten Salt	15 hrs	Molten Salt	2016

2.1.3 PS10

The PS10 is located on the Casa Quemada estate near the city of Seville, Spain. It is an 11MWe plant designed to achieve an annual electricity production of 23GWh. PS10 represents a milestone in Power tower system history as it is the first solar power tower plant developed for commercial purposes. The plant has one of the best available information in open works of literature [38]. One of the motivations for establishing the PS10 was the Spanish regulation on feed-in tariffs for electricity generated via renewable energy means [27]

Groundbreaking for PS10 construction was held at the plant site on 28th of June 2004 and commissioning for the first operation began in the year 2006. The project made use of proven and available technologies like the glass–metal heliostats and saturated steam cavity receiver developed by the TECNICAL company to produce steam at 40 bar and 250˚C [27]. The heliostat field consists of 624 heliostats with an aperture area of 120m^2, providing a total aperture area arranged in a radially staggered configuration north of the 115m receiver tower. The plant's thermal storage is geared to handle transient cloud cover by providing a 50-minute capacity at 50% load. The tower was designed to reduce visual impact by providing a narrow body with a large open space [30]. Table 2-3 highlights some of the details on the plant [13,27,29,30,39].

Table 2-3 PS10 Plant parameters

Parameter	Value
Site	Sanlúcar M. (Sevilla), Lat 37.4°, Lon 6.23°
Annual Irradiation	2063 kWh/m^2
Nominal power	11.02MWe
Design Point Day	355 (noon)
Solar Multiple/Heat storage capacity	1.15/18 MWh
Tower height	90 m
Field Type	North
Field arrangement	Radial Staggered
Receiver technology	Saturated steam
Receiver geometry	Cavity180°, 4 Panels 5 m x 12 m
Receiver diameter/Receiver Height	10.5 m /10.5 m
Receiver aperture size	13.78 m × 12 m
Heliostats Number	624
Heliostats Number/Heliostat Reflective Surface	981/91 m^2

Heliostat surface curvature Receiver	spherical
Heliostat dimensions	12.84m × 9.45m
Focal Length	500m
Mirror reflectivity	0.88
$\mathbf{o}_{\mathbf{ptical}}$	2.9 mrad
$\mathbf{s}_{\mathbf{un\ shape}}$	2.51 mrad
Thermal storage technology	Water/steam
Thermal storage capacity	15MWh, 50min at 50% Rate
Steam cycle	40 bar 250°C, 2 Pressures
Electric generation	6.3kV, 50Hz -> 66kV, 50Hz
Land	60 Has
Annual electricity production	23.0GWh

2.1.4 Gemasolar

The Gemasolar power plant, owned by MASDAR and SENER, developed by Torresol Energy and previously known as Solar Tres located on 185 hectares in Fuentes de Andalusia (Seville - Spain) began commercial operation in 2011. It is the first commercial plant supplying grid electricity to over 25,000 homes featuring a molten salt receiver with thermal storage capabilities. It is estimated to have around 30,000 tons/year savings on CO_2 emissions [40].

It has a nominal output power of 19.9 MWe with 15 hours thermal energy storage, thus enabling continuous plant operation throughout the day capable of generating 110 GWh/year. Two thousand six hundred and fifty heliostats, developed by SENER of 115m^2 area, having a total aperture area of 304,750m^2, use proprietary technology to track the sun's location. The receiver, external cylinder (16m high and 8m diameter), of 120MWth ratings mounted atop a 140m tower equally developed by SENER, receives radiation from the surrounding heliostat field. Molten salt (60% sodium nitrate and 40% potassium nitrate) is used both as HTF and storage media. Molten salt in the cold tank at 290˚C is heated by the receiver to 565˚C and then stored into the hot tank. To generate power, the hot salt is pumped to the power conversion unit in order to allow the production of superheated live steam at 100 bar and 540˚C. Technical details on the plant are interpreted in Table 2-3 [8,40–43];

Table 2-4 Gemasolar plant parameters

Characteristics	Value
Turbine Power (MWe)	19.9
Capacity factor (%)	70-75
Number of heliostats	2,650
Heliostat reflective area (m^2)	115-120
Total reflective area of the solar field (m^2)	304,750-306,658
Standard deviation surface error σs	0.94mrad
Standard deviation tracking error σt	0.63mrad
Field Type	Surround
Field arrangement	Radial Staggered
Heat Transfer Fluid	Molten salt
Tower height(m)	130-140
Receiver Power (MWth)	120-140
Receiver dimension(m), height*diameter	9-16 * 8-10
Receiver outlet temp/ Cold Storage temp(˚C)	290
Hot storage temp (˚C)	565
Storage Dimension, height * diameter (m)	10.5*23
Storage medium	Molten salt
Storage duration (hrs)	15
Power cycle	Steam Rankine
Annual generated electricity (MWh/Yr.)	110,000
Backup fuel	Natural gas

2.2 Components of the Power Tower System

The components of the power tower system are here broadly categorised into five areas: collector field, receiver sub-system, storage sub-system, heat transport system, and the power conversion unit. In Figure 2-2, the different components of the system are shown.

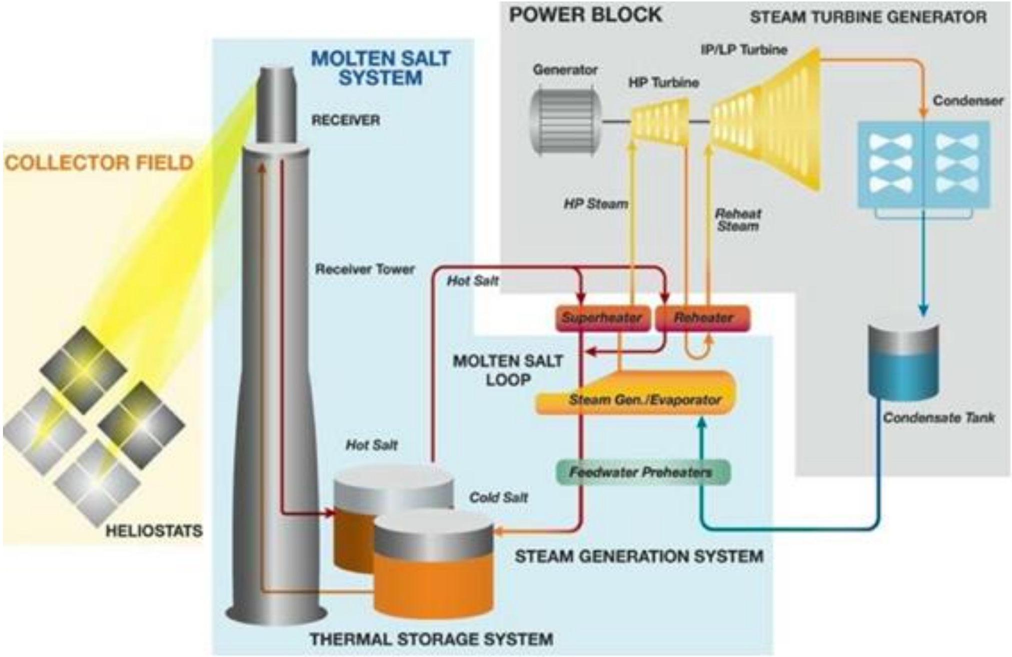

Figure 2-2-Power tower system typical configuration (with thermal storage), [44]

2.2.1 Collector Field

The collector subsystem of a solar central receiver has as its primary function, the interception, redirection, and concentration of direct solar radiation to the receiver subsystem. The collector subsystem typically consists of a field of tracking mirrors, called heliostats, and a tracking control system to maintain the continuous focus of the direct solar radiation on the receiver while energy is being collected. The heliostat, being one of the most critical components, is given a closer look.

Heliostat

A dictionary definition of a heliostat is “a mirror mounted on an axis with solar tracking, by which a sunbeam is steadily reflected to one spot”. The heliostat field is one of the essential components of the tower stream due to its impact on the plant's efficiency. The heliostat also takes the largest share of the plant’s total investment cost [14,45,46]

The reflector constitutes the central element of the collector subsystem. It has a significant role in a power tower system as earlier seen. The reflectors receive the solar radiation, and their optical performance of reflectors directly affects the overall system’s efficiency. The reflector also accounts for the large percentage of the total collector surface and heliostat component’s costs in a solar power plant [45,47].

High reflectance across the solar spectrum with a high level of specularity and durability even in harsh environments are some of the desirable characteristics of reflector materials [48]. Several types of research have been done in the field of reflector materials. The European Union Commission has highlighted reflector material to be one of the initiatives in improving the durability, optical performance and cost of the solar reflector in CSP systems [49]. They provided specific time frames that need to be achieved in the field of reflector materials including improved specular reflectance from 94% to 95-96% by 2020-2030 through the lifetime of the system [49], 25% reduction in reflector cost and 10-30% of severe outdoor conditions operation [14,50].The IEA roadmap milestone for 2018 is the development of light-weight, low-cost reflector optics [3]. The European Solar Thermal Electricity Association's strategic agenda (2020-2025) also identified priorities research area for concentrated solar power, in general, to be in developing light-weight durable reflective surfaces, enhancing anti-soiling properties and increasing the transmissivity of glass [47]. Sandia National Laboratories also highlighted its effort to increase performance and reduce costs of collector materials and systems. They identified testing and evaluation of reflective polymer films for long distance applications as one of their key research areas [51].

Various reflective materials are available for solar collectors, including silvered glass, metallised polymer film, polished and anodised aluminium, with or without anti-reflective coating [52]. Each material used as a reflector brings its own distinctive feature. Many materials used as reflectors have been studied in the past, more than 50 different materials, of which the basic types are: reflective polymer films, silvered-glass reflectors and aluminium reflectors [53].

2.2.2 Receiver Sub-system

The receiver in solar power tower plant usually mounted atop a tower is a crucial component in the system that intercepts and absorbs the solar energy radiated from the heliostat field. It is a crucial element in the plant and determines the conversion efficiency from solar radiation to heat [54,55]. The absorbed heat is transported to the HTF, which flows through tubes joined together in parallel.

Receivers can be classified based on their geometrical configuration and absorber material used on energy transfer to the fluid. Classification based on geometries are the; cavity receivers and cylindrical receivers [2].

Cavity receivers have a restricted field of vision of typically less than 180˚ as reflected radiation from the field passes through an aperture into a box-like structure before hitting on the heat transfer surface containing the HTF [33]. The restricted aperture and enclosure of the cavity-type receiver are essential to reduce the heat losses incurred due to radiative and convective heat losses without blocking incoming reflected radiation as much as possible. Due to the restricted field vision, the cavity receiver naturally supports the polar field heliostat configuration [28]. However, more aperture openings on the same tower could be possible in the type of receiver allowing a greater field of vision and hence a different heliostat field arrangement.

Cylindrical receivers, on the other hand, have a broad surround field of vison capable of absorbing reflected solar radiation from all facets in the field and thus resulting in a surround field configuration. The overall performance in cylindrical receivers exceeds cavity receivers due to the averaged values of cosine maintained throughout the day; as a result of the surround nature of the field [55].

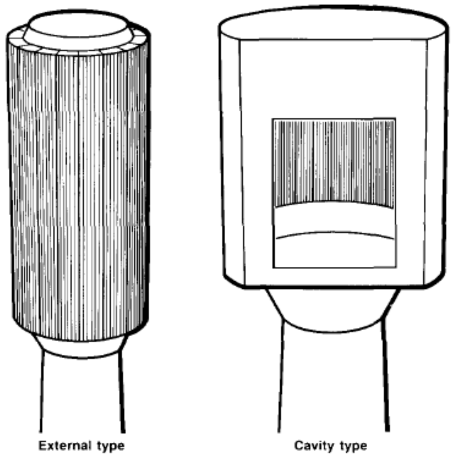

Figure 2-3 External and Cavity type receiver, [33]

Heat flux limitations on the receiver walls formed by the reflected radiation from the field apply to both kinds of the receiver and have to be kept in check in order to avoid surface overheating [55].

2.2.3 Storage Sub-system

Thermal Energy Storage (TES) allows storage of thermal energy collected in the field for utilization during periods of low insolation or later during the night. TES has made a significant impact on power tower technology. It has made it possible to attain higher capacity factors, which can potentially provide for cost-effective, dispatchable electricity capable of serving immediate and base-load power markets at a lower and competitive Levelized Cost of Electricity (LCOE) [3,10,23–25,56]. TES can be achieved directly or indirectly. In direct storage, the energy absorbed by the HTF from the receiver is used directly as a storage medium. In direct storage, the HTF itself is directly used as a storage medium. In contrast, in indirect storage, energy collected by the HTF is transferred to a storage material via a heat exchanger.

TES can be classified based on the mechanism of storage criteria; sensible, latent and chemical storage medium. Simply put, the sensible heat storage involves heating the storage medium, liquid or solid and keeping it isolated until the need for its use arises[8]. It is described as the simplest form of storing thermal energy [55]. Its principle of operation in the power tower system involves a two-tank setup where HTF from the cold tank is heated in the receiver before being directed to the hot tank. Here, the HTF in the tanks and receiver are the same, and hence no heat exchanger is necessary. Careful selection of the HTF is necessary [2,8,55,57].

Latent heat storage involves phase transition of materials. It is a widely investigated area and considered as an alternative to sensible heat storage [2,8,55]. Phase change using Phase Change Material (PCM) have higher energy density than sensible storage and can operate in narrower temperature ranges which provides the potential to store much energy while maintaining a constant temperature [58].

Chemical heat storage is also an area that is still in development and is considered for long term thermal storage involving endothermic and exothermic syntheses [2,57].

The two-tank, sensible-heat thermal storage system utilizing the molten-salt HTF is regarded as the current state of the art in power tower systems. It has been widely commercialized for the technology and other CSP systems as well [25].

2.2.4 Heat Transport System

The heat transport system fundamentally compromises of elements or components used for controlled fluid flow in the system. It mainly consists of the pumping, the piping and the HTF itself.

HTF is one of the essential components in the plant itself and has a contributing factor to the overall system's efficiency. Choosing HTF fluid for an application thus becomes necessary. The criterion for selecting an HTF is based on the characteristics of the fluid. High operating temperature, thermal stability, high energy content, low corrosion, low vapour pressure and low cost are some of the desired characteristics required of a HTF [59–61].

Four fluids have received the most consideration for use as HTF in the power tower systems. These include the water/steam, liquid sodium, molten salts and thermal oil. Amongst these, the water/steam and molten salt fluids are the more widely used solar power systems (See Table 2-1 and 2-2).

Molten-salts are one of the most widely studied HTF, mainly as a result of their high working temperature which is necessary for efficiency improvement in the system [59,60]. It is equally safe to handle, inexpensive and with high heat capacity making them attractive for use as a storage medium. Molten salts are based on nitrates/nitrites, commonly a binary mixture of sodium and potassium [33]. The insufficient worldwide nitrate salt production alongside the thermal limitations of the salts is some of the concerns in this well-touted HTF. However, they are generally categorized as the most favourable HTF [60,62].

The use of water/steam as both HTF and working fluid simplifies the system and leads to improved efficiency, and a potential decrease in the cost of electricity production due to the availability of water. The use of water/steam as HTF is matured and still being currently used in new plants like the U.S Ivanpah solar power facility in February 2014 despite water/steam disadvantages of use as a storage medium [33].

Liquid metals as HTF are also promising candidates due to their wide temperature range and efficient heat transfer. Using liquid metal has been researched since 1940. An experimental plant of 500KW was set up in 1981 in Almeria, Spain to test its performance. The plant, however, folded due to unsuccessful plant operation [61]. The option of liquid metals is still, however, being investigated due to the immense potential of the fluid for reducing costs and increasing plant efficiency, as a result of their efficient heat transfer [63]. One of the major concerns highlighted for the fluid is their relative low heat capacity (around 0.15 KJ/Kg/K) when compared with other HTFs hence making it less favourable for use as direct TES media [63].

The most significant advantage of the use of air as HTF technology is its cost-effectiveness and high efficiencies, due to the abundant nature of atmospheric air [64]. Air also has the advantages of very low dynamic viscosity and excellent flow properties despite the low thermal conductivity of air when compared to molten-salts or liquid metals [65]. The use of air as HTF is relatively new and still under development. A demonstration plant was built at Julich Germany in December 2008 of 1.5MW capacity where air is heated to a temperature of about 700˚C to generate steam [30,60,64].

2.2.5 Power Conversion Unit

The conversion of solar thermal energy absorbed from the field by the receiver into electricity generally requires the use of a thermodynamic cycle and the efficiency of conversion depends on the cycle and its components [2].

Several kinds of cycles of varying types in their design are used for the conversion of heat to electricity. All the cycles, however, have one thing in common; heat harvested from solar collectors is used to power a generator for electricity production. The three most common thermodynamic cycles are the Brayton cycle, the Rankine cycle and the Combined cycle. The most common thermodynamic cycle used is the Rankine cycle [66]. The basic principle of the Rankine cycle applies here as well. Heat for the working fluid of the cycle is supplied via heat transfer with the HTF. The pumped high-pressure liquid is heated in a boiler at a constant pressure to become saturated vapour which expands in a turbine generator to produce electricity.

Solar power tower systems predominately consist of a molten-salt steam generator that feeds a subcritical Rankine cycle with reheat. It has been promoted since the 1980s and has become the current baseline for the power conversion unit[25].

2.3 Plant Configurations

The Power tower concept can be realized in several configurations, which can ultimately be defined by the receiver or by the heat transfer fluid [28,55]. The Power tower concept can be broadly categorised into;

2.3.1 External Cylinder Configuration

The receiver consists of an external cylinder where the absorbing surface can be seen from all directions. The configuration thus supports a surround field heliostat configuration directing solar radiation onto the absorber. This often results in a shorter tower height for given field power. The configuration however exposes the absorber area thereby increasing the heat loss due to convection. Figure 2-4 shows a field with the external cylinder configuration.

Figure 2-4 Gemasolar 20MW plant in Seville with an external cylinder receiver, Spain [67]

2.3.2 Cavity Receiver Configuration

Here, the heated surface is contained in an insulated enclosure having a large aperture where the sun's radiation is refleced onto. Usually, the aperture is directed downward and toward the pole to face an array of heliostats positioned to most effectively illuminate the aperture [46]. Heliostats are primiarily laid out to be on the polar side of the aperture inorder to have the optimial angle of incidence at solar noon. In the morning and afternoon, the cosine losses are significant as a result of the angle of incidence during those periods [46].

Cavity receivers have fewer losses than the external receiver configuration. However, its tower will be taller to collect the same amount of energy[46]. Figure 2-5 shows a field having a cavity receiver with a polar field layout [69].

Figure 2-5 PS10 and PS20 power plant with cavity receiver (Source: Stela World)

2.3.3 Beam Down Configuration

The third configuration is the beam-down concept. Here, heliostats direct their beams at a virtual focus where a hyperbolic secondary mirror is placed which intercepts the light and redirects it toward the ground where the receiver is usually located as in the case of the Masdar Solar Beam Down Plant. See the configuration layout in Figure 2-6.

Figure 2-6 Masdar beam down plant [70]

2.3.4 Multi Tower Configuration

In this configuration, a certain number of towers are introduced in the field veering away from the conventional setup of a single tower system. The heliostats in the field are placed in-between the towers. A more detailed elaboration of the multi-tower system is presented in the following section.

2.4 Multi Tower Heliostat Field

Multi-tower systems have the potential to provide an overall increase in the system efficiency of the plant by reducing some of the losses entailed in a conventional single tower setup due to the possible reduction in attenuation and spillage losses as a result of the tower being closer the heliostats. This could hence increase the annual field efficiency and maximum receiver incident power. The configuration also has the potential to reduce scale-up risk commonly encountered in transition from demonstration to commercialization, reduce the significant risk associated with the take-off of sizeable commercial project plants, eliminating permitting uncertainties associated with massive towers and reducing construction and permitting delays [22].

Although it is only recently that multi-tower configurations have attracted much interest in the research community, the possibility of the configuration has been previously investigated. In 1999, Romero et al. pointed out that the centralised large solar tower plants are at odds with the increase in the shift towards a distributed energy setup and could hence face future deployment difficulties. They proposed and analysed how small tower fields could be integrated into a Modular Integrated Utility Systems (MIUS) approach in order to fully exploit the advantages of a distributed energy setup in a community. The paper advocates for the concept of a few megawatts of installed power of multi-tower systems in order to track demand and meet reliability requirements closely [71].

Schramek & Mills proposed a Multi Tower Solar Array (MTSA) system which consists of a group of solar towers densely located from one another thereby allowing for partial overlapping of the heliostats in the field hence allowing for higher utilization of the solar radiation falling on the unused ground area in the field [72]. In their model, some critical factors that determine field efficiencies like spillage and attenuation efficiency have not been considered. These losses could potentially lead to over 6% reduction in design point efficiency [55] hence resulting in an inaccurate efficiency estimation. The field in this model is laid out in order to maximize utilization of the solar radiation falling on the ground by having as little unused space in the field as possible. Method of placement of each individual heliostat is not optimised and could hence mean an individual heliostat could be reflecting reduced radiation onto a tower. Aiming strategies and techniques have not been fully explored, and issues such as over fluxing effect remain a possibility.

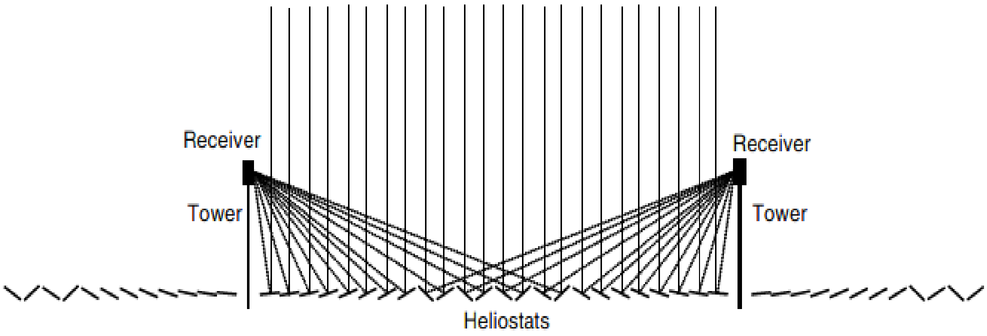

Figure 2-7 MTSA Concept showing field layout with two towers, [72]

Augsburger and Favrat proposed a method for which each heliostat is aiming at a receiver in a multi-tower setup [73]. The aiming criterion established is based on selecting a receiver having the least optical loses from the reflected radiation from a heliostat field hence allowing for estimation of the maximum radiation achievable on the receiver surface. The thermo-economic performance of a maximum of threetower heliostat field was then compared to that of an equivalent single-tower heliostat field. The comparison was made by applying all three selection criteria highlighted above. The methodology used proved that the multi-tower layout has the potential to provide better results in terms of cheaper investment costs and higher field efficiency. They then proceeded to perform a sensitivity analysis on tower separation distance, number of towers and receiver area in order to find the thermo-economic optimum transition size from a single- to a multi-towered plant. This was found to be 63 times the size of the field modelled for the three-tower configuration [73]. The field layout and configuration adopted in their model was from the Gemasolar plant and can hence be argued that field configuration has not been optimised for a multiple tower setup.

In response to a funding opportunity by the US Department of Energy to develop and evaluate utility-scale baseload CSP power plants with a capacity factor of 75% capable of generating electricity at costs competitive prices, eSolar and Inc. (B&W PGG) came together to investigate the power tower system. They decided to deviate from the traditional system and investigate the central power tower system using small heliostats with multiple receivers and towers [74].

They proposed a molten salt facility with 14 solar power towers with a 100 MWe (net) power block that is capable of delivering the 75% capacity factor [74]. Tyner and Wasyluk also presented a follow-through of the conceptual design previously reported by Pacheco et al. where several trade studies were carried out in order to arrive at the optimum and cost-effective system configuration for the multi-tower setup [75]. The concept proposed by Pacheco et al. involves replicating the field, without scaling or redesign in order to meet the capacity required. A conceptual layout of the field proposed is shown in Figure 2-8.

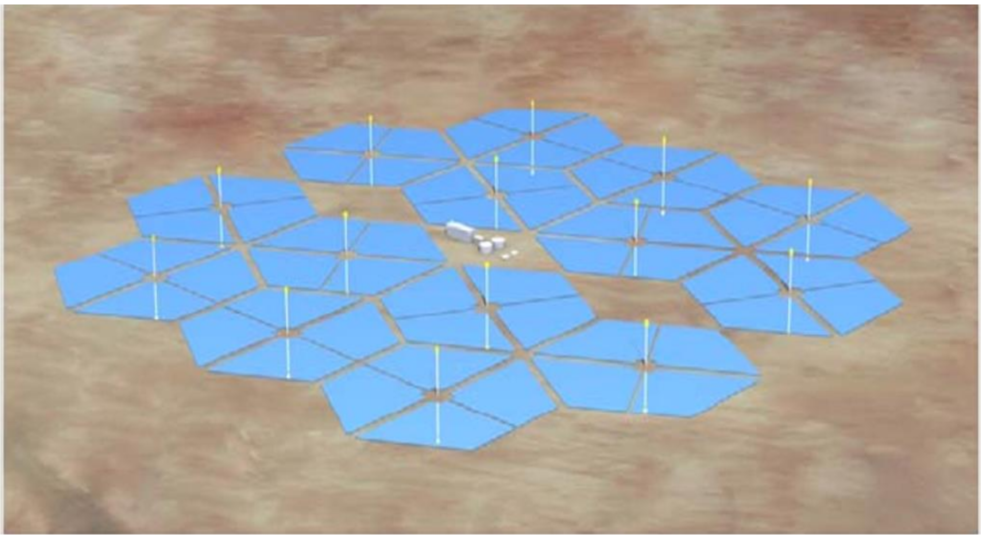

Figure 2-8 Conceptual layout of the 14 towers plant by eSolar and Babcock, [75]

In another work by Pasha Piroozmand and Mehrdad [76], an iterative algorithm was developed in order to obtain the optimum instantaneous efficiency of the heliostat in the field when selecting the tower which radiation will be reflected onto in a two-tower field set up, to maximize the annual optical efficiency of the field. As a case study, the authors used Particle Swarm Optimisation (PSO) to optimally design a two-tower spiral patterned field along the east-west line before redesigning the field using the iterative method. The authors here noted that issues such as field layouts and aiming strategies need to be further investigated in order to achieve a more optimised and comprehensive multi-tower system.

In 2018, Vast Solar, an Australian company engaged in CSP research, developed and commissioned a 1.1MWe pilot plant utilizing a modular solar array field [77]. Each of the five modular arrays in the field has a dedicated tower in which the HTF is heated at the receiver. The multiple towers are connected to a central thermal storage unit. The company is already planning to go further by developing a 30MW commercial demonstration project in Australia using the modular array field.

Multi-tower systems have shown to have numerous advantages over the single tower concept in terms of flexibility in providing power, reduced risks. Also, the concept could potentially reduce some of the optical efficiencies such as blockage, attenuation and spillage losses generally associated with the single towered system due to increasing distance of the heliostats from the tower. However, the possible increase in the LCOE due to the increase in the number of towers, receivers and piping has to be offset by the decrease of optical losses in the field. Hence, choosing the number of receivers and towers remains an important issue. Also, the optimal positions of the towers, heliostat field layout and aiming strategy remain a vital issue and an area subject to further research. The work presented in this research is on the multi-tower system.

As mentioned earlier, the classification of the plant configuration can also be based on the type of receiver and storage fluid. Conventional early receiver systems include the Water/Steam configuration, molten nitrate configuration, liquid sodium configuration and the sodium/salt binary configuration [33]. This classification can now certainly be broadened further with the emergence of several other types of receiver fluids such as liquid metals and gasses are used in solar power tower technologies [60].

Some of the other configurations in the power tower system, mainly defined by the receiver, are the multi-receiver system and the open volumetric air receivers. In the multi-receiver configuration, two more receivers, typically of cavity receiver configuration, are mounted atop a tower in order to achieve higher temperatures and hence higher thermal efficiencies. Each receiver commonly has its own subfield where the heliostats are dedicated to aiming at [78–80]. With open volumetric air receiver, radiation loss to the atmosphere is significantly reduced. The technology in itself is still under investigation. It entails the use of extremely porous materials as receivers where the reflected radiation from the field aims at hence providing a lesser temperature at the front of the receiver than the outlet air temperature due to volumetric effect [81].

2.5 Heliostat Field

In heliostat fields, the layout and pattern in which the heliostats are arranged, size of heliostats, type and dimensions of receiver and height of tower are crucial factors that have a weighing effect on the overall plant efficiency. As a result, decisions regarding the best position for locating heliostats relative to the receiver and how high to place the receiver on the tower need to be carefully studied.

Ideally, without optical losses in reflecting solar radiation onto the receiver, heliostats can be placed densely and close to the tower in order to maximize the amount of reflected solar radiation. However, due to the losses, heliostats have to be spaced away from one another and placed in regions with medium or low optical efficiency. Spacing heliostats out also means reflected radiation would have to travel further distances, up to 1 kilometre (KM) or more for larger plants before arriving at the receiver [82]. The local heliostat density at any point within the heliostat field is determined through a trade-off of cost and performance parameters influencing the pattern of the field. As heliostats are placed further from one another, the total reflected power reduces, and hence, more heliostats are needed to achieve the target power.

As a result, careful design of the heliostat arrangement pattern and optimisation of parameters that define the pattern of the heliostat field is essential for an economically viable power tower system.

2.6 Heliostat Performance Factors

2.6.1 Losses

The optimisation or design of a field layout is made with consideration of the energy losses in the heliostat field. These losses typically are: spillage loss , mirror reflectance loss, cosine loss, shading and blocking loss, and attenuation loss.In order to minimize these energy losses, heliostats have to be arranged and configured correctly [13,17,83]. An understanding of the ‘loss’ mechanism affecting heliostat field performance is useful in achieving layout patterns and an optimised field layout.

Spillage loss

The interception or spillage efficiency loss refers to the spilt reflected radiation from the heliostats that does not reach the receiver. The factor is dependent on both the heliostats in the field and the receiver design and its properties [17,84].

Mirror reflectance loss

Only a certain percentage of incident beam radiation on the heliostat surface can be reflected to the receiver. This is due to the manufacturer's specifications, coating properties and particular status (damaged or dirty) of the heliostat's reflective surface [17]. The mirror reflectivity comes second only to the cosine effect in having the most significant effect in the field's total optical efficiency [15]. Despite the increase in reflectivity of modern-day reflective surfaces, age and dust can reduce the reflective properties. Keeping the mirrors clean is hence essential.

Cosine loss

Cosine losses are realized when the collector is not perpendicular to the incoming DNI [55]. It can be is defined as the cosine of the angle formed by the incident solar beam radiation and the vector normal to the reflective heliostat surface [85]. Cosine loss is one of the most significant loss values and may be minimized through proper field design [55].

Shadowing and blocking loss

Shadowing and blocking loss efficiency factors are typically referred to as in the different works of literature as the most complicated to establish due to the complex computational effort [18,83]. This is because it is not only dependent on the position of the heliostat beingi analyzed, but also on the neighbouring heliostats. It has to be evaluated every time the position of the heliostats changes during optimisation.

Shadowing losses decrease the incoming solar radiation hence reducing the heliostat's useful area. This is due to the partial shading caused by its neighbouring heliostats or even due to the tower itself [83]. Shadowing is a phenomenon mostly seen at low sun angles [55]. Blocking losses, on the other hand, is as a result of the reduction of the heliostat's useful area, due to the presence of a heliostat in the path of the reflected radiation.

Attenuation loss

The reflected radiation from the heliostat does not reach the receiver wholly as some of this energy is scattered and absorbed by the atmosphere. Atmospheric attenuation consists of energy losses in the reflected radiation while going through the atmosphere from every heliostat to the receiver. Attenuation loss is an efficiency factor that is typically dependent on the distance of the heliostat relative to the tower, the aerosol distribution at the ground level and site altitude [86]. On a good visibility day, the energy loss will be a small percentage of energy loss per kilometre.

2.6.2 Objective Function

In solar power tower design, it is vital to identify the criteria that will drive the design. In order to design a heliostat field optimally defining an appropriate objective function becomes essential. Several parameters can be identified as the objective function. Some of the parameters commonly identified in the literature are the LCOE as see in [87], the annual optical efficiency of the field as in [45,88], the yearly irradiance weighted efficiency [17,85] and the total intercepted energy at the receiver aperture [89].

2.7 Heliostat Field Layout

As mentioned earlier, the heliostat field in solar tower systems is one of the most important subsystems due to its large contribution to the plant's total investment cost. About 40-50% of the plant's cost is attributed to the collector field [13–17]. Moreover, the field equally amounts to overall plant's power loses of about 40% [13,18–21]. It has, therefore become important to ensure that the field layout is the most optimal at collecting energy from the sun. The design and optimisation of the heliostat field is an active area of research with new optimisation tools and layout patterns actively investigated. Several methods have been proposed to improve heliostat field efficiencies and reduce losses either by improving through optimisation or suggesting new heliostat field layout pattern entirely. These methods are necessary because both the optimisation process and design of the field are a multi-faceted problem.

Lipps et al. [90] presented different field patterned layout configurations that could be applied in a heliostat field; cornfield (north-south and radial) and staggers (north-south and radial). After optimisation study of the two distinctive types of patterns in a 100MWe plant model, the stagger configuration (north-south staggers and radial staggers) was found to have better performances than the cornfield configuration.

Focusing on optimizing the shadowing and blocking effect between heliostats in the entire field, Collado and Guallar [18,43,91] developed a code-named Campo which is capable of performing considerably faster and more accurate calculations of the shading and blocking efficiency. The code builds on the radial stagger configuration to generate its layout. The layout data structure generated by the code allows an efficient selection of the relevant blocking and shading neighbours in calculating the azimuthal distance for each heliostat zone.

Reiner Buck [21] presented a method that is intended for further performance improvement of the field after an initial layout has been generated using any of the standard field layout tools. During the field optimisation, heliostats are repositioned, with or without restrictions, one after the other. This method was applied to the PS10 tower field, and an improvement of 0.8% intercepted energy was achieved owing to lower cosine losses after 145 simulation cycles.

Sanchez and Romero [82] proposed a methodology for the generation of heliostat field layout where the heliostats are not restricted by their position in the field. The Heliostat Growth Method (HGM) method proposed involves using the yearly energy usable at every pre-defined grid in the field referred to as YNES (Yearly Normalized Energy Surface). This way, the full energy potential of the field can be gauged before considering field losses. Shadowing and blocking are eventually analyzed and included in the final layout proposed.

S.L. Lutchman [89] presented a gradient-based algorithm for optimisation and field design process. The algorithm is based on sequential-approximate optimisation and quadratic approximations. Through successive iterations of sensitivity computations and field analysis, heliostats can gravitate freely to points that produce an optimal overall field performance. The proposed algorithm was applied to the PS10 redesign, and an improvement of 1.2% was achieved in the annual intercepted energy.

Yingxue Yao et al. [39] proposed the Annually Equivalent Efficiency Distribution (AEED) methodology where mean annual optical efficiency is selected as the optimisation criteria for heliostat field generation. Heliostats are added sequentially based on the annual efficiency distribution calculated in a bid to attain maximum optical efficiency. The layout methodology enables the heliostats in the field to have a higher degree of freedom. The PS10 field was redesigned using this method, and a field improvement of 0.57% was attained.

Besarati and Yogi Goswami [85] presented a graphical method for speeding up the computational time for the calculation of shading and blocking and hence speeding up the optimisation process of the field layout process. By providing a graphical representation of a particular heliostat in the field, neighbouring heliostats with the potential for shading and blocking are identified and included in the design and optimisation process, eliminating the rest of the heliostats in the field thereby speeding up the process. The shading and blocking efficiency itself is calculated by using the method proposed by Sassi [92]. An optimisation is performed as a case study to determine the optimal layout of the field for a 50MWth power tower plant in

Dagget, California, using this algorithm. The result obtained showed similar results with other works of literature.

Noone et al. [13] Introduced a completely new layout for heliostat field placement. The pattern, spiral pattern, inspired by disc phyllotaxis, was applied in heliostat field design and optimisation. An attempt to redesign the layout in the PS10 field showed improvement in the optical efficiency and a reduction in the land area utilized. The work shows that the spiral pattern method generated can perform better than the radially staggered layout fields. The pattern places more heliostats in a higher efficiency location of the field and hence would increase the overall field efficiency. The code presented by Noone et al. also provides a fast and accurate method in the calculation of shading, blocking and spillage by discretization of the heliostat surface. This discretization approach was also applied during the spiral pattern layout optimisation.

Pouyan Talebizadeh et al. [93] used the genetic algorithm (GA) as a search technique for the optimisation process of a surround field layout. The radial staggered layout is used in the heliostat layout. The most efficient heliostat field for a given receiver tower is optimised. Heliostats are optimised one after the other until the target power is achieved.

Guillermo Ortega and A Rovila [83], presented four different methods -namely: simplified ray-tracing, contour deployment, homology, and boolean operations for the evaluation of the shading and blocking efficiency of each heliostat in a central tower system. The heliostat field layout optimisation methods presented are aimed at increasing accuracy and reducing the computational time in calculating the shading and blocking efficiency.

Maimoon Atif and FA Al-Sulaiman [94] developed an optimisation model using differential evolution. The optimisation of the field is equally based on the radial staggered layout arrangement. Five optical performance parameters: the mirror or the heliostat reflectivity, the cosine factor, the atmospheric attenuation factor, the shadowing and blocking factor, and the intercept factor are all taken into consideration in the optimisation process in order to get both the weighted and unweighted annual efficiency.

Garcia et al. [84] presented an efficient and accurate method for calculation of the spillage losses in the field for each heliostat. The method adopts the model developed by HFLCAL in which the reflected image of each heliostat is described by a circular normal distribution [95] in calculating the spillage. The method also enables calculating the incident power at the receiver. Due to the simplicity of the method, the computational time for heliostat field optimisation is significantly reduced.

A new method for the design and optimisation of the heliostat field was proposed by Wei, X. et al. [16]. The method proposes different constraints based solely on the receiver's geometrical aperture and an efficiency factor (product of the annual cosine efficiency and the annual atmospheric transmission efficiency) in heliostat field layout design and optimisation. By using boundary constraints, the speed of calculation for design and optimisation of the field is greatly improved as the method generates the position of the heliostats from the very onset based on positions with higher cosine, interception and attenuation efficiencies. The method was translated into a tool named Heliostat Field Layout Design (HFLD). Different styles of layout, including the radial staggered, radial cornfield, and parallel stagger are considered in the tool. Redesign of the PS10 plant showed similar optical efficiencies.

Siala and Elayeb [96] presented a graphical method for a no-blocking heliostat field layout in the radial staggered distribution style. The arrangement ensures that no heliostat is placed directly in front of another heliostat in adjacent rings, thus ensuring that reflected beam passes through cleanly to the receiver. The method was later developed into a C++ the MUUEN. The method is deemed suitable for the preliminary heliostat field layout design phase.

Zhou et al. [97] used the Monte Carlo ray-tracing method based on Graphics Processing Unit (GPU) to calculate the annual optical efficiency of a solar tower field to a high degree of accuracy in a limited amount of time. GPU computing makes it easier to optimise and design the field layout. The method was used on radial staggered and cornfield field distribution style of heliostat arrangement.

In a paper by N.C. Cruz [17] et al. parallelization strategies were proposed and analyzed in order to achieve an objective function in heliostat field optimisation. Parallelization has shown to be extremely useful in speeding up computation during optimisation. Problems whose objective function is demanding on memory and CPU can also be easily solved using this strategy.

In another paper by N.C Cruz, Hector, a new methodology for continuous and pattern free heliostat optimisation was developed [98]. The approach optimises heliostat coordinates on a continuous search space. The underlying principle of operation involves iteratively deploying heliostats one identified promising sector at a time.

Francisco J. Collado in [99] identified the need to set a preliminary layout of the field in order to kick start the optimisation process. In his work, heliostats positions are initially defined by two parameters; blocking factor and security distance based on the radial staggered method, making initial layout design to be implementable quickly before optimisation, and other factors are considered.

Kei Ouchi et al. [100] showed that an accurate relationship between the heliostat layout and the concentrated solar radiation of each heliostat could be obtained by using the potential distribution of optical interference. This was established by applying a method for visualization, which makes it possible to obtain a new layout by visually viewing areas with optical heliostat interference. The method allows a considerable reduction in computation time by applying an approximation technique to the visualization method. Optimisation of other design like heliostat size and tower height is also mentioned to be possible by the authors.

A. Ramos and F. Ramos [101] proposed a method capable of improving plant design and accelerate optimisation procedure of field layout, tower and receiver characteristics by limiting the number of design variables to the only key and influencing variables.

E. Carrizosa et al. [102] presented a new pattern free heliostat field layout distribution style obtained by the simultaneous optimisation of both heliostat field (heliostat locations and number) and the tower (tower height and receiver size). A greedy-based heuristic algorithm method is adopted in the optimisation process.

Deng L et al. [103] proposed a new pattern on the heliostat field layout: Rose pattern based on the classic radial staggered configuration. The pattern divides the radial staggered configuration into six sectors, and some of those sectors are then optimised separately, thus increasing the optimisation variables. The work also developed an advanced DE algorithm with mutation strategy in order to reduce the computational expense in the optimisation process due to increased variables. The results show a higher optical efficiency value when compared to the optimised radial staggered field presented.

Some of the models and ideas have been translated into software packages. These software tools are intended to assist users during the process of studying and designing the heliostat field in a power tower system. An extensive review on some of these software packages has been done by P. Garcia et al. [104] and N.C. Cruz et al. [105]. In their work, the general conclusion drawn is that the numerous tools available can be categorized into two; optimisation codes and performance analysis codes. Performance analysis codes focus mainly on solar flux calculations of defined heliostat fields by applying ray-tracing techniques (often used to check flux calculations from field optimisation software). The emphasis on this project is on the tools focusing on proposing heliostat field layouts and optimisation.

2.7.1 Field Layout and Optimisation Tools

DELSOL

DELSOL is a FORTRAN code that consists of a detailed model of the optical performance, a simpler model of the non-optical performance, an algorithm for field layout, and a searching algorithm to find the best system design based on energy cost [106]. It is an application that can perform analysis design and optimisation of the power tower systems. The code is based on the radial staggered configuration of heliostat arrangement where performance is evaluated based on zones formed by sectioning of the heliostat field. DELSOL uses an analytical convolution method model in generating flux images of an analysed heliostat field. This method requires less computing time and hence making it code one of the faster tools available [33,104,107].

SAM

The System Advisor Model (SAM) is a performance and financial model developed by the National Renewable Energy Laboratory (NREL) targeted for people in the renewable energy industry field. In the solar power tower model of the tool, SAM is capable of optimising the heliostat field by integrating with DELSOL in previous versions. However, in the later versions, SAM integrates with SolarPilot, equally developed by NREL, in field optimisation which uses computationally efficient Hermite expansion technique applied each heliostat image, rather than to entire zones as seen from DELSOL. The field design optimisation strategy is based on six steps, as highlighted in the user help manual [108]. The strategy revolves around initially forming an oversized radial staggered field before progressively removing the worst-performing fields based on cosine, intercept, attenuation, reflectance and blocking field energy losses.

HFLCAL

HFLCAL code (an acronym for ‘‘Heliostats Field Layout Calculations’’) was initially developed in 1986 for the GAST hybrid concept. Recently though, it is primarily used for power tower modelling by DLR researchers. HFLCAL uses annual performance calculation for layout and optimisation of heliostat fields in power tower system. In HFLCAL the reflected image of each heliostat is described by a circular normal distribution (generated from the convolution of the sun shape, the slope error, the tracking error and astigmatism) on the receiver surface [95]. This hence makes it easier and faster to calculate the total energy collected and the flux distribution.

In other works of literature on heliostat layout and optimisation, some innovations were made on the field by way of altering or increasing some of the components in the field. P.Cadiz [15], for example, presented shadowing and blocking optimisation procedures for a variable geometry heliostat field. Variable geometry concept explored by the author allows a possibility of minimizing the cosine losses by rotating the entire field.

In a similar vein, Mohammed Aldulaimi and MS Soylemez [19] suggested a new heliostat field layout arrangement by identifying heliostats with low optical efficiency and increasing their heights in a bid to curb blocking losses and hence increase the total annual field efficiency.

Emilo Carrizosa [109] also suggested some alterations in the field by considering a field with different heliostat sizes. Expansion-contraction algorithm was used to in addressing the problem of optimisation in a field with different sized heliostats. They did conclude that with cost and size band of heliostat they worked with, there are no clear advantages.

Mani Yousefpour Lazardjan [110] presented a tool developed at solar-Institut Julich (SIJ) primarily for the optimisation of a novel micro-heliostat concept. They did mention that the tool developed could also be applied to conventional heliostat field.

In a novel and unconventional heliostat field layout design, Danielli et al. [111] developed the Concatenated Micro-Tower (CMT). In the configuration, dynamic receiver allocation mounted arrays of tower enable heliostats to direct sunlight with minimal cosine loses, thus improving the field' s overall optical efficiency.

Another unconventional heliostat field layout design involves including multiple towers, each having its receiver mounted atop, into the field. In doing so, the arrangement and configuration of the heliostat will equally have to change. The literature on multi-tower configuration has been looked at in the previous sections.

Chapter Summary

From all the works of literature observed, it can be seen that most of the methods and tools for field layout and optimisation either present an entirely new method for heliostat arrangement aimed at improving optical field efficiencies or are focused on optimisation of a particular parameter(s) that define a pattern in order to obtain a specific objective function or reduce optimisation computational time.

Layout patterns can be subcategorized into two; patterned and pattern-less field layout arrangement. Patterned field arrangement includes; the staggered and cornfield configurations as presented by Lipps et al., the biomimetic spiral layout as presented by Noone et al. The classical radial staggered has been the most widely used pattern in heliostat field arrangements, and that is why most of the optimisation techniques in the literature are aimed at improving the radial staggered pattern. However, the new biomimetic spiral layout presented has shown to provide higher optical efficiency, and lesser land area requirement, when compared to the PS10’s radial, staggered field arrangement. Also, several pattern-less field layout arrangements have been developed. The reviewed pattern-less layouts include the Heliostat Growth Method (HGM) method from Sanchez and Romero, the Annually Equivalent Efficiency Distribution (AEED) method from Yingxue Yao et al., Kei Ouchi’s layout method, E. Carrizosa et al.’s Greedy based method and N.C Cruz’s Hector. The configurations generally rely on the distribution of a parameter (energy or losses) around the field in order to gauge where best to place the heliostats. An exception to the pattern and pattern-less layout is Reiner Buck’s field refinement method where heliostats position in the field generated from standard layout tools are repositioned with or without little restrictions one after the other.

The review performed on the tools showed each one of the tools had their strengths, but equally, they come with their limitations. For research, one wants a tool with the capability and flexibility to model their particular system or application. It is suggested, therefore that the option of developing and writing one’s own tool should not be overlooked. A power tower system researcher needs not to start from scratch. Several papers have been published in which the mathematical models and algorithms have been described in detail to allow readers to develop their own code.

Due to the energy and economic impact of the heliostat field, all the methods and tools are aimed at providing field improvements. For this reason, several efforts have been made in the form of veering away from the conventional setup of the power tower system, by introducing or altering some component in the fields as seen in the works of literature discussed. This can be seen by some works like the variable geometry field by P. Cadiz, CMT by Danielli et al. and the multi-tower concept. The basis of this work is to investigate multi-tower concepts. The chapter hence emphasized review on the works of literature on the heliostat field.

3 PLANT DEFINITION

The chapter initially discusses the energy situation in Nigeria alongside the policies and strategies that guide the development of CSP systems in the chosen case study region, Nigeria. The parameters and procedures that need to be established before the design and configuration of a CSP with emphasis on the power tower systems will also be outlined. It is imperative to define the undertakings of a solar thermal plant as it is a critical prerequisite to establishing and developing the system. Emphasis is given to the heliostat field of the power tower CSP system.

3.1 Introduction

To the developed countries of the world, turning to sustainable and renewable energy provides an alternative to the finite fossil fuel resources, security in the energy sector and a reduction in greenhouse gas emissions. However, this is difficult for some, especially the developing countries because they are trying to catch up to the industrialised world so that they could achieve the same level of development. A somewhat debatable point because the global year 2000 data on CO_2 emissions shows that sub-Saharan Africa has 2 tons of CO_2 emissions per year per person and the industrialised nations like the United States have emissions reaching up to 25 tons of CO_2 emissions per year per person [112]. However, rising oil prices and the global initiative on mitigating greenhouse gases emissions have led people in the region and development communities at large, to resort to renewable energy for the combined benefits of providing cleaner energy, regional socio-economic development and fuel diversity and security.

Energy is a means to an end, vital to the eradication of poverty and meeting the Sustainable Development Goals (SDGs). Nigeria is experiencing an energy poverty crisis. Nigeria is home to an estimated 195 million people constituting of 36 states. The Human Development Index (HDI) of the United Nations Development Program (UNDP) ranks various countries in the world based on their level of human development. Education, life expectancy and Gross National Income per capita (GNI) are the primary sources of data for the indexing. Sub-Saharan Africa has the least HDI value in all regions with Nigeria ranked a poorly 157 out of the 189 ranked countries [113]. An estimated 65% of the population live in rural communities. The rural access to electricity is among the poorest in the world at 22.6% [114]. Most of the rural communities are not even connected to the national grid due to the high cost associated with it. With all these data, it is easy to see the correlation between poverty and energy. Emphasis must be put on the provision of proven sustainable energy in those regions.

Specialists often append the power sector in Nigeria as one of the critical constraints to the economic development in the region. Assessing the ease of getting electricity, the World Bank ranked Nigeria 146 of 190 countries in the Doing Business report of 2019 [115]. Once connected to the electricity provider, the erratic power supply remains a constant feature. Power failures experienced in the year 2000 alone led to power rationing and this, in turn, profoundly affected their economies and development [116]. In a bid to improve the reliability and stability of electricity, the government privatised the electricity sector in the year 2013.

Renewable energy technologies, in general, have great promise in Nigeria and could potentially meet all the energy demands in the region. However, most of that potential is either underexploited primarily due to poorly integrated structures, weak policies and planning, and technical and financial reasons or improper implementation.

3.2 Energy Situation in Nigeria

Nigeria is Africa's largest producer of oil, with proven reserves of 37 billion barrels and 5 billion cubic meters of gas reserves [117]. The country is heavily dependent on the oil and gas sector, which accounts for about 10% of the country's Gross Domestic Product (GDP). It is no surprise as to why the country relies on its fossil fuel resources for energy provision. Figure 3-1 shows the development of various energy sources over the years. Energy provision from biofuels and waste has risen in absolute terms, while oil and natural gas has remained relatively constant. Despite the country's strong potentials for renewable energy, there was no significant supply from geothermal, solar and wind up until the year 2011.

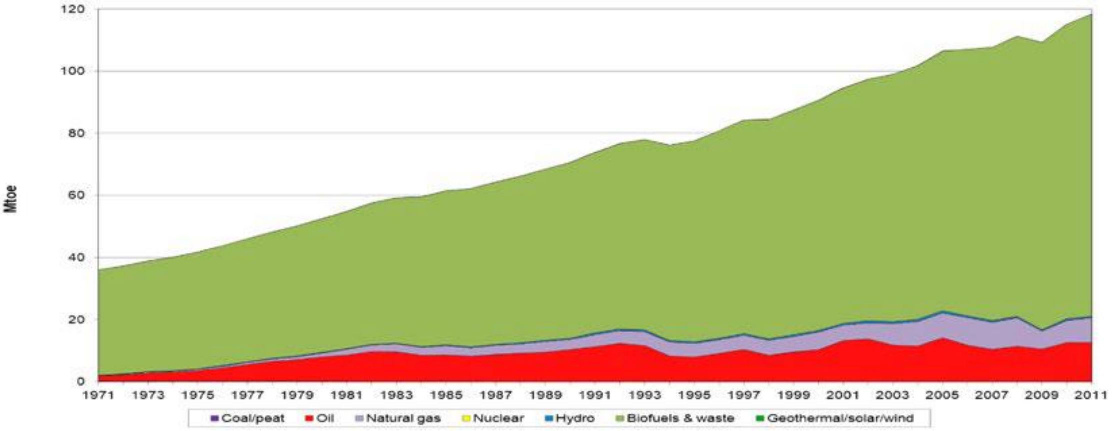

Figure 3-1 History of energy development in Nigeria [118]

The existing power plants generate about 8,441MW as at January 2019 [114], this is well short of the 35,000MW generation capacity required to support the vision of making Nigeria one of the 20 largest economies in the world; Vison 20:2020 [119]. However, unavailability of gas, breakdowns, water shortages and grid constraints severely limit the power plant performance.

In a 2013 survey, as a result of the erratic or nonexistence of power from the grid, about 80% of the Nigerians took to an alternative source of energy such as generators or solar inverters for electricity supply. Estimates suggest that between 8-14 GW of decentralised diesel generator capacity is installed in the country [120]. This has made Nigeria to lead Africa in generator importation and one of the highest importers worldwide.

There is an imperative need to aggressively develop the nation’s renewable energy resources in order to be able to meet the country’s ever-increasing demand for energy [119]. Vision 20:2020 also ties in with the government's National Adaptation Strategy and Plan of Action on Climate Change for Nigeria (NASPA-CCN) policy adopted in September 2012 in order to implement and check climate change activities in the country [118]. The policy charts a course for incorporating climate change adaptation in sustainable development; a policy that falls in line with the United Nations Framework Convention on Climate Change and the Kyoto Protocol.

In another initiative by the government, encouraged by the NASAPA-CCN, The Renewable Energy Master Plan (REMP) master plan was formulated. Although the plan does project that the energy generation backbone will remain gas for the foreseeable future, solar energy-related technologies are forecasted to exceed all the other sources, with the exception of gas-powered plants [121]. Table 3-1 shows the renewable energy potentials in the country.

Solar thermal energy for electricity generation is typically referred to as Concentrated Solar Power (CSP) [3]. CSP can potentially be a driving force in the cause of reducing CO_2 emission and could be a viable and promising option for Nigeria.

Table 3-1 Renewable energy potential in Nigeria, 2014 [121]

Resource	Potential	Current Utilization and further remarks
Large Hydropower	11,250MW	1,900 MW
Small Hydropower	3,500MW	64.2 MW
Solar	4.0kWh/m2/day – 6.5 kWh/m2/day	15 MW (estimated)
Wind	2-4 m/s at 10m height mainland	Electronic Wind Information System (WIS) available. 10MW built but not operational

Biomass (non-fossil organic matter)	Municipal waster	0.5kg/capital/day
	Fuelwood	43.4 million tonnes/yr.
	Animal waste	245 million assorted animals (2001)
	Agricultural waste	91.4 million tonnes/yr. produced
	Energy crops	28.2 million hectares arable land, 8.5% cultivated

3.2.1 Policies and Strategies

Nigeria’s energy policy aims at the overall increase in power supply from renewable energy sources, thereby increasing the role of energy in sustainable energy development. The details of the documents, drafted by the Energy Commission of Nigeria (ECN) and the UNDP, were outlined initially in the Renewable Energy Master Plan in 2005 updated again in 2012. Based on the plan, Nigeria intends to increase the supply of renewable electricity from 13% of total electricity generation as at 2015 to 23% in 2025 and 36% by 2030 thereby making Renewable electricity account for 10% of Nigeria’s total energy consumption by 2025 [120]. This potentially will make Nigeria exceed the ECOWAS regional policy targets for renewable electricity generation and energy efficiency for 2020 and beyond. The policy also highlights the role solar power could provide in the country’s energy mix; providing 1,300MW by the year 2020 and 6,800 MW by 2030 [121].

Currently, Nigeria has no commercial nor demonstration solar thermal CSP plant for electricity generation in the country. Also, the policy documents do not explicitly highlight the development of such technology. The technology can, however, be supported by the technical expertise and renewable energy research centres in the country. Primarily, one of the research centres, Sokoto Energy Research Centre, Energy Commission at Usmanu Danfodiyo University, Sokoto, Nigeria which has made much research on low and medium temperature solar thermal energy systems [122]. Technology, cost and inadequate clear policy directions are some of the significant barriers to the development of CSP in Nigeria.

Data from the International Renewable Energy Agency (IRENA) show that the global weighted-average LCOE for CSP systems have all fallen quite drastically by 46% between 2010 and 2018 (Figure 3-2).

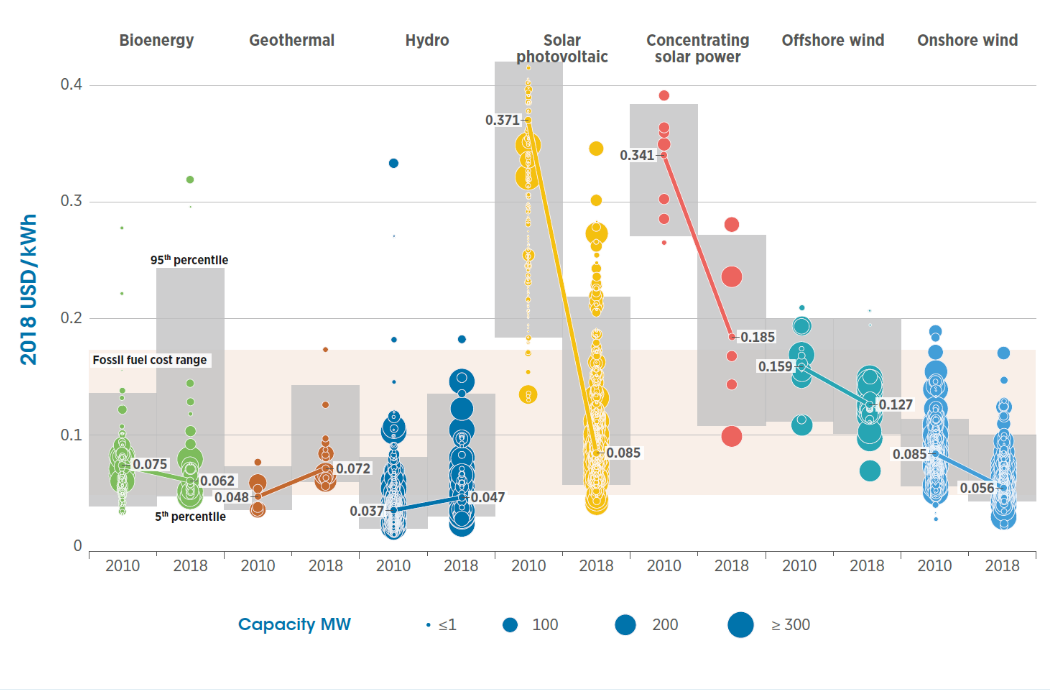

Figure 3-2 Global LCOE of utility-scale renewable power generation technologies, 2010–2018 [123]

Although the global weighted-average electricity costs are in the top half of the fossil-fuel cost range, their costs, however, continue to fall, suggesting that between 2020 and 2022, the technology become highly competitive [123]. Also, the role the technology has on sustainable energy provision and greenhouse gas mitigation, the country needs to put in the right strategies and policies in place.

Some of the strategies highlighted in the policy document include intensifying research, training and development, and providing fiscal incentives for the installation of solar energy systems. However, given the enormous potential of CSP systems, the country needs to establish further regulations specific to CSP and offer incentives for investors, both local and foreign so that the technology may be taken up in the soonest.

3.3 Site Selection Criteria and feasibility analysis

The site selection process for CSP systems, in general, leads to the potential identification of sites for deployment. The decision here is mainly based on the technical concept. Technical concepts refer to project economics, regional government guidelines and restrictions in addition to other technical aspects such as solar irradiance, site characteristics and infrastructure connection [124]. Martin Schlecht et al. provided a general layout for the CSP site selection and qualification process, as highlighted in Figure 3-3 [124]. The scope of the feasibility study in this project is focused on the technical aspects.

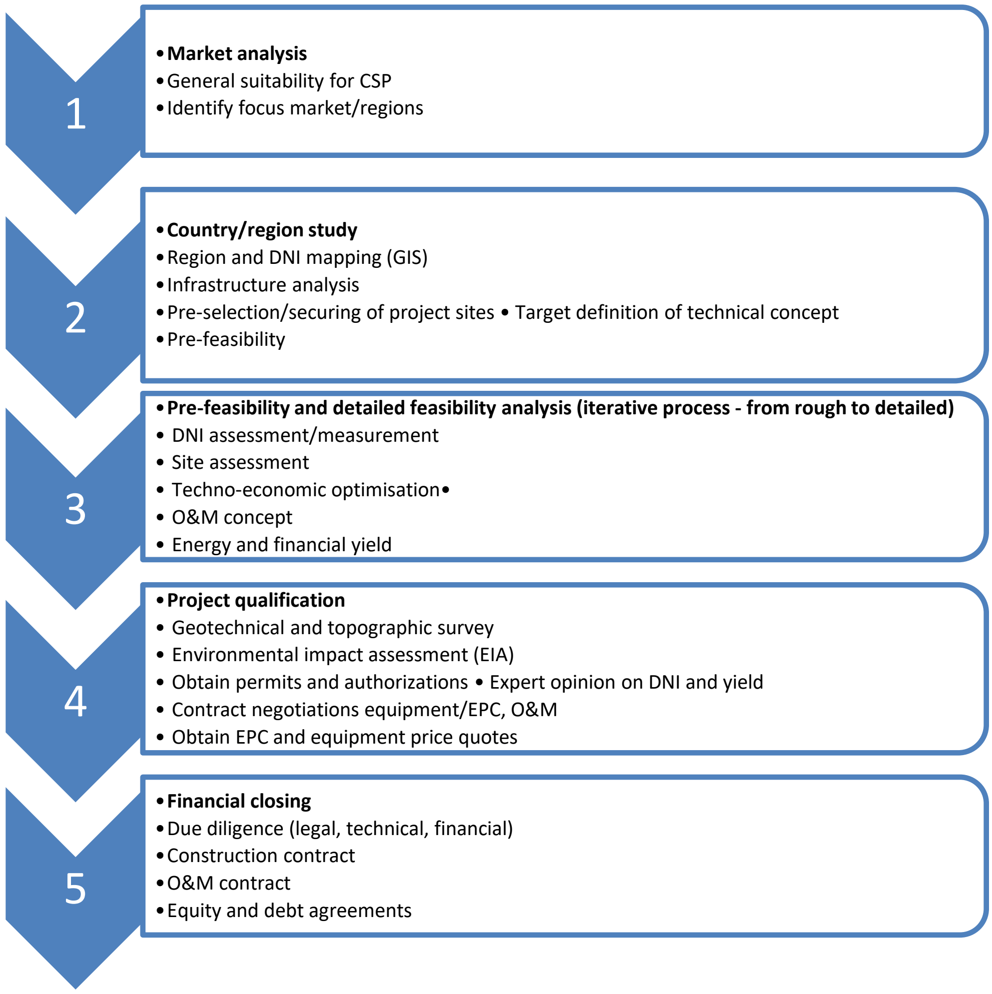

Figure 3-3 CSP site selection and qualification process [124]

For solar power tower technologies, some of the primary criteria used for site selection include insolation, land use and land cover and infrastructure [22,125–127]. The selected site is located at latitude $12°.393'$ and longitude $7°.496'$. A Google Earth snapshot of the location is shown in Figure 3-4.

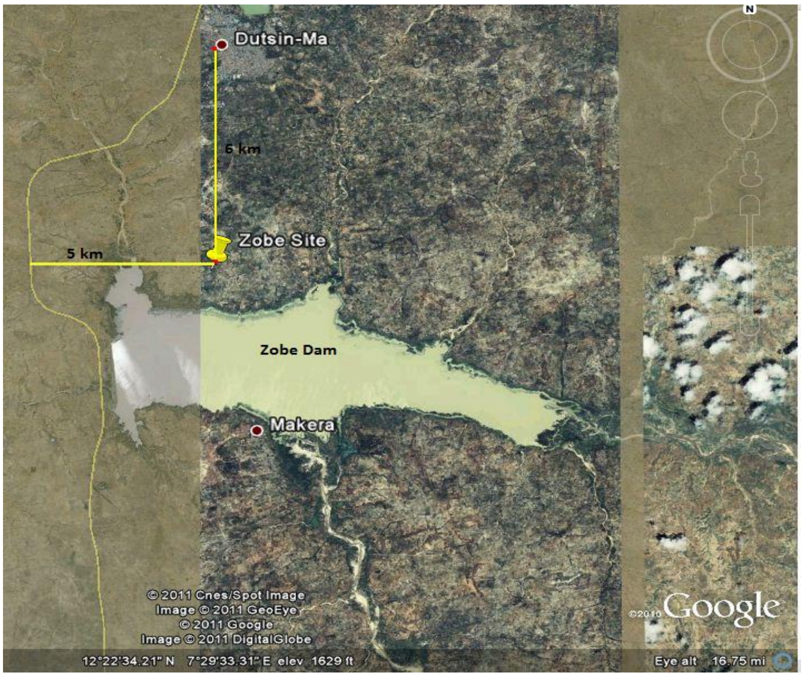

Figure 3-4 Identified site for CSP Installation

3.3.1.1 Assessment of land use and land cover

The amount of land required for a solar power tower plant can be attributed to the configuration of the plant, the electrical power output of the plant and the solar multiple. As a rule of thumb, the minimum land area requirement for CSP plants is 5 acres per MW of electricity production [128]. For large power tower plants, a higher land requirement of about 8 acres per MW of electricity [33] is expected. Flat land is preferable. However, an overall slope of about 4% is deemed acceptable [10], although at the price of a higher cost.

Another essential factor in sighting the power tower or any plant for that matter is the potential agricultural or residential use of the land. Wastelands unsuitable for agricultural and residential purposes are preferable in siting the plant.

The large area of land required to set up a CSP plant can be comfortably met with the selected site. Although the area has been used by local farmers to grow crops, the land is not, particularly of high agricultural value and biodiversity. The vegetation mainly consists of stunted baobab and cotton trees scattered across the lands. A cluster of trees is found only where the afforestation program has been put in place [129,130]. The soils are slightly acidic, mostly of loamy, sandy surfaces having low to medium fertility [130]. This makes the land a suitable candidate for CSP installation. The site itself has slight to moderate slopes in the order of 1°-2°.

3.3.1.2 Assessment of Infrastructures

Access to transmission line, roads and water are some of the feasibility studies that have to be made before deployment of the technology. The availability of water makes it possible to employ wet cooling in the plant; otherwise, dry cooling must be employed.

The proposed site is ideally located close to the 2x60MVA, 132/33kV transmission substation that connects Dutsinma to the national grid. One of the primary reasons for selecting the site is the presence of Karaduawa River. This enables the use of steam cycles. Also, the proximity enables the plant to utilise wet evaporative cooling; hence, potentially reducing parasitic plant losses and investment costs sustained should dry cooling be utilised [131].

3.3.1.3 Assessment of solar radiation resources

Solar power tower only utilises the Direct Normal Irradiance (DNI) due to its directional properties which can be accurately utilised in concentrating solar radiation onto the receiver. Due to the nature of the technology, high DNI is required for cost-effective operation. Several works of literature have put a minimum yearly averaged value of $(5\ kWh/m2)/day$ as the minimum amount of solar radiation falling a site before any CSP technology deployment. Sites with high DNI values could offer a potentially lower LCOE [33,125]. Figure 3-5 shows the global 22-year average daily DNI distribution over a unit surface area $(kWh/m2/day)$.

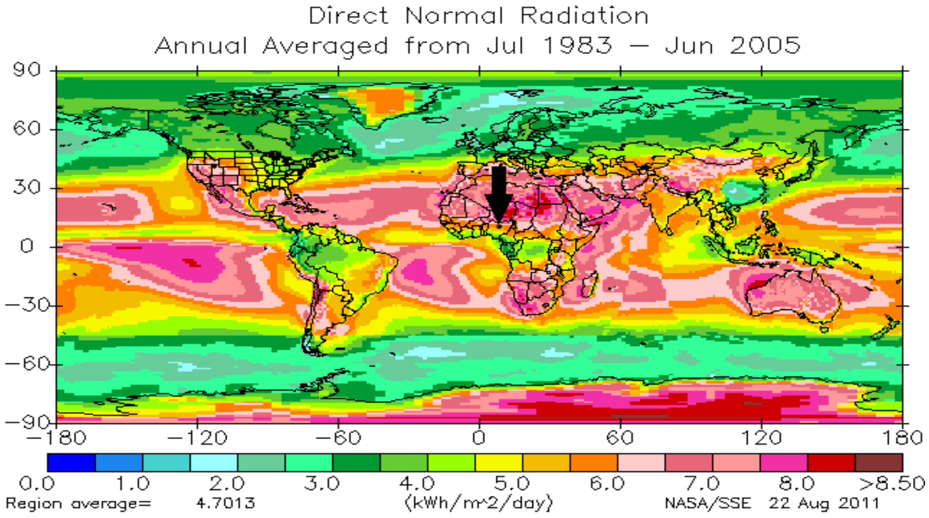

Figure 3-5 Global direct normal irradiation (Source: Global Solar Atlas)

Nigeria's geographical location is highly suitable for the deployment of solar energy technologies, especially in the northern parts of the country. For regions in Northern parts of

Nigeria, a DNI average value of around $(5.5\ kWh/m2)/day$ is obtainable [132] as shown in Figure 3-5. As can be seen from the same Figure 3-5, the highlighted region, Dutsinma in Katsina State falls among the recommended DNI average value.

The following section provides a broader look into solar energy and solar radiation assessment.

3.4 Solar Energy

The sun is an abundant and free source of energy. The sun emits radiation over a wide range of wavelengths; most are in the visible and near-infrared. An approximate total of $3.8 \times 10^{26}\ J/s$ of radiation is emitted by the sun [133]. The intensity of the energy from the sun is reduced at the surface of the earth as it travels through a mean earth-sun distance of 1.46×10^{22}. A value of about 1367 W/m^2 is witnessed at the surface [24]. This value does, however, vary due to the Earth's elliptical orbit about the sun. The incoming solar energy is further reduced as it passes through the Earth's atmosphere [134]. Figure 3-6 shows the nature of solar energy distribution.

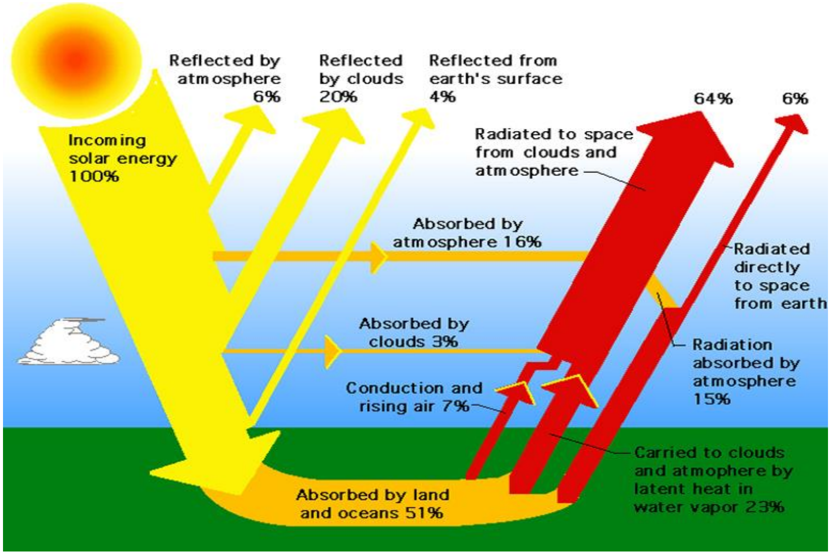

Figure 3-6 Sun's energy distribution (Source: Solar cell central)

Solar energy is time, location and weather dependent. In many regions of the world, a total of 100-130GWh of solar electricity could be harnessed on one square KM of land per annum. This is equivalent to the annual production of a 50MW conventional gas plant [135].

Solar radiation at the ground can be classified into;

- Direct beam radiation, which is the incoming energy from the solar disc.
- Diffuse radiation, which is the scattered beam radiation by the dust and clouds.

Some solar collectors can collect both the beam and diffuse component while others are only capable of collecting the beam radiation due to its directional nature, see Figure 3-7.

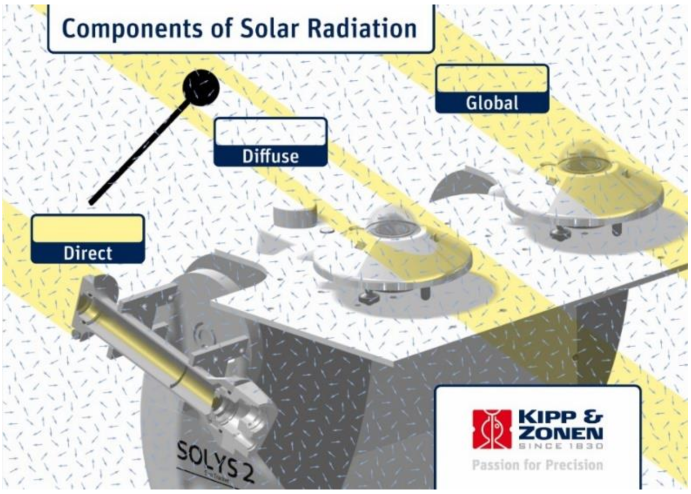

Figure 3-7 Components of solar radiation (Source: Kipp & Zonen)

3.4.1 Solar Insolation, Time and Angles

Figure 3-8 shows the angles with which the beam radiation makes with the solar collector [134].

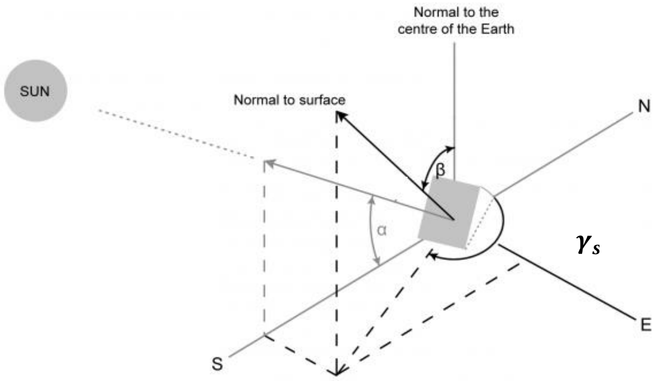

Figure 3-8 Solar collector angles

Where γ_S is the solar azimuth angle, α is the altitude angle, and β is the tilt angle.

The motion of the sun through the entire day in a particular location, the angle at which radiation strikes the ground at different times of the year and position of the collector aperture are some of the factors that have to be established in calculating the amount of solar energy yield on the collector. Some of the determinant factors can be outlined in [134] by Duffie and Beckman:

h. Latitude φ - Angular location relative to the equator
i. Declination angle δ – Angular position of the sun at solar noon on the equatorial plane. It is given by equation 15 where n represents the day number of the year.
j. Hour angle ω – East or west angular displacement of the sun about the local meridian due to earth's rotation about its polar axis. It is represented in the equation below with t being 24hr local time.
k. Incidence angle θ_z- Zenith angle between surface's beam radiation and the normal.

The solar insolation of the selected site has been obtained from NiMet (Nigerian Metrological Agency). The data obtained only represents daily radiation values. See Appendix A1 for the NiMet Data. As mentioned in the previous section, an hourly distribution of solar radiation data is needed for the system design. Estimation of hourly radiation values from daily data on the Duffie and Beckman recommended representative day of the month [134] was hence made (see Table 3-2).

Table 3-2 Recommended typical day of the month

Month	Date of month	Declination angle, δ
January	17	-20.9
February	16	-13.0
March	16	-2.4
April	15	9.4
May	15	18.8
June	11	23.1
July	17	21.2
August	16	13.5
September	15	2.2
October	15	-9.6
November	14	-18.9

December	10	-23.0

3.4.2 Estimation of Hourly Solar Radiation

Studies of the statistical distribution of total horizontal solar radiation at various weather stations presented the approximation used in estimating the hourly radiation from daily radiation data. It involved the use of the ratio r_t , which is the ratio of hourly total radiation to the total daily radiation (Equation 1).

$$r_t = \frac{H_{hourly\ total}}{H_{daily\ total}} \tag{1}$$

With due knowledge of the length of day and specific time of day, the ratio r_t can be estimated as validated by Collares-Pereira and Rabl. r_t can thus be expressed by Equation 2 [134,136].

$$r_t = \frac{\pi}{24}(a + b\cos\omega) \times \frac{cos\omega - cos\omega_s}{sin\omega_s - \frac{\pi\omega_s}{180}cos\omega_s} \tag{2}$$

coefficients a and b are correctional factors applied to the ratio [134,136] where:

$$a = 0.409 + 0.5016\sin(\omega_s - 60) \tag{3}$$

$$b = 0.6609 - 0.4767\sin(\omega_s - 60) \tag{4}$$

ω_s is the sunset hour angle which corresponds to the solar hour angle with which the sun sets. It is calculated from Equation 5 [137].

$$cos\ \omega_s\ = -\ tan\varphi\ \times tan\delta \tag{5}$$

The hour angle ω is represented in Equation 6 with t being 24hr local time.

$$\omega = 15^{\circ}\ \times (t - 12) \tag{6}$$

The method presented produced conservative estimates of long-time process performance and have been proven to work best for clear days, as mentioned in Duffie & Beckman.

Similarly, the same analogy was used to estimating the average hourly diffuse radiation from the daily average diffuse radiation as presented originally by Liu and Jordan's. The ratio used for the diffuse radiation, r_d is expressed by Equation 7 [134,136]:

$$r_d = \frac{\pi}{24} \times \frac{cos\omega - cos\omega_s}{sin\omega_s - \frac{\pi\omega_s}{180}cos\omega_s} \tag{7}$$

With r_t and r_d established, the hourly total radiation and hourly diffuse radiation can be estimated from the daily total and diffuse total, respectively (as depicted in Equation 8 and 9 respectively).

$$H_{hourly\ total} = H_{daily\ total} \times r_t \tag{8}$$

$$H_{hourly\ diffuse} = H_{daily\ diffuse} \times r_d \tag{9}$$

The components of the solar radiation on a horizontal surface are shown in Figure 3-9.

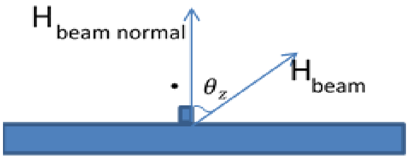

Figure 3-9 Components of solar radiation on a horizontal surface

The work presented above depicts the radiation on a horizontal surface. The daily beam radiation along the surface normal (Figure 3-9) can hence be calculated by Equation 10;

$$H_{hourly\ beam} = \frac{\left(H_{hourly\ total} - H_{hourly\ diffuse}\right)}{cos\ \theta_z} \tag{10}$$

where θ_z denotes the zenith angle of the sun, i.e. the angle between the beam component and the vertical.

Table 3-3 shows the result produced from splitting the daily data obtained from NIMET into hourly values in order to obtain the hourly distribution of beam radiation for the January sun (periods of no radiation are excluded here). Results from the rest of the months (February to December sun) are shown in Appendix A2. The DNI at the identified site averages out of 5.53 kWh/m^2/day.

Table 3-3 January Sun, hourly distribution of beam radiation

January

January 17th

Sunrise time	**6.321 hrs**
Sunset time	**17.679 hrs**
Sunset hour angle	**85.182 °**
a	**0.622**
b	**0.458**

Solar Time (hrs)	Solar hour angle (°)	Ratio of hourly total to total daily radiation r_t	Hourly radiation, $\left(\frac{kWh}{m^2}\right)$	Ratio of hourly diffuse to daily total diffuse radiation, r_d	Diffuse radiation, $\left(\frac{kWh}{m^2}\right)$	Beam radiation, $\left(\frac{kWh}{m^2}\right)$
7	75	0.0195	0.110	0.0263	0.0412	0.4307
8	60	0.0532	0.301	0.0625	0.0981	0.5335
9	45	0.0886	0.500	0.0935	0.1469	0.6217
10	30	0.1197	0.676	0.1174	0.1844	0.6894
11	15	0.1410	0.797	0.1325	0.2079	0.7320
12	0	0.1486	0.840	0.1376	0.2160	0.7465
13	-15	0.1410	0.797	0.1325	0.2079	0.7320
14	-30	0.1196	0.676	0.1174	0.1844	0.6894
15	-45	0.0885	0.500	0.0936	0.1469	0.6217
16	-60	0.0532	0.301	0.0625	0.0981	0.5335
17	-75	0.0195	0.110	0.0263	0.0412	0.4307
Total			**5.608**		**1.5731**	**6.7610**

The beam irradiance curve for the specific days of each month of the year is given in Figure 3-10. The period with the least DNI is in August despite a long duration of sunshine hours (see Appendix A1). In that month, a double maxima of rainfall is witnessed bringing about a high cloud cover, hence making the DNI to be scattered by the prevalent and heavy cloud cover. The highest DNI irradiance is witnessed in January.

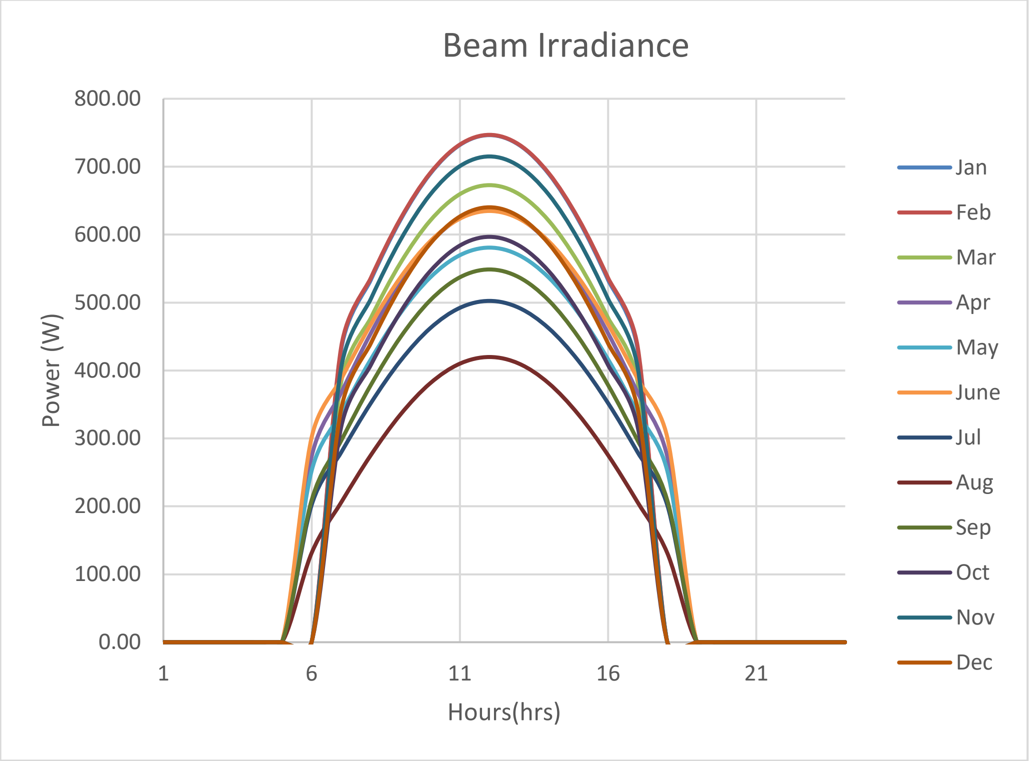

Figure 3-10 Beam irradiance curve for the specific days of each month of the year

3.5 System Configuration and Design

The design point of solar thermal energy systems is typically determined by a combination of the design objectives, the Direct Normal Irradiance DNI and the field performance specifications. The DNI is considered as the parameter having the most significant effect on the thermal energy yield in the design of a CSP plant [33,138]. As the DNI value changes through the course of the day, the plant rating is thus defined by a single point in time referred to as the design point DNI which determines how all systems and components are sized. Choosing an appropriate design point DNI is vital, as a lower design point DNI translates to smaller and lower system components costs at the expense of lower energy output and dumping of excess energy during periods of high insolation. A higher design point DNI, on the other hand, may result in higher energy output, however, in periods of low insolation, the system components will be grossly oversized and hence resulting in a more expensive plant [28,33,139].

Typical dates for the DNI design point operating conditions are mostly based on either summer solstices, June 21st, (for regions North of the equator) or spring equinox, March 21st, at solar noon time primarily because they represent high and moderate sun position respectively [85,94,146–148,108,109,140–145]. An appropriate design point is then selected based on the requirements of the system. The design point for the various cases is determined by a combination of the design objectives, the DNI and the field performance specifications [33]. DNI frequency distribution in the form of a sun path diagram or the like is hence used to establish the solar radiation energy utilisation efficiency.

On establishing the solar radiation energy utilisation efficiency for specific regions that lie below the earth's tilt angle 23.45° (limited to the Northern hemisphere), it was found that general statements attributing the sun's highest elevation angle to Summer Solstices (June 21st) does not apply to such regions. This is true for design point conditions-based on spring equinox as well. This implies the potential to lose a significant amount of energy that could otherwise have been utilized. Hence, the general statements, as seen in several works of literature of basing design in summer solstices for the region north of the equator does not apply for all locations.

3.5.1 Design Point Operating Conditions

On plotting the sun-path diagram for the given location, Figure 3-11, the highest elevation angle is found not to be during the summer solstices but instead on the date of April the 20th[149].

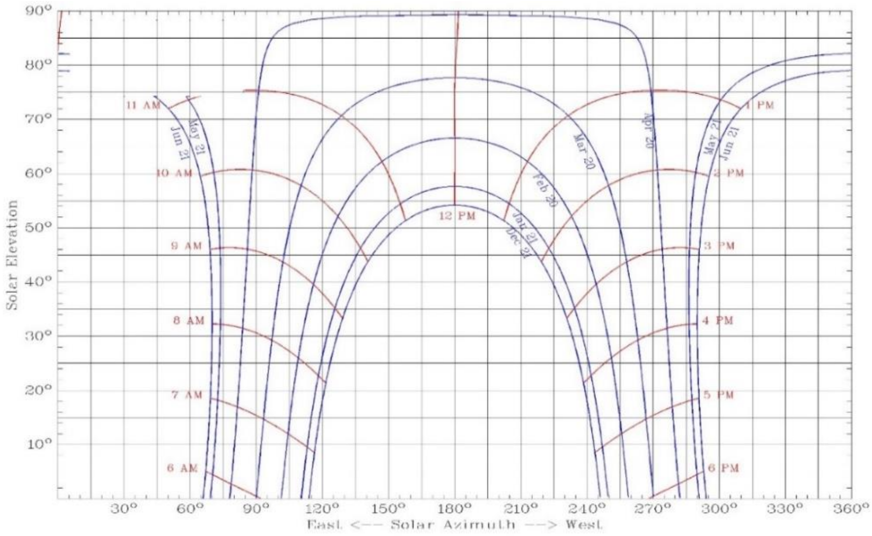

Figure 3-11 Sun path diagram at lat. 12.393˚N (SMRL University of Oregon)

There is an apparent correlation between sun's altitude and the design point power, efficiency and annual performance in solar thermal systems. In Figure 3-12, the solar altitude of different latitudinal location is shown at solar noon for different months throughout the year. The sun's highest altitude does not however always fall on the Northern hemisphere summer solstices of June 21st. Every location, especially for those close to the equator has a different date in which the highest sun altitude is recorded.

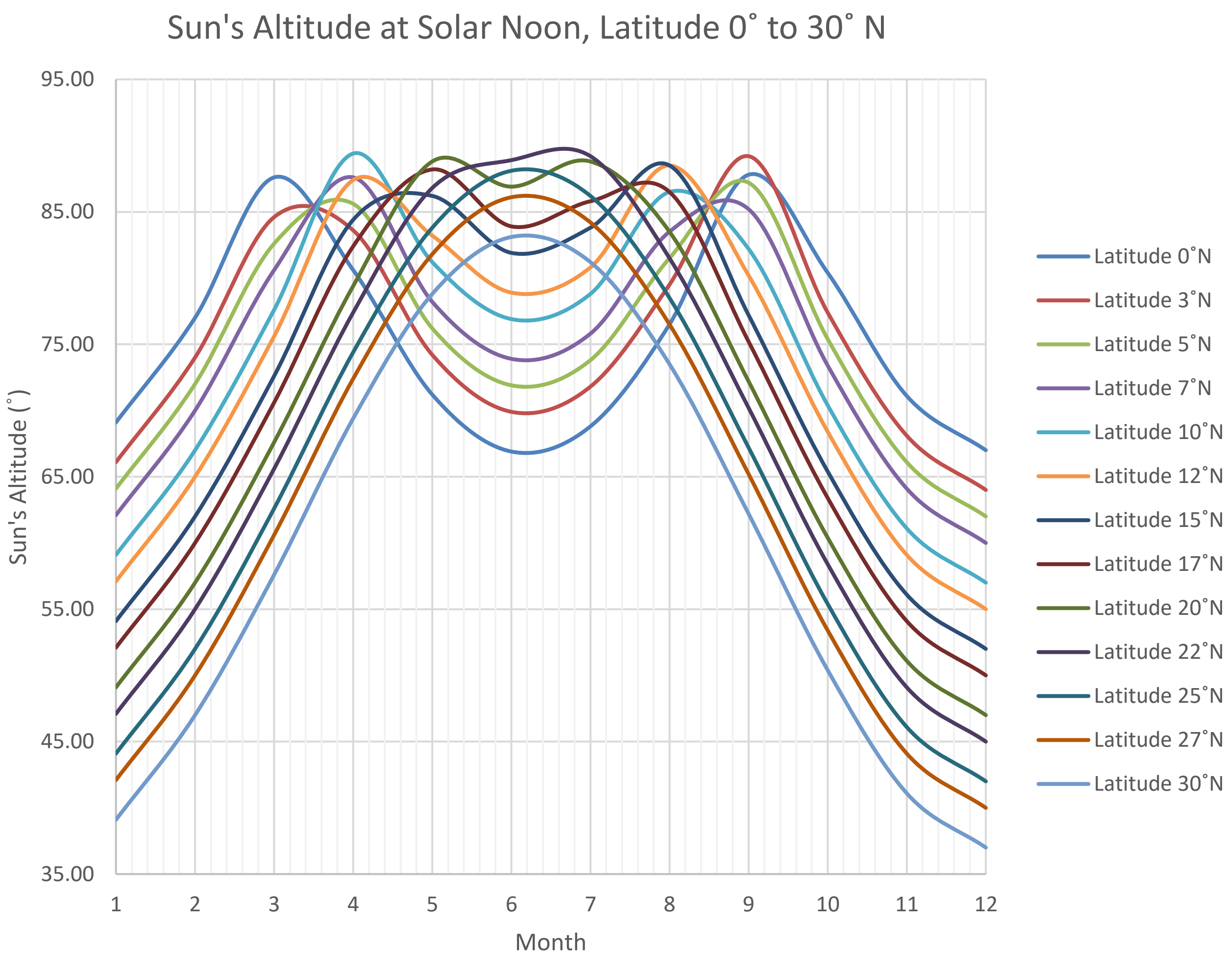

Figure 3-12 Sun's altitude at solar noon, latitude 0˚ to 30˚ N

The closer a location is to the equator, the more the sun crosses to the north of the equator. At the equator two peaks solar altitude are witnessed, all during spring and fall equinoxes. This phenomenon gradually depreciates until the altitude levels out to a single maxima value. This happens at latitude 23.5^0 in the Northern hemisphere.

For this work, the highest sun's altitude at the selected site April 20th is chosen as the design point operation period.

3.5.2 Design Point Power

The design point DNI must be one that is expected to be met most of the time. Figure 3-13 shows the occurrence of the DNI values represented in the form of a histogram chart. Although the highest DNI occurrences are between 378-412 (W/m^2), the thermal rating cannot be at those values as the plant will be grossly undersized, and energy has to be dumped continuously.

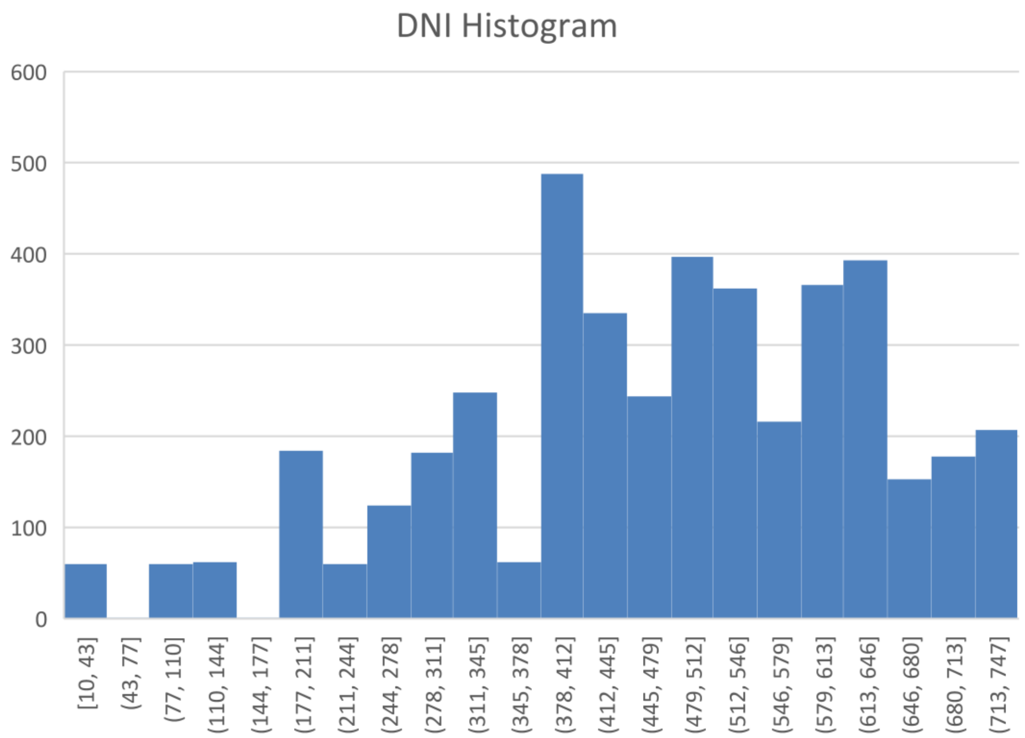

Figure 3-13 Histogram chart showing the occurrence of the DNI values

From SAM in [108], a Cumulative Density Function (CDF) in Figure 3-14 can be drawn up from which one can estimate a safe threshold of thermal rating in which the receiver sub-system will not exceed thereby ensuring appropriate sizing. In this case, a CDF of 86% is selected which assumes that all other components, from the receiver subsystem to the power conversion unit, are within a good range of the system's design power thus ensuring sunlight hours will exceed the plant's thermal rating by only 14% of the time. As shown in the figure above, at 86% CDF, the DNI value is 640 (W/m^2).

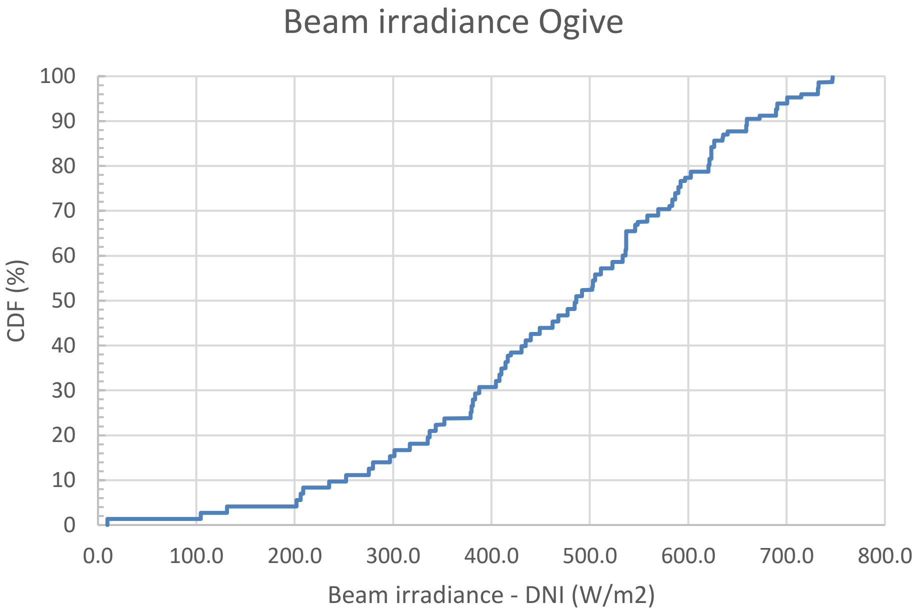

Figure 3-14 DNI Cumulative Density Function

3.5.3 Plant Configuration

The size range for a solar thermal central receiver field is initially limited to 50MWth. Only the field thermal energy output will be considered in this work.

Defining the configuration of the solar plant includes specifying the receiver fluid. Plant configurations are primarily dependent on the plant's mission, the receiver fluid and receiver type. The work in this project is mainly targeted to the heliostat field. Therefore, only the relevant components will be further discussed.

3.5.4 Field Layout and Receiver Type

As described earlier in Chapter 2, the field layout can either be polar or surround, and each type supports certain receiver types. The work here investigates multi-tower systems. A polar and cavity field is capable of limiting the effects of an auxiliary tower. In order to avoid such limitations, the surround field layout with a cylindrical receiver is adopted.

3.5.5 Tower

The tower houses the receiver and pipes amongst its purposes. The tower structure is made up of either steel lattice or reinforced concrete. Steel lattice tower provides slightly less shadowing of the heliostat field over the reinforced concrete tower. The choice of the reinforced concrete tower over steel lattice tower in this work is because of the cost estimates available from literature on the former.

3.6 Heliostat Field Cost Model

A brief look into the various cost models, specifically in the solar field is being looked at. The cost models include the heliostat, receiver and the tower. The cost model here refers only to direct capital costs, which represents the onetime expense incurred on the purchase of a piece of equipment or installation service that applies in year zero of the cash flow.

3.6.1 Tower

In work by SANDIA Kolb et al. on-Power Tower Cost Reduction Roadmap in 2011, the cost of the tower is included with that of the receiver. The receiver amounts for 59% of the cost and the tower 21%in heliostat field cost breakdown. The calculations are based on the Utility Study plant reported in 1988 (figures readjusted to 2010 US Dollars) [25]. Two different values from individual studies were provided in addition to the estimated workshop value drawn up from responses from individuals and organizations. Note that cost values include riser and downcomer pipes.

Abengoa Study, 910MWth Plant ($40/kWth) =$36.40M

Utility Study, 470MWth Plant ($41/kWth) = $19.27M

Sandia Roadmap Workshop Goal Figure = $62.8/kWth

The cost estimates in the report do not, however, tie the value to the height of the tower. This results in the discrepancy seen amongst the figures.

In another report from SANDIA by Gregory J. Kolb, the tower cost for 100MWe is $11.75M [26]. The height of the tower is equally not disclosed here. The cost here is also excluding the riser and downcomer pipes which amount to $16/kWth totalling $19.27M for a 540MWth receiver.

In another work, this time by NREL, for its System Advisor Model or SAM [150], produced a report that describes a component-based cost model developed for molten-salt power tower solar power plants. SAM utilizes the DELSOL tower cost algorithm [106]. The cost model provides a reference plant that interfaces with NREL's System Advisor Model or SAM. The reference plant assumes a nominal 100-MWe (net) power tower running, 670MWth Receiver design thermal power. The Tower cost in SAM 2010 amounts to $28.5M [151]. The same Tower in SAM 2018 provides a very similar result; \$29.7M. SAM Uses the following expression in Equation 11 to calculate the tower cost.

$$Total\ Tower\ Cost\ = e^{(Tower\ Cost\ Scaling\ Exponent\ \times\ (Tower\ Height\ -\ Receiver\ Height\ \div\ 2\ +\ Heliostat\ Height\ \div\ 2\ ))} \tag{11}$$

The fixed tower in SAM 2018 is provided as \$3M, and the cost scaling exponent as 0.0113 [106,108,150]. The fixed tower cost account for tower construction, materials and labour costs. Estimates in this work assume the optical tower height.

WorleyParsons provided the NREL with a report with a capital cost estimate for the construction of a state-of-the-art solar power tower plant in Tucson, AZ. They provided input to NREL's Life Cycle Assessment (LCA) of the particular plant [150]. The plant is designed to generate ~100MWe net. For a concrete tower, the following formula (Equation 12) for the cost as a function of tower height was developed.

$$y_t\ =\ 1835.7{x_t}^2\ \text{-}\ 285868x_t\ +\ 3E7 \tag{12}$$

Where y_t is the tower cost and x_t is the tower height in metres.

Using the correlation provided by WorleyParsons, the 100MWe Plant, with assumed 203-meter tower and 670MWth receiver thermal power plant, sums up to \$47.61M.

The literature reviewed defines the tower cost either based on the height or the receiver thermal rating. The classification on the thermal rating categorizes a 100MWe electric plant with either a 540MWth or 670MWth receiver design. For uniformity, all the 100MWe plants reviewed earlier are assumed to have a 670MWth receiver and 203-meter high tower as depicted by SAM [150]. The various studies are now then reconstituted and extrapolated to a 670MWth receiver with a 203m high tower. With the assumptions, the following deductions can be drawn based on different studies (Table 3-4).

Table 3-4 Cost estimate of a 203-meter tower based on different studies

Study	Cost,100 MWe (670MWth Receiver), 203M Tower (\$)
Abengoa Study	26,800,000.00
Utility Plant Study	27,470,000.00
SANDIA Study	22,470,000.00
Power Tower RoadMap Workshop Study	42,076,000.00
SAM,2010	28,500,000.00

WorleyParsons	47,610,000.00

From the estimates given for the tower cost, methods and parameters that present estimates of the tower cost by the meter are given keen interest. In Figure 3-15, the tower cost estimates from different studies at various heights are shown.

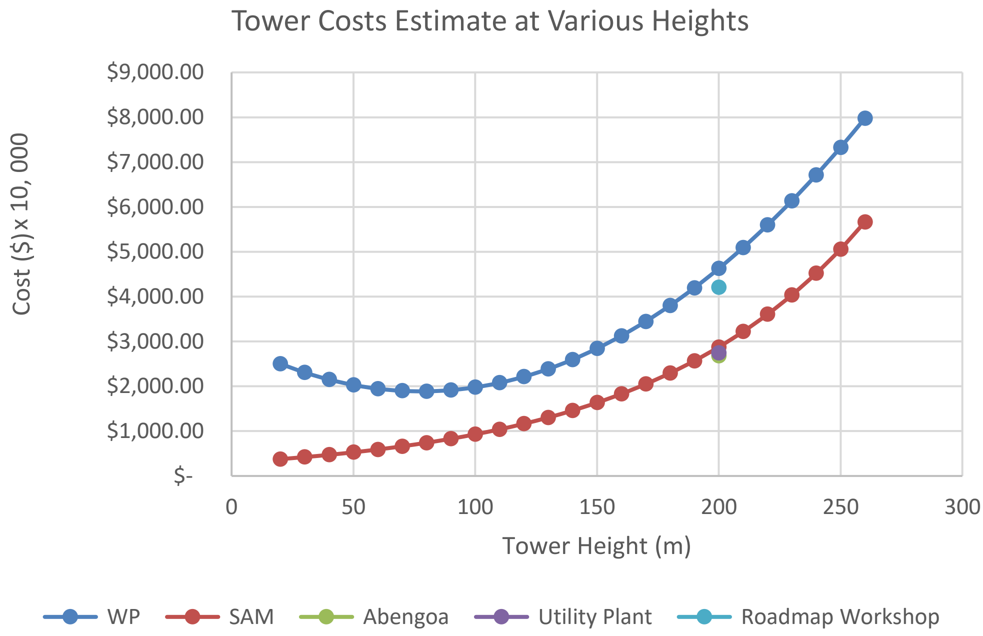

Figure 3-15 Tower cost estimates at different heights

3.6.2 Heliostat

The heliostats account for most of the cost in the solar field. Over 40% of the cost in the field is as a result of the heliostats [10]. The cost of the heliostats are typically seen in numerous works of literature to range from 150-237 USD/m^2 [14,25], and the target is set as low as 75-120 USD/m^2 [58,152,153]. The variation in the cost is a function of the design variables of a heliostat which typically include the size, tracking error, mirror canting and focusing, reflector material and type [14]. Multi-year-production of a particular heliostat design also affects the cost.

At the behest of the United States Department of Energy (DOE), a detailed cost estimate by AD Little (ADL) was made on a 148m^2 heliostat design. The cost estimate covers all aspects from design drawings to material and installation cost. Similar work was conducted by SunLab. SunLab is a collaboration of SANDIA National Laboratories and NREL working on CSP technology for the DOE. SunLab utilizes industry data and engineering evaluation to arrive at its cost estimate. Sargent & Lundy received and organized data from all the sources aforementioned to verify and provide a comprehensive estimate. For a 95m^2 heliostat, the cost estimate for initial deployment was \$160/m^2. A scaling factor of 0.8 was used in evaluating the cost estimate [154]. The economy of scale (Equation 13) was used to evaluate the cost estimate of new sizes from the initial \$160/m^2 estimate made for a 95m^2 heliostat.

$$C2 = C1\left(\frac{S2}{S1}\right)^{sf} \tag{13}$$

Where:

C2 = Desired cost of equipment at size (or capacity) of S2

C1 = Desired cost of equipment at size (or capacity) of S1

Sf = Scaling factor

The varying cost estimates seen on the heliostats makes it challenging to adopt one. However, the detailed and extensive work by Sargent and Lundy can be adopted to estimate the cost for various heights. SAM 2018 maintained a figure of \$140/m^2 (same as the 2013 NREL SAM report), cost inclusive of the installation of the heliostats, heliostat parts, field wiring, drives, labour and equipment. The baseline cost adopted by SANDIA, obtained from numerous studies, is \$200/m^{2,} and the 10-year cost goal placed in the power tower road map [25] is at \$120/m^2. The figures are compared to one another using economy of scale at 0.8 scaling factor in Figure 3-16.

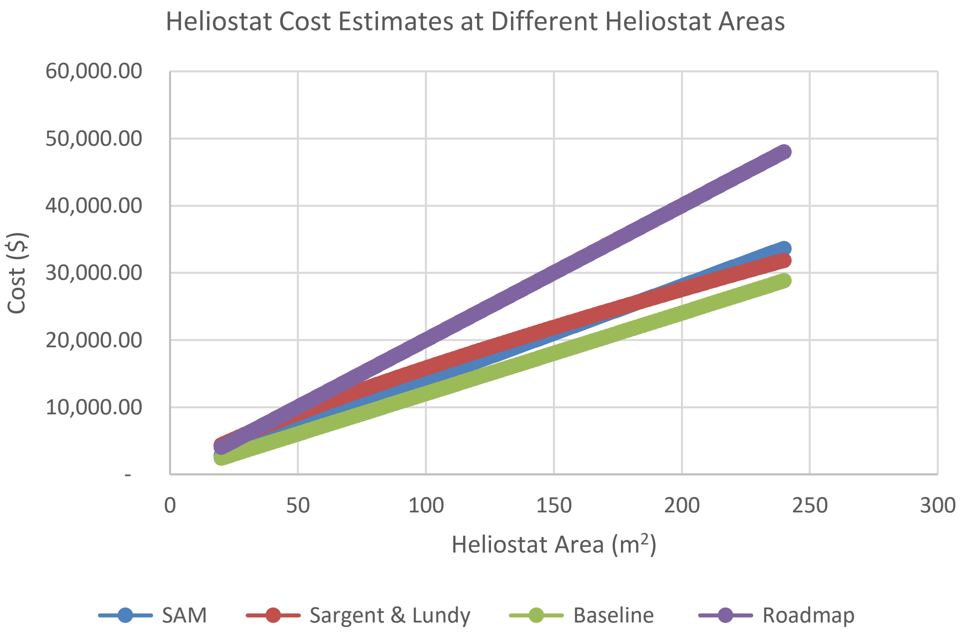

Figure 3-16 Heliostat cost estimate at different heliostat area

3.6.3 Receiver

As mentioned above, the receiver amounts for 59% of field cost based on calculations based on the Utility Study plant [25]. As seen previously, several figures for the cost of the receiver are being estimated in the literature with the actual cost from developers itself a closely kept secret. The baseline cost for the receiver, as reported in the 2010 Sandia Workshop is \$118/kWth [25]. In other studies, from the same literature, the following costs were obtained;

Abengoa Plant, 910MWth receiver study (\$58/kWth) =\$52.78M

Utility Plant, 470 MWth receiver study (\$71/kWth) = \$33.37M

SunLab baseline cost estimate for the SolarTwo 100m^2, 42MWth receiver, is at \$9.1M in the year 2000 [154,155]. The adjusted year 2010 cost would hence be \$10.78M.

The cost of the tower is expected to vary based on the type of the receiver. Most specifications do not, however, highlight the area of the receiver. This is important during the optimisation process, and a criterion that defines the cost based on the receiver dimensions is necessary. This criterion is only seen in the molten salt power tower cost model for SAM [150] and Sargent and Lundy study [154].

In SAM model 2018, the base reference cost of the receiver is \$103M over a reference area of $1{,}571\mathrm{m}^2$: a slight difference from the NREL SAM 2013 model report (\$85.1M over a reference area of $1{,}133\mathrm{m}^2$). The base reference cost for the SunLab estimated of Solar Two is 43MWth over a reference area of 100M^2. A sizing factor of 0.7 [150,154] is used in finding the cost estimates using the economy of scale. The receiver reference cost here accounts for installation costs, including both labour and equipment. In Figure 3-17, the cost estimates at different receiver dimensions from the two models are shown.

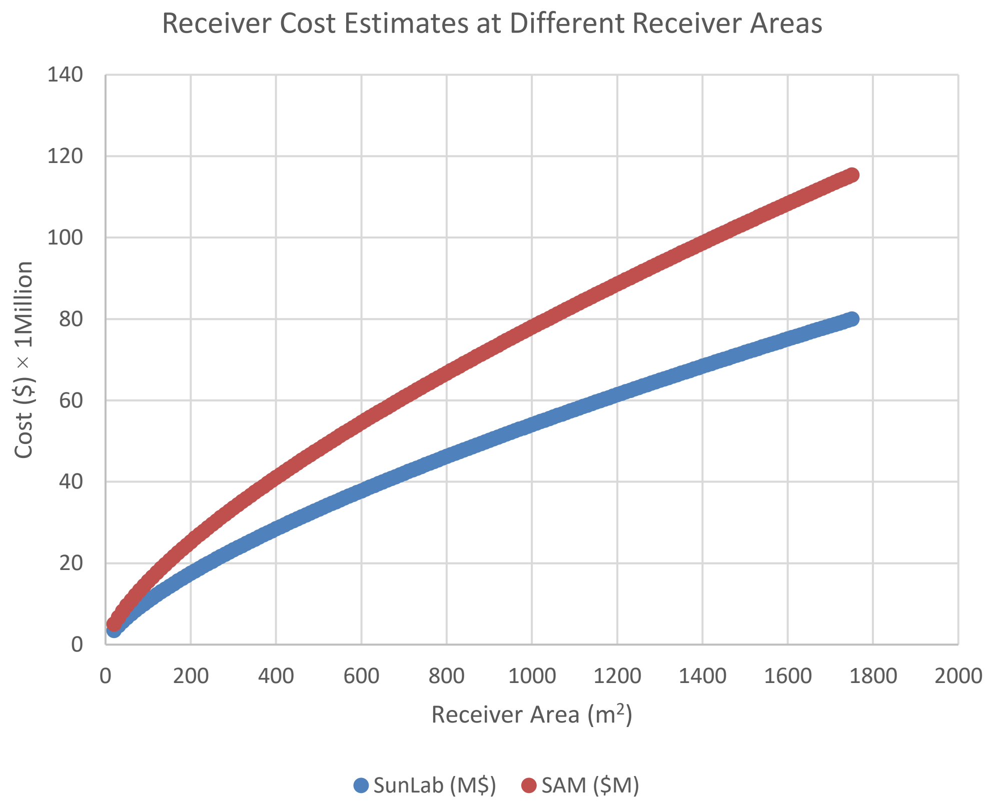

Figure 3-17 Receiver cost estimates at different at area

From all the literature reviewed, there is an apparent discrepancy in all the cost models for the different heliostat field components. In order to maintain consistency, the SAM cost model is adopted for all the components in this study.

Chapter Summary

Due to the declining patronage on nuclear energy and volatile petroleum and natural gas prices, coupled with the rising global temperature predominately as a result of the atmospheric build-up of CO_2, nations at large are opting and considering renewable energy technologies for their power generation. Solar energy, in particular, is seen as an extremely viable option, especially in areas with good solar insolation. The power sector in Nigeria is one of the most critical constraints to economic development in the region. The erratic power supply remains a constant feature. Given the geographical location of some regions, solar energy electricity generation in the form of Concentrated Solar Power (CSP) could potentially be a viable and promising option for Nigeria in combating climate change and providing energy security. Application of site selection and feasibility analysis cleared site $12°.393'$ and longitude$7°.496'$ for the deployment of a power tower CSP system.

The parameters and procedures that need to be established before the design and configuration of the power system were also outlined. This procedure is a significant prerequisite to establishing and developing the system. Upon establishing the solar radiation energy utilisation efficiency for specific regions that lie below the earth's tilt angle 23.45°, in the Northern hemisphere, it was found that general statements attributing the sun's highest elevation angle to summer solstices of June 21st do not apply to such regions. This is true for design point conditions-based on spring equinox as well. This implies the potential to lose a significant amount of energy that could otherwise have been utilized. Hence, the general statements, as seen in several works of literature of basing design in summer solstices for the region north of the equator does not apply for all locations. The design point period was hence selected at the highest elevation angle at the site, April the 20th.

An overview of the heliostat field cost model demonstrates several discrepancies in the different models. The System Advisor Model from the National Renewal Energy Laboratory (NREL) cost model was hence adopted for all the components in this project.

4 CONVENTIONAL POWER TOWER HELIOSTAT FIELD

In this chapter, the model and method used for the design and configuration of a conventional power tower system are outlined. This chapter forms the initial stage that needs to be established before the multi-tower configuration can be developed. The model developed for the multi-tower system is built upon the conventional field developed here. The chapter begins by describing the model for the conventional field.

4.1 Model Description

4.1.1 Sun's Position

Finding the position of the sun is one of the very first steps that need to be addressed. The position can be characterized by the altitude (α) and azimuth angle (γ). Figure 4-1 shows the angles defining the apparent position of the sun [17,134].

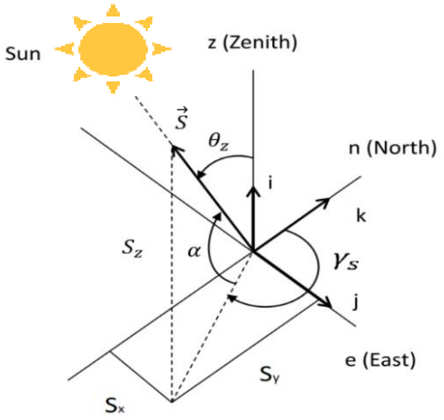

Figure 4-1 Solar vector

where θ_z is the zenith angle and S_x, S_y, and S_z denote the vector components $\vec{S}$ of the sun's radiation. The solar altitude is given by Equation 14 [134].

$$\mathrm{Sin}\,\alpha = \mathrm{Sin}\,\varphi\,\mathrm{Sin}\,\delta + \mathrm{Cos}\,\varphi\,\mathrm{Cos}\,\delta\,\mathrm{Cos}\,\omega \tag{14}$$

Here Latitude φ - Angular location relative to the equator; Declination angle δ – Angular position of the sun at solar noon on the equatorial plane. The declination angle is given by Equation 15, where n represents the day number of the year [134].

$$\delta = 23.45\,\mathrm{Sin}\left(360 \times \frac{284 + n}{365}\right) \tag{15}$$

Hour angle ω – East or west angular displacement of the sun about the local meridian due to earth's rotation about its polar axis. It is represented in Equation 16 with *t* being the solar time [134].

$$\delta = 23.45 \text{ Sin} \left(360 \times \frac{284+n}{365}\right) \tag{16}$$

The azimuth angle, on the other hand, is given by Equation 17 [134]

$$\text{Sin}\, \gamma_s = \frac{\text{Cos}\, \delta \text{ Sin}\, \omega}{\text{Cos}\, \alpha} \tag{17}$$

As stated in Chapter 3, solar insolation data was for the selected site in Katsina, Nigeria, at Latitude: 12.39 ˚N and Longitude: 7.60 ˚E. The solar insolation of the selected site; Katsina, Nigeria (Latitude: 12.39 ˚N Longitude: 7.60 ˚E) was obtained from the metrological agency in Nigeria, NIMET. The DNI at the identified site works out to an average of 5.53 kWh/m^2/day. Details on the site have been highlighted previously in Chapter 3.

4.1.2 Optical Efficiency

The optical efficiency of the field measures the capability of each heliostat to concentrate and reflect radiation to the receiver. Every heliostat has a particular optical efficiency value due to its position in the field and its interaction with the other elements in the field. The overall value for the field is then calculated by averaging each particular result. Field optical efficiency is typically expressed by Equation 18 [13,17,83];

$$\eta_{field} = \eta_{cos} \times \eta_{sb} \times \eta_{att} \times \eta_{int} \times \eta_{ref} \tag{18}$$

where $\eta_{cos}, \eta_{sb}, \eta_{att}, \eta_{int}$, and η_{ref} represent losses due to cosine, shadowing and blocking, atmospheric attenuation, interception and mirror reflectivity factors, respectively. Maximizing field efficiency is an important task that ensures the optical losses are reduced as much as possible. Another look into the optical efficiency loss factors is made here with more efforts put on the outlining the methodologies.

4.1.1.1 Shading and Blocking Efficiency Loss

Shadowing and blocking losses are as a result of the reduction of the heliostat's useful area, due to the presence of a heliostat in the path of the incident radiation or reflected radiation respectively. In Figure 4-2, the contour of the representative heliostat and the projected contour of the two adjacent heliostats in a radial staggered configuration is shown.

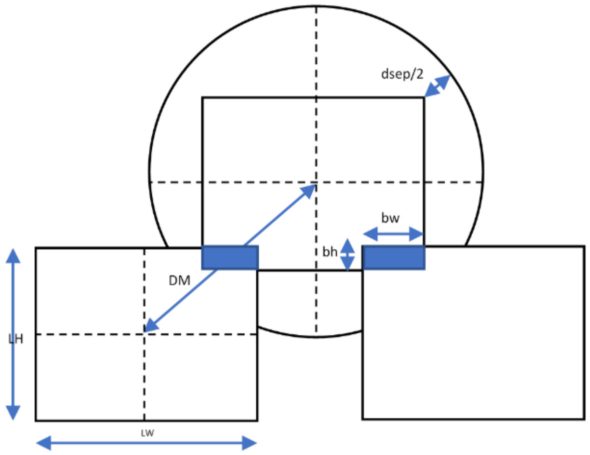

Figure 4-2 Blocking and shadowing showing the contour of the representative heliostat and the projected contour of two adjacent heliostats in the first-row

Here, assuming bh and bw are the blocking and shadowing portions of the representative heliostat. *LH* and *LW* are the heliostat's length and width, respectively. *DM* is the diameter of the heliostat, inclusive of dsep (the extra security distance between adjacent heliostats).

The blocking model adopted the simplified calculation method developed by Sassi [92], using the outline projections of the neighbouring heliostats. This method divides the surfaces of each heliostat into strips, and those strips identified to have the potential for shadowing and blocking are projected onto the surface of the problem heliostat. Among all blocking projections, the maximum height is selected for each strip. The fraction of the area free from blocking gives the blocking efficiency value.

As to the identification and selection of the blocking heliostats, the method outlined in [85] by Besarati and Goswami is adopted. This methodology considers only a subset of the heliostats that have a high potential for shadowing and blocking. With the radial staggered configuration (the adopted field layout generation methodology), identification of the blocking heliostats makes it easier, as this can quickly be done by considering the 'shoulder' heliostats at the next row (Figure 2) of the analysed heliostat and the one that is two rows over and directly in front of it [156].

Shading in the field by the heliostats was ignored. This is due to the fact that blocking usually has a more definite effect in the losses entailed with heliostat field layouts [33] and also to reduce the computational expense and complexity of the modelling.

4.1.1.2 Cosine Efficiency Loss

The cosine efficiency loss is one of the most critical energy loss source in the heliostat field and often represents the most significant loss term [55]. As earlier mentioned in Chapter 2, it can be defined as the cosine of the angle formed by the incident solar beam radiation and the vector normal to the reflective heliostat surface [85]. The efficiency factor depends on both the position of the sun and heliostat [17]. It defines the total percentage of reflective area that can be directed towards the receiver. Figure 4-3 shows the effect of cosine on reflected rays from the heliostat [55].

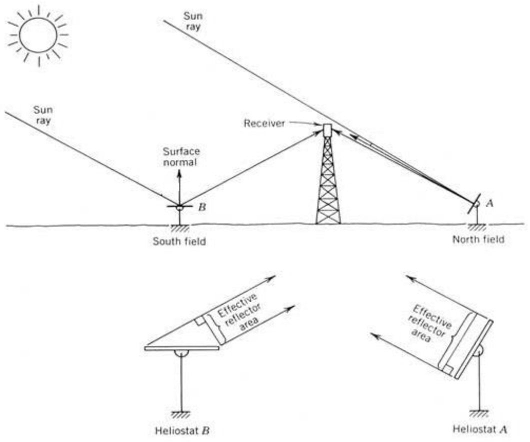

Figure 4-3 Figure showing the effect of cosine on reflected rays in heliostat A and B [55]

To evaluate the vector normal to the heliostat surface, two other vectors need to be defined, i.e., the vectors from the centre of the heliostat to the sun, $\vec{S}$, and those to the desired image location on the receiver surface, $\vec{r}$. Assuming x, y, and z are the coordinates of the heliostat centre, and TH is the tower height, the components of the unit vector of the reflected ray, $\vec{r}$ can be given by Equation 19 [142,157]:

$$\vec{r} = \left[\frac{-x}{\sqrt{x^2 + y^2 + (TH - z)^2}}, \frac{-y}{\sqrt{x^2 + y^2 + (TH - z)^2}}, \frac{(TH - z)}{\sqrt{x^2 + y^2 + (TH - z)^2}}\right] \tag{19}$$

Vector $\vec{S}$ components are formed from Figure 4-1. With $\vec{S}$ and $\vec{r}$ defined, the components of the unit vector normal of the heliostat surface can then be evaluated (Equation 20):

$$\vec{m} = \frac{\vec{S} + \vec{r}}{\left|\vec{S} + \vec{r}\right|} \tag{20}$$

The cosine efficiency can now be calculated as the dot product of the unitary vectors $\vec{m}$ and $\vec{S}$, as shown in Equation 21:

$$\eta_{cos} = \vec{m} \cdot \vec{S} \tag{21}$$

4.1.1.3 Attenuation Efficiency Loss

Atmospheric attenuation consists of energy losses in the reflected radiation while going through the atmosphere from every heliostat to the receiver [86]. The reflected beam radiation from the surface of the heliostat may be scattered, depending on the distance between the heliostat and the receiver. This atmospheric attenuation efficiency can be calculated by Equation 22 for fields with a distance between heliostat and receiver aim point below 1,000 meters [158]:

$$\eta_{att} = 0.99321 - 0.0001176D + 1.97 \times 10^{-8} \times D^2 \quad D \leq 1000m \tag{22}$$

The formula (Equation 22) got further extended by M.Schmitz et al. for larger slant range values in order to give more realistic results [159]. This is represented in Equation 23.

$$\eta_{att} = exp(-0.0001106D) \quad D > 1000m \tag{23}$$

Where *D* is the distance between the heliostat and the aim point of the receiver.

4.1.1.4 Interception Efficiency Loss

Interception efficiency loss, otherwise known as spillage, refers to reflected energy directed towards the receiver that does not fall on the absorbing area. The factor is dependent on both the heliostats in the field and the receiver design and properties [17]. While this ‘spill’ of the reflected radiation can be reduced by increasing the receiver size, consideration of other receiver energy losses and receiver cost must be made. The spillage can be calculated through an integration of the image shape produced by the mirror over the receiver domain [84,95,159–161]. A description of the spilt radiation is shown in Figure 4-4.

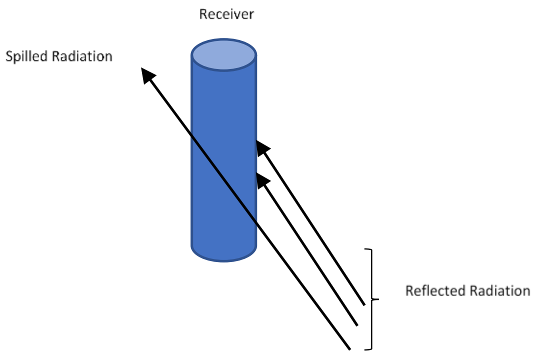

Figure 4-4 A demonstration of spillage on the receiver

The University of Zaragoza (UNIZAR) [160] and HFLCAL [95] methods are used for the analytical expressions of spillage, and as appropriate tools for design and optimisation. The HFLCAL model, from the German Aerospace Centre (DLR), is applied in this paper. The model is adjudged to be both simpler and slightly more accurate than the UNIZAR method [161]. The HFLCAL model's flux density expression is a circular normal distribution. The spillage efficiency loss is expressed by initially, calculating the intersected radiation from the heliostat, Equation 24 [95,159];

$$\eta_{int} = \frac{1}{2\pi\sigma^2{}_{tot}} \int_{x'}^{\cdot} \int_{y'}^{\cdot} exp\left(-\frac{x^2 + y^2}{2\sigma^2{}_{tot}}\right) dy\, dx \tag{24}$$

Where x′ and y′ are coordinates of the plane normal to the receiver surface and σ_{tot} is the standard deviation of the flux distribution on the receiver plane given by Equation 25;

$$\sigma_{tot} = \sqrt{D^2(\sigma^2{}_{sun} + \sigma^2{}_{bq} + \sigma^2{}_{ast} + \sigma^2{}_{tr})} \tag{25}$$

σ_{sun}, σ_{bq}, σ_{ast}, σ_{tr} are the standard deviations due to sun shape error, mirror slope error, astigmatic error, and tracking error, respectively. A sun shape error value, as measured in Planta Solar Almeria (PSA) [156], of 2.51 mrad is applied here. The beam quality value is assumed to be 1.88 mrad, as reported in [43]. Also, as from [43], the σ_{tr} is assumed at 0.63, a value obtained from tests on Sener heliostat under low wind conditions. The astigmatism effect σ_{ast}, can be calculated by Equation 26 [159];

$$\sigma_{ast} = \frac{\sqrt{0.5\,(H_t^2 + W_s^2\,)}}{4D} \tag{26}$$

H_t and W_s are the image dimensions in the tangential and sagittal planes at the receiver position. The values are given by Equation 27 [159];

$$H_t = \sqrt{LW + LH}\left|\frac{D}{f} - \mathrm{Cos}\,\varepsilon\right| ,W_s = \sqrt{LW + LH}\left|\frac{D}{f}\mathrm{Cos}\,\varepsilon - 1\right| \tag{27}$$

where f is the focal distance of the heliostat surface and $Cos\ \varepsilon$ is the incidence cosine between the sunrays and the heliostat normal.

4.1.1.5 Mirror Reflectivity Loss

Mirror reflectivity affects the amount of radiation that can be redirected by the heliostat. This is primarily due to the design specification and condition of the heliostat. A uniform reflectivity value of 0.88 is adopted here as in [13,43]. The reflectivity efficiency can hence be fully expressed as (Equation 28);

$$\eta_{ref} = 0.88 \times (0.95) \tag{28}$$

where 0.95 factor is the nominal value adopted for cleanliness. In this work, η_{ref} is assumed constant for all heliostats in the field.

4.2 Field Layout

In this paper, the proposed method for the field layout and generation is the radial staggered distribution. The configuration provides a well-established and tested methodology for the generation of a heliostat field. The radial staggered arrangement ensures that no heliostat is placed directly in front of another heliostat in adjacent rings. In this way, a reflected beam from any heliostat passes between its adjacent neighbours on the way to the receiver [18,96]. Radial staggered geometries have proved to be efficient in optimizing tower height vs receiver dimensions vs field layout in achieving the low Levelized Energy cost and optimum field efficiency. Figure 4-5 shows a typical representation of the radial staggered configuration [157].

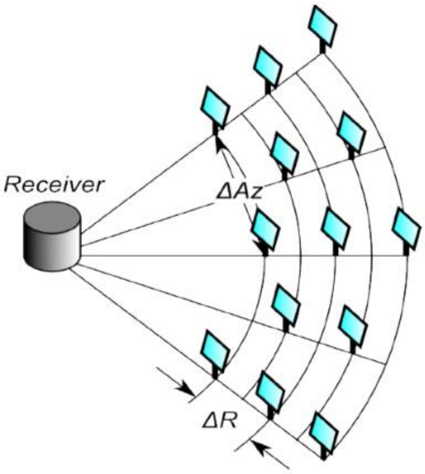

Figure 4-5 Radial staggered configuration

4.2.1 Field Layout Model

The method, campo, for the generation of radial-staggered layout presented by [18] is mostly adopted here. One of the bases of the code, as developed by FJ Collado, is to improve the accuracy and speed with which heliostats field are optimised and designed by making regular but flexible staggered configuration. This makes it convenient for the intended application here and the reason for its adoption. Details of the campo steps for generating the circular heliostat fields are outlined in [18].

The field is initially laid out by developing the densest field made up of concentric rows of heliostats. The field is gradually expanded by altering the radial separation distances, *ΔR*, during the optimisation process. The parameters in the layout of the field are shown in Figure 4-6.

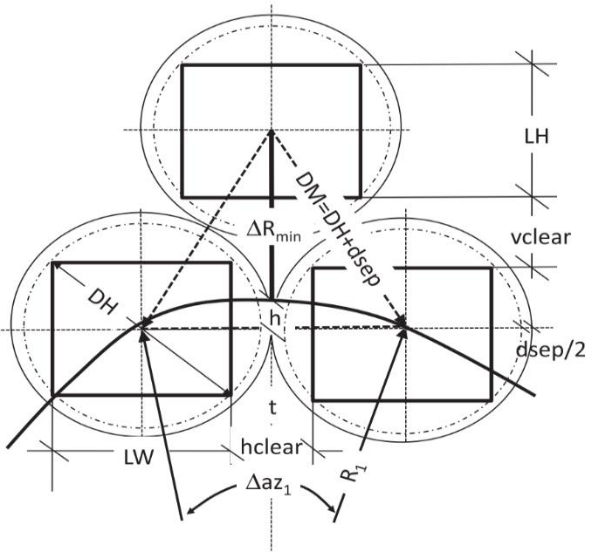

Figure 4-6 Parameters defining the layout of the field

The densest field has ΔR_{min}, the minimum radial increase at (Equation 29);

$$\Delta R_{min} \;=\; DM\ Cos\ 30^0 \tag{29}$$

where *DM* is the horizontal clearance, $dsep$, added to the heliostat diagonal length (*DH*). *DM* is given by Equation 30.

$$DM \;=\; DH \;+\; dsep \tag{30}$$

The heliostat field layout generation procedure for the configuration begins by placing the first heliostat tangent to the Y-axis (North) at a radius distance *R1* from the centre where the tower is situated. The second heliostat is placed at the same *R1*, at an azimuth angle distance, Δaz_1, from the initially paced heliostat. This placement continues through the entire row. This process is continued on subsequent rows on the field; with the first row being odd and the second row being even (starting point here is at the Y-axis), in order to provide the needed staggered configuration. The azimuthal distance Δaz_1, can be expressed by Equation 31;

$$\Delta az_1 = 2\,\mathrm{Sin}^{-1}\left(\frac{DM}{2R1}\right) \tag{31}$$

R1 can be determined by Equation 32;

$$R1 = Nhel_1 \left(\frac{DM}{2\pi}\right) \tag{32}$$

$Nhel_1$ is the number of heliostats in the first row.

As the consecutive rows are increased, the distance between the heliostats widens until it eventually becomes higher than *DM*. At this point, a new Zone is created in which the layout generation is started afresh. The number of Zones in this developed model is limited to three.

In the new Zone, the radius from the tower can be calculated by Equation 33;

$$R_i = 2^{i-1} \left(\frac{DM}{\Delta az_1}\right) \tag{33}$$

i signifies the subsequent Zones in the field. The angular spacing in the i^{th} Zone in the field can now be determined by Equation 34;

$$\Delta az_i = \left(\frac{\Delta az_1}{2^{i-1}}\right) \tag{34}$$

With the field layout generated, expansion and optimisation of the field can then be initiated. In this particular model, the optimisation is not only limited to improving the optical efficiency but also obtaining the parameters of the field. The parameters in the field constitute the design variables, namely, the number of heliostats in the first row, heliostat area, tower height, consecutive row separation distance in the first, second and third Zone. The design variables are optimised using a Genetic Algorithm (GA) within the context of the chosen objective function to arrive at the required field thermal power. The model is developed using the computer programming language MATLAB developed by MathWorks.

4.2.2 Field Model Validation

Table 4-1 compares the results presented in the reference model, campo, by F.J Collado [43] to the one developed here. The campo model uses the data and references from the Gemasolar plant in Sevilla, the first commercial plant with molten salt storage. The field data and specifications used for the model validation in the Gemasolar like plant are outlined in [43].

Table 4-1 Model results in comparison to the campo method

Zones	Zone 1			Zone 2			Zone 3		
	Field Efficiency								
Row Spacing (m)	Ref Model (%)	Model (%)	Diff (%)	Ref Model (%)	Model (%)	Diff (%)	Ref Model (%)	Model (%)	Diff (%)
ΔR1 = 0.866DM **ΔR2 = 0.866DM** **ΔR3 = 0.866DM**	65.34	65.21	0.20	55.42	55.12	0.54	37.54	37.34	0.53
ΔR1 = 0.866DM **ΔR2 = 1.4DM** **ΔR3 = 1.4DM**	65.36	65.21	0.23	58.45	58.59	−0.24	48.05	47.79	0.54
ΔR1 = 0.866DM **ΔR2 = 1.6DM** **ΔR3 = 1.6DM**	65.36	65.21	0.23	57.85	57.86	−0.02	48.35	48.27	0.17
ΔR1 = 0.866DM **ΔR2 = 1.4DM** **ΔR3 = 1.6DM**	65.36	65.21	0.23	58.66	58.79	−0.22	50.26	49.98	0.56
ΔR1 = 0.866DM **ΔR2 = 1.4DM** **ΔR3 = 1.8DM**	65.36	65.21	0.23	58.77	58.89	−0.20	51	50.78	0.43
ΔR1 = 0.866DM **ΔR2 = 1.4DM** **ΔR3 = 2.0DM**	65.36	65.21	0.23	58.75	58.89	−0.24	51.07	50.69	0.74
ΔR1 = 0.866DM **ΔR2 = 1.4DM** **ΔR3 = 2.2DM**	65.36	65.21	0.23	58.68	58.89	−0.36	50.9	50.58	0.63

The results from Table 1 shows that all the field efficiency values are within a 1% margin difference. The differences can mainly be attributed to the solar radiation data used. Although the data is from the same location in Seville Spain, the reference model uses Typical Meteorological Year (TMY) data. (35) In contrast, the model developed utilizes measured data at the site for a limited period (the Year 2013-2014). The difference can also be as a result of the optical loss model for blocking utilized which defers from the one in the reference model.

Upon validation of the model developed, the procedure was applied to the selected site to design for the 50MWth field.

4.2.3 Design and Optimisation

As earlier stated in the previous chapters, the field in power tower systems have a significant weighting effect on the overall plant efficiency. This, in addition to being the most expensive part of the plant, further necessitates the importance of optimisation in designing the heliostat field layout.

In this work, the primary objective function considered in optimisation is in the form of minimizing a simplified Levelized Cost of Heat (LCOH) given by Equation 35 [162–164]. In calculating LCOH, only an independent generating system is assumed.

$$\begin{aligned} &\frac{Total\ Heliostat\ Field\ Life\ Time\ Cost}{Total\ Life\ Time\ Output\ of\ Annual\ Thermal\ Energy\ Generated\ at\ Receiver\ Surface} \\ &. \\ &= \frac{Field\ Installed\ Cost \times CRF}{E_{th}} + O\&M \end{aligned} \tag{36}$$

Where O&M signifies the operating and maintenance cost and CRF is the uniform series capital recovery factor. The CRF is given by Equation 36;

$$CRF = \frac{ir(1+i)^N}{(1+ir)^N - 1} \tag{37}$$

Where N is the lifespan of the project, and ir is the interest rate. The lifespan of the project is assumed to be 25 Years on a lending rate of 9%, values similar to those adopted in [151]. This equates the CRF to 0.1018.

A report by IRENA in 2014 [165] put the total O&M of an entire CSP plant between 0.02 to 0.04$/kWh. For the purpose of this paper, because the work is limited only to the heliostat field and thermal power, the lower end of the spectrum at 0.02$/kWht, is taken as the O&M cost.

The annual thermal energy at the receiver's aperture, E_{th} is given by the summation of the product of the instantaneous optical efficiency value for each heliostat, heliostat area, and the instantaneous beam radiation befalling an individual heliostat for all heliostats in the field (this also represents the power sent out from each heliostat). The power from each heliostat is then summed over the beam radiation at all sunshine hours on a representative day of the month [134], *I_day*. This is done for all months in the calendar year. Equation 38 describes the annual thermal energy at the receiver surface:

$$E_{th} = \sum_{1}^{Hel} \left[\sum_{I\_day}^{Year} \eta_{hel} \times I \times A_h \right] \tag{38}$$

where A_h is the heliostat area (m), η_{hel} is the instantaneous heliostat optical efficiency (%), *I* is the instantaneous beam radiation during sunshine hours (kWh/m^2), and Hel is the number of heliostats in the field. Only some days in the year are recommended to be used as average days for the month, and those were used in this work. The total heliostat field cost is a function of the tower cost, receiver cost, and heliostat cost. The cost model utilized NREL System Advisor Model (SAM) is applied here [106,108,150]. The system cost in SAM is limited only to direct capital costs.

As an example, the computed value for the LCOH in the Gemasolar plant using Equation 35 with heliostat field cost at $114,260,000 and E_{th} at 408.330GWht as depicted in [151] is 0.0485 $/kWht. The result assumes a CRF value of 0.1018 and O&M at 0.02$/KWht.

The optimisation code is developed using MATLAB GA from the global optimisation toolbox. [85,93,166]. Genetic algorithm is one of the most popular techniques in evolutionary computation research based on the mechanics of natural selection and natural genetics due to its ability to work with only one set of solution at a time aiding in avoiding the local minima [167]. The algorithm uses the design variables (Table 4-2) to calculate the objective function. The algorithm picks the design variables randomly and uses them as parents, after accessing its fitness function, in order to produce the children for the next generation in achieving the optimal solution. In this model, in order to reduce computational expense, a lower and upper bound of the design variables are set during optimisation. In this highly non-convex optimisation problem, as the search algorithm used is stochastic, to guarantee optimality, multiple simulations have been undertaken. The optimal value of the objective function was recorded after establishing the spread of deviation from the mean [168,169].

Table 4-2 Conventional field model design variables with lower and upper bounds.

Design Variables	Variables Range
Number of Heliostats in 1st row (Zone 1)	10–46
Heliostat Area (m^2)	25–120
Receiver Dimensions(m^2)	25–226
Tower Height (m)	25–140
Heliostat Row Separation Distance Zone 1 (m)	(0.866 – 1.666) × DM
Heliostat Separation Distance Zone 2 (m)	(0.866 – 2.666) × DM

Heliostat Separation Distance Zone 3 (m)	(0.866 – 3.666) × DM

4.3 Results and Discussion

One of the defining constraints in the optimiser is the thermal power of the field. In a random selection of the design variables, it is possible to reach a value that is below or above the set goal of 50MWth. The optimiser is then made to disregard such results from the population. Results of the conventional field from the optimisation in the model developed are summarized in Table 4-3.

Table 4-3 Summary of Key results from 50MWth conventional power tower field from the model developed and SAM

Parameter	Model	System Advisor Model (SAM)
Heliostat Area (m^2)	95.17	95.17
Central Tower Height (m)	91.48	83.98
Central Receiver Area (m^2)	55.84	91.43
Levelized Cost of Heat, LCOH (\$/kWht)	0.0473	0.0481
Power (MWth)	49.89	50
Efficiency Design Point (%)	60.59	-
Mean Annual Efficiency (%)	55.63	55.63
Reflective Surface Area (m^2)	152,270.72	136,011.51
Annual Energy (MWht)	151,849.08	149,560.720
System Cost (\$)	40,652,834.350	41,253,240.000

For a 50MWth field, the LCOH obtained was 0.0473\$/kWh, with the annual thermal energy at 152,270 MWth, and the total field cost at \$40,652,834.350. The mean annual efficiency for the designed and optimised plant was 55.63%. In order to further validate the model developed, SAM was used to generate and optimise a 50MWth field. The results were then compared with the model developed. To calculate the LCOH using SAM, Equation 36 was applied using the same values for the CRF. The comparison between the results is shown again in Table 4-3. A marginal difference was observed in the LCOH from both models, showing a good correlation.

In Figure 4-7, the field layout from the conventional field model is shown, representing the mean annual heliostat efficiency. In Appendix B1 and B2, the full layout of the conventional field is shown under different optical efficiency loss factors and the mean annual efficiency layout for the typical selected day through all the months are shown respectively. The results of the optimisation from other thermal powers in the conventional field are also shown in Appendix B3.

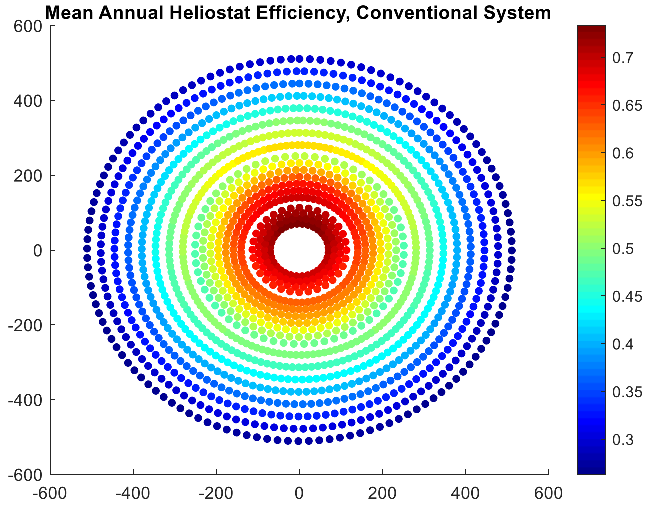

Figure 4-7 Field layout of 50MWth field showing the mean annual heliostat efficiency

An apparent reduction in the mean annual efficiency of the heliostats is witnessed across the Zones in the field from Figure 4-7. In Zone 1, the mean annual efficiency is at 69.18%; Zone 2 at 57.96%, and finally, Zone 3 at 39.75%. Similarly, the annual thermal energy sent out by the heliostats across all the Zones is 10,733 MWht, 40,904 MWht and 99,506 MWht for Zones 1, 2 and 3 respectively. The month on month variation of the mean annual efficiency and energy output of the field across all the three Zones in the field is shown in Figure 4-8 a & b respectively. In Figure 4-8b, it is worth mentioning that the dip witnessed between month 6 to 8 is a result of the poor DNI values as a result of the cloud cover during that period (NiMet Data, Appendix A).

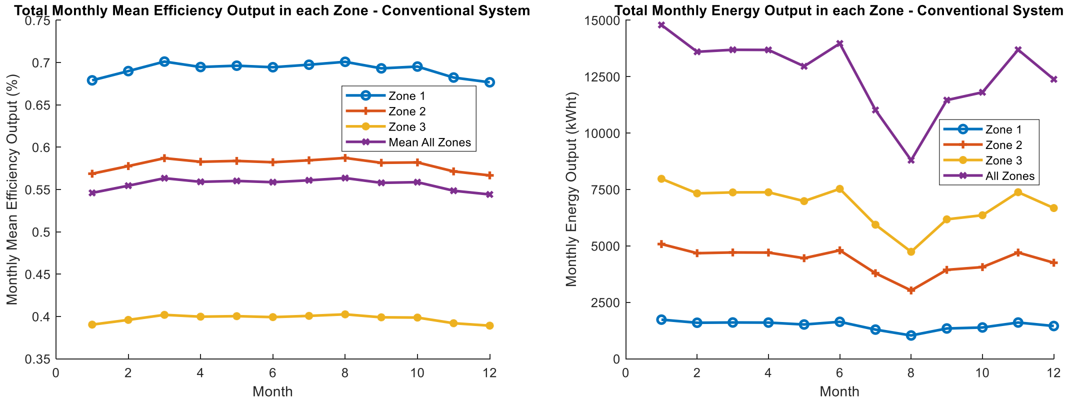

(a) (b)

Figure 4-8 a) Total monthly mean efficiency output in all zones in the field. b) Total monthly mean energy output in all Zones in the field

In Table 4-4, the contribution of each optical loss parameter to the overall field efficiency in each Zones is shown.

Table 4-4 Mean Annual optical efficiency Values in all zones in the field

Parameter	Mean Annual Efficiency Zone 1 (%)	Mean Annual Efficiency Zone 2 (%)	Mean Annual Efficiency Zone 3 (%)	Mean Annual Efficiency All Zones (%)
Spillage Efficiency	99.48	94.00	69.96	87.82
Cosine Efficiency	83.23	77.38	72.92	77.84
Attenuation Efficiency	97.83	96.87	94.88	96.52
Blocking Efficiency	100.00	96.48	95.79	97.42

The results from Table 4-4 shows a continuous reduction in all the optical loss models with cosine efficiency, having the largest share of optical losses. The losses become more pronounced in Zone 3 due to the increasing distance of the heliostats from the aim point.

Chapter Summary

A MATLAB program that models and simulates the heliostat field of a power tower system using the radial staggered configuration was developed. The method, campo, for the generation of configuration was adopted in the work presented here.

Different models of the optical loss parameters were then applied in order to measure the strength of the reflected radiation arriving at the receiver surface, so the target field power of 50MWth can be met. At 50MWth, all the design variables in the field including; heliostat area, receiver dimensions, tower height and successive heliostat row separation distance were optimised using Genetic Algorithm (GA) in order to meet the primary objective function. The objective function is in the form minimizing the Levelized Cost of Heat (LCOH) given by the ratio of the total heliostat field cost to the annual field thermal energy output.

For a 50MWth field, the LCOH was obtained to be at 0.0473$/kWh with the annual thermal energy at 151,849MWth, and a mean annual efficiency value at 55.63%. The results were compared with a field of similar thermal rating using the National Renewable Energy Laboratory’s (NREL) System Advisor Model (SAM) model, and a good correlation between the two models was achieved.

5 MULTI-TOWER HELIOSTAT FIELD

In this chapter, the configuration of multi-tower fields was investigated. Multi-tower configurations here emphasize adding auxiliary tower(s) to a conventional field. This forms the basis of the first type of field to be discussed. A paper has been published in [22] on this regard Subsequently, field improvement strategies on the multi-tower configuration were also discussed and analysed. This led to the proposal of a new configuration for multi-tower configuration. The chapter begins by discussing the positions in which the auxiliary towers are sited.

5.1 Auxiliary Tower Positioning and Aim Selection Criteria

As earlier highlighted, in this work, a different architecture of the multi-tower configuration is investigated. The configuration provides an alternate viewpoint to the usual mainstream multi-tower configuration, by adding auxiliary towers to an existing surrounding field. One of the first questions to be addressed is the position in which the auxiliary tower will be placed. The auxiliary tower location here was calculated based on the region with the lowest efficiency and reflected energy [22]. This provides an outlook of the region most in need of an additional tower and thus forms the basis of the decision made here. The mean annual heliostat efficiency representation of the conventional field previously computed in Chapter 4 is evaluated to aid in identifying the region with the lowest efficiency. In order to simplify the computation, the field is divided only into four quadrants. On each quadrant, the mean annual efficiency is computed. See Figure 5-1 and Table 5-1.

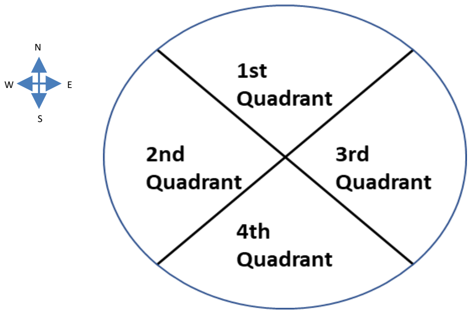

Figure 5-1 Position of the four identified quadrants in the field

Table 5-1Mean annual efficiency at the four identified quadrants

Averaged Annual Efficiency in the 1st Quadrant (%)	Averaged Annual Efficiency in the 2nd Quadrant (%)	Averaged Annual Efficiency in the 3rd Quadrant (%)	Averaged Annual Efficiency in the 4th Quadrant (%)
55.36	54.83	55.19	54.04

The results from Table 5-1 clearly show the region having the least mean annual efficiency value. This is predominantly as a result of the more substantial cosine losses in that region of the field. This corroborates with plant locations north of the equator favouring north-facing fields [55,157]. In a conference paper presented by the author [170], the effect of citing the tower at different regions in the field is computed. The results from the paper show that by putting the auxiliary tower at the weakest region (which computes to be in the fourth quadrant), the most significant improvement on the power and efficiency of the field is seen.

With the multi-tower field generated, the criteria on how heliostats aim at the receivers in the field are defined. The heliostats are not restricted by which tower they are allowed to focus on. Each heliostat decides on the receiver to target based on the strength of the reflected radiation. In other words, the optical efficiency losses are simultaneously computed for each heliostat in all the scenarios; aiming at the central tower and the auxiliary tower(s) [22]. The aim point bearing the lesser loss, based on the combined optical efficiency loss parameter, is selected.

5.2 Multi-Tower configuration

5.2.1 One Auxiliary Tower

With one extra tower in the field, the location of the additional tower to be introduced is sighted at the central position of the weakest quadrant: the fourth quadrant (see Figure 5-2).

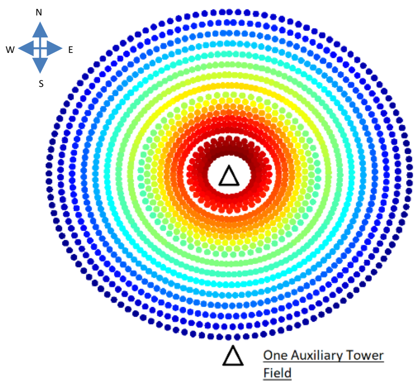

Figure 5-2 Description of the auxiliary tower position

An overall assessment of the potential of adding an auxiliary tower to the 50MWth optimised conventional field was conducted. This assessment can be considered as an evaluation for upgrading or retrofitting a pre-existing conventional field. The auxiliary tower was added under varying receiver dimensions, tower height and tower displacement distance. Variables' ranges for the auxiliary tower are highlighted in Table 5-2. The results in Figures 5-3a&b show an evident increase in the field efficiency values and the thermal energy for different combinations of additional tower input variables (Table 5-2). In Figure 5-3a, at no point does the LCOH of the field with the auxiliary tower and converge with the conventional field, signifying that at that particular field power, the auxiliary tower would always have a higher LCOH [22]. With increasing values of the design variables, the LCOH of the auxiliary tower becomes higher (Figure 5-3a).

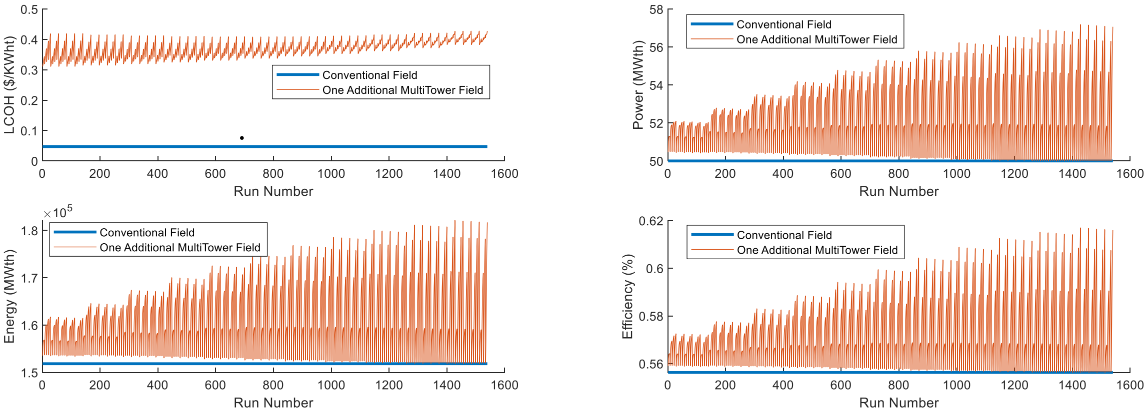

(a) (b)

Figure 5-3 a) LCOH and energy output one additional multi-tower system b) Thermal Power and mean annual efficiency, one additional multi-tower system

The additional design variables for the multi-tower configuration are utilized in the optimisation process for the 50MWth field with the same objective function of LCOH earlier highlighted in equation 36. This would increase the number of design variables in the optimisation process. The updated number of design variables are highlighted in Table 5-2.

Table 5-2 Multi-tower (one additional tower) field model design variables with the lower and upper bound

Design Variables	Variables Range
Number of Heliostats in 1st row (Zone 1)	10 – 46
Heliostat Area (m^2)	25 – 120
Receiver Dimensions(m^2)	25-226
Tower Height (m)	25 – 140

Heliostat Row Separation Distance Zone 1, ΔR1 (m)	(0.866 – 1.666) * DM
Heliostat Row Separation Distance Zone 2, ΔR2 (m)	(0.866 – 2.666) * DM
Heliostat Row Separation Distance Zone 3, ΔR3 (m)	(0.866 – 3.666) * DM
Auxiliary Tower Placement Distance (m)	((0.866 – 1.666) * DM) + Df
Auxiliary Tower Height (m)	25 – 140
Auxiliary Tower Receiver Dimensions(m^2)	6-226

Df is the final distance between the central tower and the furthest heliostat in the same axis location of the auxiliary tower location.

In the multi-tower setup, the same objective function as the conventional field is applied, minimizing the LCOH. However, in the multi-tower field, there are additional objective functions hence making it a multi-objective optimisation problem. These include the total heliostat reflective surface area and the annual mean efficiency of the field. In order to simplify the solution process, the additional objectives are handled as constraints [22]. This is in addition to the initial constraint limiting the optimiser to computing results only at a field power of 50MWth. With the field efficiency constraint, only values that are higher than the computed result from the conventional setup are considered in the optimiser. The total reflective surface area constraint, on the other hand, limits the optimiser from finding solutions that exceed the total reflective surface area of the conventional field [22]. After a certain number of repeated optimisations runs, the objective function was recorded after achieving a low spread between the lowest and highest value of the optimum LCOH computed.

5.2.2 Two Auxiliary Towers

With two extra towers in the field, the region of focus on the field is in the lower half (southern half). If the conventional field is divided into two halves; North and South, the former results in an annual mean efficiency value of 57.58% and the latter 54.49%. The additional towers here are therefore positioned to provide a target for as many heliostats as possible within the weaker half of the field. The points selected for the two auxiliary towers; the first auxiliary tower placed at angle 202.5° (in-between the 2nd and 3rd quadrant) and the second tower at 292.5° (in-between the 3rd and 4th quadrant). The positions of the towers are shown in Figure 5-4.

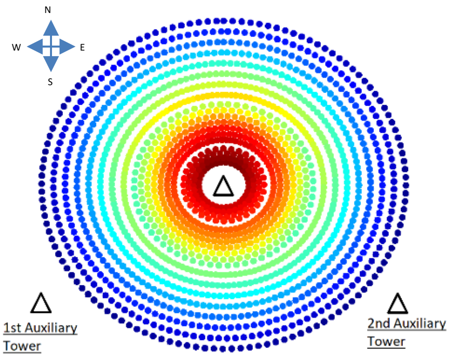

Figure 5-4 Description of the field with two auxiliary towers

Following the same procedure in the field with one auxiliary tower, an overall assessment of the potential of adding two auxiliary towers to the optimised 50MWth conventional field was evaluated. The results are presented in Figure 5-5. All the design variables for the two extra towers in the field are considered in the evaluation process (Table 5-3). The results present a higher field efficiency, thermal power and energy when compared to both the conventional field and one auxiliary tower multi-tower field but at the cost of a higher LCOH (Figure 5-5a).

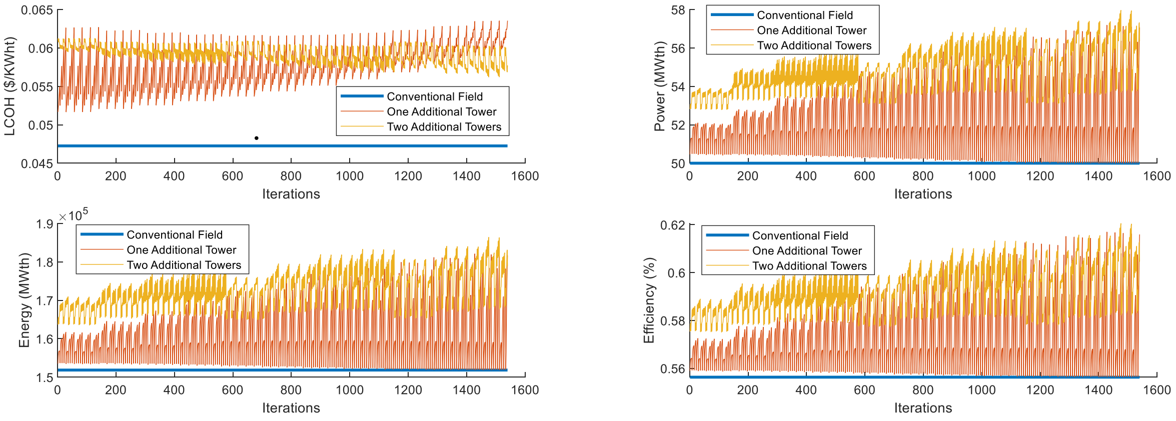

(a) (b)

Figure 5-5 a) LCOH and energy output two additional multi-tower system b) Thermal Power and mean annual efficiency, two additional multi-tower system

The updated design variables for the optimisation process for the two auxiliary tower system are highlighted in Table 5-3.

Table 5-3 Multi-tower (one auxiliary tower) field model design variables with the lower and upper bound

Design Variables	Variables Range
Number of Heliostats in 1st row (Zone 1)	10 – 46
Heliostat Area (m^2)	25 – 120
Receiver Dimensions(m^2)	25-226
Tower Height (m)	25 – 140
Heliostat Row Separation Distance Zone 1, ΔR1 (m)	(0.866 – 1.666) * DM
Heliostat Row Separation Distance Zone 2, ΔR2 (m)	(0.866 – 2.666) * DM
Heliostat Row Separation Distance Zone 3, ΔR3 (m)	(0.866 – 3.666) * DM
1st Auxiliary Tower Placement Distance (m)	((0.866 – 1.666) * DM) + Df
1st Auxiliary Tower Height (m)	25 – 120
1st Auxiliary Tower Receiver Dimensions(m^2)	6-100
2nd Auxiliary Tower Placement Distance (m)	((0.866 – 1.666) * DM) + Df
2nd Auxiliary Tower Height (m)	25 – 120
2nd Auxiliary Tower Receiver Dimensions(m^2)	6-100

The methodology for optimisation here follows a similar procedure as highlighted previously in the multi-tower field, having one auxiliary tower. However, the constraints here limit the optimiser to only results having a higher annual mean-field efficiency and a total reflective surface area lower than the one auxiliary tower configuration. The primary constraint of the field thermal power, 50MWth, in this case, remains the same.

5.2.3 Results and Discussion

The results from the optimisation process from both multi-tower configurations are highlighted in Table 5-4. In order to provide a comparative description, the results from the multi-tower fields are compared alongside the results from the single tower conventional field.

Table 5-4 Comparison of Conventional, and optimised multi-tower field results

Parameter	Conventional Field	Multi-tower Field (One Auxiliary Tower)	Multi-tower Field (Two Auxiliary Towers)
Heliostat Area (m^2)	95.17	93.99	91.57
Central Tower Height (m)	91.48	92.91	85.95
Central Receiver Area (m^2)	55.84	40.36	132.84
1st Auxiliary Tower Height (m)	-	92.94	35.08
1st Auxiliary Receiver Area (m^2)	-	66.38	13.68
2nd Auxiliary Tower Height (m)	-	-	38.60
2nd Auxiliary Receiver Area (m^2)	-	-	11.10
levelized Cost of Heat ($/kWht)	0.0473	0.0575	0.0591
Field Power (MWth)	50	50	50
Efficiency Design Point (%)	60.59	63.12	67.62
Mean Annual Efficiency (%)	55.63	58.79	62.89
Mean Annual Attenuation Efficiency (%)	96.52	97.07	97.03
Mean Annual Blocking Efficiency (%)	97.42	94.41	98.09
Mean Annual Cosine Efficiency (%)	77.84	84.47	89.87
Mean Annual Spillage Efficiency (%)	87.82	92.70	99.05
Reflective Surface Area (m^2)	152,270	140,987	122,154
Number of Heliostats	1,600	1,500	1,334
Annual Energy (MWht)	151,849	155,610	157,464
1st Auxiliary Receiver Thermal Power (MWth)	-	11.55	1.81
2nd Auxiliary Receiver Thermal Power (MWth)	-	-	1.15
System Cost ($)	40,652,834	57,198,009	60,482,916

One Auxiliary Tower

As shown in Table 5-4, with one additional tower in the multi-tower field, a marked increase in the optical field efficiency value is observed. A 3.16% increase in the mean annual field efficiency and 2.53% in the design point efficiency is observed when compared to the results obtained in a conventional field setup. The most considerable improvement in optical efficiency is seen in the cosine efficiency value. This is primarily because the additional tower in the field provides an alternate aim point for the heliostats having the least reflecting efficiency. The LCOH, however, is higher in the new configuration. This indicates that the benefits due to the increment in the optical efficiency values and annual energy output do not out-weigh the cost of installing an additional tower and receiver [22].

In the new configuration, the number of heliostats aiming at the one auxiliary tower changes through the months and the day (see Figure 5-6a & 5-6b). At the design point date, April 20th, a total number of 317 heliostats aim at the auxiliary tower at solar noon (Figure 5-6a). The number of heliostats aiming at the auxiliary tower at solar noon peak in January and December when the sun's position is low making it difficult for the 'weak' heliostats to reflect radiation onto the main central tower without incurring enormous cosine losses (Figure 5-6a). On the other hand, during sunshine hours, and at around solar noon, a reduced number of heliostats aim at the auxiliary tower. This is predominately due to the lesser cosine losses from the heliostats aiming at the main central tower and, hence becoming a preferred target [22].

The computed thermal power rating of the auxiliary tower is 11.55 MWth. The main central tower, which caters to the bulk of the heliostats in the field, now has a computed thermal rating of 38.45 MWth.

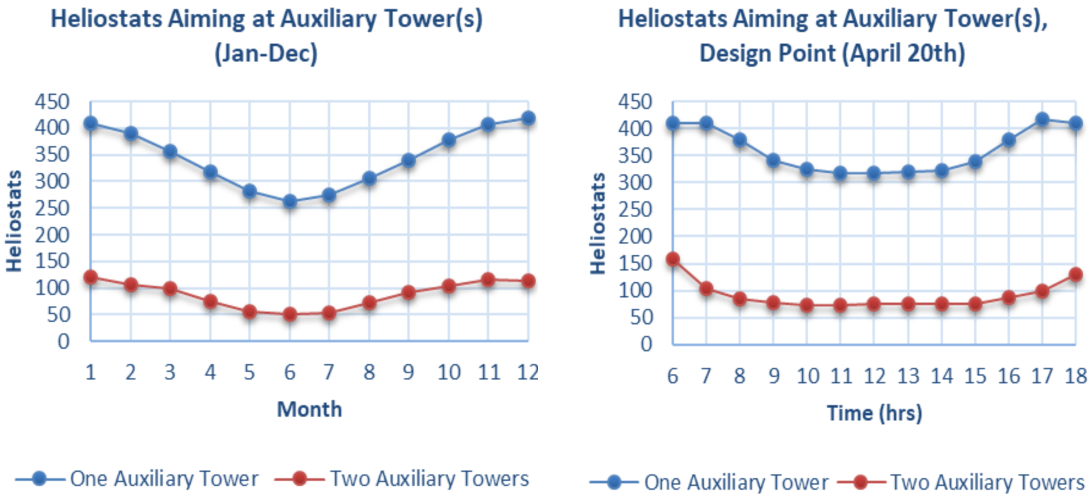

Figure 5-6 a) Heliostats aiming at the auxiliary tower(s) through the year b) Heliostats aiming at the auxiliary tower(s) during sunshine hours at the design point date.

In Figure 5-7a and 5-7b, the month on month variation of the total energy output and mean efficiency values for both the conventional field and the multi-tower field is shown. A marked improvement in the mean efficiency value is observed through January to December from the two models in Figure 5-7b. In Figure 5-7a, it is worth mentioning that the dip witnessed between month 6 to 8 is a result of the poor DNI values as a result of the cloud cover during that period (from NiMet data) [22].

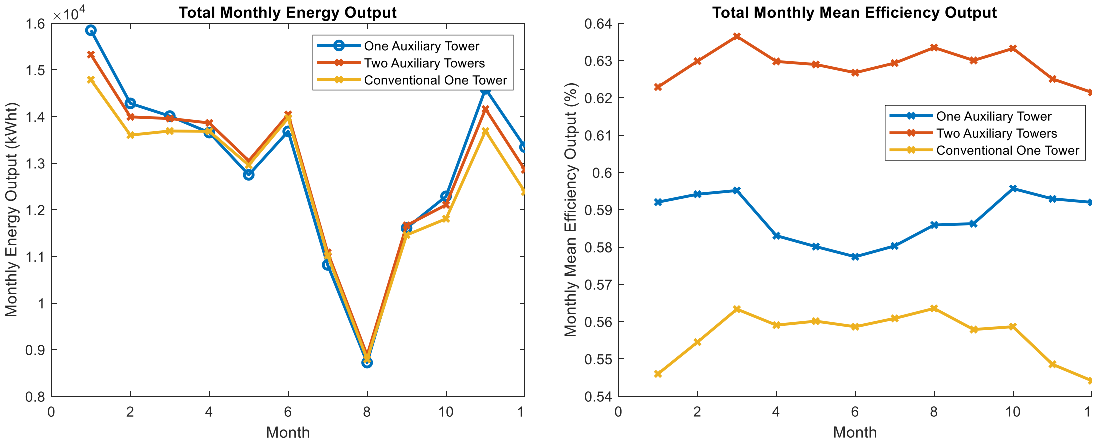

(a) (b)

Figure 5-7 a) Total monthly energy output, conventional and one additional tower field b) Total monthly mean efficiency output, conventional and one additional tower field

A more explicit demonstration of the effect of the multi-tower field is shown in Figure 5-8. The mean annual efficiency field layout for the conventional system and the one additional tower field is seen in Figure 5-8a and 5-8b. The change in shading matrices of the optical losses model from the conventional field to the multi-tower field can be seen in Figure 5-6d, e, g, h, j, k, m & n. See Appendix C1 for the representative day of the month field outlook in the multi-tower field configuration through the year.

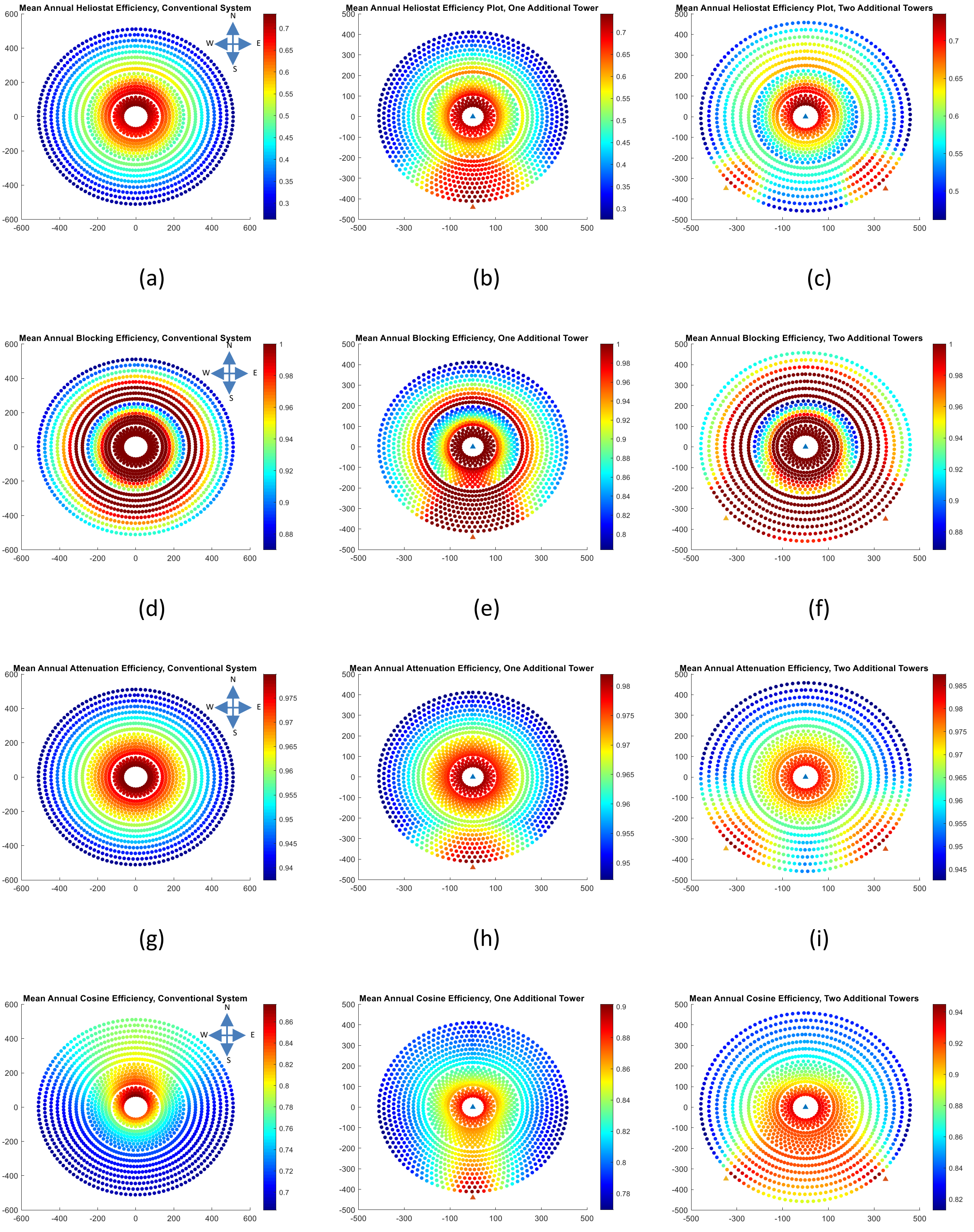

(a) (b) (c)

(d) (e) (f)

(g) (h) (i)

(j) (k) (l)

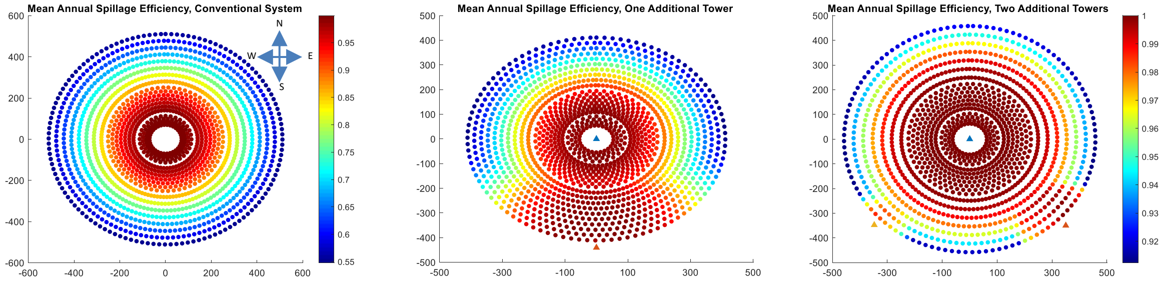

(m) (n) (o)

Figure 5-8 a, d, g, jam) Conventional field: mean annual efficiency, blocking, attenuation, cosine, and spillage respectively b, e, h, k,n) One auxiliary tower: mean annual efficiency, blocking attenuation, cosine, and spillage respectively c,f,I,l,o)Two auxiliary towers: mean annual efficiency, blocking attenuation, cosine, and spillage respectively

Two Auxiliary Towers

With two auxiliary towers, an even higher field efficiency is recorded; 8.09% higher than the conventional field. One of the notable differences is the central receiver's area at 132.84 m^2. The optimisation converges at a much higher receiver area in order to compensate for the expected increase in the field's cost obtained from the presence of two additional towers and their receivers. Despite the low tower height and receiver area dimensions of the auxiliary towers, the cost of the field totals to $60,482,196, about 20 million dollars higher than the conventional field and about three million dollars higher than the field with one auxiliary tower. The major contributing component to the total cost is from the main central tower's receiver, which alone costs $18,272,261.

The total number of heliostats aiming at the auxiliary towers at solar noon on the representative day of every month is shown in Figure 5-6a. The total heliostats covered by the auxiliary towers are a lot less when compared to those covered by the central tower. The reach from the large central receiver covers almost the entire heliostats in the field hence the small thermal rating on the auxiliary receivers. This can be seen from the thermal receiver sizes; main central tower at 47.04 MWth, first auxiliary tower at 1.15MWth and the second auxiliary tower at 1.81MWth. In Figure 5-9, the number of heliostats aiming at auxiliary towers in the field is shown at different times of the day. Due to the position of the tower (Figure 5-4) and sun in the early hours of the morning, the first auxiliary tower presents a preferable target for heliostats in the third quadrant of the field (Figure 5-1). Later in the day, a fewer number of heliostats are able to target the first auxiliary tower primarily due to the position of the sun. The heliostats hence opt for other targets in the field, in this case, the central and second auxiliary tower. The vice versa is seen with the second auxiliary tower.

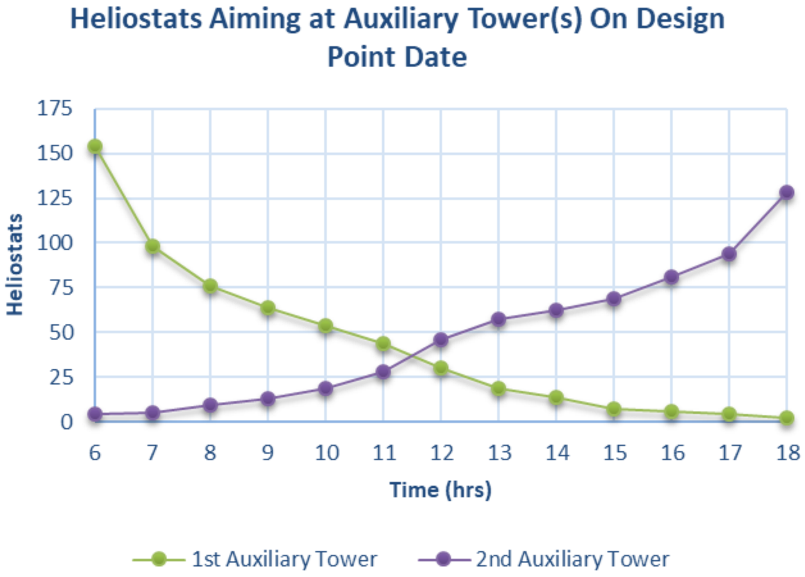

Figure 5-9 Heliostats aiming at the first and second auxiliary tower on design point date 14th April.

The two auxiliary towers configuration does lead to a slightly higher annual thermal energy output at 157,464MWht when compared to both the conventional and one auxiliary tower field. However, the gain recorded in the annual energy output is not enough to make the configuration achieve a lower LCOH value when compared to both the conventional and one auxiliary tower field.

In Figure 5-8 f, i, l & o the shading matrix for all the optical efficiency factors in a two auxiliary tower field is shown. In Figure 5-8c, the mean annual field efficiency is also shown.

The entire optimisation for the multi-tower field was initially made for a 50MWth field. A broader range of thermal powers was examined so a more critical analysis of the effect of a multi-tower field can be observed [22]. In Appendix C2, the summarized results showing the LCOH, efficiency, reflective surface area and the number of heliostats for all thermal powers using the multi-tower field configuration are outlined. Figure 5-10 shows the LCOH results from both the conventional field model and the multi-tower field model at various power thermal field values.

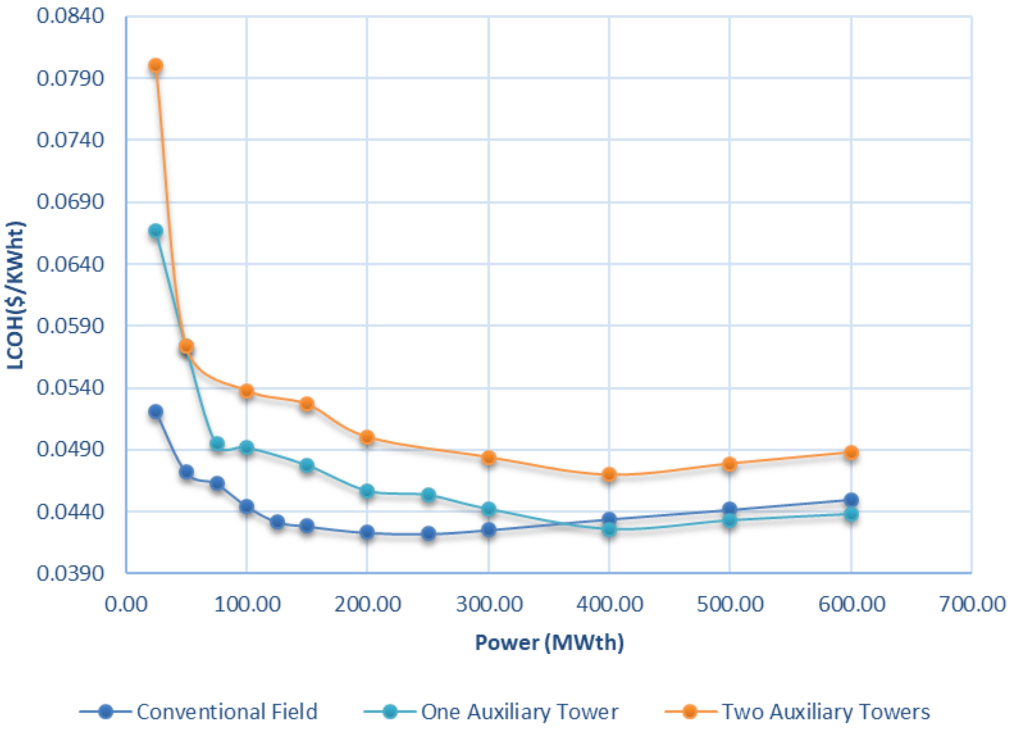

Figure 5-10 Levelized Cost of Heat (LCOH), conventional field and multi-tower field

Results from Figure 5-10 clearly shows the promising LCOH trend of both multi-tower fields configurations discussed at higher thermal power figures and larger fields. In larger fields, a higher number of weaker heliostats are witnessed in the field, making the need and use of an additional tower all the more critical [22]. The heliostats at the weaker region in the field of a multi-tower field are provided with an additional tower to reflect the sun's radiation, thereby considerably cutting down on cosine, spillage and attenuation losses which in turn gives rise to higher total energy output [22]. At some point, as seen in the trend, the multi-tower field continuously provides a lower LCOH value when compared to the conventional field of similar thermal power. This is seen explicitly at the 400MWth range in the one auxiliary tower configuration, where expanding the conventional field in order to attain a higher thermal field output becomes less effective due to the significant optical losses gained as a result of the size of the field [22].

In the two auxiliary tower field (for the given thermal powers considered) at no point does the configuration converge or best both the conventional and one auxiliary tower field. This may as well change at much higher thermal powers. However, the study here is limited to the current estimated thermal fields powers at around 600MWth: much like the Noor III plant in Ouarzazate, Morocco [171].

5.3 Auxiliary Tower with Subfields Configuration (ATS)

The Auxiliary Tower with Subfield configuration (ATS) can be regarded as a continuation of the earlier configuration discussed in Chapter Section 5.2. In this configuration, heliostats are added near the position of the auxiliary tower, thereby creating another region in the field regarded herein as a subfield. The configuration shares a close resemblance with much of the works of literature reviewed on multi-towers which have a surrounding field for each of the towers in the field. ATS, however, differs by developing a subfield that is complementary to a multi-tower setup. The auxiliary towers in ATS act as targets for both the weak heliostats in the main field (as highlighted in 5.2) and the newly added heliostats in the subfield sited near the auxiliary towers. Like in section 5.2, the configuration will be looked at for both one and two auxiliary tower(s). In both configurations, the subfield is generated using the same standard radial staggered methodology as described in 4.2.1. The field generation is however limited to only half of a field. This necessitates the auxiliary's tower receiver to be of the cylindrical type; serve as a target for both heliostats in the main field and the subfield. The ATS configuration can be viewed from the perspective of updating or retrofitting an existing conventional field. The computed optimised conventional field is maintained in applying the ATS model.

5.3.1 One Auxiliary Tower

A suitable location for the auxiliary tower has already been previously addressed in Section 5.1. The heliostats in the subfield are placed near the auxiliary tower. A depiction of the ATS configuration in a one auxiliary tower configuration is shown in Figure 5-11.

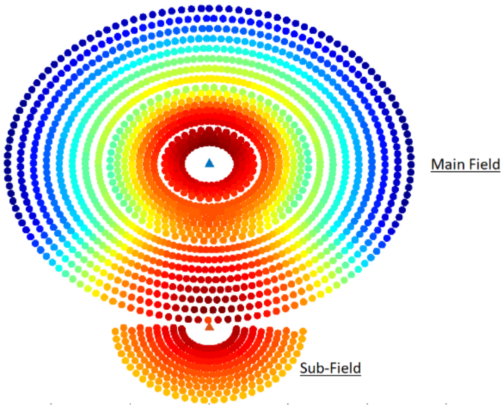

Figure 5-11 One auxiliary tower multi-tower configuration with Sub-Field

The configuration is initially applied in a 50MWth multi-tower field. The design variables for the 50MWth multi-tower field have been earlier computed (Table 5-4), and hence maintained. The design variables for the subfield in this new multi-tower field configuration are similar to those highlighted earlier in Table 4-2. The subfield in which the heliostats are placed is regarded as zone 4. Table 5-5 highlights the design variables and their respective range here.

Table 5-5 Design Variables and range for a 50MWth multi-tower configuration with one auxiliary tower subfield

Design Variables	Variables Range
Number of Heliostats in 1st row (Zone 4)	20 – 80
Heliostat Row Separation Distance Zone 4, ΔR4 (m)	(0.866 – 1.066) * DM
Auxiliary Tower Placement Distance (m)	((0.866 – 1.066) * DM) + Df
Auxiliary Tower Height (m)	25 – 140
Auxiliary Tower Receiver Dimensions(m^2)	6-120

Df is the final distance between the central tower and the furthest heliostat in the same axis direction of the auxiliary tower location.

The heliostat area all through the fields remains the same. In this case, for the 50MWth field, the heliostat area is at 95.17 m^2. The maximum number of heliostats that can be added in the subfield is limited to the initial number of the heliostat in the main field, 1,600 in the case of a 50MWth field. This constraint is meant to restrict the subfield from becoming larger than the main field and also to reduce the computational load of having too many variables. In the ATS configuration, heliostats are continuously added, with different design variables (Table 5-5). The results are then computed and compared with different conventional field thermal field.

5.3.2 Two Auxiliary Towers

With two auxiliary towers in the ATS, two additional subfields are created in the field. Like in the one auxiliary tower case, the position of the auxiliary towers has been already previously identified in 5.2.2. In Figure 5-12, the layout of the configuration having two subfields is shown.

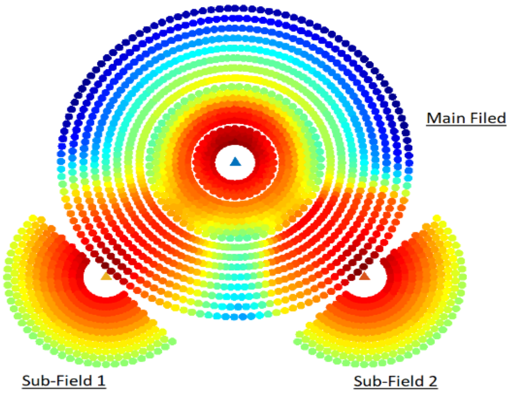

Figure 5-12 Two auxiliary towers multi-tower configuration with sub-fields

In a similar manner to the one auxiliary tower with subfield configuration, the optimised conventional field is maintained, and the effect of adding two auxiliary towers each having a subfield of its own is evaluated. The heliostats in the subfield are simultaneously added into the field. The configuration was equally initially simulated in a 50MWth field. The heliostats in each subfield here are limited to the number of heliostats in the main field. For the 50MWth field, for example, a total of around 3,200 heliostats are being considered; 1,600 in each of the subfield.

The subfields in the ATS configuration are equally generated using the radial staggered configuration from F.J Collado's Campo [18]. The design variables and their range in this model are highlighted in Table 5-6. The design variables in each subfield are replicated in the second subfield. Heliostats region in subfield 1 and 2 are referred to as Zone 4 and 5 respectively.

Table 5-6 Design variables for a 50MWth multi-tower configuration with two auxiliary towers subfields

Design Variables	Variables Range
Number of Heliostats in 1st row (Zone 4 & Zone 5)	20 – 160
Heliostat Row Separation Distance Zone 4 & Zone 5, ΔR4, ΔR5 (m)	(0.866 – 1.066) * DM
1st and 2nd Auxiliary Tower Placement Distance (m)	((0.866 – 1.066) * DM) + Df
1st and 2nd Auxiliary Tower Height (m)	25 – 140
1st and 2nd Auxiliary Tower Receiver Dimensions(m^2)	6-180

Df is the final distance between the central tower and the furthest heliostat in the same axis location of the auxiliary tower location.

5.3.3 Results and Discussion

The result and discussion section are divided into two, each for the different configurations for the ATS.

One Auxiliary Tower

In Figure 5-13a-d, the results from adding heliostats to the subfield in a 50MWth field are shown. See Appendix D1, for additional results from the configuration with one additional tower.

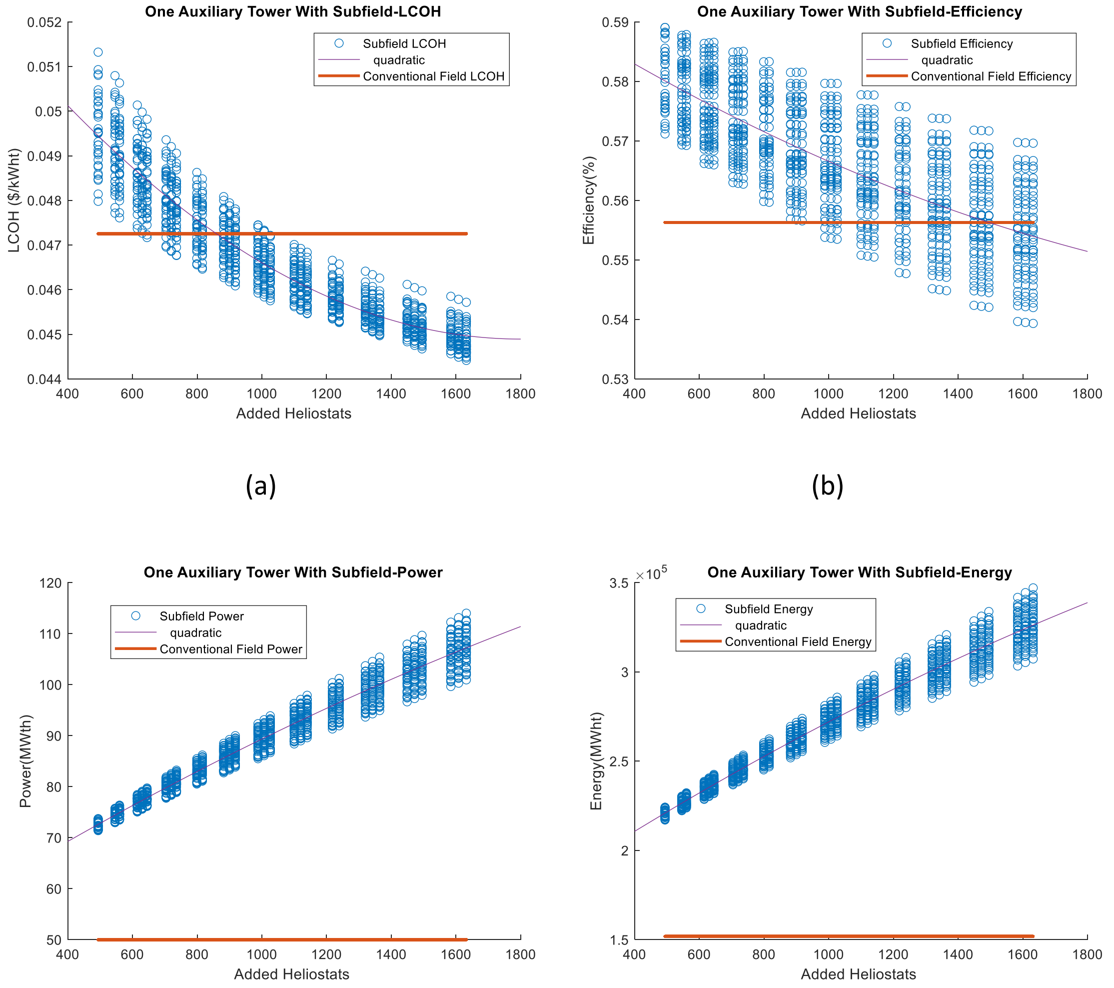

(a) (b)

(c) (d)

Figure 5-13 Computational results are showing the effect of adding heliostats in a subfield with an auxiliary tower for different parameters a) LCOH b) Mean annual efficiency c) Field thermal power d) Annual thermal energy

In Figure 5-13a, the trend in change of the LCOH can be seen with a varying number of heliostats added onto the subfield. As the heliostats are added, an improvement in the LCOH is continuously observed within the limits of the 1,600-maximum number of added heliostats in the subfield. At around the 1100th added heliostat, the rate of reduction in the LCOH gradually decreases. The LCOH of the 50MWth conventional configuration field at 0.0473 $/kWht shown in the figure indicates at the 855th added heliostat; better LCOH values are obtainable in the ATS configuration. At the 1088th added heliostat in the subfield, all LCOH values obtained within the limits of the design variables, are lower when compared to the conventional 50MWth field.

In Figure 5-13b, the conventional field mean-annual efficiency at 54.80% cuts across the different values of annual mean efficiency obtained in the ATS configuration. At the 988th added heliostat, mean annual efficiency values lower than conventional fields become obtainable. Lower values of annual mean efficiency progressively increase from the 988th added heliostat. When heliostats are added in the subfield, a continuous decrease in the efficiency is witnessed. This is as a result of the increase in the optical losses incurred as heliostats in the 4th zone move further away from the auxiliary tower. An overall reduction in the mean efficiency is ultimately witnessed, as shown in Fig 5-13b. The mean efficiency value can serve as a good indicator as to which point the addition of heliostats in the subfield can be stopped.

Figure 5-13c&d provide the thermal field power, and energy outlook of the field as heliostats are added into the subfield. As more heliostats are added, a steady increase in the power and annual field energy is observed. At all the points of added heliostats considered, the configuration provides a higher value of both the energy and power when compared to the conventional field.

As mentioned earlier, the maximum number of heliostats added in the ATS model is limited to the initial number of heliostats computed in the conventional field. With 1,600 heliostats only considered in the subfield, the calculated LCOH across all design variables is on a steady decline (Figure 5-13a). This, however, changes with much larger quantities of the added heliostats in the subfield, as shown in Figure 5-14.

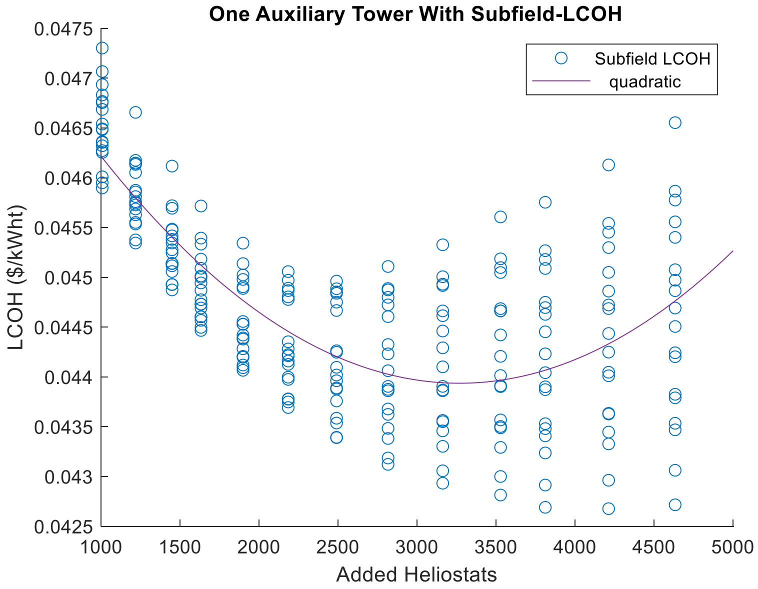

Figure 5-14 Computational results showing the LCOH effect of adding 4,600 heliostats in a subfield with an auxiliary tower.

The results obtained from the ATS configuration cannot be compared against the 50MWth conventional field. This is as a result of the direct correlation between the added heliostats and the thermal field power and energy (Figure 5-13). For example, the optimum LCOH value from the ATS configuration at 75MWth thermal field power is achieved when 615 heliostats are added in the subfield. The calculated LCOH at that point is 0.0479$/kWht. When compared to a conventional 75MWth field (with LCOH at 0.0463$/kWht), the LCOH is slightly higher. The layout of such a field is shown in Figure 5-15. With the addition of the auxiliary tower to the 50MWth field, at the design point and date, the total field power now becomes 52.61MWth. With 615 heliostats added to the subfield in Zone 4, the total thermal field power then computes to 75.21MWth. The mean annual field efficiency, on the other hand, becomes 56.77%, an increment of 1.14% and 1.73% from a 50MWth and 75MWth conventional field respectively.

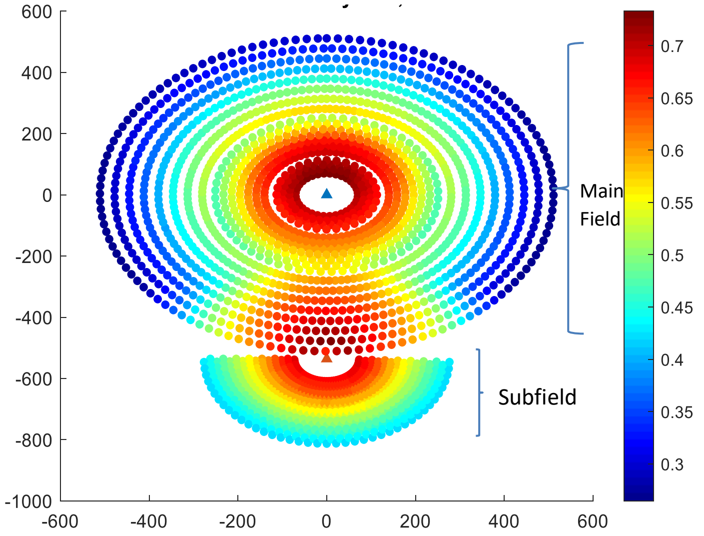

Figure 5-15 One ATS configuration showing the layout of 75MWth thermal field.

In Figure 5-16, the optimum LCOH values obtained from different thermal powers obtainable in a 50MWth ATS configuration are compared with the LCOH values in a conventional field. Here, despite the improvement in energy output recorded by the inclusion of a subfield in the ATS configuration, the conventional field LCOH delivers better results. The gain recorded from the increase in energy cannot offset the additional cost from the auxiliary tower, receiver and additional heliostats from Zone 4.

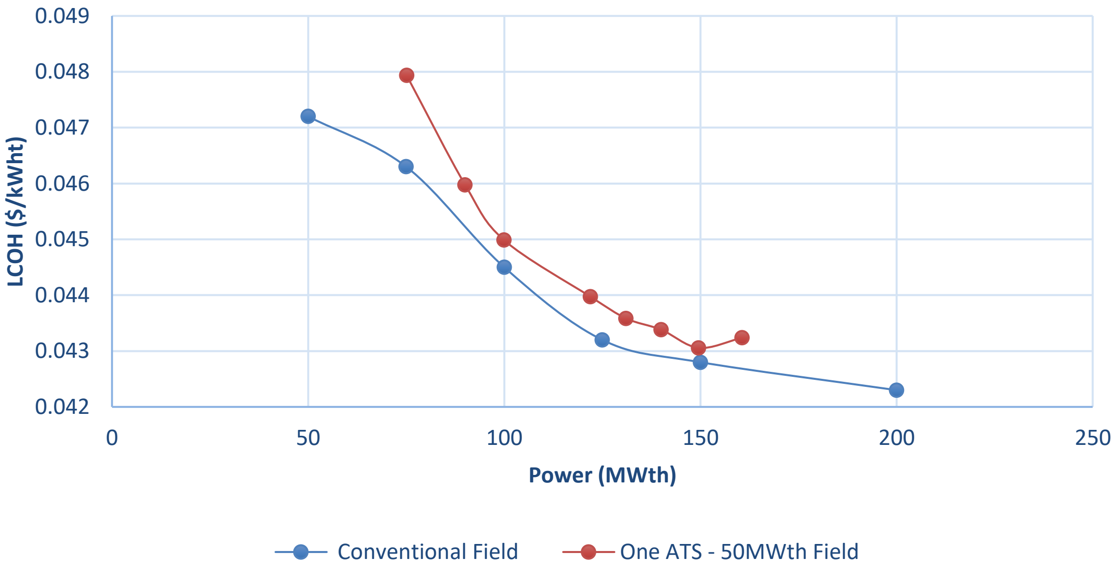

Figure 5-16 Figure showing the LCOH at different thermal powers from a 50MWth ATS and the LCOH of the conventional field at varying thermal powers.

Two Auxiliary Towers

The model developed for the two ATS configuration presents the results with the two subfields combined. Figures 5-15 shows the results from having two subfields, each with its own set number of heliostats in a 50MWth field. See Appendix D2, for additional results from the configuration.

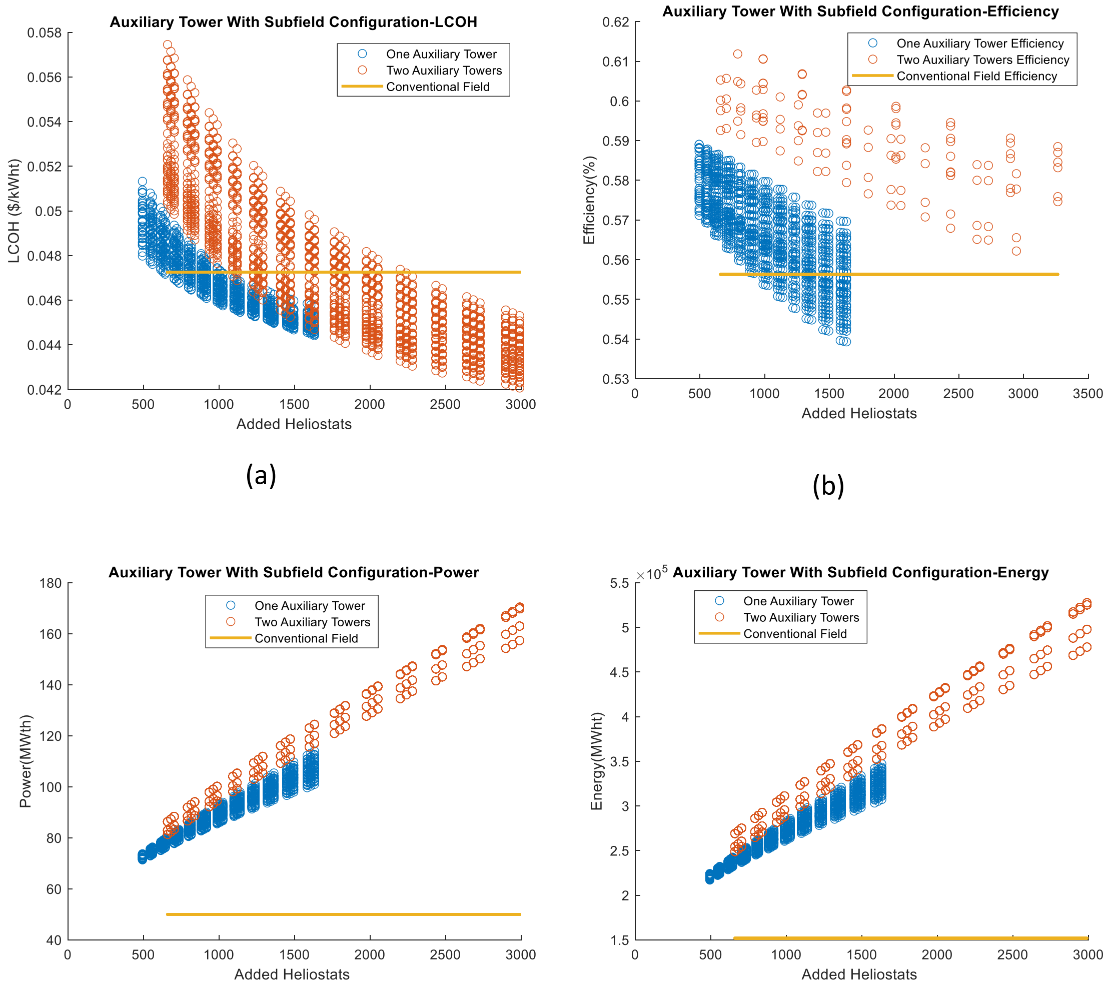

(a)

(b)

(c)

(d)

Figure 5-17 Computational results showing the effect of adding heliostats in subfields with two auxiliary towers for different parameters a) LCOH b) Mean Annual Efficiency c) Field Thermal Power d) Annual Thermal Energy

Figure 5-17 has a very much a similar interpretation with the previously seen One ATS configuration. Fig 5-17a shows a steady decline in the LCOH values when both subfields have heliostats continuously added onto them. When compared to the subfield configuration with one auxiliary tower, lower LCOH values are obtained although only when much higher number of heliostats are added. This is mainly as a result of the additional cost from the presence of two additional subfields which pushes the LCOH further down the curve.

As shown from Figures 5-17b, the mean annual efficiency decreases as more heliostats are added on the subfields. Much higher values of efficiencies are, however, recorded when compared with the One ATS configuration. The setup of the field provides additional targets for the weaker heliostats in the main field, and the added heliostats in the subfield contribute to the high-efficiency values attained. For this same reason, higher values of power and energy are recorded, as shown in Figure 5-17c and Figure 5-17d, respectively.

Similarly, in this configuration, the results from the ATS configuration cannot be compared with the conventional field due to the different values of power attained with each added heliostat. Although several values of LCOH can be obtained for different thermal powers, in Figure 5-18, the optimum LCOH for selected thermal powers drawn from a 50MWth ATS configuration is shown.

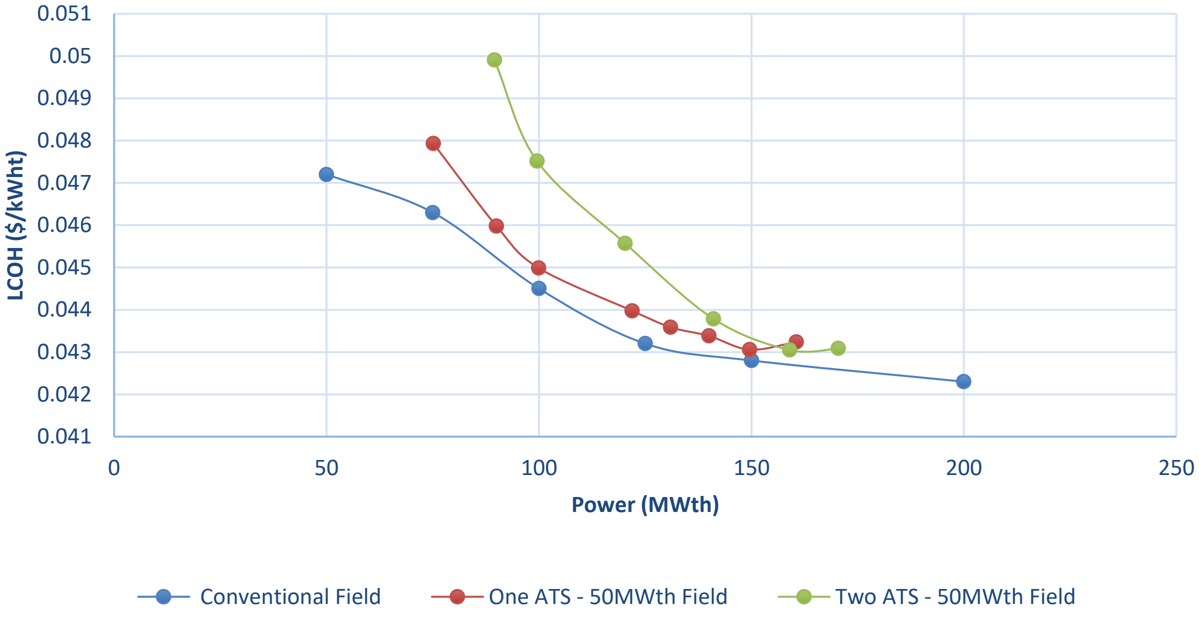

Figure 5-18 Figure showing the LCOH at different thermal powers from a 50MWth one and two ATS configuration and the LCOH of the conventional field at varying thermal powers.

In Figure 5-18, for the Two ATS configuration, a much higher LCOH is observed when compared to the One ATS configuration and Conventional field. This can be attributed to the additional cost from the auxiliary towers, receivers and additional heliostats in the field. As more heliostats are added, a drastic drop in the LCOH is observed due to the increased amount of energy generated. Although the reduced LCOH from the Two ATS performs better than the One ATS at around the 160MWth, it still falls short when compared to the conventional field.

In Figure 5-19, the optimum LCOH of a 90MWth Two ATS field attained from a 50MWth conventional field is shown.

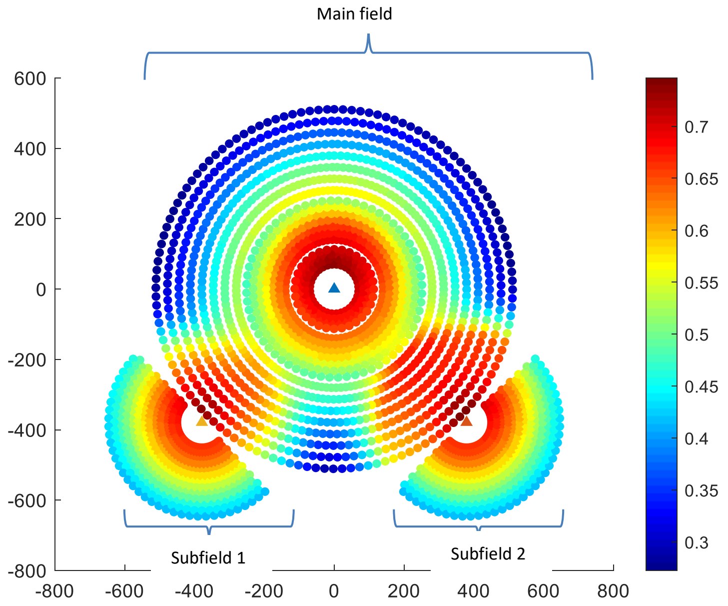

Figure 5-19 Two ATS configuration showing the layout of 90MWth thermal field.

The two auxiliary towers in the field contribute an additional 4.79MWth to the initial 50MWth conventional field. With the addition of 936 heliostats (468 heliostats in each subfield), an additional 17.01MWth and 18.2MWth is being added into the field from subfield 1 and subfield 2 respectively. Subfield 1, with a receiver dimension of 24.51m^2 and tower height at 60m, has mean efficiency value of 56.09%. Subfield 2, on the other hand, has a mean efficiency value of 56.15% (receiver dimension at 41.35m^2 and tower height at 67m). The new mean annual efficiency computes to 58.08%, up from 55.63% and 54.98% obtained in a 50MWth and 90MWth conventional field respectively.

The Auxiliary Tower with Subfields Configuration produces different results of LCOH and efficiency when applied to a conventional field. This is mainly because of the change in the initial thermal field power as a result of the addition of heliostats. In the initial analysis covered, only a 50MWth field is considered. In order to compare the fields from the ATS configuration and conventional field, broader ranges of thermal power are considered. The optimum LCOH for different ranges of thermal power in the One and Two ATS configuration is shown in Figure 5-19a&b, respectively (see Appendix D for a more comprehensive representation of the results showing the field efficiency and total reflective area with this configuration). The addition of heliostats is stopped when the heliostat count is twice the main field's or the LCOH trend begins to rise.

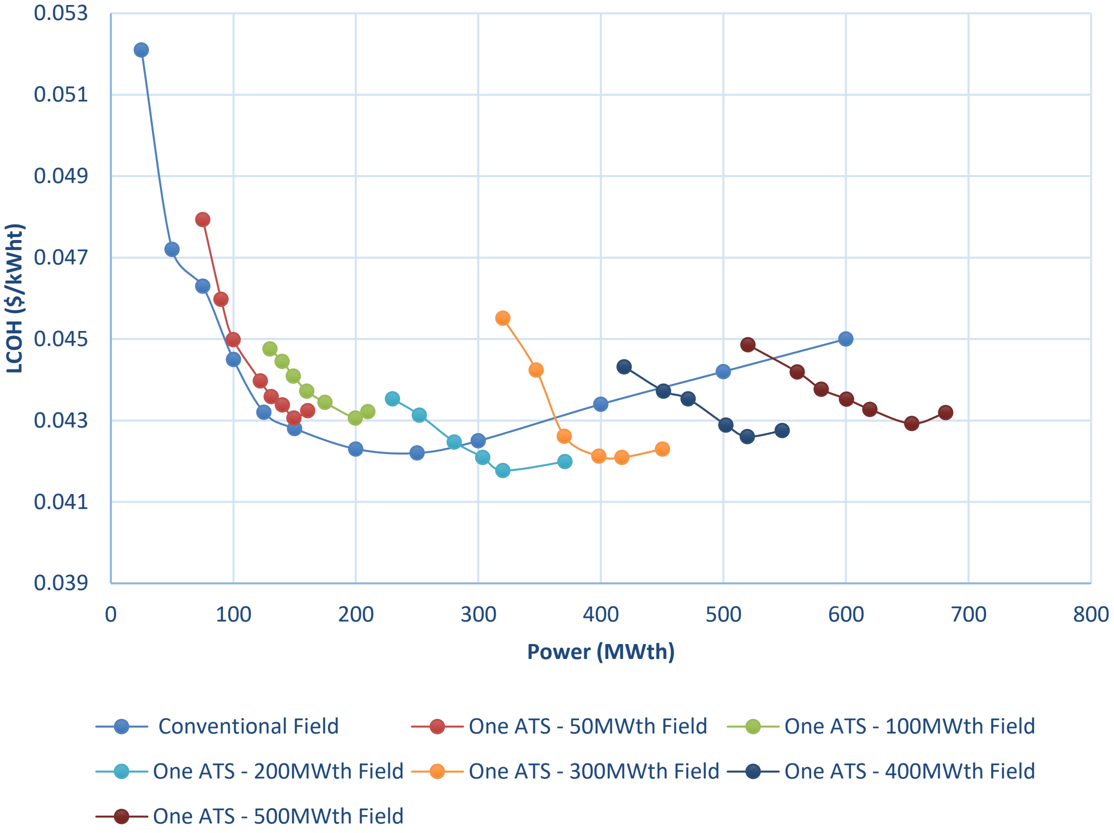

(a)

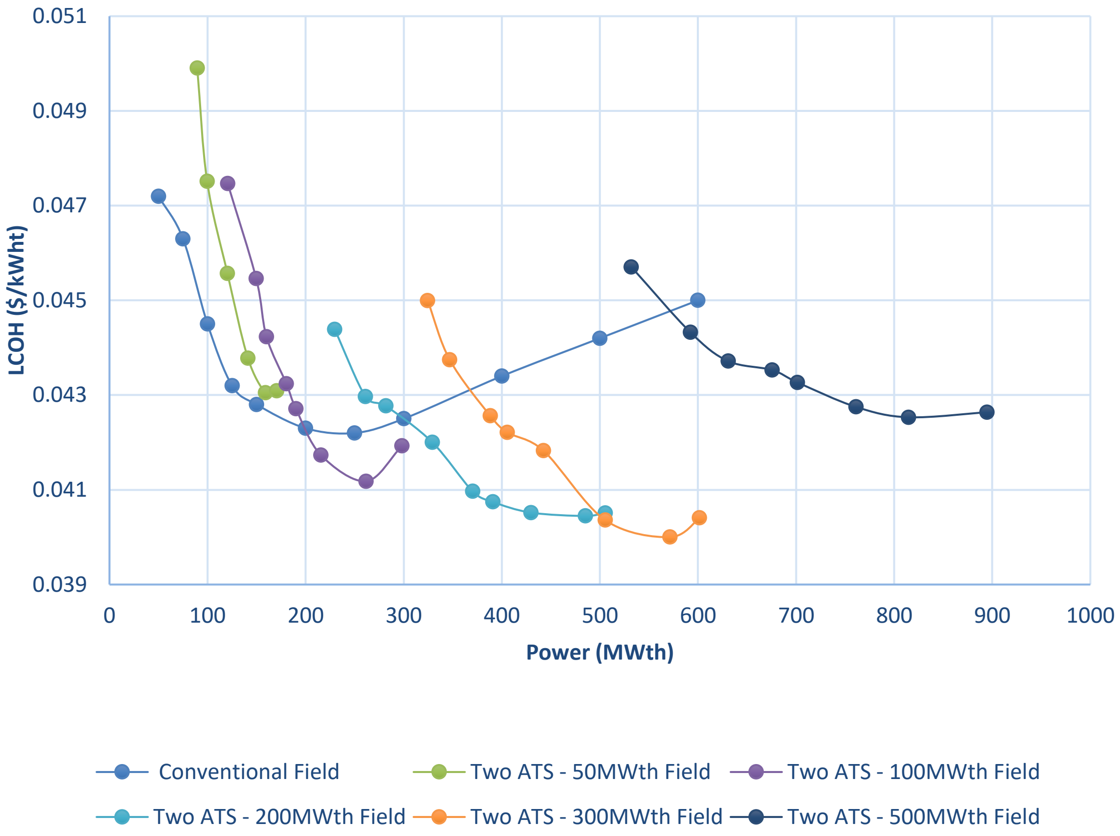

(b)

Figure 5-20 a) LCOH for conventional field and one ATS configuration at different thermal powers b) LCOH for conventional field and two ATS configuration at different thermal powers

In Figure 5-20a, it can be seen that only in larger multi-tower fields, starting from 200MWth does the One ATS begin to provide a lower LCOH when compared to the optimised conventional fields. An improved LCOH value is observed at around the 300MWth power. This improvement continues until 370MWth when the downward trend begins to change. At higher conventional field powers and larger field sizes, the ATS configuration provides lower LCOH for broader ranges of thermal powers. In the One ATS configuration developed from a 300MWth, 400MWth and 500MWth conventional fields, the improvement in the LCOH continues for a range 80MWth, 100MWth and 120MWth respectively. In Figure 5-20b, the Two ATS configuration begins at a higher LCOH when compared to the One ATS configuration from the same thermal field power. The Two ATS configuration does, however, provide lesser LCOH than a 200MWth and 250MWth conventional field even at a 100MWth ATS field. As the Two ATS configuration fields are progressively becoming higher, the range in which the ATS configuration LCOH continuously decreases becomes broader.

5.4 Heliostat Repositioning Configuration

The Heliostat Repositioning Configuration (HRC) is a novel field layout methodology introduced specifically for multi-tower field layouts. In this work, the HRC model is limited to application only in conventional fields. This outlook thus presents a retrofitting or upgrade option of existing conventional fields: much like the ATS configuration seen in Chapter 5.3. This, however, does not limit the application to only retrofitting. The application can just as well be made on new plants. In a similar work by the author [172], the HRC is applied to a developed and optimised multi-tower field (similar to the one presented in Chapter 5.2) at the same site and with the same conditions presented here.

In HRC, the field is initially scanned for the heliostats having the least solar radiation reflection efficiency on the field. The identified heliostats are progressively moved from their initial position to a region near the location of an auxiliary tower (subfield). The height of the auxiliary tower, its distance from the central tower and receiver dimensions are all considered as design variables. The procedure continues until the objective function (optimum LCOH) is attained. The recently moved heliostats are set up to follow the patterned radial staggered configuration field layout. The configuration will equally be assessed with both one and two auxiliary towers.

5.4.1 One Auxiliary Tower

The location of the auxiliary tower in a multi-tower configuration, as earlier discussed in 5.1 is maintained. In Figure 5-21, a depiction of the HPC layout is shown.

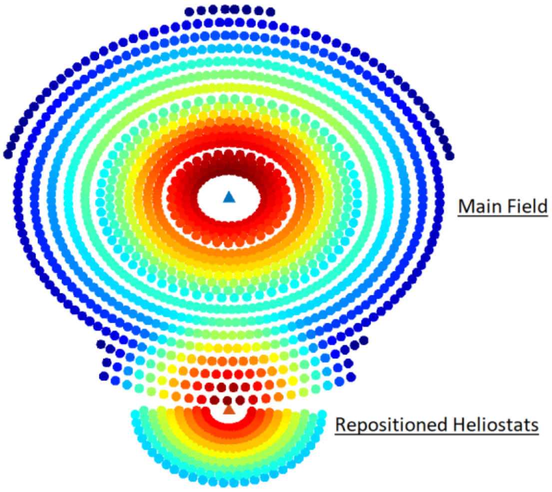

Figure 5-21 Heliostat Repositioning Configuration with one auxiliary tower

The configuration is also initially applied to the base case power of 50MWth. In order to find the optimum LCOH using the HRC model, a range of design variables is equally considered for the multi-tower configuration field (Section 5.2). The design variables are similar to Table 5-5 from the one auxiliary tower ATS configuration. They, however, vary slightly due to the limited number of heliostats that can be repositioned. The design variables and their respective ranges are highlighted in Table 5-7.

Table 5-7 Design variables and range for a 50MWth Heliostat Repositioning Configuration with one auxiliary tower

Design Variables	Variables Range
Number of Heliostats in 1st row (Zone 4)	25 – 68
Heliostat Row Separation Distance Zone 4, ΔR4 (m)	(0.866 – 1.066) * DM
Auxiliary Tower Placement Distance (m)	((0.866 – 1.066) * DM) + Df
Auxiliary Tower Height (m)	25 – 140
Auxiliary Tower Receiver Dimensions(m^2)	6-120

Df is the final distance between the central tower and the furthest heliostat in the same axis direction of the auxiliary tower location.

5.4.2 Two Auxiliary Tower

The sample layout of the HRC, including the positions of the auxiliary tower, is shown in Figure 5-22.

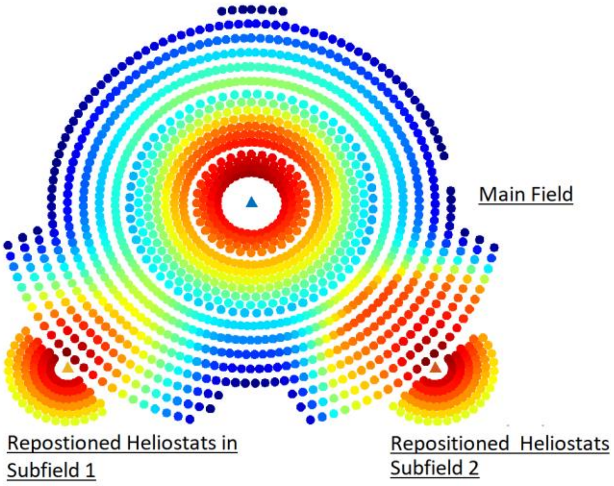

Figure 5-22 Heliostat Repositioning Configuration with two auxiliary towers

As with the one auxiliary tower, the configuration is also initially applied to the base case power of 50MWth. The design variables with their ranges used here are highlighted in Table 5-8. The methodology here follows the same as highlighted initially. However, with two auxiliary towers, in this model, the repositioning of heliostats to the two subfields is made simultaneously.

Table 5-8 Design Variables and range for a 50MWth Heliostat Repositioning Configuration with two auxiliary towers

Design Variables	Variables Range
Number of Heliostats in 1st row (Zone 4 & Zone 5)	25 – 140
Heliostat Row Separation Distance Zone 4 & Zone 5, ΔR4, ΔR5 (m)	(0.866 – 1.066) * DM
1st and 2nd Auxiliary Tower Placement Distance (m)	((0.866 – 1.066) * DM) + Df
1st and 2nd Auxiliary Tower Height (m)	25 – 140
1st and 2nd Auxiliary Tower Receiver Dimensions(m^2)	6-120

Df is the final distance between the central tower and the furthest heliostat in the same axis location of the auxiliary tower location.

5.4.3 Results and Discussion

The results and discussion section here are equally done in two parts. The two different configurations for the HRC configurations are individually discussed.

One Auxiliary Tower

In Figure 5-23, the HPC configuration, from a 50MWth field, results are shown under different parameters; LCOH, efficiency, energy and power. See Appendix E1, for additional results from the configuration.

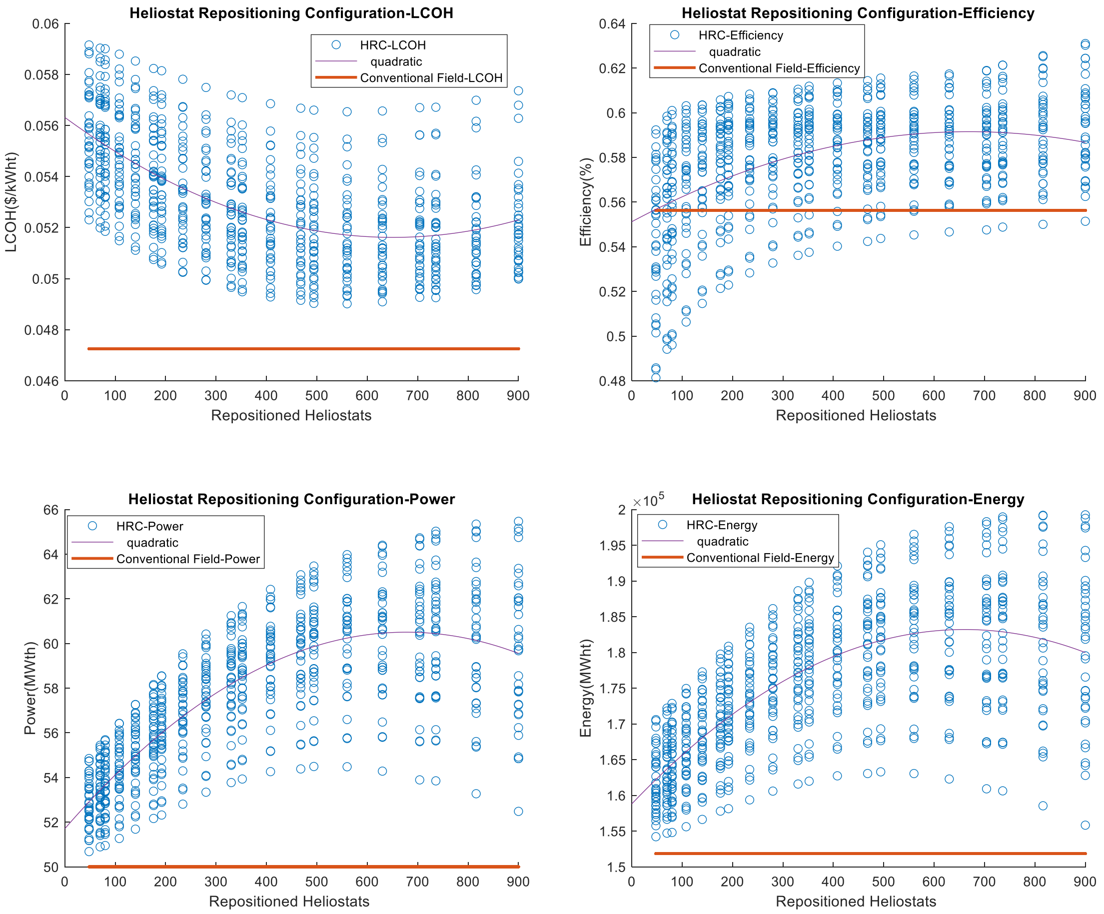

Figure 5-23 Computational results showing the effect of repositioning heliostats with one auxiliary tower under different parameters: a) LCOH b) Mean annual efficiency c) Field thermal power d. Annual thermal energy

From Figure 5-23a, a gradual reduction in the LCOH is seen as heliostats are being repositioned from the main field to be the subfield. Within the specified design variables (Table 5-7), the minimum LCOH at 0.0486 $/kWht is observed when the 560th heliostat is being repositioned. With the HRC, the optical losses in the main field are reduced as heliostats are moved to a higher energy prone region in the subfield. This invariably increases the total energy output from the overall field. The gain recorded in the LCOH, however, is still is not enough to compare with the 50MWth conventional fields.

From Figure 5-23c&d, an evident increase in energy and power is seen. Repositioning of the heliostat under the specified design variables can potentially increase the power up to 65.5MWth, an increase of 15.5MWth from the initial field's power of 50MWth. This value is achievable when 900 heliostats are repositioned in the field. At this point, however, the receiver area and tower height have large values ($50.24m^2$ and 120m respectively) hence contributing to the high LCOH at 0.0574 $/MWht at that point.

In Figure 5-23b, the effect of repositioning on the general field efficiency is shown. In moving the weaker heliostats from the main field to the subfield, a general improvement in the efficiency is observed. This is a result of the field efficiency improving from the main field; as the weaker heliostats are being taken out, thereby improving the total efficiency, and the subfield with the repositioned heliostats now having a higher solar radiation efficiency. With more heliostats added to the subfield, the optical efficiency losses increase as a result of the heliostat's growing distance from the auxiliary tower. The rising heliostats count in the subfield consequently causes the total field efficiency increment to slow considerably and eventually fall. In Figure 5-24, the effect of repositioning heliostats from the 3rd Zone of the main field (predominantly the weakest Zone) and the subfield is shown.

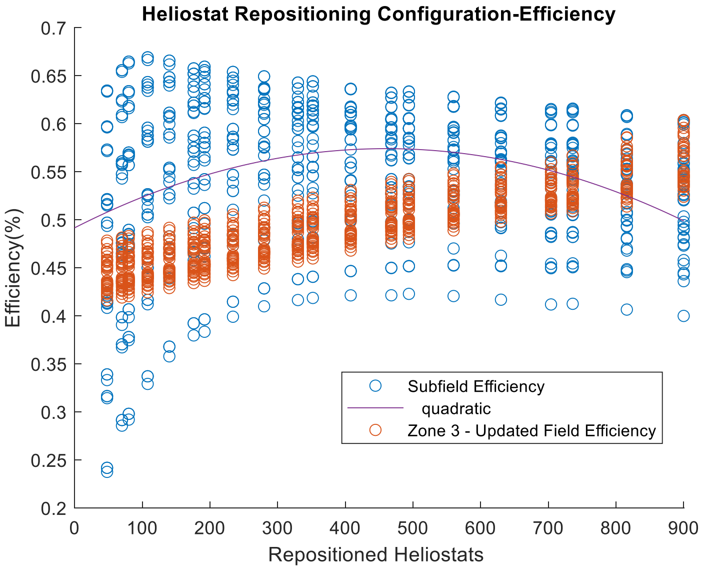

Figure 5-24 HRC effect on the efficiency of zone 3 in the main field and the Subfield

In Figure 5-24, the rising efficiency trend in the 3rd Zone from the configuration can be seen. When the weaker heliostats are being progressively removed, the Zone is left with the most efficient heliostats hence its upward trend. On the other hand, the repositioned heliostats begin to lose efficiency when about 494 heliostats are added signifying the limit of the subfield region and a pointer as to when the repositioning process can or should be halted. In Figure E1-e from the appendices, the effect of the thermal energy output in Zone 3 and the subfield is shown.

In Table 5-7, parameters of the computed optimum LCOH for a 50MWth field in the HRC are outlined and compared with the conventional 50MWth field.

Two Auxiliary Tower

In Figure 5-25, the HPC configuration for two auxiliary towers in a 50MWth field results are shown under different parameters; LCOH, efficiency, energy and power. The figure also compares the results of two auxiliary tower HRC with results from the conventional field and one auxiliary tower HRC. See Appendix E2, for additional results from the two auxiliary tower configuration.

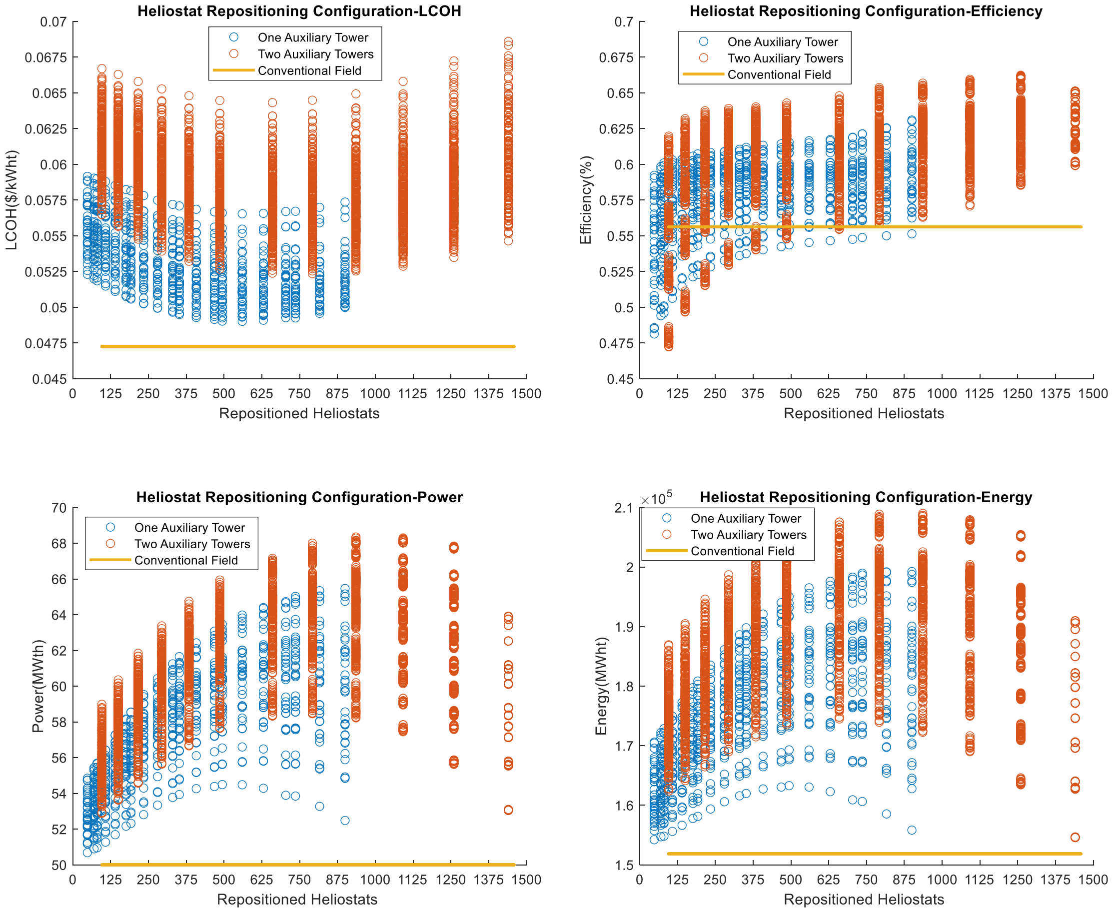

Figure 5-25 Computational results showing the effect of repositioning heliostats with tow auxiliary towers under different parameters: a. LCOH b. Mean annual efficiency c. Field thermal Power d. Annual thermal energy

In Figure 5-25a, a similar trend to Figure 5-23a is observed. In comparison, the additional components in the two auxiliary towers configuration increase the LCOH values despite the rise in energy recorded (Figure 5-25d). However, the presence of the two auxiliary towers extends the number of heliostats that can be repositioned in the lower LCOH boundary. The minimum LCOH recorded here is at 0.0524$/kWht, obtained when 792 heliostats are repositioned. In Figure 5-25b, a similar trend as the one auxiliary tower is observed, an upward trend in the efficiency value as more heliostats are repositioned. The presence of an additional tower in the configuration enables a more significant number of weaker heliostats to be repositioned to potentially higher energy prone regions (subfields). In Figure 5-25c, the resulting increase in thermal power; due to the increase in efficiency, is also observed. Within the settings of the design variables, the thermal power can reach up to 68.35MWth, 2.85MWth higher than the recorded value at one auxiliary tower and 18.35MWth higher than the conventional field.

It should be recalled that the HRC is developed from an optimised conventional field. HRC represents an innovative type of the multi-tower configuration where the conventional field can thus be improved upon. Table 5-9 compares the optimum results computed from a 50MWth field using the HRC and that from a conventional field.

Table 5-9 Comparison of conventional field, and multi-tower fields using Heliostat Repositioning Configuration.

Parameter	Conventional Field	Heliostat Repositioning Method- One Auxiliary Tower	Heliostat Repositioning Method- Two Auxiliary Tower
Heliostat Area (m^2)	95.17	95.17	95.17
Central Tower Height (m)	91.48	91.48	91.48
Central Receiver Area (m^2)	55.84	55.84	55.84
1st Auxiliary Tower Height (m)	-	60	60
1st Auxiliary Receiver Area (m^2)	-	18.85	28.28
2nd Auxiliary Tower Height (m)	-	-	72
2nd Auxiliary Receiver Area (m^2)	-	-	12.57
LCOH` (\$/kWht)	0.0473	0.0486	0.0524
Field Power (MWth)	50.00	60.86	65.75
Efficiency Design Point (%)	60.59	64.48	67.79
Mean Annual Efficiency (%)	55.63	58.87	62.28
Mean Annual Attenuation Efficiency (%)	96.52	92.93	98.21
Mean Annual Blocking Efficiency (%)	97.42	99.92	99.98

Mean Annual Cosine Efficiency (%)	77.84	85.87	86.20
Mean Annual Spillage Efficiency (%)	87.82	97.39	97.67
Reflective Surface Area (m^2)	152,270	152,270	152,270
Number of Heliostats	1,600	1,600	1,600
Heliostats Repositioned	-	560	792
Annual Energy (MWht)	151,849	183,323	199,563
1st Auxiliary Receiver Thermal Power (MWth)	-	26.09	21.84
2nd Auxiliary Receiver Thermal Power (MWth)	-	-	19.89
System Cost ($)	40,652,834	51,450,834	63,558,090

In all the HRC reviewed, the dimensions of parameters in the main field (heliostat area, tower height and receiver area) of the conventional optimised setup remain the same. Similarly, the number of heliostats and the total reflective surface area remains unchanged. In the one auxiliary tower configuration, the optimum LCOH is achieved at 0.0486$/kWht when 560 heliostats have been repositioned from the main field to the subfield positioned near the auxiliary tower location. The difference in LCOH when compared to the 50MWth Conventional field is 0.0013$/kWht. All the repositioned heliostats are from the 3rd Zone of the main field; 560 heliostats repositioned from the initial 1024 heliostats in Zone 3. Despite the introduction of an additional tower, the improvement in the LCOH when compared to the conventional field is notable. The consequential repositioning of weaker heliostats to the subfield regions where the distance between the heliostats and the auxiliary tower is closer, thereby reducing some of the optical losses associated with increasing distance from a tower. This can be vividly seen in the overall improvement in the field’s optical efficiency; from 55.63% to 58.87%. The subfield amounts to the biggest improvement in the efficiency to 57.88%, 15.40% higher than Zone 3’s initial efficiency at 42.48%. The improvement in the field efficiency invariably increases the field thermal power and energy output. The overall thermal power now computes to 60.86MWth: 26.09MWth from the auxiliary tower’s receiver (22.30MWth from the subfield’s heliostats and 3.79MWth from heliostats in the 3rd Zone) and 23.91 MWth from the central receiver. In Figure 5-26, the layout of the optimum computed HRC field with the one auxiliary tower is highlighted.

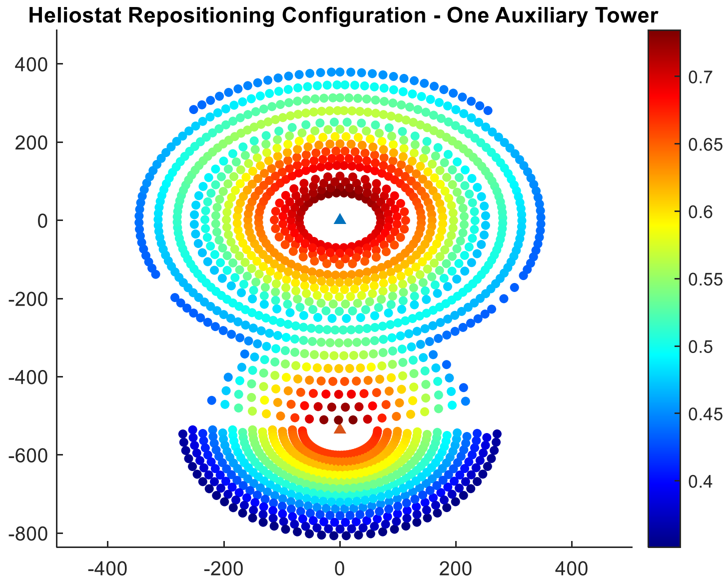

Figure 5-26 One auxiliary tower Heliostat Repositioning Configuration field layout from a 50MWth conventional field.

In the two auxiliary towers HRC, the presence of two additional towers provides the opportunity to reposition an even greater number of weaker heliostats which aids in the high mean annual efficiency realisation of the overall plant. The subfields have an efficiency of 62.58% and 62.51% for subfield 1 and 2 respectively contributing to the overall mean efficiency of 62.28%. This thus produces a corresponding increase in the power and energy of the field. The field power with the optimum LCOH computes to 65.75MWth, 4.89MWth and 15.75MWth higher than the one auxiliary HRC and conventional field respectively. The first auxiliary tower has a total contribution of 21.84MWth to the new design point power: 16.95MWth from the 1st subfield and 4.89MWth from the 3rd Zone in the main field. Additionally, the second auxiliary tower thermal rating sums up to 19.89MWth: 16.50MWth from the 2nd subfield and 3.39MWth from the 3rd Zone in the main field. A total of 792 heliostats are repositioned, 396 repositioned to each of the subfields using the HRC in order to attain the optimum LCOH at 0.0524 $/kWht. In Figure 5-27, the HRC field layout with two auxiliary towers from a 50MWth Conventional field is shown.

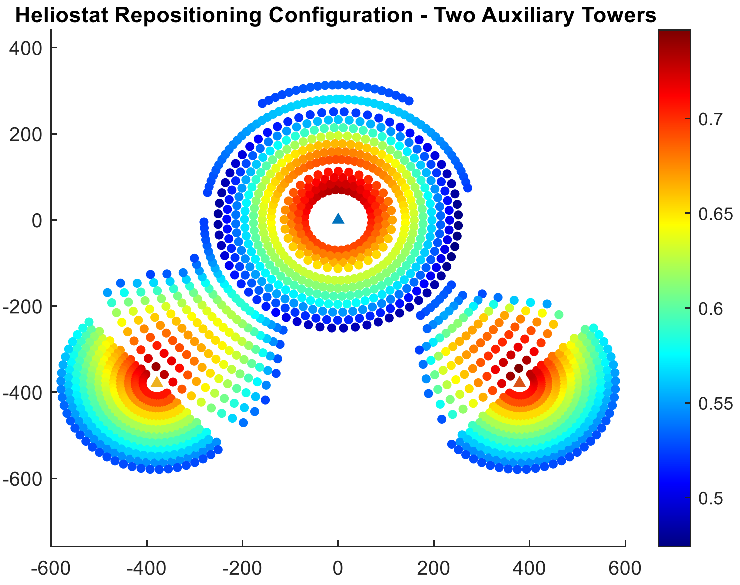

Figure 5-27 Two auxiliary towers Heliostat Repositioning Configuration field layout from a 50MWth Conventional field.

The application of HRC methodology in a conventional field has a drastic impact on the overall performance on the field. This is evident, as seen from the LCOH reduction and field efficiency improvement recorded on a 50MWth conventional field. A comprehensive comparison of the newly configured HRC field and conventional field cannot, however, be made due to primarily the difference in thermal powers. In Figure 5-28, the optimum LCOH obtained when using HRC methodology is compared with conventional fields at larger field thermal powers; the figure establishes the trend in LCOH from both methodologies. See Appendix E for a more detailed representation of the results using this configuration.

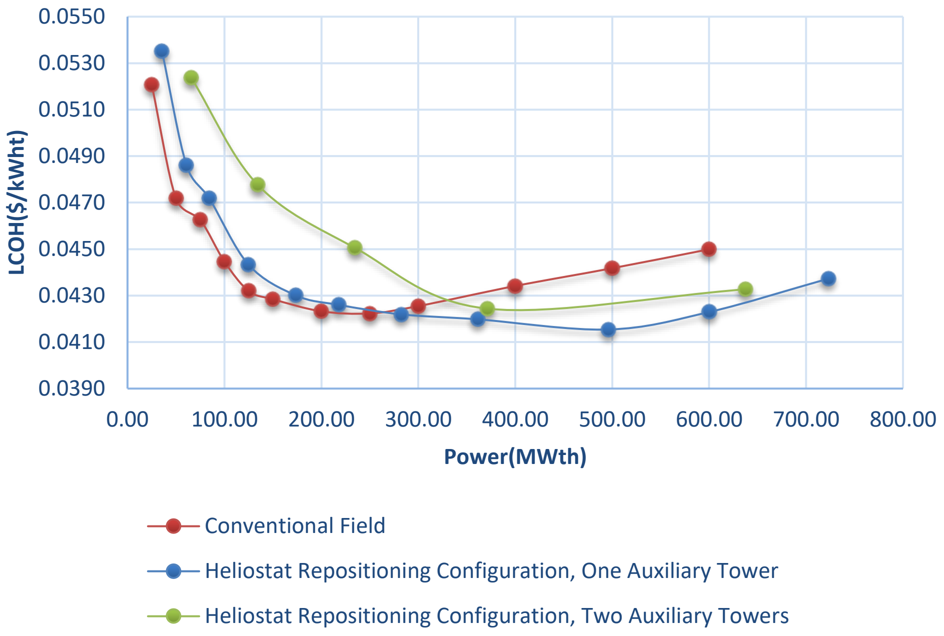

Figure 5-28 Optimum Levelized Cost of Heat from the conventional field and Heliostat Repositioning Configuration

On larger thermal field powers and field sizes, as seen from Figure 5-28, the HRC configuration produces a field with lower LCOH. For the one auxiliary tower HRC, at around 300MWth, the LCOH is at 0.0421$/kWht. Whereas a conventional field with the same field thermal power has a higher LCOH at 0.0425$/kWht. In larger fields, there is a higher number of heliostats with poor radiation reflection efficiency. When such identified heliostats are repositioned to the subfields, their reflective radiation efficiency improves. This is mainly because the heliostats now have a closer target with the auxiliary tower(s) hence reducing optical efficiency losses such as spillage, cosine and attenuation. For example, at a 283MWth thermal field (with one auxiliary tower HRC), a high number of heliostats totalling 2,175 have to be repositioned in order to attain the optimum LCOH. In Table 5-10, the results of the different thermal powers using HRC, optimum LCOH and reflective surface area of heliostats repositioned are highlighted.

Table 5-10 Optimum Levelized Cost of Heat, gained thermal power and reflective surface area of repositioned heliostats from the Heliostat Repositioning Configuration in comparison to the initial conventional field.

Conventional Field			***HRC, One Auxiliary Tower***			***HRC, Two Auxiliary Towers***		
Power (MWth)	**Reflective Surface Area (m²)**	**LCOH ($/kWht)**	**Reflective Surface Area of Repositioned Heliostats (m²)**	**Optimum LCOH ($/kWht)**	**Gained Thermal Power (MWth)**	**Reflective Surface Area of Repositioned Heliostats (m²)**	**Optimum LCOH ($/kWht)**	**Gained Thermal Power (MWth)**
25.00	88,191.35	0.0521	52,557.76	0.0535	35.57	-	-	-
50.00	152,272.00	0.0472	53,295.20	0.0486	60.86	75374.64	0.0524	65.75
75.00	233,843.28	0.0463	59,986.80	0.0472	84.45	-	-	-
100.00	326,501.70	0.0445	133,546.56	0.0443	124.86	167915.16	0.0478	134.47
150.00	463,377.20	0.0428	121,190.96	0.0430	173.82	-	-	
200.00	566,928.29	0.0423	104,758.49	0.0426	218.11	186237.31	0.0451	234.72
250.00	787,060.56	0.0422	177,284.25	0.0422	282.55	-	-	-
300.00	1,013,460.80	0.0425	388,588.20	0.0420	361.39	454918.64	0.0424	371.42
400.00	1,473,615.36	0.0434	498,880.20	0.0415	496.07	-	-	-
500.00	1,775,854.08	0.0442	628,948.32	0.0423	600.18	760325.28	0.0433	637.77
600.00	2,342,322.84	0.0450	813,933.12	0.0437	723.17	-	-	-

The least LCOH value of 0.0415$/kWht with one HRC is obtained at a field thermal power of 496MWth. This value is attained from reconfiguring a 400MWth conventional field. By applying HRC, the LCOH improves by 0.0027$/kWht when compared to a conventional field with a similar thermal power rating at 500MWth.

With two auxiliary towers HRC, the reduction in LCOH is slow as a result of the cost implications associated with two additional towers. This, however, changes at around 370MWth when it performs better than a conventional field with a similar field thermal power rating. In this configuration, much like the previous ones, the limit of the conventional field thermal power considered is at 600MWth.

Chapter Summary

Here, three different aspects of multi-towering are developed; multi-tower field optimisation, Auxiliary Tower with Added Subfield (ATS) and Heliostat Repositioning Configuration (HRC). A suitable location for citing the auxiliary tower was initially determined. This was done by determining the region on the field with the lowest efficiency and reflected energy. The result showed that the lesser performing heliostats are in the bottom half (Southern part) of the field. The auxiliary towers were hence placed in that region. The heliostats are not restricted by which tower they are allowed to focus on. Each heliostat decides on the receiver to target based on the strength of the reflected radiation.

In the first multi-tower configuration, auxiliary towers were added, and the entire field optimised for Levelized Cost of Energy (LCOH). The design variables during the optimisation in the field included the auxiliary tower height and its receiver dimensions. The presence of the auxiliary tower provided an overall increase in the system efficiency of the field by reducing some of the losses entailed in a conventional single-tower setup, by providing the less efficient heliostats in the region a more favorable tower to target. The gain recorded from the energy in the multi-tower setup has to outweigh the incurred cost from the auxiliary tower. In smaller fields and lower thermal field sizes, the LCOH becomes higher when compared to the conventional field of the same thermal power. At 50MWth, the optimum LCOH is 0.0102$/kWht higher in the multi-tower field when compared to a conventional field size of the same thermal rating. This, however, changes in larger fields due to the higher number of weaker heliostats that are present, giving the need and use of an additional tower all the more critical. The heliostats at the weaker region in the field of a multi-tower field are provided with an additional tower to reflect the sun's radiation, thereby considerably cutting down some of the associated optical losses. The optimum transition size from a conventional to a multi-tower field using this configuration was hence found to be at the 380MWth field thermal rating. The optimisation of the multi-tower field with two auxiliary towers in the field was equally performed. The higher gain in energy and efficiency in the field here is overcome by the additional costs from the two extra towers, thereby pushing the LCOH even higher when compared to a conventional field. This occurs even at higher thermal powers and larger field sizes.

In ATS, heliostats are added near the position of the auxiliary tower, thereby creating another region in the field (subfield). The auxiliary towers in ATS configuration act as targets for both the weak heliostats in the main field and the newly added heliostats in the subfield. ATS hence depicts a field layout that capitalizes fully on multi-tower configuration. As heliostats are added in the subfield, a gradual improvement in the LCOH is recorded as a result of the gain in overall energy and thermal power output from the field. This, however, quickly changes when the added heliostats in the subfield begins to lose efficiency as a result of their increasing distance from the auxiliary tower. The optimum LCOH values from the configuration, for different ranges of thermal powers, obtained in varying field sizes are compared against optimised conventional fields of similar thermal ratings. The results show that only in larger fields, starting from 200MWth does the ATS configuration with one auxiliary tower begins to provide a lower LCOH when compared to optimised conventional thermal fields. At even higher conventional field powers and larger field sizes, the ATS configuration provides lower LCOH values for broader ranges of thermal powers. Similarly, for the ATS configuration with two auxiliary towers, lesser LCOH are attained at even lower ATS thermal fields.

The third multi-tower configuration developed is the Heliostat Repositioning Configuration (HRC). HRC involves progressively repositioning underperforming heliostats from the entire field to a region near the location of an auxiliary tower (subfield). The total reflective surface area in the field here remains unchanged. The configuration equally represents a different setup for multi-towering. The results from this configuration showed an increase in the overall efficiency, energy and power of the field as the relocated heliostats have a high solar energy conversion efficiency. When heliostats performing better in the main field are repositioned, a corresponding reduction in the energy, power and efficiency is recorded. This can be seen to equally translate in the increased LCOH value in the field. Just like in the previous configuration, the effect of this model is most seen on larger thermal field sizes due to the presence of higher number of heliostats with poor radiation reflection efficiency. The identified weaker heliostats are thus repositioned to the subfields, where their reflecting radiation efficiency improves. For the one auxiliary tower HRC, the optimum LCOH for a 300MWth field performs better than a conventional field with the same field thermal power rating. This is mainly because the heliostats in the subfield are provided with a closer target in the auxiliary tower hence reducing optical efficiency losses. With two auxiliary towers in the HRC, a similar result is equally obtained. However, HRC here provides a lower LCOH, when compared to the conventional case, only from a higher HRC thermal field of 370MWth. This is as a result of the cost implications associated with two additional towers.

6 CASE STUDY: GEMASOLAR FIELD- MODEL APPLICATION

In this Chapter, the Gemasolar field is reconfigured. The configurations: Auxiliary Tower with Subfield configuration (ATS) and Heliostat Repositioning Configuration (HRC) outlined in Chapter 5 are applied to the Gemasolar field. The Chapter initially begins by developing a model of the Gemasolar plant.

6.1 Gemasolar Plant Model

Previously in Chapter 2, a brief description of the Gemasolar Power Plant has been made. The Gemasolar plant is the first commercial solar power tower plant supplying grid electricity to over 25,000 homes featuring a molten salt receiver with thermal storage capabilities [40]. The plant has a nominal output of 19.9MWe with up to 15 hours thermal energy storage, thus enabling continuous plant operation throughout the day capable of generating 110GWh/year. Two thousand six hundred fifty heliostats over 195 hectares track the sun's location. Most information on the plant stated here is from the Gemasolar fact sheet on the Torresol company website [67].

The Gemasolar plant operates on two main systems: storage system and generation system (Figure 6-1). The subject of interest in the work is the storage system which entails of the solar field [40]. The required heat is pumped from the hot tank into the Power Conversion Unit (PCU).

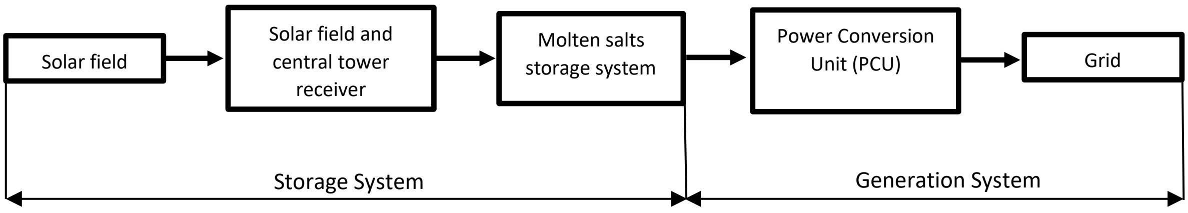

Figure 6-1 Storage subsystem, Gemasolar field

Some critical information for the Gemasolar Plant remains confidential company data and hence the varying values in some of the field parameters, as highlighted in Table 2-3. In 2013, the National Renewable Energy Laboratory (NREL) performed a case study on the Gemasolar plant using SAM [42]. The parameters in the SAM model (Table 6-1) were developed using estimates to represent the real-life plant as close as possible.

The parameters are hence applied in the model developed using MATLAB (Chapter 4) to replicate the Gemasolar field. In Table 6-1, the field parameters and performance from the NREL

SAM's model and the model developed here (representing the field design parameters) are highlighted. Results from the SAM model are extracted from [3].

Table 6-1 Plant Parameters from the developed model and SAM's model

Parameter	SAM Model	MATLAB Model
Heliostat Area (m^2)	115.25	115.25
Central Tower Height (m)	140	140
Central Receiver Area (m^2)	384.24	384.24
Annual Direct Solar Energy ($kWh/m^2/year$)	2,089.69	2,534.43
Reflective Surface Area (m^2)	305,401.90	305,401.90
Number of Heliostats	2,650	2,650
Annual Direct Solar Energy (MWht)	638,195.30	774,020.32
Mean Field Efficiency	54.46	51.22
Levelized Cost of Heat, (LCOH) ($/kWht)	0.0484	0.0449
Receiver Thermal Power (MWth)	120.72	120.68
Annual Incident Receiver Energy (MWht)	347,561.16	396,453.21
System Cost ($)	97,025,168.28	97,025,168.28

Table 6-1 shows some resemblance with the Gemasolar field characteristics given in NREL's SAM case study. One of the fundamental differences is in the DNI for the location. As earlier highlighted in Chapter 4, the MATLAB model developed utilizes a provided measured data at the site for a limited period (the Year 2013-2014). The DNI is directly responsible for the higher value of annual direct incident solar energy on the field and, subsequently, the annual incident receiver energy from the model. The different methodologies used in calculating the optical losses models produce a mean-field efficiency of 51.22% in the MATLAB model and 54.46% in the SAM model. Also, the system cost remains the same as the SAM cost model was adopted for the developed MATLAB model. Although some variances are recorded from the two models, the model developed is used here and applied as the base case.

Figure 6-2 shows the layout of the field, demonstrating the individual mean annual efficiency in the model field. The shading matrix from Figure 6-2 shows more efficient heliostats in the Northern region of the field. This is consistent with sites at latitude 23.5^0 or more where a single maxima peak of solar altitude is witnessed during summer solstices (Figure 3-12) thereby favouring energy utilization from south-facing collectors. In Appendix F1, the mean annual optical losses in the Gemasolar field are also shown.

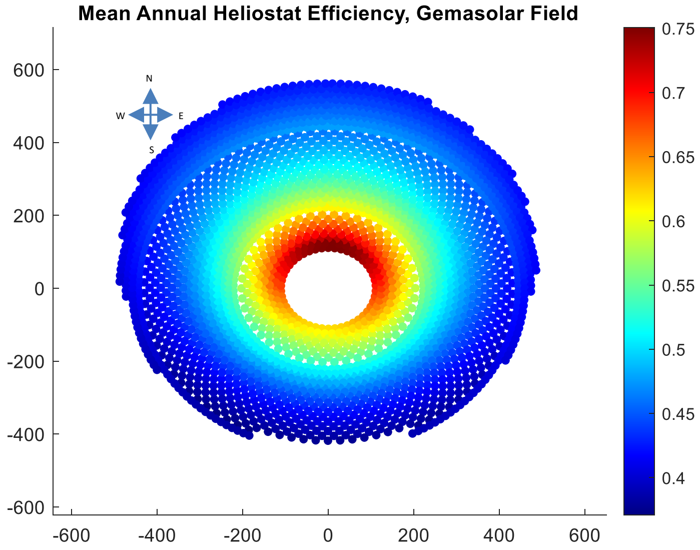

Figure 6-2 Mean annual field efficiency of the developed Gemasolar field

In Figure 6-3, a presentation of the monthly energy output and efficiency of the developed field is shown. The high energy output and efficiency around the summer solstices are equally consistent with the site's latitudinal angle.

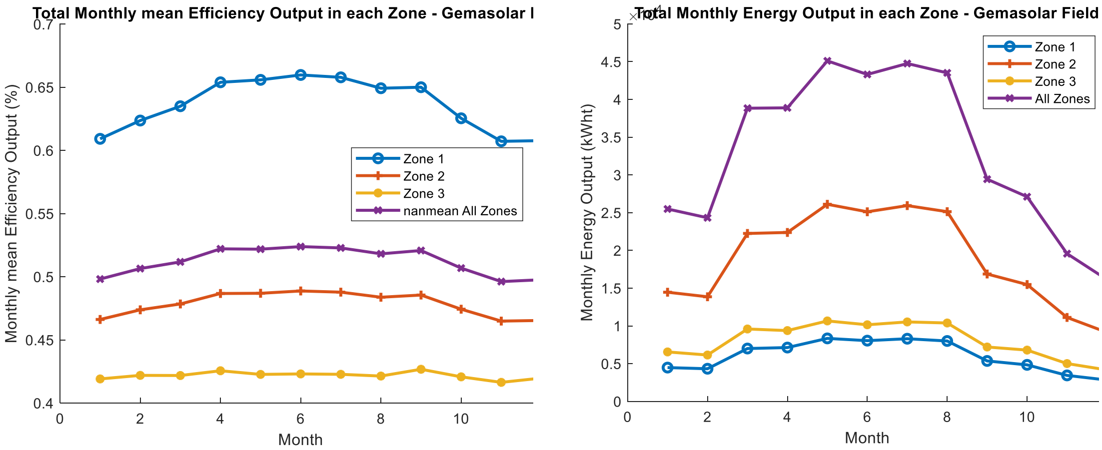

Figure 6-3 Total monthly mean efficiency output in all zones in the Gemasolar field. b) Total monthly mean energy output in all zones in the Gemasolar field

Table 6-2 shows the contribution of the optical loss parameters to the overall field efficiency in the different Zones of the field.

Table 6-2 Mean annual optical efficiency values in all zones of the Gemasolar field

Parameter	Mean Annual Efficiency Zone 1 (%)	Mean Annual Efficiency Zone 2 (%)	Mean Annual Efficiency Zone 3 (%)	Mean Annual Efficiency All Zones (%)
Spillage Efficiency	100.00	99.89	99.16	99.69
Cosine Efficiency	80.93	75.59	75.12	77.21
Attenuation Efficiency	96.92	95.39	94.02	95.44
Blocking Efficiency	96.60	81.13	74.50	84.08

From Table 6-2, a continuous reduction in all the optical loss models is seen with increasing distance from the tower with the cosine loss having the highest penalty. The marginal difference in cosine between Zone 3 and Zone 2 can be attributed to the layout of the Gemasolar field which ensures fewer heliostats in the lesser performing lower half of the field hence, a reduced loss from that region.

In upgrading an existing field, using either the ATS or HRC configuration, three different upgrade options have been identified in this context:

l. The subfield discharges at the main field's storage tank. Here, the Thermal Energy Storage (TES) system is shared (See Figure 6-4). Although, the full capacity of the storage tank is not known, In the existing context, the large amounts of thermal energy from the subfield cannot be stored in the main field's storage tank as it is assumed the tank is designed to capacity.

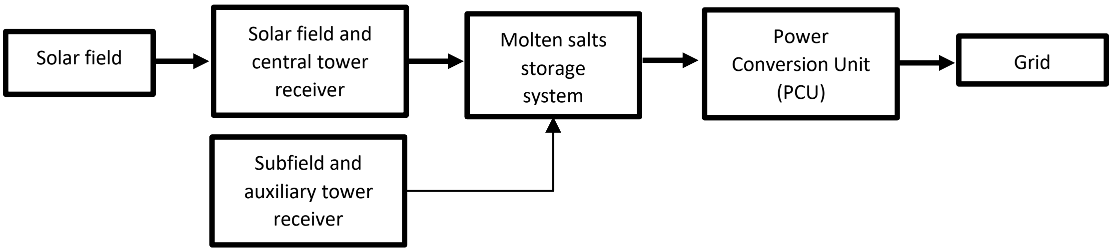

Figure 6-4 Upgrade option with subfield sharing storage

m. In this setup, a secondary TES is installed. The storage systems can run concurrently with the initial TES or serve as an extension of storage duration in the system. An alternative approach in this configuration would be developing a bigger TES system, thereby eliminating the need for a secondary TES (see Figure 5-5). The configuration here may well find application in a plant with a limited duration of storage. However, the application of the models developed in this setup would entail extending the duration of operation during hours without solar radiation on the Gemasolar plant. The Gemasolar plant currently operates on 15 hours of storage without radiation thus enabling 24 hours of plant operation at nominal power [40]. Additional storage time for the Gemasolar plant is thus not required unless in a situation where the autonomous period of operation is need of extending.

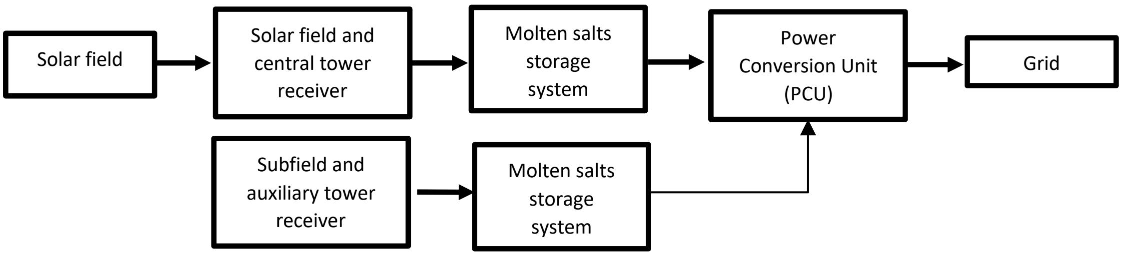

Figure 6-5 Upgrade option with subfield sharing the PCU

n. Here, both the main and subfield share limited resources. The subfield has its storage system which caters for the PCU dedicated to the nominal power computed from the subfield.

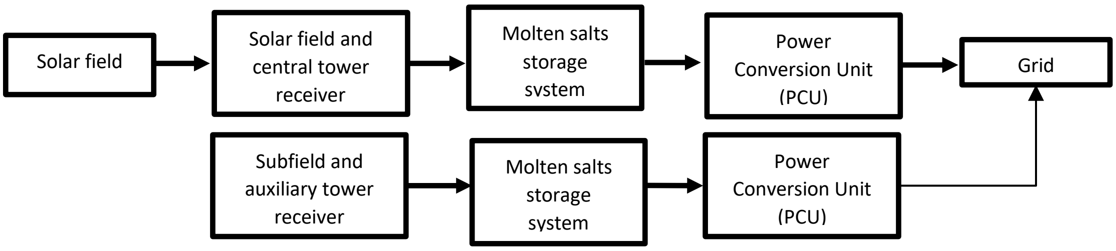

Figure 6-6 Upgrade option where little or no sharing exists.

6.1.1 Auxiliary Tower Positioning

The methodology for siting an auxiliary tower: based on the region having the weakest reflected energy is maintained. The reconfiguration of the Gemasolar plant is limited to only one auxiliary tower. As in Chapter 5.1, the field is divided into four quadrants. The results are shown in Table 6-3.

Table 6-3 Mean annual efficiencies at the four identified quadrants in the Gemasolar field

Averaged Annual Efficiency in the 1st Quadrant (%)	Averaged Annual Efficiency in the 2nd Quadrant (%)	Averaged Annual Efficiency in the 3rd Quadrant (%)	Averaged Annual Efficiency in the 4th Quadrant (%)
50.88	52.25	49.76	48.75

The weakest region is found in the 4th quadrant with a mean-field efficiency of 48.75%. The auxiliary tower is sighted at the central position of the weakest quadrant. If the field were to be divided into two halves, the lower half of the field (Southern half) has an efficiency of 53.56% while the upper half efficiency is 49.51%.

6.2 Gemasolar Field: Auxiliary Tower with Subfield Configuration (ATS)

The ATS configuration, developed in Chapter 5, is applied to the Gemasolar field. The application of the model represents a retrofitting option for the already existing plant. Here, heliostats of the same area are added at varying design parameters to the subfield.

The same design variables as in Table 5-5, with a slightly different range as is used here. The higher thermal power from the field necessitates the need to consider a slightly higher range of the design variables. The design variables and their range are thus highlighted in Table 6-4. The objective function here remains the same: improving the LCOH of the field.

Table 6-4 Design variables with variables range for an Auxiliary Tower with Subfield configuration of the Gemasolar field.

Design Variables	Variables Range
Number of Heliostats in 1st row (Zone 4)	20 – 100
Heliostat Row Separation Distance Zone 4, ΔR4 (m)	(0.866 – 1.066) * DM
Auxiliary Tower Placement Distance (m)	((0.866 – 1.066) * DM) + Df
Auxiliary Tower Height (m)	25 – 140
Auxiliary Tower Receiver Dimensions(m²)	6-180

6.2.1 Results and Discussion

The results from applying the ATS configuration on the field is shown in Figure 6-7.

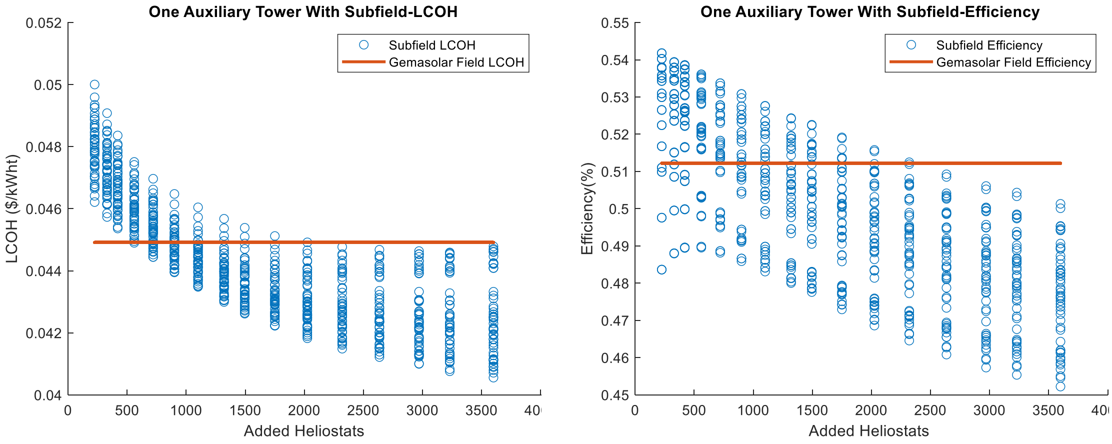

(a) (b)

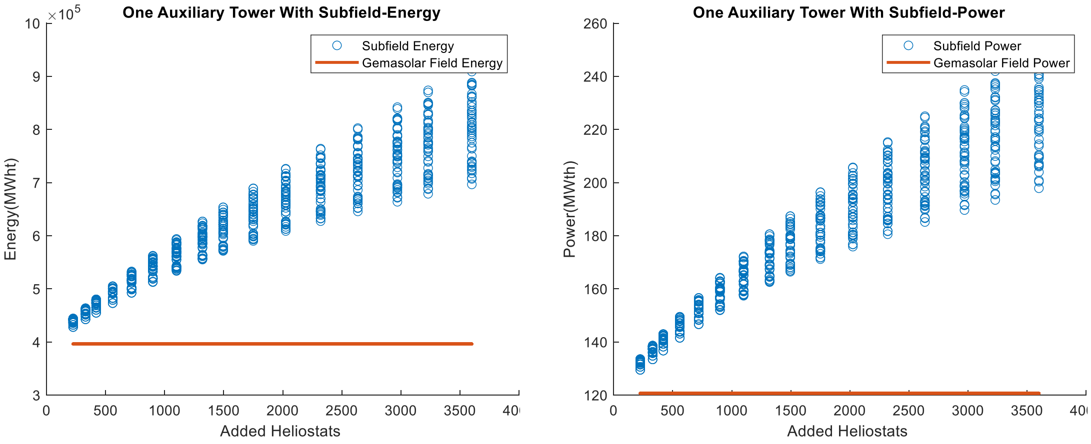

(c) (d)

Figure 6-7 Computational results showing the effect of adding heliostats in a subfield with an auxiliary tower for different parameters: a. Levelized Cost of Heat b. Mean annual efficiency c. Annual thermal energy d. Field thermal power

From Figure 6-7, the trend in LCOH, Energy, Power and Efficiency follows a similar pattern as previously seen from the ATS configuration highlighted in Chapter 5.3. LCOH progressively decreases as more heliostats are added until the radiation reflection efficiency in the subfield reduces to the point where additional heliostats are having an adverse effect. Optimum LCOH here would be the least value for specific thermal power. Energy and Power (Figure 6-7c&d) are invariably increasing with the addition of heliostats in the field.

The best-identified upgrade option for the new field here would entail an independent storage system and PCU (Figure 6-6). This is due to the possible limitations in the capacity of storage and PCU from the Gemasolar Plant. From the results in Figure 6-7, the ATS field configuration increases the power and energy in the field even when large number of heliostats are added. In Table 6-5, the results at optimum LCOH for the different overall field thermal powers are shown. The optimal LCOH is checked at field thermal powers, each within the range of +/-1MWth.

Table 6-5 Auxiliary Tower with Subfield results at optimum levelized Cost of Heat for different overall field thermal powers in a Gemasolar field

Total Field Thermal Power (MWth)	Annual Power at Auxiliary Receiver (MWth)	Annual Energy at Auxiliary Receiver (MWth)	Optimum Levelized Cost of Heat ($/MWht)	Mean Annual Field Efficiency (%)	Total Field Energy (MWht)	Total Field Reflective Surface Area (m^2)
120.68 (Initial Gemasolar Field)	-	-	0.0449	51.22	396,453.21	305,401.90
139.37	18.69	64,575.02	0.0454	50.90%	465,380.50	353,805.22
160.10	41.12	147,351.09	0.0440	51.79%	547,916.60	409,123.30
179.50	60.62	225,024.68	0.0429	50.75%	625,546.20	477,694.67
199.68	82.05	303,231.33	0.0419	50.68%	703,556.00	538,775.05
221.17	104.72	386,149.73	0.0412	50.41%	786,279.00	609,075.11
239.12	121.49	460,126.44	0.0410	48.92%	860,451.10	720,287.50

Table 6-5 shows a more concise trend of Figure 6-7a in the LCOH as heliostats are added on to the subfield. A Lower LCOH (0.0440 $/MWht) from the initial field is only attained when 420 heliostats are added onto the field. At that point, the energy gained outweighs the cost of the auxiliary tower. The overall field's thermal power at that point, however, increases to 160MWth. For the rest of the new field thermal powers, the LCOH continues to decrease. However, the rate of reduction in the LCOH progressively reduces as heliostats are added in the field. This is as a result of the reduction in the overall field's efficiency. When high number of heliostats are added in the subfield, the efficiency in that region begins to rapidly reduce. This is mostly as a result of the accumulation of cosine losses from the North facing subfield heliostats with increasing distance from the tower (Table 6-2).

The total reflective surface area from Table 6-5 in the field shows a progressive increase in the relative surface area at the field's thermal powers. At 180MWth for example, an increment of half the initial field rating, the reflective surface area at 477,694.67 m^2 corresponds to 1.56 of the original field's area. This worsens at even higher thermal powers. This, once more, can be attributed to the more reduced energy conversion efficiency of the heliostats in the subfield at that point hence the need for more heliostats. In Figure 6-8, the thermal area per square meter for the different thermal powers from the added heliostats in the ATS configuration is shown.

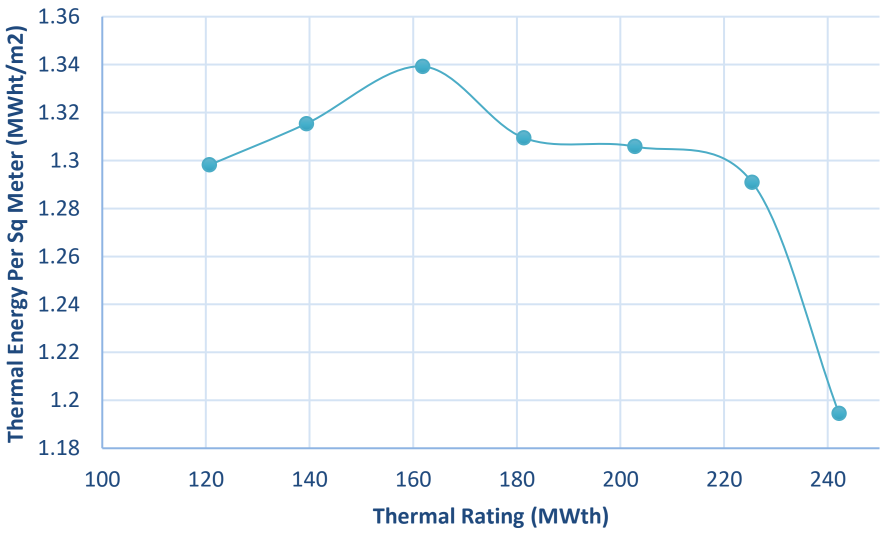

Figure 6-8 Thermal energy per square meter attained in the Auxiliary Tower with Subfield configuration

In Figure 6-8, from 140MWth of field power, the gain in the thermal energy is slightly higher than the increase in the total reflective surface area. This, however, changes from thermal field power of 220MWth when the increase in energy is being outweighed by the increase in reflective surface area. In this case, the optimum value would be at 160MWth of field power when more energy is gained for the amount of heliostat added onto the field. Similarly, at 160MWth of power (from Table 6-3) the peak increase in the field efficiency is also attained. Through the field analysis, this would thus define the optimum position for upgrading the Gemasolar field using the ATS configuration. In Figure 6-9, the layout of the configuration with a total field power of 160MWth is shown.

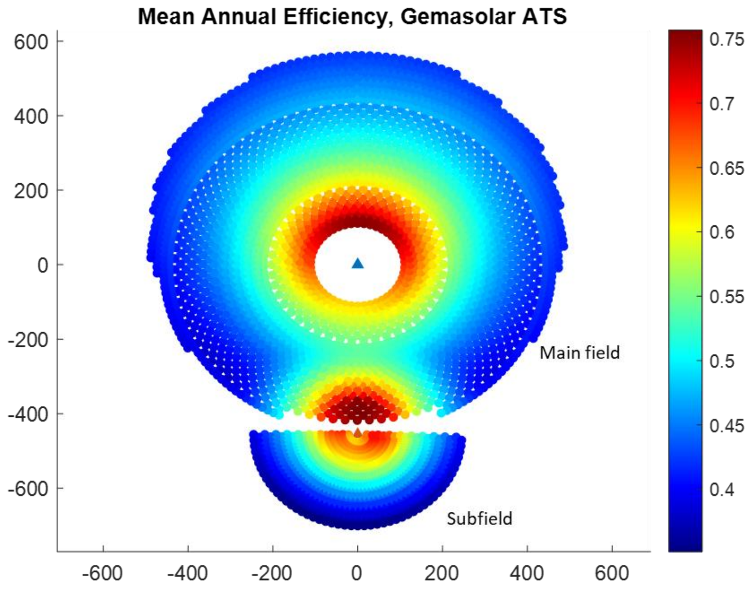

Figure 6-9 Layout of 160MWth field using the Auxiliary Tower with Subfield layout on Gemasolar field

6.3 Gemasolar Field: Heliostat Repositioning Configuration (HRC)

The Heliostat Repositioning Configuration (HRC) discussed in Chapter 5.4 is applied here as well to the Gemasolar field. In like the previous section, the configuration here is equally applied to explore the possibility of upgrading or retrofitting the Gemasolar field.

The design variables (and the corresponding range) from Table 6-4 is adopted here. Minimizing the LCOH is equally chosen as the objective function in this configuration. ‘

6.3.1 Results and Discussion

The results from applying HRC configuration on the field are shown in Figure 6-10.

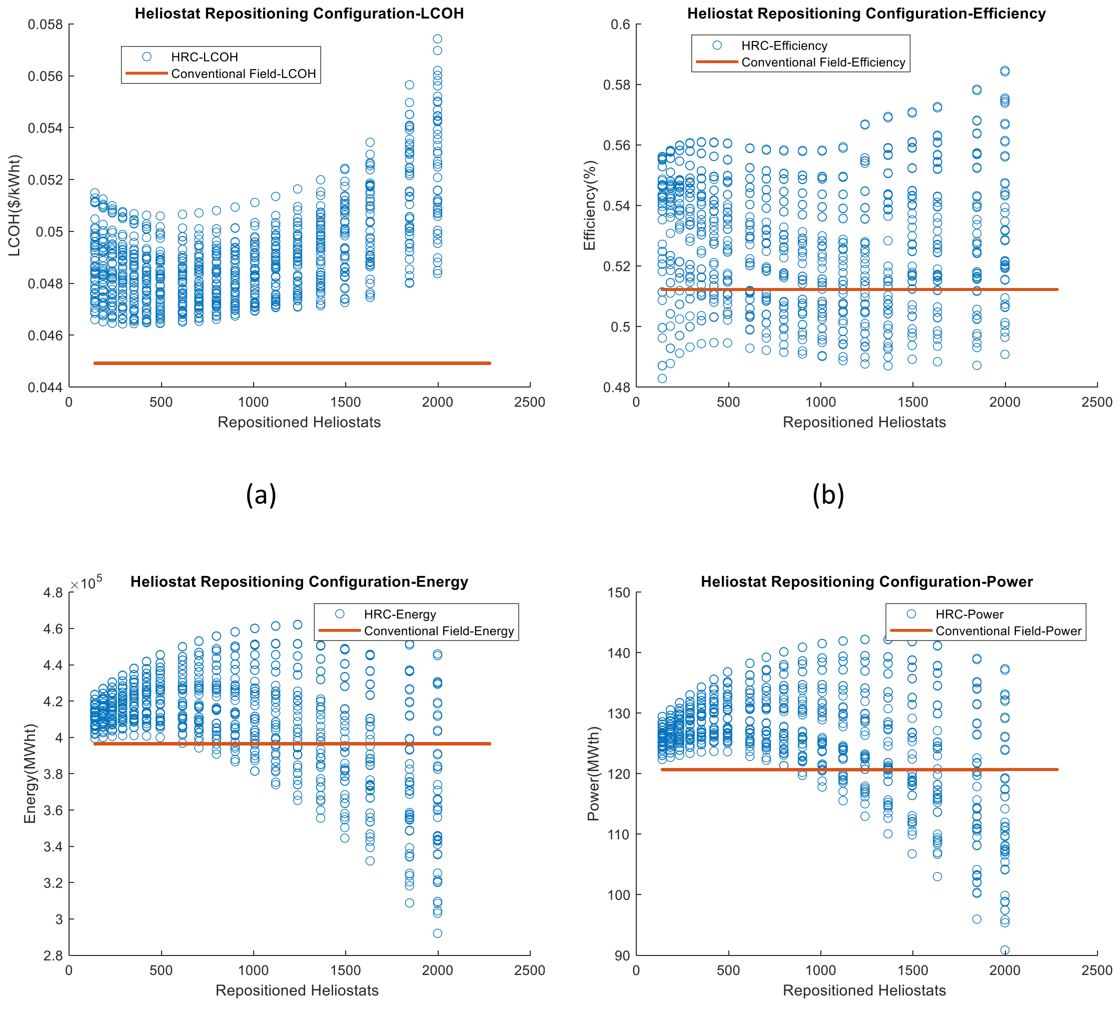

(a) (b)

(c) (d)

Figure 6-10 Computational results showing the effect of repositioning heliostats to the subfield having one auxiliary tower for different parameters a. levelized Cost of Heat b. Mean annual efficiency c. Annual thermal energy d. Field thermal power

The results from Figure 6-10 shows a similar pattern with Figure 5-23. For the given number of heliostats repositioned, an initial reduction in the LCOH is obtained, Figure 6-10a. This begins to quickly change when moving heliostats to the subfield overcrowds the region as the mean radiation reflection efficiency dips. This thus causes a consequential reduction in the overall attained energy and power (Figure 6-10b, c & d).

The reduction in LCOH attained from repositioning the weaker heliostats in the main field remains higher than the initial Gemasolar LCOH computed. The lowest LCOH recorded is equally regarded as the optimum point here. In Table 6-6, the results from the optimum LCOH field is compared with the initial Gemasolar field.

Table 6-6 Optimum levelized Cost of Heat field using Heliostat Repositioning Configuration compared with the initial Gemasolar field

Parameter	Conventional Field	Heliostat Repositioning Configuration Field
Heliostat Area (m²)	115.25	115.25
Central Tower Height (m)	140	140
Central Receiver Area (m²)	384.24	384.24
Auxiliary Tower Height (m)	-	88.00
Auxiliary Receiver Area (m²)	-	37.70
Levelized Cost of Heat, LCOH ($/kWht)	0.0449	0.0462
Field Power (MWth)	120.68	127.81
Mean Annual Efficiency (%)	51.22	53.81
Mean Annual Attenuation Efficiency (%)	95.44	94.29
Mean Annual Blocking Efficiency (%)	84.08	93.18
Mean Annual Cosine Efficiency (%)	77.21	80.95
Mean Annual Spillage Efficiency (%)	99.67	99.85
Reflective Surface Area (m²)	305,401.90	305,401.90
Number of Heliostats	2,650	2,650
Heliostats Repositioned	-	816
Total Incident Annual Energy (MWht)	396,453.21	438,379.46
Auxiliary Receiver Thermal Power (MWth)	-	36.43
System Cost ($)	97,025,168.28	113,016,397.18

The results from 6-6 show an evident increase in the power and energy of the overall field from HRC, by 7.13MWth and 41,929.25MWht, respectively. The overall efficiency of the plant increases by 2.59% to a value of 53.81%.

The Gemasolar field is set up to have more heliostats in the North (upper half), thereby reducing the possible losses that can be incurred due to cosine from the heliostats placed in the South lower half). This however still does not exempt the Southern part of the field from incurring the most losses: particularly in the 4th quadrant as earlier seen (Table 6-3). This thus explains why even in 2nd Zone from the main field, where heliostats are in closer proximity to the central tower, 310 heliostats (from the 816 heliostats repositioned) are identified with lower conversion efficiency and repositioned to the subfield. Although an increase in thermal energy is witnessed, the additional cost from the presence of an auxiliary tower causes the LCOH to be 0.0013$/MWht higher in the new field.

From figure 6-10, it can be deduced that from the optimum LCOH point, the following repositioned heliostats higher than 816 and at thermal powers greater than 127.81MWth, the corresponding LCOH increases. As earlier stated, this is because, within the specified designed variables and their ranges, all the possible heliostats that can be repositioned to a more efficient region are exhausted. This occurrence is an indicator to the possibility of more heliostats being repositioned in conventional fields with larger fields and higher thermal field powers. The 660MWth receiver power [171] Noor III plant in Morocco with similar partners as the Gemasolar could provide entirely different results. However, due to limited data, the configuration cannot be currently established here. In Figure 6-11, the layout of the field at the optimum LCOH attained is shown.

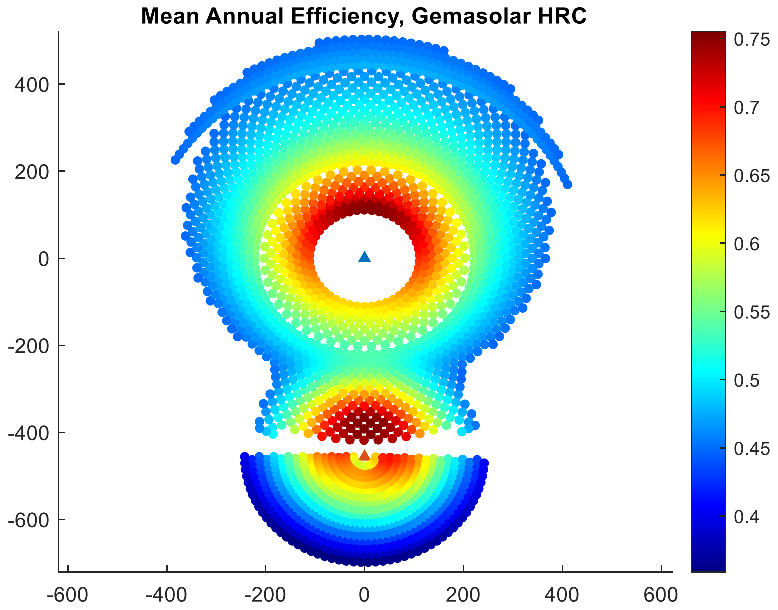

Figure 6-11 Layout showing the mean annual efficiency at optimum levelized Cost of Heat using the Heliostat Repositioning Configuration in a Gemasolar field

The HRC has the potential to be applied in an existing field and can easily be integrated with the first highlighted upgrade option where the storage unit and PCU are shared. This is mainly because of the limited increase in the incident thermal energy into the storage unit primarily as a result of the unchanged number heliostats in the field. Most of the components in a plant have a higher threshold of operating capacity. If the tank's capacity can absorb the increased thermal energy, a higher plant's duration of operation or plant electrical output can be attained (provided the system can absorb the additional energy within the safe operation threshold). Other upgrade options are equally applicable here. However, the additional cost that may arise from the other options, considering the limited increase in thermal energy from this configuration, may prove it prohibitive.

From the two configurations investigated, the results show that the ATS configuration holds the most potential in the upgrade or retrofitting of the Gemasolar field. The ATS configuration involves adding an auxiliary tower with a receiver and heliostats onto the field. The positioning of the tower is based on the region, which has the lowest field efficiency. This was identified to be in the fourth quadrant of the field. Heliostats are then added in a location close to the auxiliary tower which drastically increases the overall energy output and efficiency in the field. The increase in the overall field's energy and power is only limited by the number of heliostats added in the subfield region. A resulting decrease in the total field efficiency is, however, witnessed when heliostats in the subfield perform very poorly in reflecting the sun’s radiation due to the huge optical losses incurred mainly as a result of large distances from the target auxiliary tower.

Within the set design variables, the LCOH initially progressively decreases as heliostats are added to subfield. However, at an overall incident power of 160MWth, the energy attained per square meter and field efficiency is highest. This would hence indicate the optimum position that can be considered when retrofitting the field using the configuration. An increment of over 151,000MWht of energy is made available from the field, signifying a 38% rise. The additional energy can be stored in an independent storage system or shared with the primary storage system, thereby potentially providing more duration of storage during periods of low or no solar insolation. In the Gemasolar plant, even in the absence of the sun’s energy, 15 hours of storage at nominal power is realizable. This thus limits the need for the additional storage duration. The most suited upgrade option here will then be building an independent storage system and PCU in order to increase the overall nominal output from the plant. This, however, comes with a higher cost due to the requirement of the additional components (TES and PCU). The cost-benefit study of such an upgrade option will have to be further investigated. The subject of this case study was to explore retrofitting only the field of the Gemasolar plant. The ATS configuration provided a viable option where the LCOH, efficiency and thermal energy per heliostat area all recorded an improvement.

In Appendix F2, an optimised Gemasolar field replica having one auxiliary tower is modelled. This would signify a complete remodelling of the field. The results are compared with the Gemasolar field to aid a better understanding of multi-towering. The multi-tower field improvement strategies, ATS and HRC are also applied in this complete remodelling of the Gemasolar field and their results presented in F2.

Chapter Summary

Here, two different multi-tower concepts: Auxiliary Tower with Subfield (ATS) and the Heliostat Repositioning Configuration (HRC) were applied to the Gemasolar field. The chapter describes how the models can be applied in upgrading an existing plant.

HRC involves identifying the poor performing heliostats in the field and relocating them to a region near the auxiliary tower. The process of repositioning continues until the optimum LCOH is attained when the highest gain in energy, within the set design variables, is reached. HRC can be integrated into the existing field by either sharing the plant's existing storage unit and Power Conversion Unit (PCU) or developing a new set of storage unit and PCU. At the optimum LCOH, of the 2650 heliostats in the field, 816 heliostats are repositioned to the subfield leading to an increase in the annual energy in the field by 41,926MWth. The increased thermal energy output, however, is still incapable of offsetting the initial plants LCOH of 0.0449$/kWht. This is primarily due to the fewer number of heliostats that can be repositioned as a result of the field's thermal power and size, thus limiting upgrading the Gemasolar using this configuration.

The second configuration, ATS, involves adding heliostats to the field in a location close to an auxiliary tower. An overall increase in the energy output and efficiency of the field is witnessed as heliostats are continuously added in the subfield. This, however, changes when the solar radiation reflection efficiency of the subfield begins to fall, which leads to a corresponding increase in the overall field's LCOH. The total field efficiency and energy attained per square meter in this configuration are highest at an overall incident field power of 160MWth. This thus indicates the optimum position in upgrading the field. At this position, the LCOH is lower than the initial Gemasolar field and the additional energy gained can either be stored hence providing more duration of storage during periods of no solar insolation or channelled to an independent PCU for an increase in the total nominal power of the plant.

7 DISCUSSION AND CONCLUSION

The heliostat field in solar tower systems is one of the essential subsystems in the plant due to its significant contribution to the plant's total investment cost. About 40-50% of the plant's cost is attributed to the collector field. The field equally amounts to an overall plant's power loses of about 40%. This thus necessitates that the field layout is most optimal at collecting energy from the sun. Several methods have thus been proposed to improve heliostat field efficiencies and reduce losses either by improving through optimisation or suggesting new heliostat field layout pattern entirely. These methods are necessary because both the optimisation process and design of the field are a multi-faceted problem. In several works of literature on heliostat layout and optimisation, some innovations were made on the field by way altering or increasing some of the components in the field.

One of the unconventional heliostat field layout design involves including multiple towers, each having its receiver mounted atop, into the field hence deviating away from the conventional setup where a single tower is dedicated to a field. Literature review on multi-tower systems has shown the configuration to have numerous advantages over the single tower concept in terms of flexibility in providing power and reduced risks. Also, some of the optical efficiencies such as blockage, attenuation and spillage losses generally associated with the single towered system due to increasing distance of the heliostats from the target aim point are generally reduced with multi-towers. However, the increase in the Levelized Cost of Heat (LCOH) as a result of the increase in the number of towers, receivers and piping must be offset by the decrease of optical losses in the field. Choosing the number of receivers and towers remains a critical issue in the optimisation process. The optimum transition size from single to multi-tower field must hence be established. Furthermore, from the literature, in all the multi-tower configurations reviewed, each tower has its own heliostat field; the field appears as several individual units of the conventional system.

The basis of this work is investigating a different architecture of the multi-tower configuration. An alternate set up to the usual mainstream multi-tower configuration is the main subject of examination. The configuration involves adding auxiliary towers alone to a conventional field with a surrounding layout. This aspect has been published in a work by the author in [22]. Additionally, there are limited literature developing multi-tower field layout methodologies. This, by contrast, is not the case when likened to typical conventional fields, where several field layout optimisation and improvement techniques exist. The thesis hence also investigates and develops multi-tower field improvement strategies.

The methodology in this work initially develops a conventional field. This was done in order to establish a base for which the multi-tower field can be built upon and compared against. Nigeria was identified as the location in which the plant would be sited.

The power sector in Nigeria is one of the most critical constraints to economic development in the region. The erratic power supply remains a constant feature. This has led the Government to actively pursue alternate sources of energy and veer away from the centralised system of electricity production to a decentralised energy system. The decentralised energy model is closely associated with renewable energy resources. Also, declining patronage on the country's volatile petroleum and natural gas prices, coupled with the rising global temperature predominately as a result of the atmospheric build-up of CO_2, further influenced the consideration of renewable energy technologies for its power generation. Given the geographical location of some regions, solar energy electricity generation in the form of Concentrated Solar Power (CSP) is regarded as a viable and promising option for Nigeria in combating climate change and providing energy security.

For regions in the northern parts of Nigeria, the (DNI) average value is around $5.5\ \mathrm{kWh/m^2/day}$, thus making the area suitable for CSP deployment. At the selected site, in Katsina State, Nigeria (Latitude: 12.39 ˚N Longitude: 7.60 ˚E), data obtained from the metrological agency in Nigeria, NiMet (Nigerian Metrological Agency) shows an average DNI value of 5.53 $\mathrm{kWh/m^2/day}$. Also, the site: having low biodiversity with a slight slope; in close proximity to a transmission substation; and having a nearby source of water in the Karaduwa river has further validated the selection of the site for the deployment of a power tower CSP system.

The parameters and procedures that need to be established before the design and configuration of the power system were also outlined. This procedure is a significant prerequisite to establishing and developing the system. In selecting the design point date by establishing the solar radiation energy utilisation efficiency at the site, it was found that general statements attributing the sun's highest elevation angle to the Summer solstices of June 21st does not apply here. This thus contradicts the typical DNI design point operating conditions of summer solstices, June 21st, or spring equinox, March 21st (for regions North of the equator) CSP plant design. At the site, the design point date with the highest output parameter is found when the highest elevation angle from the sun is reached, which is on April 20th.

7.1 Conventional Power Tower Field

A 50MWth field was, initially, highlighted as the design point power. The model and method used for the design and configuration of a conventional power tower system were outlined. Defining the conventional field forms the basis with which the multi-tower field is developed. A description of the model included identifying the position of the sun. This included establishing all the vector components of the sun typically characterised by the altitude and azimuth angle; and defining the optical efficiency models including the cosine efficiency loss factor, blocking and shadowing efficiency loss factor, attenuation efficiency loss factor and the mirror reflectivity loss factor. A MATLAB program that models and simulates the heliostat field of a power tower system using campo's radial staggered configuration was developed. The radial staggered configuration was used as it a well-established and tested methodology for the generation of the heliostat field. Also, FJ Collado's campo improves the accuracy and speed with which the heliostat field can be optimised and designed.

With the field layout generated, expansion and optimisation of the field were then initiated. In this particular model, the optimisation was not only limited to improving the optical efficiency but also obtaining the parameters of the field. The parameters of the field constitute the design variables (namely, the number of heliostats in the first row, heliostat area, tower height, and consecutive row separation distance in the first, second, and third zones). The design variables were optimised using Genetic Algorithm (GA), developed from the Global Optimisation toolkit in MATLAB, within the context of the objective function in order to arrive at the required field thermal power. The objective function is in the form minimising the Levelized Cost of Heat (LCOH) given by the ratio of the total heliostat field cost to the annual thermal energy at the receiver surface. Different models of the optical loss parameters were then applied in order to measure the strength of the reflected radiation arriving at the receiver surface, so the target field power of 50MWth can be met. At 50MWth, the GA algorithm picks the design variables (Table 4-2) randomly. It uses them as parents to produce the children for the next generation in achieving the optimal solution for the given thermal power (which acts as a constraint here).

For a 50MWth field, the LCOH was obtained to be at 0.0473$/kWh with the annual thermal energy at 151,849MWth, and a mean annual efficiency value at 55.63%. In order to further validate the model developed, the results were compared to the National Renewable Energy Laboratory's (NREL) System Advisor Model (SAM) model, and a good correlation between the two models was achieved. This was shown in Table 4-3. An apparent reduction in the mean annual efficiency of the heliostats was witnessed across the Zones in the field, as seen from Figure 4-7. This was as a result of the continuous reduction in all the optical loss models with cosine efficiency having the largest share of optical losses between Zone 1 to Zone 3.

7.2 Multi-Tower Field Configuration

With the model established for the conventional field. The algorithm for the multi-tower field was then developed. The first step entailed choosing the region where the auxiliary tower would be sited. The auxiliary tower location was designed based on the region with the lowest efficiency and reflected energy. This was to ensure that the heliostats in the weakest region of the field are presented with an alternate target where higher radiation reflecting efficiency is achievable. The lower half of the field (southern half) has the lowest conversion efficiency. With the field divided into four quadrants (Figure 5-1), the fourth quadrant (in the lower half) has the least efficiency. All auxiliary towers added in the model were hence sited in the field's lower half. The effects of adding one and two auxiliary towers in the developed 50MWth conventional field are shown in Figure 5-5. The results show an evident increase in the field efficiency values and the thermal energy for different combinations of additional tower input variables highlighted in Table 5-2 and 5-3.

The first configuration on the multi-tower field involved optimising the entire field in order to achieve the best possible combination of design variables for a 50MWth field that meets the objective function. The additional objectives in the optimisation process: efficiency and the total reflective area are treated as constraints in order to simplify the solution process and reduce the computational expense. Although a reduction in the reflective area and an increase in the efficiency and annual thermal energy is recorded, at a field size of 50MWth, the LCOH for the one and two auxiliary towers configuration is higher than a conventional field of similar thermal rating. The full results are disclosed in Table 5-4. This thus indicates that the benefits due to the increment in the optical efficiency values and annual energy output do not outweigh the cost of installing an additional tower and receiver.

In order to establish the optimum transition size from a single to multi-tower field, a broader range of thermal powers were examined. The same procedure in the design and optimisation, as in the case for the 50MWth field, was followed. Results show that in larger thermal field sizes, the one auxiliary optimised multi-tower field performs better than a conventional field.

Due to their sizes, bigger thermal fields have a larger reflective surface area. In a conventional system, this corresponds to a higher number of weaker heliostats as a result of the increasing distance of the heliostats from the aim point target. In a multi-tower configuration, the heliostats at the weaker region of a multi-tower field are provided with an additional tower to reflect the sun's radiation, thereby considerably cutting down on cosine, spillage and attenuation losses. For the one auxiliary multi-tower configuration, the optimum transition size from a conventional to a multi-tower field is at 380MWth (see Figure 5-10). In the two auxiliary multi-tower fields, at no point (within the range of thermal powers considered) does the configuration records a lower LCOH when compared to a conventional field. The cost from the presence of two additional towers and receivers does not offset the gain in energy recorded.

The most recent plants built around the world have large reflective surface areas and high receiver incident thermal powers. The 150MWe Noor III plant in Ouarzazate, Morocco, for example, has a receiver thermal power rating of 660MWth. Multi-tower field, have shown it possible to reduce the reflective surface area, increase the field efficiency, generate larger thermal energy and lower the field's LCOH for a conventional field of the same rating. For the design site in Katsina State Nigeria, this happens at the 380MWth field output power. The multi-tower configuration thus provides a viable alternative way in which such large power tower systems can be built.

7.3 Multi-Tower Field Improvement Strategies

Multi-tower configuration could also be applied in existing fields by updating or retrofitting existing conventional fields and adding auxiliary towers. Multi-tower field improvement strategies are limited when compared to the several field optimisation and improvement methods seen in conventional fields. The techniques for developing the field by reconfiguring the field layout to reflect the multi-tower setup is hence developed. Two configurations were developed: Auxiliary Tower with Subfield (ATS) and Heliostat Repositioning Configuration (HRC).

In ATS, heliostats are added near the position of the auxiliary tower, thereby creating another region in the field. The auxiliary tower acts as a target for the heliostats in the main field and the newly added heliostats in the subfield. Both the main field and the subfield are generated using the same standard radial staggered methodology. Different optimised conventional field thermal powers are reconfigured and upgraded with the ATS configuration. From the results, an evident steady increase in the field's thermal power is observed with the addition of heliostats in the subfield. The different thermal powers in the configuration, when compared against conventional fields, shows a better LCOH in large fields starting from the 200MWth field. In a 200MWth One ATS field, within the set design variables, when the field power reaches 300MWth as a result of the addition of heliostats, a lower LCOH is obtained when compared to a conventional field of the same thermal rating. The LCOH continues to decrease until a change in trajectory is witnessed at the 370MWth field mark. For two ATS, a lower LCOH can be seen at even lower fields starting from a 100MWth field. The presence of two additional towers enables more heliostats to be added in the field in potentially high energy prone regions. In Figure 5-20, the result from other thermal fields in both the one and two ATS configurations are shown. The ATS multi-tower configuration shares a close resemblance with typical multi-tower setups where each tower has a surrounding heliostat. However, here, the auxiliary tower has a field that best utilises the existing space near it by introducing heliostats. The auxiliary tower also serves as a target for both the weak heliostats in the main field and the newly added heliostats in the subfield.

HRC is an innovative multi-tower setup that involves repositioning poor solar radiation reflecting heliostats from the main field to the subfield region close to an auxiliary tower. In this configuration, the total reflective surface area in the field remains the same. As the weak heliostats are continuously repositioned to the subfield, the auxiliary tower provides a closer target, thereby reducing some of the associated optical losses entailed in heliostats sited far away from their target. The configuration thus has the most effect when a high number of heliostats in the main field are deemed as 'weak'. Optical losses are more compounded in large fields, thus increasing the number of weak heliostats. In such large thermal fields, the identified weaker heliostats are repositioned to the subfields, where their reflecting radiation efficiency improves. The gain in efficiency from the repositioned heliostats leads to a corresponding increase in the thermal power and energy output from the field. The optimum transition size for the one auxiliary tower HRC is seen at the 280MWth thermal field power where a lower LCOH is recorded when compared to a conventional field of similar thermal power rating. In two auxiliary towers HRC, a similar result in larger fields is obtained, with the optimum transition size at the 320MWth thermal field. The two auxiliary towers provide an additional target for the weaker heliostats here. However, it takes a much larger field before HRC advantages can manifest and able to offset the LCOH in a conventional field of similar rating.

The ATS configuration and HRC denote field improvement strategies that are specific to the multi-tower configuration. The configuration can find application in existing conventional fields by way upgrading and retrofitting or even in the design of new plants. The addition of auxiliary tower has already shown to hold much potential in large plants. ATS and HRC have shown that the same field thermal power can be reached with a lesser LCOH when compared to conventional fields and even optimised multi-tower fields of similar thermal ratings. The results show a clear advantage that multi-tower configuration holds over the conventional field and thus provides a viable alternative to them. To further examine the upgrading options in multi-towers, an existing plant, the Gemasolar plant, is taken as a case study.

7.4 Gemasolar Field Case Study

The Gemasolar plant was chosen as a case study for applying the multi-tower configuration due to its long history of research and available data from different works of literature. The study was made in order to further explore the effects of multi-towering in an existing field. The weakest region in the field was initially identified by dividing it into segments, and an auxiliary tower was added. The two field improvement systems, ATS and HRC, were applied into the developed Gemasolar field model.

In the HRC model, the process of repositioning the identified weak heliostats to the subfield, closer to the auxiliary tower, continues until the optimum LCOH is attained when the highest gain in energy is reached. This happens when 816 heliostats (from the available 2,650) are repositioned to the subfield, which led to an increase in the annual energy in the field by 41,926MWth. The increased thermal energy output was, however, found to be incapable of offsetting the computed LCOH of the conventional Gemasolar field at 0.0449$/kWht.

The Gemasolar field is set up to have more heliostats in the North (upper half), thereby reducing the possible losses that can be incurred due to cosine from the heliostats placed in the South lower half). This considerably reduces the number of weak heliostats in the southern half of the field. Although increased thermal energy is attained, the fewer number of weaker heliostats that can be repositioned limits adopting this configuration in upgrading the Gemasolar field.

In the ATS model, an overall increase in the LCOH and efficiency of the field is witnessed when the number of heliostats added to the subfield (which is sited near the auxiliary tower) have high solar radiation reflecting efficiency. The corresponding increase in the overall thermal power of the field prevents direct comparisons with the Gemasolar field based on the LCOH alone. The total field efficiency and energy attained per square meter in this configuration are highest at an overall incident field power of 160MWth. The position indicates a 38% increase in the thermal energy output of the field at a 34% increment in the total field's reflective surface area. This would hence indicate the optimum transition size in which the Gemasolar field can be upgraded. The additional energy gained here can either be stored hence providing more duration of storage during periods of no solar insolation or channelled to an independent PCU for an increase in the total nominal power of the plant. The limitation on the existing storage needs to be taken to account.

From the two multi-tower configurations, the ATS provided the most viability in upgrading the Gemasolar field. Although the Gemasolar thermal field output rating represents a small fraction of the most recent plants being built, the prospects and benefits can be seen from the results presented. In larger conventional field plants having a similar setup as the Gemasolar, the effect of the multi-tower configurations can be more pronounced.

Multi-tower field improvement configurations are not only limited to upgrading and retrofitting from conventional fields as shown here. In Appendix F, a completely remodelled Gemasolar field with multi-tower is shown. Also, in a conference paper by the author, HRC was applied to an optimised multi-tower field [172]. New plants can hence be designed based on multi-tower configurations in general as results presented here have shown a significant increase in the LCOH and efficiency over typical conventional setups.

The study presented here provides an in-depth overview of multi-towers. An entirely different configuration of multi-towers was investigated where an auxiliary tower alone is added to an existing main field. The configuration provided an overall increment in the heliostat field efficiency by reducing some of the losses entailed in a conventional single tower field setup due to the increasing distance of the heliostat from its aim point. The auxiliary tower, cited at the weakest region in the field, provides an alternate target which in large solar fields, provides a substantial increment in the thermal energy output of the field. The increment in thermal energy output offsets the additional cost in the field due to the presence of the auxiliary tower, thereby providing a lower LCOH than a conventional field of similar rating. The study goes further to develop multi-tower field improvement strategies by introducing the ATS and HRC configurations. The results from the configurations equally show that on large solar fields, even higher field efficiency and thermal energy output are recorded. Multi-tower fields have thus shown, through the research shown here, the potential to change the way power tower fields are being built in the future.

7.5 Recommendations and Future Work

The study here is based entirely on the typical recommended days of the month. A more accurate description of the results will be made when the daily DNI in the form of TMY data is used in the simulation. This can be incorporated in future works.

The economic assessment is a critical factor in meeting the objective function. The approach made here does not represent a holistic description of all the costs on the field. Although the lumped sum for the tower includes the riser and downer pipes, the piping cost to the discharge point in the storage unit is not included in the economic assessment. The total cost would be more pronounced, thereby affecting the LCOH in the multi-tower fields where the Heat Transfer Fluid will have to be discharged via extended pipe networks to the storage tank. In a multi-tower configuration where the storage unit is shared, the pipe network will also have to be optimised. Pipe insulation cost, which has not been factored in the study, could also have a weighty effect in the LCOH computation. Also, the effect of scaling due to production volume can be considered in future works. This may lower the cost in large-sized fields, due to the high volume of production.

In the field's optical model, shadowing optical efficiency losses reduce the incoming solar radiation and hence potentially reduces the heliostat's useful area. In this study, the optical efficiency, loss models developed did not take shadowing into account because the included blocking model has a more definite effect in the losses entailed with heliostat field layouts and to reduce the computational expense and complexity of the modelling. Shadowing losses can be as a result of neighbouring heliostats and in multi-tower fields, be from both the main and auxiliary tower. An improved representation of the optical loss will have the shadowing model included as well. Similarly, the optical field losses calculation was convolution method based. Employing raytracing in future studies would present a more accurate depiction of the field losses.

Finally, the multi-tower field improvement strategies developed can be utilized directly in the process of designing and optimizing a new field. In the present study, the improvement configurations were developed over conventional fields. It would be recommended in further studies to develop an entirely new field that optimises the field's design variables all at once so the most optimal solution for the HRC or ATS configuration can be obtained. Also, the optimisation process can be improved by adopting an unconstrained objective function so Pareto front can be established in finding the optimal solution.

REFERENCES

1. UNFCCC. Report of the Conference of the Parties on its twenty-first session, held in Paris from 30 November to 13 December 2015. Report of the Conference of the Parties on its twenty-first session, held in Paris from 30 November to 13 December 2015. 2015. Available at: http://unfccc.int/resource/docs/2015/cop21/eng/10a01.pdf

2. Behar O., Khellaf A., Mohammedi K. A review of studies on central receiver solar thermal power plants. Renewable and Sustainable Energy Reviews. Elsevier; 2013; 23: 12–39. Available at: DOI:10.1016/j.rser.2013.02.017

3. IEA. Technology Roadmap Solar Thermal Electricity. International Energy Agency (IEA). 2014; : 52. Available at: DOI:10.1007/SpringerReference_7300

4. Caldés N., Lechón Y. 5 – Socio-economic and environmental assessment of concentrating solar power (CSP) systems. Concentrating Solar Power Technology. 2012; : 120–150. Available at: DOI:10.1533/9780857096173.1.120

5. Estela., Greenpeace., SolarPACES. Solar Thermal Electricity - Global Outlook 2016. 2016; : 114.

6. Baharoon DA., Rahman HA., Omar WZW., Fadhl SO. Historical development of concentrating solar power technologies to generate clean electricity efficiently – A review. Renewable and Sustainable Energy Reviews. Elsevier; 2015; 41: 996–1027. Available at: DOI:10.1016/j.rser.2014.09.008

7. Konstandopoulos AG., Pagkoura C., Dimitrakis DA., Lorentzou S., Karagiannakis GP. Solar Hydrogen Production. Springer, Dordrecht; 2015. pp. 283–311. Available at: DOI:10.1007/978-94-017-7330-0_10 (Accessed: 14 October 2019)

8. Zhang HL., Baeyens J., Degrève J., Cacères G. Concentrated solar power plants: Review and design methodology. Renewable and Sustainable Energy Reviews. 2013; 22: 466–481. Available at: DOI:10.1016/j.rser.2013.01.032

9. Kalogirou SA. Solar thermal collectors and applications. Progress in Energy and Combustion Science. 2004. 231–295 p. Available at: DOI:10.1016/j.pecs.2004.02.001

10. IRENA. Renewable Energy Technologies Cost Analysis Series: Concentrating Solar Power. Comprehensive Renewable Energy. 2012; 3(2): 595–636. Available at: DOI:10.1016/B978-0-08-087872-0.00319-X

11. Fritsch A., Flesch J., Geza V., Singer C., Uhlig R., Hoffschmidt B. Conceptual Study of Central Receiver Systems with Liquid Metals as Efficient Heat Transfer Fluids. Energy Procedia. Elsevier B.V.; 2015; 69(0): 644–653. Available at: DOI:10.1016/j.egypro.2015.03.074

12. Răboacă MS., Badea G., Enache A., Filote C., Răsoi G., Rata M., et al. Concentrating Solar Power Technologies. Energies. 2019; 12(6): 1048. Available at: DOI:10.3390/en12061048

13. Noone CJ., Torrilhon M., Mitsos A. Heliostat field optimization: A new computationally efficient model and biomimetic layout. Solar Energy. Elsevier Ltd; 2012; 86(2): 792–803.

Available at: DOI:10.1016/j.solener.2011.12.007

14. Kolb GJ., Jones S a., Donnelly MW., Gorman D., Thomas R., Davenport R., et al. Heliostat Cost Reduction Study. Sandia National Laboratories. 2007. Available at: DOI:10.2172/912923

15. Cádiz P., Frasquet M., Silva M., Martínez F., Carballo J. Shadowing and Blocking Effect Optimization for a Variable Geometry Heliostat Field. Energy Procedia. Elsevier B.V.; 2015; 69: 60–69. Available at: DOI:10.1016/j.egypro.2015.03.008

16. Wei X., Lu Z., Wang Z., Yu W., Zhang H., Yao Z. A new method for the design of the heliostat field layout for solar tower power plant. Renewable Energy. Elsevier Ltd; 2010; 35(9): 1970–1975. Available at: DOI:10.1016/j.renene.2010.01.026

17. Cruz NC., Redondo JL., Berenguel M., Álvarez JD., Becerra-Teron A., Ortigosa PM. High performance computing for the heliostat field layout evaluation. Journal of Supercomputing. Springer US; 2016; 73(1): 1–18. Available at: DOI:10.1007/s11227-016-1698-7

18. Collado FJ., Guallar J. Campo: Generation of regular heliostat fields. Renewable Energy. 2012; 46: 49–59. Available at: DOI:10.1016/j.renene.2012.03.011

19. Aldulaimi KM., Söylemez MS. Performance Analysis Of Multilevel Heliostat Field Layout. 2016; 11(2): 11–20.

20. Besarati SM., Yogi Goswami D., Stefanakos EK. Optimal heliostat aiming strategy for uniform distribution of heat flux on the receiver of a solar power tower plant. Energy Conversion and Management. Elsevier Ltd; 2014; 84: 234–243. Available at: DOI:10.1016/j.enconman.2014.04.030

21. Buck R. Heliostat Field Layout Improvement by Nonrestricted Refinement. Journal of solar energy engineering. 2013; 136(2): 21014. Available at: DOI:10.1115/1.4025293

22. Hussaini ZA., King P., Sansom C. Numerical simulation and design of multi-tower concentrated solar power fields. Sustainability (Switzerland). 2020; 12(6): 13–16. Available at: DOI:10.3390/su12062402

23. Weinrebe G., von Reeken F., Wöhrbach M., Plaz T., Göcke V., Balz M. Towards Holistic Power Tower System Optimization. Energy Procedia. Elsevier; 2014; 49: 1573–1581. Available at: DOI:10.1016/j.egypro.2014.03.166

24. Mills D. Advances in solar thermal electricity technology. Solar Energy. 2004; 76(1–3): 19–31. Available at: DOI:10.1016/S0038-092X(03)00102-6

25. Kolb G., Ho C., Mancini T., Gary J. Power tower technology roadmap and cost reduction plan. SAND2011-2419, Sandia …. 2011; (April): 38. Available at: DOI:10.2172/1011644

26. Kolb GJ. An Evaluation of Possible Next-Generation High-Temperature Molten-Salt Power Towers. Sandia National Laboratories (SNL). 2011; (SAND2011-9320): 121. Available at: DOI:SAND20011-9320

27. Romero-Alvarez M., Eduardo Zarza. Concentrating Solar Thermal Power. In: Kreith F, Goswami DY (eds.) Handbook of Energy Efficiency and Renewable Energy. Florida:

Taylor & Francis Group L.L.C; 2007. pp. 21.1-21.97. Available at: DOI:10.1201/9781420003482

28. Vant-Hull LL. Central tower concentrating solar power (CSP) systems. Concentrating Solar Power Technology: Principles, Developments and Applications. Woodhead Publishing Limited; 2012. pp. 240–283. Available at: DOI:10.1016/B978-1-84569-769-3.50008-X

29. Romero M., Buck R., Pacheco JE. An Update on Solar Central Receiver Systems, Projects, and Technologies. Journal of Solar Energy Engineering. 2002; 124(2): 98. Available at: DOI:10.1115/1.1467921

30. NREL. Power Tower Projects. 2016. Available at: https://www.nrel.gov/csp/solarpaces/power_tower.cfm (Accessed: 6 March 2017)

31. SunLab. Solar Two Demonstrates Clean Power for the Future. Sun Lab SnapShot. Washington, DC, USA; 2000. Available at: http://www.uclm.es/area/amf/Antoine/Fusion/SolarTwo.pdf

32. Pacheco JE. Final Test and Evaluation Results from the Solar Two Project. Sandia National Laboratories. 2002; (January): 294. Available at: DOI:10.2172/793226

33. Falcone PK. A handbook for solar central receiver design. Albuquerque, NM, and Livermore, CA (United States): Cambridge University Press; 1986. Available at: DOI:10.2172/6545992

34. SunLab. Solar Two Demonstrates Clean Power for the Future. Sun Lab SnapShot. Washington, DC, USA; 2000.

35. CSPWorld.org. CSP World Map. 2015. Available at: http://cspworld.org/cspworldmap?field_country_map_tid=All&field_purpose_tid=247&field_status_tid=244&order=field_technology_map&sort=asc (Accessed: 7 February 2017)

36. Pavlović TM., Radonjić IS., Milosavljević DD., Pantić LS. A review of concentrating solar power plants in the world and their potential use in Serbia. Renewable and Sustainable Energy Reviews. 2012; 16(6): 3891–3902. Available at: DOI:10.1016/j.rser.2012.03.042

37. eSolar. eSolar projects. 2016. Available at: http://www.esolar.com/projects/ (Accessed: 7 February 2017)

38. A. Mustafa M., Abdelhady S., A. Elweteedy A. Analytical Study of an Innovated Solar Power Tower (PS10) in Aswan. International Journal of Energy Engineering. 2012; 2(6): 273–278. Available at: DOI:10.5923/j.ijee.20120206.01

39. Yao Y., Hu Y., Gao S. Heliostat field layout methodology in central receiver systems based on efficiency-related distribution. Solar Energy. Elsevier Ltd; 2015; 117: 114–124. Available at: DOI:10.1016/j.solener.2015.04.029

40. Burgaleta JI., Arias S., Ramirez D. Gemasolar: The First Tower Thermosolar Commercial Plant with Molten Salt Storage System. SolarPACES International Conference. 2012; (Sept.): 11–14.

41. Binotti M., De Giorgi P., Sanchez D., Manzolini G. Comparison of Different Strategies for Heliostats Aiming Point in Cavity and External Tower Receivers. Journal of Solar Energy Engineering. 2016; 138(2): 021008. Available at: DOI:10.1115/1.4032450

42. NREL. System Advisor Model (SAM) Case Study: Gemasolar. 2013. Available at: https://sam.nrel.gov/sites/sam.nrel.gov/files/content/case_studies/sam_case_csp_physical_trough_andasol-1_2013-1-15.pdf

43. Collado FJ., Guallar J. A review of optimized design layouts for solar power tower plants with campo code. Renewable and Sustainable Energy Reviews. 2013; 20: 142–154. Available at: DOI:10.1016/j.rser.2012.11.076

44. reneweconomy. Concentrated Solar Power. Available at: https://reneweconomy.com.au/category/solar/ (Accessed: 14 August 2020)

45. Mutuberria A., Pascual J., Guisado M V., Mallor F. Comparison of Heliostat Field Layout Design Methodologies and Impact on Power Plant Efficiency. Energy Procedia. Elsevier B.V.; 2015; 69: 1360–1370. Available at: DOI:10.1016/j.egypro.2015.03.135

46. Yu Q., Wang Z., Xu E., Li X., Guo M. Modeling and dynamic simulation of the collector and receiver system of 1MWe DAHAN solar thermal power tower plant. Renewable Energy. Elsevier Ltd; 2012; 43: 18–29. Available at: DOI:10.1016/j.renene.2011.11.040

47. García-Segura A., Fernández-García A., Ariza MJ., Sutter F., Valenzuela L. Durability studies of solar reflectors: A review. Renewable and Sustainable Energy Reviews. 2016; 62: 453–467. Available at: DOI:10.1016/j.rser.2016.04.060

48. Sansom C., Comley P., Bhattacharyya D., Macerol N. A comparison of polymer film and glass collectors for concentrating solar power. Energy Procedia. Elsevier B.V.; 2013; 49: 209–219. Available at: DOI:10.1016/j.egypro.2014.03.023

49. European Commission. Materials Roadmap Enabling Low Carbon Energy Technologies. SEC(2011) 1609 final. 2011; Available at: DOI:10.1017/CBO9781107415324.004

50. Kennedy C., Terwilliger K., Milbourne M. Development and Testing of Solar Reflectors. DOE Solar Energy DOE Technologies. 2005; (January).

51. Laboratories SN. Energy & CLimiate - R&D Activities. 2015. Available at: http://energy.sandia.gov/energy/renewable-energy/solar-energy/csp-2/csp-rd-activities/ (Accessed: 6 March 2017)

52. Jorgensen G., Gee R., DiGrazia M. Development and testing of abrasion resistant hard coats for polymer film reflectors. SolarPaces Conference. 2010; (October).

53. Fend T., Hoffschmidt B., Jorgensen G., Küster H., Krüger D., Pitz-Paal R., et al. Comparative assessment of solar concentrator materials. Solar Energy. 2003; 74(2): 149–155. Available at: DOI:10.1016/S0038-092X(03)00116-6

54. Platzer W., Hildebrandt C. Absorber materials for solar thermal receivers in concentrating solar power (CSP) systems. Concentrating Solar Power Technology: Principles, Developments and Applications. 2012. pp. 469–494. Available at: DOI:10.1016/B978-1-84569-769-3.50015-7

55. Stine WB., Geyer MM. Power From The Sun. William B. Stine and Michael Geyer. William B. Stine and Michael Geyer; 2001. Available at: http://www.powerfromthesun.net/book.html (Accessed: 16 June 2017)

56. Steinmann W-D. Thermal energy storage systems for concentrating solar power (CSP) plants. Concentrating Solar Power Technology. 2012. pp. 362–394. Available at: DOI:10.1533/9780857096173.2.362

57. Kuravi S., Trahan J., Goswami DY., Rahman MM., Stefanakos EK. Thermal energy storage technologies and systems for concentrating solar power plants. Progress in Energy and Combustion Science. Elsevier Ltd; 2013; 39(4): 285–319. Available at: DOI:10.1016/j.pecs.2013.02.001

58. Li PW., Chan CL., Hao Q., Deymier PA., Muralidharan K., Gervasio DF., et al. Concentrating Solar Power Program Review 2013. SunShot Concentrating Solar Power Program Review. 2013; April 2013: 85–86.

59. Praveen Kumar V MS. Analysis of Heat Transfer Fluids in Concentrated Solar Power (CSP) A Review Paper. 2014; Vol. 3-I(Vol. 3-Issue 12 (December-2014)): 239–240. Available at: http://www.ijert.org/view-pdf/11962/analysis-of-heat-transfer-fluids-in-concentrated-solar-power-csp-a-review-paper

60. Vignarooban K., Xu X., Arvay A., Hsu K., Kannan AM. Heat transfer fluids for concentrating solar power systems - A review. Applied Energy. Elsevier Ltd; 2015; 146(May): 383–396. Available at: DOI:10.1016/j.apenergy.2015.01.125

61. Pacio J., Wetzel T. Assessment of liquid metal technology status and research paths for their use as efficient heat transfer fluids in solar central receiver systems. Solar Energy. Elsevier Ltd; 2013; 93: 11–22. Available at: DOI:10.1016/j.solener.2013.03.025

62. Ortega JI., Burgaleta JI., Tellez FM. Central receiver system solar power plant using molten salt as heat transfer fluid. Journal of Solar Energy Engineering, Transactions of the ASME. 2008; 130(2): 245011–245016. Available at: DOI:10.1115/1.2807210

63. Boerema N., Morrison G., Taylor R., Rosengarten G. Liquid sodium versus Hitec as a heat transfer fluid in solar thermal central receiver systems. Solar Energy. Elsevier Ltd; 2012; 86(9): 2293–2305. Available at: DOI:10.1016/j.solener.2012.05.001

64. Zunft S., Hänel M., Krüger M., Dreißigacker V., Göhring F., Wahl E. Jülich Solar Power Tower—Experimental Evaluation of the Storage Subsystem and Performance Calculation. Journal of Solar Energy Engineering. 2011; 133(3): 031019. Available at: DOI:10.1115/1.4004358

65. Liu M., Belusko M., Steven Tay NH., Bruno F. Impact of the heat transfer fluid in a flat plate phase change thermal storage unit for concentrated solar tower plants. Solar Energy. March 2014; 101: 220–231. Available at: DOI:10.1016/j.solener.2013.12.030 (Accessed: 12 July 2017)

66. Barlev D., Vidu R., Stroeve P. Innovation in concentrated solar power. Solar Energy Materials and Solar Cells. Elsevier; 2011; 95(10): 2703–2725. Available at: DOI:10.1016/j.solmat.2011.05.020

67. Torresol Energy. Gemasolar. 2008. Available at:

https://torresolenergy.com/en/gemasolar/ (Accessed: 4 March 2020)

68. Khalsa SSS., Ho CK. Radiation Boundary Conditions for Computational Fluid Dynamics Models of High-Temperature Cavity Receivers. Journal of Solar Energy Engineering. 2011; 133(3): 031020. Available at: DOI:10.1115/1.4004274

69. STELAWORLD. STE/CSP TECHNOLOGIES - CENTRAL RECEIVER. 2017. Available at: http://www.stelaworld.org/central-receivers/ (Accessed: 2 March 2017)

70. Masdar. Solar Energy - Concentrated Solar Power. Available at: https://masdar.ae/en/masdar-clean-energy/technologies/concentrated-solar-power (Accessed: 14 August 2020)

71. Romero M., Marcos MJ., Téllez FM., Blanco MJ., Fernández V., Baonza F., et al. Distributed power from solar tower systems: a {MIUS} approach. Solar Energy. 1999; 67(4–6): 249–264. Available at: DOI:10.1016/S0038-092X(00)00059-1

72. Schramek P., Mills DR. Multi-tower solar array. Solar Energy. 2003; 75(3): 249–260. Available at: DOI:10.1016/j.solener.2003.07.004

73. Augsburger G., Favrat D. From Single- to Multi-Tower Solar Thermal Power Plants: Investigation of the Thermo-Economic Optimum Transition Size. Proceedings of the SolarPACES 2012 Conference on Concentrating Solar Power and Chemical Energy Systems. 2012;

74. Pacheco JE., Moursund C., Rogers D., Wasyluk D. CONCEPTUAL DESIGN OF A 100 MWe MODULAR MOLTEN SALT POWER TOWER PLANT Vice President Molten Salt Systems - eSolar. 2011;

75. Tyner C., Wasyluk D. eSolar's Modular, Scalable Molten Salt Power Tower Reference Plant Design. Energy Procedia. Elsevier; 2014; 49: 1563–1572. Available at: DOI:10.1016/j.egypro.2014.03.165

76. Piroozmand P., Boroushaki M. A computational method for optimal design of the multi-tower heliostat field considering heliostats interactions. Energy. Elsevier Ltd; 2016; 106: 240–252. Available at: DOI:10.1016/j.energy.2016.03.049

77. Wood C., Drewes K. Vast Solar : improving performance and reducing cost and risk using high temperature modular arrays and sodium heat transfer fluid. SolarPaces Conference. 2019.

78. Ben-Zvi R., Epstein M., Segal A. Simulation of an integrated steam generator for solar tower. Solar Energy. Elsevier Ltd; 2012; 86(1): 578–592. Available at: DOI:10.1016/j.solener.2011.11.001

79. Carrizosa E., Domínguez-Bravo C., Fernández-Cara E., Quero M. Optimization of multiple receivers solar power tower systems. Energy. 2015; 90: 2085–2093. Available at: DOI:10.1016/j.energy.2015.08.005

80. Eck M., Buck R., Wittmann M. Dual Receiver Concept for Solar Towers up to 100 MW. Journal of Solar Energy Engineering-Transactions of the Asme. 2006; 128(3): 293–301. Available at: DOI:10.1115/1.2210501

81. Sharma P., Sarma R., Chandra L., Shekhar R., Ghoshdastidar PS. On the design and evaluation of open volumetric air receiver for process heat applications. Solar Energy. Elsevier B.V.; 2015; 121: 41–55. Available at: DOI:10.1016/j.solener.2015.05.027

82. Sánchez M., Romero M. Methodology for generation of heliostat field layout in central receiver systems based on yearly normalized energy surfaces. Solar Energy. 2006; 80(7): 861–874. Available at: DOI:10.1016/j.solener.2005.05.014

83. Ortega G., Rovira A. Proposal and analysis of different methodologies for the shading and blocking efficiency in central receivers systems. Solar Energy. Elsevier Ltd; 2017; 144: 475–488. Available at: DOI:10.1016/j.solener.2017.01.054

84. García L., Burisch M., Sanchez M. Spillage Estimation in a Heliostats Field for Solar Field Optimization. Energy Procedia. Elsevier B.V.; 2015; 69: 1269–1276. Available at: DOI:10.1016/j.egypro.2015.03.156

85. Besarati SM., Yogi Goswami D. A computationally efficient method for the design of the heliostat field for solar power tower plant. Renewable Energy. 2014; 69: 226–232. Available at: DOI:10.1016/j.renene.2014.03.043

86. Ballestrín J., Marzo A. Solar radiation attenuation in solar tower plants. Solar Energy. 2012; 86(1): 388–392. Available at: DOI:10.1016/j.solener.2011.10.010

87. Morin G. Optimisation of concentrating solar power (CSP) plant designs through integrated techno-economic modelling. Concentrating Solar Power Technology: Principles, Developments and Applications. 2012; : 495–535. Available at: DOI:10.1016/B978-1-84569-769-3.50016-9

88. Barberena JG., Larrayoz AM., Sánchez M., Bernardos A. State-of-the-art of Heliostat Field Layout Algorithms and their Comparison. Energy Procedia. The Author(s); 2016; 93(March): 31–38. Available at: DOI:10.1016/j.egypro.2016.07.146

89. Lutchman SL., Groenwold AA., Gauché P., Bode S. On using a gradient-based method for heliostat field layout optimization. Energy Procedia. Elsevier B.V.; 2013; 49: 1429–1438. Available at: DOI:10.1016/j.egypro.2014.03.152

90. Lipps FW., Vant-Hull LL. A cellwise method for the optimization of large central receiver systems. Solar Energy. 1978; 20(6): 505–516. Available at: DOI:10.1016/0038-092X(78)90067-1

91. Collado FJ., Guallar J. Quick design of regular heliostat fields for commercial solar tower power plants. Energy. Elsevier Ltd; 2019; 178: 115–125. Available at: DOI:10.1016/j.energy.2019.04.117

92. Sassi G. Some notes on shadow and blockage effects. Solar Energy. 1983; 31(3): 331–333. Available at: DOI:10.1016/0038-092X(83)90022-1

93. Talebizadeh P., Mehrabian Ali M., Rahimzadeh H. Optimization of Heliostats Layout in Central Receiver Solar Power Plants. Journal of Energy Engineering. 2014; 140(4): 04014005.

94. Atif M., Al-Sulaiman FA. Optimization of heliostat field layout in solar central receiver systems on annual basis using differential evolution algorithm. Energy Conversion and

Management. Elsevier Ltd; 2015; 95: 1–9. Available at: DOI:10.1016/j.enconman.2015.01.089

95. Schwarzbözl P., Pitz-Paal R., Schmitz M. Visual HFLCAL - A Software Tool for Layout and Optimisation of Heliostat Fields. 16 September 2009; Available at: http://elib.dlr.de/60308/ (Accessed: 19 June 2017)

96. Siala FMF., Elayeb ME. Mathematical formulation of a graphical method for a no-blocking heliostat field layout. Renewable energy. 2001; 23(1): 77–92. Available at: DOI:10.1016/S0960-1481(00)00159-2

97. Zhou Y., Zhao Y. Heliostat field layout design for solar tower power plant based on GPU. IFAC Proceedings Volumes (IFAC-PapersOnline). IFAC; 2014; 19(3): 4953–4958. Available at: DOI:10.3182/20140824-6-ZA-1003.01581

98. Cruz NC., Salhi S., Redondo JL., Álvarez JD., Berenguel M., Ortigosa PM. Design of a parallel genetic algorithm for continuous and pattern-free heliostat field optimization. Journal of Supercomputing. Springer US; 2018; : 1–16. Available at: DOI:10.1007/s11227-018-2404-8

99. Collado FJ. Preliminary design of surrounding heliostat fields. Renewable Energy. Elsevier Ltd; 2009; 34(5): 1359–1363. Available at: DOI:10.1016/j.renene.2008.09.003

100. Ouchi K., Kaneko H., Tamaura Y. HELIOSTAT FIELD DESIGN USING VISUALIZATION METHOD FOR OPTICAL HELIOSTAT INTERACTION. ASME 2011. Washington, DC, USA; 2011.

101. Ramos A., Ramos F. Strategies in tower solar power plant optimization. Solar Energy. Elsevier Ltd; 2012; 86(9): 2536–2548. Available at: DOI:10.1016/j.solener.2012.05.024

102. Carrizosa E., Domínguez-Bravo C., Fernández-Cara E., Quero M. A heuristic method for simultaneous tower and pattern-free field optimization on solar power systems. Computers & Operations Research. Elsevier; 2015; 57: 109–122. Available at: DOI:10.1016/j.cor.2014.11.017

103. Deng L., Wu Y., Guo S., Zhang L., Sun H. Rose pattern for heliostat field optimization with a dynamic speciation-based mutation differential evolution. International Journal of Energy Research. 2019; (October): 1–20. Available at: DOI:10.1002/er.5048

104. Garcia P., Ferriere A., Bezian JJ. Codes for solar flux calculation dedicated to central receiver system applications: A comparative review. Solar Energy. 2008; 82(3): 189–197. Available at: DOI:10.1016/j.solener.2007.08.004

105. Cruz NC., Redondo JL., Berenguel M., Álvarez JD., Ortigosa PM. Review of software for optical analyzing and optimizing heliostat fields. Renewable and Sustainable Energy Reviews. Elsevier; 2017; 72(May 2016): 1001–1018. Available at: DOI:10.1016/j.rser.2017.01.032

106. Kistler BL. A user's manual for DELSOL3: A computer code for calculating the optical performance and optimal system design for solar thermal central receiver plants. Other Information: Portions of this document are illegible in microfiche products. Original copy available until stock is exhausted. Includes 5 sheets of 48x reduction microfiche. 1986; : Medium: X; Size: Pages: 231. Available at: DOI:SAND86-8018

107. Bode S-J., Gauché P. Review of optical software for use in concentrating solar power systems. SASEC: 1st Southern African Solar Energy Conference. 2012; : 1–8. Available at: http://blogs.sun.ac.za/sterg/files/2012/06/CSP-06.pdf

108. NREL. System Advisor Model (SAM). NREL; 2014.

109. Carrizosa E., Domínguez-Bravo C-A., Fernández-Cara E. An optimization tool to design the field of a solar power tower plant allowing heliostats of different sizes. INTERNATIONAL JOURNAL OF ENERGY RESEARCH. 2017; Available at: DOI:10.1002/er.3684

110. Lazardjani MY., Kronhardt V., Dikta G., G??ttsche J. Simultaneous optimization of micro-heliostat geometry and field layout using a genetic algorithm. AIP Conference Proceedings. 2016; 1734. Available at: DOI:10.1063/1.4949052

111. Danielli A., Yatir Y., Mor O. Improving the optical efficiency of a concentrated solar power field using a concatenated micro-tower configuration. Solar Energy. Elsevier Ltd; 2011; 85(5): 931–937. Available at: DOI:10.1016/j.solener.2011.02.009

112. J.C.MacKay. Sustainable Energy—Without the Hot Air S. American Journal of Physics. Cambridge: UIT Cambridge Ltd; 2009. Available at: DOI:10.1119/1.3273852

113. UNDP. Human Development Indices and Indicators: 2018 Statistical Update. 2018.

114. The World Bank. The World Bank Data- Nigeria. Available at: https://data.worldbank.org/country/nigeria (Accessed: 8 October 2019)

115. WB. Doing Business 2019: Training for Reform. World Bank. 2019; : 304. Available at: DOI:10.1596/978-1-4648-1326-9

116. The World Bank. World Development Report 2011. Washington DC; 2011.

117. Organization of the Petroleum Countries. OPEC : Nigeria. Available at: https://www.opec.org/opec_web/en/about_us/167.htm (Accessed: 12 October 2019)

118. GOPA-International Energy Consultants GmbH. The Nigerian Energy Sector(NESP). Bad Homburg: Deutsche Gesellschaft für Internationale Zusammenarbeit (GIZ) GmbH; 2015.

119. Ngozika MM. Nigeria Vision 2020 Economic Transformation Plan: Addressing Nigeria Development and the Structure of the Economy through Education. Knowledge Review. 2015; 33(2): 1–11.

120. GIZ. GIZ Progress Report on Sustainability 2015. 2015.

121. Energy Commission of Nigeria. Draft National Renewable Energy and Energy Efficieny Policy (NREEEP). Federal Ministry of Science and Technology. 2014; (March).

122. Sokoto Energy Research Centre. Sokoto Energy Research Centre, Energy Commission of Nigeria, Usmanu Danfodiyo University, Sokoto – SERC. Available at: http://serc.org.ng/ (Accessed: 12 October 2019)

123. International Renewable Energy Agency (IRENA). RENEWABLE POWER GENERATION COSTS IN 2018. Abu Dhabi; 2018.

124. Schlecht M., Meyer R. Site selection and feasibility analysis for concentrating solar power (CSP) systems. Concentrating Solar Power Technology: Principles, Developments and Applications. 2012. pp. 91–119. Available at: DOI:10.1016/B978-1-84569-769-3.50004-2

125. Kaygusuz K. Prospect of concentrating solar power in Turkey: The sustainable future. Renewable and Sustainable Energy Reviews. 2010; 15: 808–814. Available at: DOI:10.1016/j.rser.2010.09.042

126. Xu X., Vignarooban K., Xu B., Hsu K., Kannan AM. Prospects and problems of concentrating solar power technologies for power generation in the desert regions. Renewable and Sustainable Energy Reviews. Elsevier; 2016; 53: 1106–1131. Available at: DOI:10.1016/j.rser.2015.09.015

127. Hang Q., Jun Z., Xiao Y., Junkui C. Prospect of concentrating solar power in China—the sustainable future. Renewable and Sustainable Energy Reviews. 2008; 12: 2505–2514. Available at: DOI:10.1016/j.rser.2007.06.002

128. Müller-Steinhagen H., Trieb F. Concentrating solar power - A review of the technology. Quarterly of the Royal Academy of Engineering. 2004. Available at: DOI:10.1126/science.1168539

129. I.I. Abbas KMM., Ukoje JA. Mapping Land Use-land Cover and Change Detection in Kafur Local Government,Katsina, Nigeria (1995-2008) Using Remote Sensing and Gis. Research Journal of Environmental and Earth Sciences. 2009; : 6–12.

130. Chukwujekwu OM. Analysis Of Agroforestry Practices In Katsina State, Nigeria. Jos: University of Jos; 2010. Available at: http://irepos.unijos.edu.ng/jspui/bitstream/123456789/189/1/Analysis of Agroforestry Practice.pdf

131. Poullikkas A., Hadjipaschalis I., Kourtis G. A comparative overview of wet and dry cooling systems for Rankine cycle based CSP plants. Trends in Heat and Mass Transfer. 2013; 13(June): 27–50.

132. National Aeronautic and Space Agency (NASA). Surface Metreology and Solar Energy. Available at: http://eosweb.larc.nasa.gov/cgi-bin/sse/sse.cgi?+s01#s01 (Accessed: 9 September 2011)

133. Mills DR., Schramek P., Dey C., Buie D., Haynes BS., Morrison GL. Multi Tower Solar Array Project. 2002; (November 2015).

134. Duffie JA., Beckman WA. Solar Engineering of Thermal Processes. 4th Editio. New Jersey: John Wiley & Sons Inc; 2013.

135. Aringhoff R., Brakmann G., Teske S. Exploiting the Heat From the Sun To Combat Climate Change Concentrated Solar Thermal Power – Now ! Energy. Amsterdam; 2005.

136. Mousavi Maleki S., Hizam H., Gomes C. Estimation of Hourly, Daily and Monthly Global Solar Radiation on Inclined Surfaces: Models Re-Visited. Energies. 2017; 10(1): 134. Available at: DOI:10.3390/en10010134

137. Badescu V. Modeling Solar Radiation at the Earth ’ s Surface. 2008. 536 p. Available at:

DOI:10.1007/978-3-540-77455-6

138. Chhatbar K. The Influence of Meteorological Parameters on The Energy Yield of Solar Thermal Power Plants. 17th SolarPACES Conference. 20-23rd September. Granada, Spain; 2011.

139. Wirz M., Roesle M., Steinfeld A. Design Point for Predicting Year-Round Performance of Solar Parabolic Trough Concentrator Systems. Journal of Solar Energy Engineering. 2013; 136(2): 021019. Available at: DOI:10.1115/1.4025709

140. Segal A., Epstein M. Optimized working temperatures of a solar central receiver. Solar Energy. 2003; 75(6): 503–510. Available at: DOI:10.1016/j.solener.2003.08.036

141. Spelling J., Favrat D., Martin A., Augsburger G. Thermoeconomic optimization of a combined-cycle solar tower power plant. Energy. Elsevier Ltd; 2012; 41(1): 113–120. Available at: DOI:10.1016/j.energy.2011.03.073

142. Weijie D., Xuemei Z. Modeling and Simulation of Heliostats Field in Solar Power Tower. 2017; : 3246–3251.

143. Luo Y., Du X., Wen D. Novel design of central dual-receiver for solar power tower. Applied Thermal Engineering. Elsevier Ltd; 2015; 91: 1071–1081. Available at: DOI:10.1016/j.applthermaleng.2015.08.074

144. Pidaparthi AS., Landman WA., Hoffmann JE., Dinter F. Optical Performance Considerations for Analysis and Simulation of Power Tower Plants. 2016; 160021: 1–2. Available at: DOI:10.1063/1.4984555

145. Montes MJ., Abánades A., Martínez-Val JM. Performance of a direct steam generation solar thermal power plant for electricity production as a function of the solar multiple. Solar Energy. 2009; 83(5): 679–689. Available at: DOI:10.1016/j.solener.2008.10.015

146. Segal A., Epstein M. The optics of the solar tower reflector. Solar Energy. 2001; 69: 229–241. Available at: DOI:10.1016/S0038-092X(00)00137-7

147. Yu Q., Wang Z., Xu E., Zhang H., Lu Z., Wei X. Modeling and simulation of 1 MWe solar tower plant's solar flux distribution on the central cavity receiver. Simulation Modelling Practice and Theory. Elsevier B.V.; 2012; 29: 123–136. Available at: DOI:10.1016/j.simpat.2012.07.011

148. Gadalla M., Saghafifar M. Thermo-economic and comparative analyses of two recently proposed optimization approaches for circular heliostat fields: Campo radial-staggered and biomimetic spiral. Solar Energy. Elsevier Ltd; 2016; 136: 197–209. Available at: DOI:10.1016/j.solener.2016.07.006

149. University of Oregon Solar Radiation Monitoring Laboratory. UO SRML: Sun chart program. Available at: http://solardat.uoregon.edu/SunChartProgram.html (Accessed: 6 May 2019)

150. Turchi CS., Heath GA. Molten Salt Power Tower Cost Model for the System Advisor Model (SAM) Molten Salt Power Tower Cost Model for the System Advisor Model (SAM). Energy. 2013; (February). Available at: DOI:10.2172/1067902

151. Collado FJ., Guallar J. Two-stages optimised design of the collector field of solar power tower plants. Solar Energy. The Author(s); 2016; 135: 884–896. Available at: DOI:10.1016/j.solener.2016.06.065

152. Coventry J., Pye J. Heliostat cost reduction - Where to now? Energy Procedia. Elsevier B.V.; 2013; 49: 60–70. Available at: DOI:10.1016/j.egypro.2014.03.007

153. Papanicolas C., Collares M. State of the Art in Heliostats and Definition of Specifications Survey for a low cost heliostat development. 2014;

154. Llc L., Group C. Assessment of Parabolic Trough and Power Tower Solar Technology Cost and Performance Forecasts Assessment of Parabolic Trough and Power Tower Solar Technology Cost and Performance Forecasts. 2003; (October).

155. Sun Lab. Solar Two Demonstrates Clean Power for the Future. Sun Lab SnapShot. Washington, DC, USA: Sandia National Laboratories and the National Renewable Energy Laboratory, DOE national laboratories.; 2000. Available at: http://www.uclm.es/area/amf/Antoine/Fusion/SolarTwo.pdf

156. Collado FJ., Turégano JA. Calculation of the annual thermal energy supplied by a defined heliostat field. Solar Energy. 1989; 42(2): 149–165. Available at: DOI:10.1016/0038-092X(89)90142-4

157. Wagner MJ. Simulation and Predictive Performance Modeling of Utility-Scale Central Receiver System Power Plants. 2008; : 259. Available at: http://sel.me.wisc.edu/publications/theses/wagner08.zip

158. Leary, P L; Hankins JD. User's guide for MIRVAL: a computer code for comparing designs of heliostat-receiver optics for central receiver solar power plants. Livermore, CA: Sandia National Lab.; 1976. Available at: DOI:10.2172/6371450

159. Schmitz M., Schwarzbözl P., Buck R., Pitz-Paal R. Assessment of the potential improvement due to multiple apertures in central receiver systems with secondary concentrators. Solar Energy. 2006; 80(1): 111–120. Available at: DOI:10.1016/j.solener.2005.02.012

160. Collado FJ., Gómez A., Turégano JA. An analytic function for the flux density due to sunlight reflected from a heliostat. Solar Energy. 1986; 37(3): 215–234. Available at: DOI:10.1016/0038-092X(86)90078-2

161. Collado FJ. One-point fitting of the flux density produced by a heliostat. Solar Energy. Elsevier Ltd; 2010; 84(4): 673–684. Available at: DOI:10.1016/j.solener.2010.01.019

162. Gabbrielli R., Castrataro P., Del Medico F., Di Palo M., Lenzo B. Levelized cost of heat for linear Fresnel concentrated solar systems. Energy Procedia. Elsevier B.V.; 2014; 49: 1340–1349. Available at: DOI:10.1016/j.egypro.2014.03.143

163. Louvet Y., Fischer S., Furbo S., Giovanetti F., Mauthner F., Mugnier D., et al. LCOH for Solar Thermal Applications. 2017; (1): 1–5. Available at: http://task54.iea-shc.org/

164. Baez MJ., Martinez TL. Technical Report on the Elaboration of a Cost Estimation Methodology. http://www.front-rhc.eu/wp-content/uploads/2014/11/FROnT_D3.1_elaboration-of-a-cost-estimation-

methodology_2015.07.22.pdf. 2016; : 1–28.

165. Taylor M., Daniel K., So EY. IRENA: Renewable Power Generation Costs in 2014: An Overview. 2014. Available at: http://www.irena.org/ DocumentDownloads/Publications/Overview_Renewable Power Generation Costs in 2012.pdf

166. Atashkari K., Nariman-Zadeh N., Pilechi A., Jamali A., Yao X. Thermodynamic Pareto optimization of turbojet engines using multi-objective genetic algorithms. International Journal of Thermal Sciences. 2005; 44(11): 1061–1071. Available at: DOI:10.1016/j.ijthermalsci.2005.03.016

167. Sharma N., Varun., Siddhartha. Stochastic techniques used for optimization in solar systems: A review. Renewable and Sustainable Energy Reviews. Elsevier Ltd; 2012; 16(3): 1399–1411. Available at: DOI:10.1016/j.rser.2011.11.019

168. Pitz-Paal R., Botero NB., Steinfeld A. Heliostat field layout optimization for high-temperature solar thermochemical processing. Solar Energy. Elsevier Ltd; 2011; 85(2): 334–343. Available at: DOI:10.1016/j.solener.2010.11.018

169. Lauritzen N. Convex optimization. Undergraduate Convexity. 2013. 223–251 p. Available at: DOI:10.1142/9789814412520_0010

170. Hussaini ZA., King P., Sansom C. Design and Configuration of A Multi-Tower Field Layout From A Conventional Power Tower System. 7th Eur. Conf. Ren. Energy Sys. 10-12 June. Madrid, Spain; 2019.

171. Relloso S., Gutiérrez Y. SENER molten salt tower technology. Ouarzazate NOOR III case. AIP Conference Proceedings. 2017; 1850(June). Available at: DOI:10.1063/1.4984384

172. Hussaini ZA., King P., Sansom C. Design and Configuration of Solar Thermal Multi-Tower Field Layout. 25th SolarPACES Conference. 1-4th October. Daegu, South Korea; 2019.

173. Relloso S., García E. Tower Technology Cost Reduction Approach after Gemasolar Experience. Energy Procedia. Elsevier B.V.; 2015; 69: 1660–1666. Available at: DOI:10.1016/j.egypro.2015.03.125

APPENDICES

Appendix A Solar Radiation Data

This section details the solar radiation data from the site.

A.1 Nigerian Meteorological Agency (NiMet)

The data in Table A.1 is curled from NiMet for solar radiation at selected site.

A-1 NiMet Data at Selected Site

Station	**Katsina (4270)**								
Year	**1990-2006**								
Site Location	**Latitude:**	**12°.393'**	**North**						
	Longitude:	**7°.496'**	**East**						
Month	**Solar radiation on horizontal surface (kWh/m^2)**	**Diffuse radiation (kWh/m^2)**	**Beam radiation (kWh/m^2)**	**Beam normal radiation (kWh/m^2)**	**Annual Mean Temp (°C)**	**Cloud cover fraction (octas)**	**Daily solar radiation on horizontal surface (kWh/m^2)**	**Daily diffuse radiation (kWh/m^2)**	**Daily beam normal radiation (kWh/m^2)**
January	175	49	126	207	21.2	2	5.65	1.57	6.66
February	178	52	126	183	24.3	0	6.36	1.87	6.52
March	209	73	136	184	28.5	0	6.73	2.34	5.95
April	208	77	131	172	31.4	0	6.94	2.56	5.74
May	206	80	126	166	31.5	1	6.63	2.59	5.36
June	205	72	133	177	29.2	1	6.85	2.41	5.92
July	190	83	107	144	27.0	3	6.13	2.67	4.66
August	176	88	88	115	26.1	4	5.66	2.83	3.71
September	184	75	109	149	27.2	3	6.13	2.49	4.96
October	185	72	113	161	27.7	3	5.97	2.32	5.20
November	173	53	120	181	24.7	3	5.76	1.76	6.05
December	158	54	104	176	21.7	2	5.10	1.74	5.68

A.2 Hourly Distribution of the DNI

In Table A-2 to A1-13, the computation for the hourly DNI at the selected site is made for the January to December sun. The recommended day of the month are only considered.

Table A-2 Hourly DNI radiation January sun

January
January 17th

Sunrise time	6.32
Sunset time	17.68
Sunset hour angle	85.18
a	0.62
b	0.46

Solar Time	Solar hour angle,	Ratio of hourly total to daily total radiation	Hourly radiation	Ratio of hourly diffuse to daily total diffuse radiation	Diffuse radiation	Beam radiation on Horizontal Surface	Beam normal radiation
1	165	0.00	0.00	0.00	0.00	0.00	0.00
2	150	0.00	0.00	0.00	0.00	0.00	0.00
3	135	0.00	0.00	0.00	0.00	0.00	0.00
4	120	0.00	0.00	0.00	0.00	0.00	0.00
5	105	0.00	0.00	0.00	0.00	0.00	0.00
6	90	0.00	0.00	0.00	0.00	0.00	0.00
7	75	0.02	0.11	0.03	0.04	0.07	0.43
8	60	0.05	0.30	0.06	0.10	0.20	0.53
9	45	0.09	0.50	0.09	0.15	0.35	0.62
10	30	0.12	0.68	0.12	0.18	0.49	0.69
11	15	0.14	0.80	0.13	0.21	0.59	0.73
12	0	0.15	0.84	0.14	0.22	0.62	0.75
13	-15	0.14	0.80	0.13	0.21	0.59	0.73
14	-30	0.12	0.68	0.12	0.18	0.49	0.69
15	-45	0.09	0.50	0.09	0.15	0.35	0.62
16	-60	0.05	0.30	0.06	0.10	0.20	0.53
17	-75	0.02	0.11	0.03	0.04	0.07	0.43
18	-90	0.00	0.00	0.00	0.00	0.00	0.00
19	-105	0.00	0.00	0.00	0.00	0.00	0.00
20	-120	0.00	0.00	0.00	0.00	0.00	0.00
21	-135	0.00	0.00	0.00	0.00	0.00	0.00
22	-150	0.00	0.00	0.00	0.00	0.00	0.00
23	-165	0.00	0.00	0.00	0.00	0.00	0.00
24	-180	0.00	0.00	0.00	0.00	0.00	0.00
			5.61			**4.03**	**6.76**

Table A-3 Hourly DNI radiation February sun

February	
February 16th	
Sunrise time	6.19
Sunset time	17.81
Sunset hour angle	87.10
a	0.64
b	0.44

Solar Time	Solar hour angle,	Ratio of hourly total to daily total radiation	Hourly radiation, (kWh/m²)	Ratio of hourly diffuse to daily total diffuse radiation	Diffuse radiation (kWh/m²)	Beam radiation (kWh/m²)	Beam normal radiation, (kWh/m²)
1	165	0.00	0.00	0.00	0.00	0.00	0.00
2	150	0.00	0.00	0.00	0.00	0.00	0.00
3	135	0.00	0.00	0.00	0.00	0.00	0.00
4	120	0.00	0.00	0.00	0.00	0.00	0.00
5	105	0.00	0.00	0.00	0.00	0.00	0.00
6	90	0.00	0.00	0.00	0.00	0.00	0.00
7	75	0.02	0.14	0.03	0.06	0.09	0.43
8	60	0.05	0.35	0.06	0.12	0.23	0.54
9	45	0.09	0.56	0.09	0.17	0.39	0.62
10	30	0.12	0.75	0.12	0.22	0.54	0.69
11	15	0.14	0.88	0.13	0.24	0.64	0.73
12	0	0.15	0.93	0.13	0.25	0.67	0.75
13	-15	0.14	0.88	0.13	0.24	0.64	0.73
14	-30	0.12	0.75	0.12	0.22	0.54	0.69
15	-45	0.09	0.56	0.09	0.17	0.39	0.62
16	-60	0.05	0.35	0.06	0.12	0.23	0.54
17	-75	0.02	0.14	0.03	0.06	0.09	0.43
18	-90	0.00	0.00	0.00	0.00	0.00	0.00
19	-105	0.00	0.00	0.00	0.00	0.00	0.00
20	-120	0.00	0.00	0.00	0.00	0.00	0.00
21	-135	0.00	0.00	0.00	0.00	0.00	0.00
22	-150	0.00	0.00	0.00	0.00	0.00	0.00
23	-165	0.00	0.00	0.00	0.00	0.00	0.00
24	-180	0.00	0.00	0.00	0.00	0.00	0.00
			6.30				**6.78**

Table A-4 Hourly DNI radiation March sun

March

March 16th

Sunrise time	6.04
Sunset time	17.96
Sunset hour angle	89.47
a	0.66
b	0.43

Solar Time	Solar hour angle	Ratio of hourly total to daily total radiation	Hourly radiation (kWh/m²)	Ratio of hourly diffuse to daily total diffuse radiation	Diffuse radiation (kWh/m²)	Beam radiation (kWh/m²)	Beam normal radiation (kWh/m²)
1	165	0.00	0.00	-0.13	0.00	0.00	0.00
2	150	0.00	0.00	-0.12	0.00	0.00	0.00
3	135	0.00	0.00	-0.10	0.00	0.00	0.00
4	120	0.00	0.00	-0.07	0.00	0.00	0.00
5	105	0.00	0.00	-0.04	0.00	0.00	0.00
6	90	0.00	0.00	0.00	0.00	0.00	0.00
7	75	0.03	0.17	0.03	0.08	0.09	0.38
8	60	0.06	0.38	0.07	0.15	0.23	0.48
9	45	0.09	0.60	0.09	0.22	0.38	0.56
10	30	0.12	0.79	0.11	0.27	0.52	0.62
11	15	0.14	0.91	0.13	0.30	0.62	0.66
12	0	0.14	0.96	0.13	0.31	0.65	0.67
13	-15	0.14	0.91	0.13	0.30	0.62	0.66
14	-30	0.12	0.79	0.11	0.27	0.52	0.62
15	-45	0.09	0.60	0.09	0.22	0.38	0.56
16	-60	0.06	0.38	0.07	0.15	0.23	0.48
17	-75	0.03	0.17	0.03	0.08	0.09	0.38
18	-90	0.00	0.00	0.00	0.00	0.00	0.00
19	-105	0.00	0.00	0.00	0.00	0.00	0.00
20	-120	0.00	0.00	0.00	0.00	0.00	0.00
21	-135	0.00	0.00	0.00	0.00	0.00	0.00
22	-150	0.00	0.00	0.00	0.00	0.00	0.00
23	-165	0.00	0.00	0.00	0.00	0.00	0.00
24	-180	0.00	0.00	0.00	0.00	0.00	0.00
			6.65				**6.07**

Table A-5 Hourly DNI radiation April sun

					April April 15th		
Sunrise time	5.86						
Sunset time	18.14						
Sunset hour angle	92.09						
a	0.68						
b	0.41						
Solar Time	**Solar hour angle**	**Ratio of hourly total to daily total radiation**	**Hourly radiation (kWh/m²)**	**Ratio of hourly diffuse to daily total diffuse radiation**	**Diffuse radiation (kWh/m²)**	**Beam radiation (kWh/m²)**	**Beam normal radiation (kWh/m²)**
1	165	0.00	0.00	0.00	0.00	0.00	0.00
2	150	0.00	0.00	0.00	0.00	0.00	0.00
3	135	0.00	0.00	0.00	0.00	0.00	0.00
4	120	0.00	0.00	0.00	0.00	0.00	0.00
5	105	0.00	0.00	0.00	0.00	0.00	0.00
6	90	0.00	0.02	0.00	0.01	0.01	0.27
7	75	0.03	0.20	0.04	0.09	0.10	0.37
8	60	0.06	0.41	0.07	0.17	0.24	0.45
9	45	0.09	0.62	0.09	0.24	0.38	0.53
10	30	0.11	0.80	0.11	0.29	0.51	0.59
11	15	0.13	0.92	0.12	0.32	0.60	0.62
12	0	0.14	0.96	0.13	0.33	0.64	0.64
13	-15	0.13	0.92	0.12	0.32	0.60	0.62
14	-30	0.11	0.80	0.11	0.29	0.51	0.59
15	-45	0.09	0.62	0.09	0.24	0.38	0.53
16	-60	0.06	0.41	0.07	0.17	0.24	0.45
17	-75	0.03	0.20	0.04	0.09	0.10	0.37
18	-90	0.00	0.02	0.00	0.01	0.01	0.27
19	-105	0.00	0.00	0.00	0.00	0.00	0.00
20	-120	0.00	0.00	0.00	0.00	0.00	0.00
21	-135	0.00	0.00	0.00	0.00	0.00	0.00
22	-150	0.00	0.00	0.00	0.00	0.00	0.00
23	-165	0.00	0.00	0.00	0.00	0.00	0.00
24	-180	0.00	0.00	0.00	0.00	0.00	0.00
			6.88				**6.31**

Table A-6 Hourly DNI radiation May sun

		May **May 15th**					
Sunrise time	5.71						
Sunset time	18.29						
Sunset hour angle	94.29						
a	0.69						
b	0.39						
Solar Time	**Solar hour angle**	**Ratio of hourly total to daily total radiation**	**Hourly radiation (kWh/m²)**	**Ratio of hourly diffuse to daily total diffuse radiation**	**Diffuse radiation (kWh/m²)**	**Beam radiation (kWh/m²)**	**Beam normal radiation (kWh/m²)**
1	165	0.00	0.00	0.00	0.00	0.00	0.00
2	150	0.00	0.00	0.00	0.00	0.00	0.00
3	135	0.00	0.00	0.00	0.00	0.00	0.00
4	120	0.00	0.00	0.00	0.00	0.00	0.00
5	105	0.00	0.00	0.00	0.00	0.00	0.00
6	90	0.01	0.04	0.01	0.02	0.02	0.25
7	75	0.03	0.20	0.04	0.10	0.10	0.34
8	60	0.06	0.40	0.07	0.17	0.22	0.42
9	45	0.09	0.59	0.09	0.24	0.35	0.48
10	30	0.11	0.75	0.11	0.28	0.47	0.54
11	15	0.13	0.86	0.12	0.31	0.55	0.57
12	0	0.14	0.90	0.13	0.33	0.58	0.58
13	-15	0.13	0.86	0.12	0.31	0.55	0.57
14	-30	0.11	0.75	0.11	0.28	0.47	0.54
15	-45	0.09	0.59	0.09	0.24	0.35	0.48
16	-60	0.06	0.40	0.07	0.17	0.22	0.42
17	-75	0.03	0.20	0.04	0.10	0.10	0.34
18	-90	0.01	0.04	0.01	0.02	0.02	0.25
19	-105	0.00	0.00	0.00	0.00	0.00	0.00
20	-120	0.00	0.00	0.00	0.00	0.00	0.00
21	-135	0.00	0.00	0.00	0.00	0.00	0.00
22	-150	0.00	0.00	0.00	0.00	0.00	0.00
23	-165	0.00	0.00	0.00	0.00	0.00	0.00
24	-180	0.00	0.00	0.00	0.00	0.00	0.00
			6.59				5.77

Table A-7 Hourly DNI radiation June sun

June

June 11th

Sunrise time	5.64
Sunset time	18.36
Sunset hour angle	95.37
a	0.70
b	0.38

Solar Time	**Solar hour angle**	**Ratio of hourly total to daily total radiation**	**Hourly radiation (kWh/m^2)**	**Ratio of hourly diffuse to daily total diffuse radiation**	**Diffuse radiation (kWh/m^2)**	**Beam radiation (kWh/m^2)**	**Beam normal radiation (kWh/m^2)**
1	165	0.00	0.00	0.00	0.00	0.00	0.00
2	150	0.00	0.00	0.00	0.00	0.00	0.00
3	135	0.00	0.00	0.00	0.00	0.00	0.00
4	120	0.00	0.00	0.00	0.00	0.00	0.00
5	105	0.00	0.00	0.00	0.00	0.00	0.00
6	90	0.01	0.05	0.01	0.03	0.03	0.30
7	75	0.03	0.22	0.04	0.10	0.12	0.39
8	60	0.06	0.41	0.07	0.16	0.25	0.47
9	45	0.09	0.61	0.09	0.22	0.39	0.54
10	30	0.11	0.77	0.11	0.26	0.51	0.59
11	15	0.13	0.88	0.12	0.29	0.59	0.62
12	0	0.13	0.92	0.12	0.30	0.62	0.63
13	-15	0.13	0.88	0.12	0.29	0.59	0.62
14	-30	0.11	0.77	0.11	0.26	0.51	0.59
15	-45	0.09	0.61	0.09	0.22	0.39	0.54
16	-60	0.06	0.41	0.07	0.16	0.25	0.47
17	-75	0.03	0.22	0.04	0.10	0.12	0.39
18	-90	0.01	0.05	0.01	0.03	0.03	0.30
19	-105	0.00	0.00	0.00	0.00	0.00	0.00
20	-120	0.00	0.00	0.00	0.00	0.00	0.00
21	-135	0.00	0.00	0.00	0.00	0.00	0.00
22	-150	0.00	0.00	0.00	0.00	0.00	0.00
23	-165	0.00	0.00	0.00	0.00	0.00	0.00
24	-180	0.00	0.00	0.00	0.00	0.00	0.00
			6.81				**6.45**

Table A-8 Hourly DNI radiation July sun

July

July 17th

Sunrise time	5.67
Sunset time	18.33
Sunset hour angle	94.89
a	0.70
b	0.39

Solar Time	**Solar hour angle**	**Ratio of hourly total to daily total radiation**	**Hourly radiation (kWh/m²)**	**Ratio of hourly diffuse to daily total diffuse radiation**	**Diffuse radiation (kWh/m²)**	**Beam radiation (kWh/m²)**	**Beam normal radiation (kWh/m²)**
1	165	0.00	0.00	0.00	0.00	0.00	0.00
2	150	0.00	0.00	0.00	0.00	0.00	0.00
3	135	0.00	0.00	0.00	0.00	0.00	0.00
4	120	0.00	0.00	0.00	0.00	0.00	0.00
5	105	0.00	0.00	0.00	0.00	0.00	0.00
6	90	0.01	0.04	0.01	0.03	0.02	0.20
7	75	0.03	0.19	0.04	0.11	0.09	0.28
8	60	0.06	0.37	0.07	0.18	0.19	0.35
9	45	0.09	0.54	0.09	0.24	0.30	0.41
10	30	0.11	0.69	0.11	0.29	0.40	0.46
11	15	0.13	0.79	0.12	0.32	0.47	0.49
12	0	0.14	0.83	0.12	0.33	0.50	0.50
13	-15	0.13	0.79	0.12	0.32	0.47	0.49
14	-30	0.11	0.69	0.11	0.29	0.40	0.46
15	-45	0.09	0.54	0.09	0.24	0.30	0.41
16	-60	0.06	0.37	0.07	0.18	0.19	0.35
17	-75	0.03	0.19	0.04	0.11	0.09	0.28
18	-90	0.01	0.04	0.01	0.03	0.02	0.20
19	-105	0.00	0.00	0.00	0.00	0.00	0.00
20	-120	0.00	0.00	0.00	0.00	0.00	0.00
21	-135	0.00	0.00	0.00	0.00	0.00	0.00
22	-150	0.00	0.00	0.00	0.00	0.00	0.00
23	-165	0.00	0.00	0.00	0.00	0.00	0.00
24	-180	0.00	0.00	0.00	0.00	0.00	0.00
			6.09				**4.91**

Table A-9 Hourly DNI radiation August sun

August

August 16th

Sunrise time	5.80
Sunset time	18.20
Sunset hour angle	93.01
a	0.68
b	0.40

Solar Time	Solar hour angle	Ratio of hourly total to daily total radiation	Hourly radiation (kWh/m2)	Ratio of hourly diffuse to daily total diffuse radiation	Diffuse radiation (kWh/m^2)	Beam radiation (kWh/m^2)	Beam normal radiation (kWh/m^2)
1	165	0.00	0.00	0.00	0.00	0.00	0.00
2	150	0.00	0.00	0.00	0.00	0.00	0.00
3	135	0.00	0.00	0.00	0.00	0.00	0.00
4	120	0.00	0.00	0.00	0.00	0.00	0.00
5	105	0.00	0.00	0.00	0.00	0.00	0.00
6	90	0.00	0.02	0.01	0.02	0.01	0.13
7	75	0.03	0.17	0.04	0.11	0.06	0.21
8	60	0.06	0.33	0.07	0.19	0.14	0.28
9	45	0.09	0.50	0.09	0.26	0.24	0.34
10	30	0.11	0.65	0.11	0.31	0.33	0.38
11	15	0.13	0.74	0.12	0.35	0.40	0.41
12	0	0.14	0.78	0.13	0.36	0.42	0.42
13	-15	0.13	0.74	0.12	0.35	0.40	0.41
14	-30	0.11	0.65	0.11	0.31	0.33	0.38
15	-45	0.09	0.50	0.09	0.26	0.24	0.34
16	-60	0.06	0.33	0.07	0.19	0.14	0.28
17	-75	0.03	0.17	0.04	0.11	0.06	0.21
18	-90	0.00	0.02	0.01	0.02	0.01	0.13
19	-105	0.00	0.00	0.00	0.00	0.00	0.00
20	-120	0.00	0.00	0.00	0.00	0.00	0.00
21	-135	0.00	0.00	0.00	0.00	0.00	0.00
22	-150	0.00	0.00	0.00	0.00	0.00	0.00
23	-165	0.00	0.00	0.00	0.00	0.00	0.00
24	-180	0.00	0.00	0.00	0.00	0.00	0.00
			5.62				**3.90**

Table A-10 Hourly DNI radiation September sun

September

September 15th

Sunrise time	5.97
Sunset time	18.03
Sunset hour angle	90.49
a	0.66
b	0.42

Solar Time	**Solar hour angle**	**Ratio of hourly total to daily total radiation**	**Hourly radiation (kWh/m²)**	**Ratio of hourly diffuse to daily total diffuse radiation**	**Diffuse radiation (kWh/m²)**	**Beam radiation (kWh/m²)**	**Beam normal radiation (kWh/m²)**
1	165	0.00	0.00	0.00	0.00	0.00	0.00
2	150	0.00	0.00	0.00	0.00	0.00	0.00
3	135	0.00	0.00	0.00	0.00	0.00	0.00
4	120	0.00	0.00	0.00	0.00	0.00	0.00
5	105	0.00	0.00	0.00	0.00	0.00	0.00
6	90	0.00	0.00	0.00	0.00	0.00	0.21
7	75	0.03	0.16	0.03	0.09	0.08	0.30
8	60	0.06	0.35	0.07	0.16	0.19	0.38
9	45	0.09	0.54	0.09	0.23	0.31	0.45
10	30	0.12	0.71	0.11	0.28	0.43	0.50
11	15	0.13	0.82	0.13	0.31	0.51	0.54
12	0	0.14	0.86	0.13	0.32	0.54	0.55
13	-15	0.13	0.82	0.13	0.31	0.51	0.54
14	-30	0.12	0.71	0.11	0.28	0.43	0.50
15	-45	0.09	0.54	0.09	0.23	0.31	0.45
16	-60	0.06	0.35	0.07	0.16	0.19	0.38
17	-75	0.03	0.16	0.03	0.09	0.08	0.30
18	-90	0.00	0.00	0.00	0.00	0.00	0.21
19	-105	0.00	0.00	0.00	0.00	0.00	0.00
20	-120	0.00	0.00	0.00	0.00	0.00	0.00
21	-135	0.00	0.00	0.00	0.00	0.00	0.00
22	-150	0.00	0.00	0.00	0.00	0.00	0.00
23	-165	0.00	0.00	0.00	0.00	0.00	0.00
24	-180	0.00	0.00	0.00	0.00	0.00	0.00
			6.06				**5.30**

Table A-11 Hourly DNI radiation October sun

October

October 15th

Sunrise time	6.14
Sunset time	17.86
Sunset hour angle	87.87
a	0.64
b	0.44

Solar Time	**Solar hour angle**	**Ratio of hourly total to daily total radiation**	**Hourly radiation (kWh/m2)**	**Ratio of hourly diffuse to daily total diffuse radiation**	**Diffuse radiation (kWh/m^2)**	**Beam radiation (kWh/m^2)**	**Beam normal radiation (kWh/m^2)**
1	165	0.00	0.00	0.00	0.00	0.00	0.00
2	150	0.00	0.00	0.00	0.00	0.00	0.00
3	135	0.00	0.00	0.00	0.00	0.00	0.00
4	120	0.00	0.00	0.00	0.00	0.00	0.00
5	105	0.00	0.00	0.00	0.00	0.00	0.00
6	90	0.00	0.00	0.00	0.00	0.00	0.00
7	75	0.02	0.14	0.03	0.07	0.07	0.32
8	60	0.06	0.33	0.06	0.15	0.18	0.41
9	45	0.09	0.53	0.09	0.22	0.31	0.49
10	30	0.12	0.70	0.12	0.27	0.44	0.55
11	15	0.14	0.82	0.13	0.30	0.52	0.58
12	0	0.14	0.86	0.13	0.31	0.55	0.60
13	-15	0.14	0.82	0.13	0.30	0.52	0.58
14	-30	0.12	0.70	0.12	0.27	0.44	0.55
15	-45	0.09	0.53	0.09	0.22	0.31	0.49
16	-60	0.06	0.33	0.06	0.15	0.18	0.41
17	-75	0.02	0.14	0.03	0.07	0.07	0.32
18	-90	0.00	0.00	0.00	0.00	0.00	0.00
19	-105	0.00	0.00	0.00	0.00	0.00	0.00
20	-120	0.00	0.00	0.00	0.00	0.00	0.00
21	-135	0.00	0.00	0.00	0.00	0.00	0.00
22	-150	0.00	0.00	0.00	0.00	0.00	0.00
23	-165	0.00	0.00	0.00	0.00	0.00	0.00
24	-180	0.00	0.00	0.00	0.00	0.00	0.00
			5.91				**5.28**

Table A-12 Hourly DNI radiation November sun

			November **November 14th**				
Sunrise time		6.29					
Sunset time		17.71					
Sunset hour angle		85.68					
a		0.63					
b		0.45					
Solar Time	**Solar hour angle**	**Ratio of hourly total to daily total radiation**	**Hourly radiation, H (kWh/m²)**	**Ratio of hourly diffuse to daily total diffuse radiation**	**Diffuse radiation (kWh/m²)**	**Beam radiation (kWh/m²)**	**Beam normal radiation (kWh/m²)**
1	165	0.00	0.00	0.00	0.00	0.00	0.00
2	150	0.00	0.00	0.00	0.00	0.00	0.00
3	135	0.00	0.00	0.00	0.00	0.00	0.00
4	120	0.00	0.00	0.00	0.00	0.00	0.00
5	105	0.00	0.00	0.00	0.00	0.00	0.00
6	90	0.00	0.00	0.00	0.00	0.00	0.00
7	75	0.02	0.12	0.03	0.05	0.07	0.40
8	60	0.05	0.31	0.06	0.11	0.20	0.51
9	45	0.09	0.51	0.09	0.16	0.35	0.59
10	30	0.12	0.69	0.12	0.21	0.48	0.66
11	15	0.14	0.81	0.13	0.23	0.58	0.70
12	0	0.15	0.85	0.14	0.24	0.61	0.72
13	-15	0.14	0.81	0.13	0.23	0.58	0.70
14	-30	0.12	0.69	0.12	0.21	0.48	0.66
15	-45	0.09	0.51	0.09	0.16	0.35	0.59
16	-60	0.05	0.31	0.06	0.11	0.20	0.51
17	-75	0.02	0.12	0.03	0.05	0.07	0.40
18	-90	0.00	0.00	0.00	0.00	0.00	0.00
19	-105	0.00	0.00	0.00	0.00	0.00	0.00
20	-120	0.00	0.00	0.00	0.00	0.00	0.00
21	-135	0.00	0.00	0.00	0.00	0.00	0.00
22	-150	0.00	0.00	0.00	0.00	0.00	0.00
23	-165	0.00	0.00	0.00	0.00	0.00	0.00
24	-180	0.00	0.00	0.00	0.00	0.00	0.00
			5.72				**6.44**

Table A-13 Hourly DNI radiation December sun

December

December 10th

Sunrise time	6.36
Sunset time	17.64
Sunset hour angle	84.64
a	0.62
b	0.46

Solar Time	Solar hour angle	Ratio of hourly total to daily total radiation	Hourly radiation (kWh/m2)	Ratio of hourly diffuse to daily total diffuse radiation	Diffuse radiation (kWh/m^2)	Beam radiation (kWh/m^2)	Beam normal radiation (kWh/m^2)
1	165	0.00	0.00	0.00	0.00	0.00	0.00
2	150	0.00	0.00	0.00	0.00	0.00	0.00
3	135	0.00	0.00	0.00	0.00	0.00	0.00
4	120	0.00	0.00	0.00	0.00	0.00	0.00
5	105	0.00	0.00	0.00	0.00	0.00	0.00
6	90	0.00	0.00	0.00	0.00	0.00	0.00
7	75	0.02	0.09	0.03	0.04	0.05	0.34
8	60	0.05	0.27	0.06	0.11	0.16	0.44
9	45	0.09	0.45	0.09	0.16	0.29	0.52
10	30	0.12	0.61	0.12	0.21	0.41	0.59
11	15	0.14	0.72	0.13	0.23	0.49	0.63
12	0	0.15	0.76	0.14	0.24	0.52	0.64
13	-15	0.14	0.72	0.13	0.23	0.49	0.63
14	-30	0.12	0.61	0.12	0.21	0.41	0.59
15	-45	0.09	0.45	0.09	0.16	0.29	0.52
16	-60	0.05	0.27	0.06	0.11	0.16	0.44
17	-75	0.02	0.09	0.03	0.04	0.05	0.34
18	-90	0.00	0.00	0.00	0.00	0.00	0.00
19	-105	0.00	0.00	0.00	0.00	0.00	0.00
20	-120	0.00	0.00	0.00	0.00	0.00	0.00
21	-135	0.00	0.00	0.00	0.00	0.00	0.00
22	-150	0.00	0.00	0.00	0.00	0.00	0.00
23	-165	0.00	0.00	0.00	0.00	0.00	0.00
24	-180	0.00	0.00	0.00	0.00	0.00	0.00
			5.06				**5.68**

Appendix B Conventional Field Layout

Here, the results from the conventional field developed at the site are laid out.

B.1 Conventional Field: Optical Efficiency Loss Factors

The field layout showing the optical efficiency loss factors for the 50MWth conventional field is shown in Figure B1

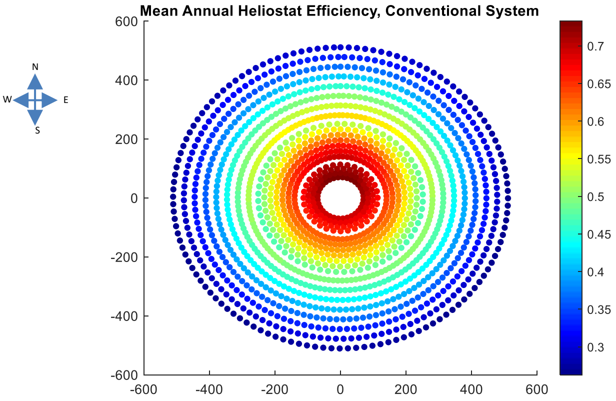

(a)

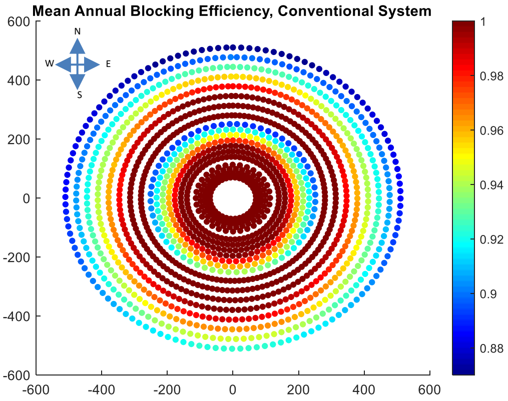

(b)

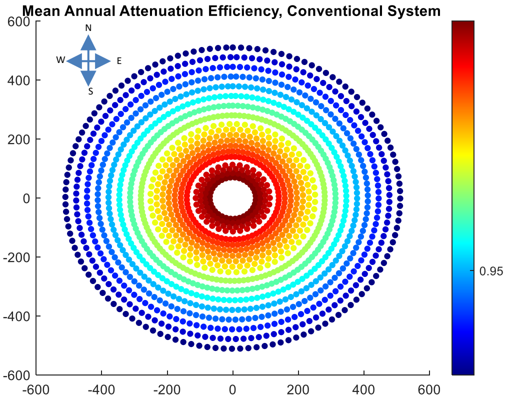

(c)

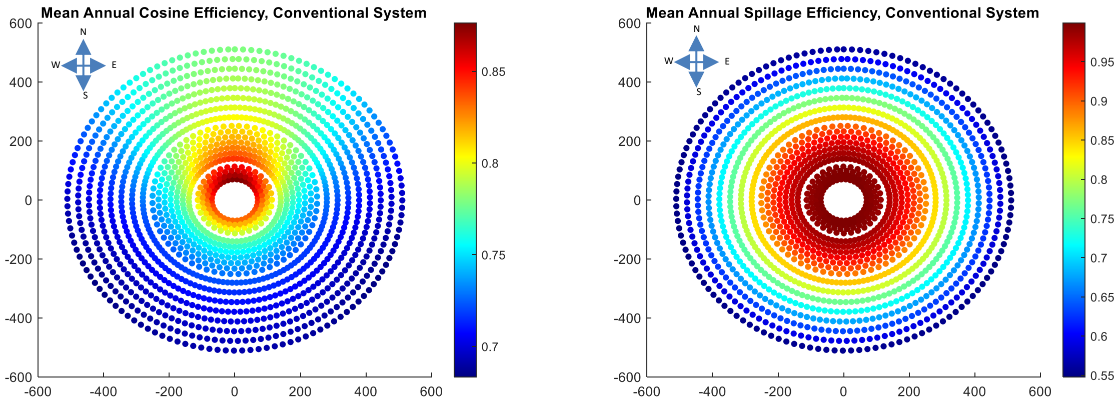

(d) (e)

Figure B-1 50MWth Conventional field showing a) mean annual efficiency, b) blocking loss, c) attenuation loss, d) cosine loss, and e) spillage loss respectively

B.2 Conventional Field: Mean Annual Efficiency Jan-Dec

In Figure B2, the mean annual efficiency layout during the typical recommended day for each month of the year in a 50MWth conventional field are shown.

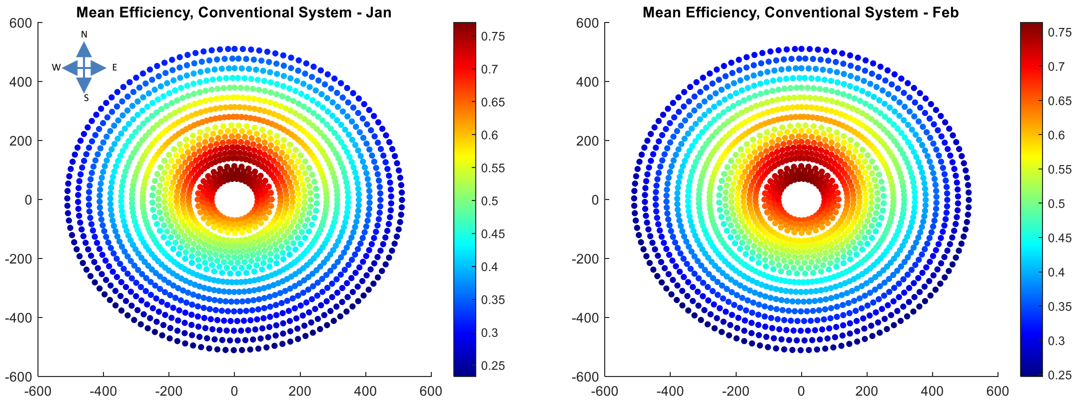

(a) (b)

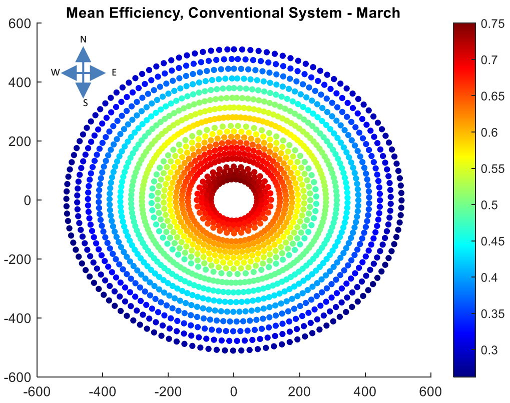
Mean Efficiency, Conventional System - March

(c)

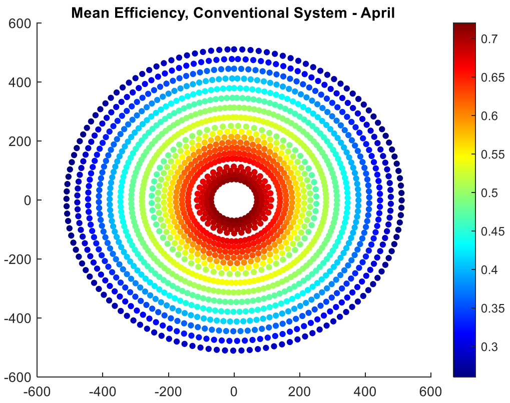
Mean Efficiency, Conventional System - April

(d)

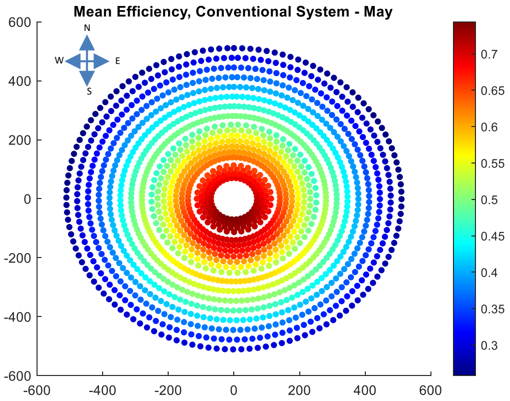
Mean Efficiency, Conventional System - May

(e)

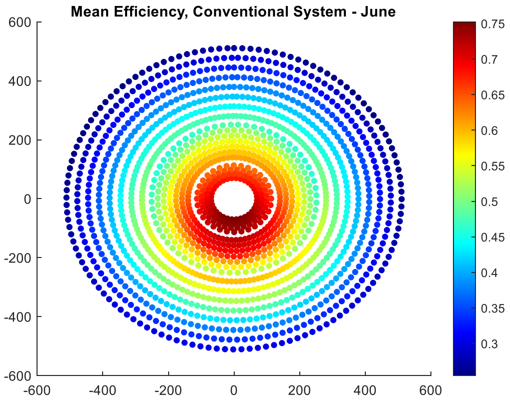
Mean Efficiency, Conventional System - June

(f)

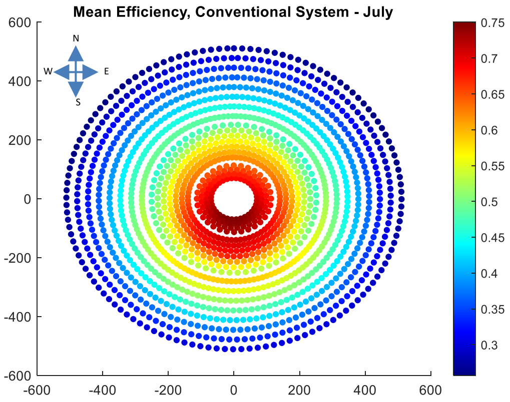
Mean Efficiency, Conventional System - July

(g)

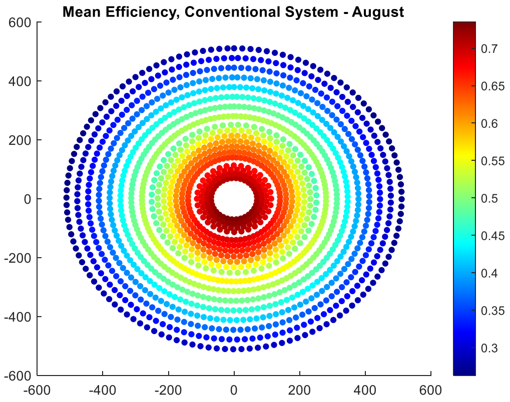
Mean Efficiency, Conventional System - August

(h)

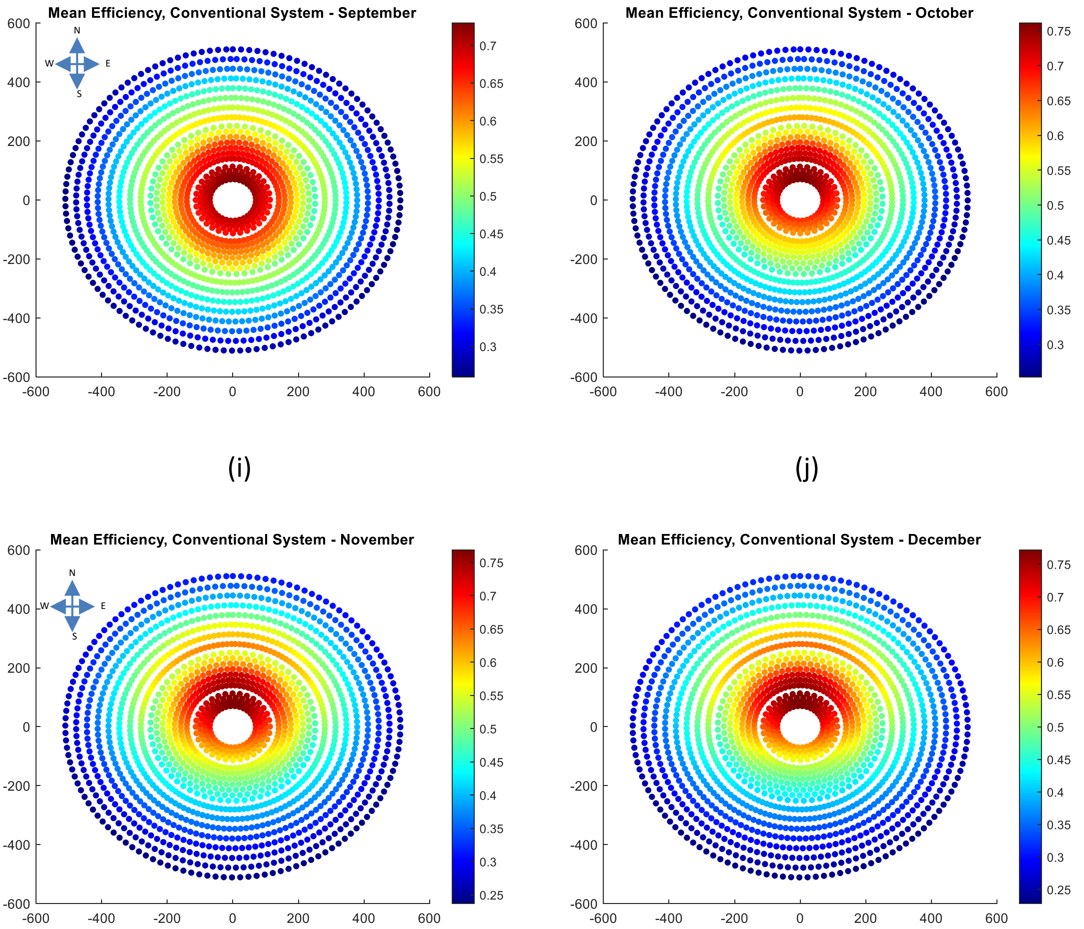

(i) (j)

(k) (l)

Figure B-2 Mean annual efficiency field layout in a representative day of the month for a 50MWth conventional field. a-x) January to December

B.3 Conventional Field: Results

Here, the results from the optimised conventional field at various thermal powers are shown.

Table B-1 Conventional Field result from optimisation at different thermal powers

Conventional Field					
Power (MWth)	**Number of Heliostats**	**Heliostat Area (m²)**	**Reflective Surface Area (m²)**	**Field Efficiency (%)**	**LCOH (\$/kWht)**
25.00	1,235.00	71.41	88,191.35	56.60%	0.0521
50.00	1,600.00	95.17	152,272.00	54.80%	0.0472
100.00	3,990.00	81.83	326,501.70	53.14%	0.0445
150.00	5,720.00	81.01	463,377.20	52.50%	0.0428
200.00	4,968.00	114.12	566,928.29	52.11%	0.0423

300.00	14,240.00	71.17	1,013,460.80	48.52%	0.0425
400.00	16,128.00	91.37	1,473,615.36	47.76%	0.0434
500.00	18,816.00	94.38	1,775,854.08	45.87%	0.0442
600.00	24,818.00	94.38	2,342,322.84	44.00%	0.0450

Appendix C Multi-Tower Field

In this section, the results from the optimised multi-tower field are shown.

C.1 Multi-Tower Field Layout- Mean Annual Efficiency, Jan-Dec

In Figure C1, the mean annual efficiency layout during the typical recommended day for each month of the year in a 50MWth multi-tower field layout is shown.

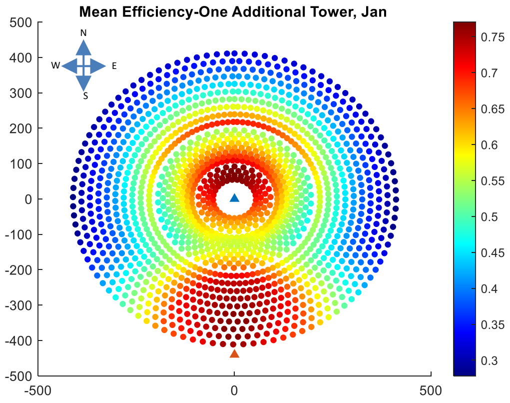

(a)

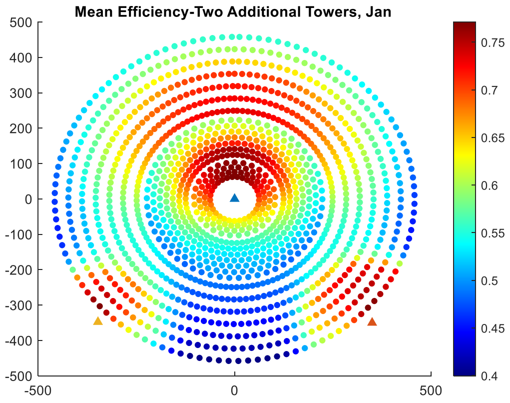

(b)

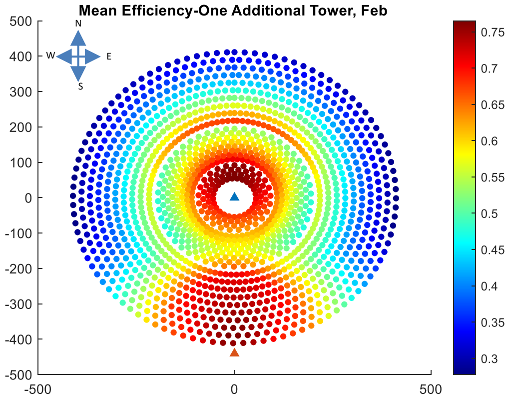

(c)

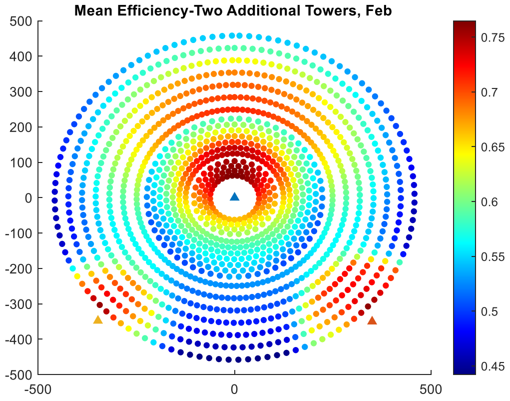

(d)

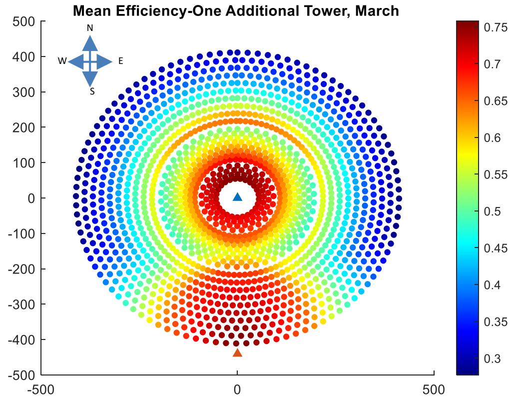
Mean Efficiency-One Additional Tower, March

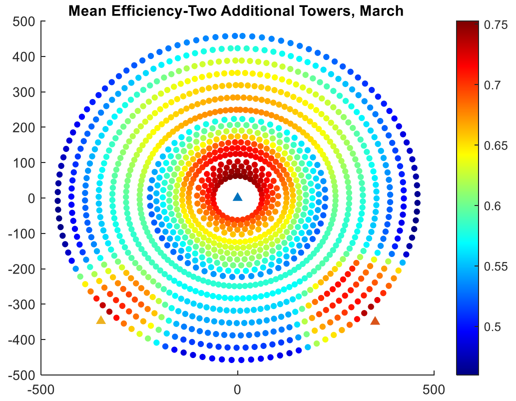
Mean Efficiency-Two Additional Towers, March

(e)

(f)

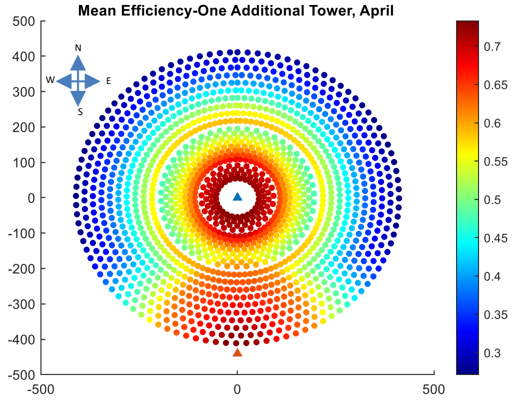
Mean Efficiency-One Additional Tower, April

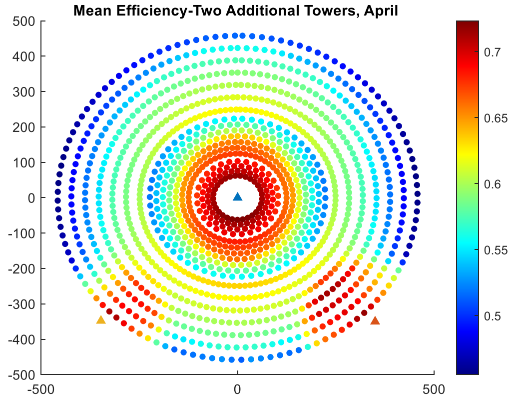
Mean Efficiency-Two Additional Towers, April

(g)

(h)

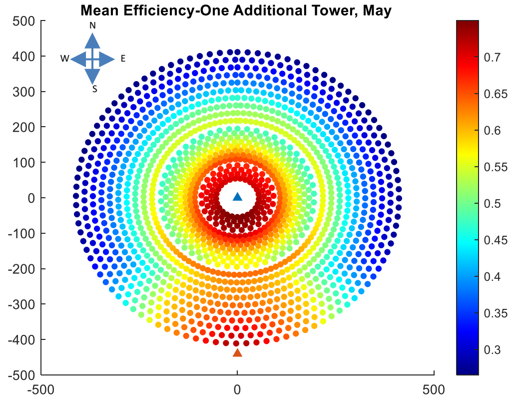
Mean Efficiency-One Additional Tower, May

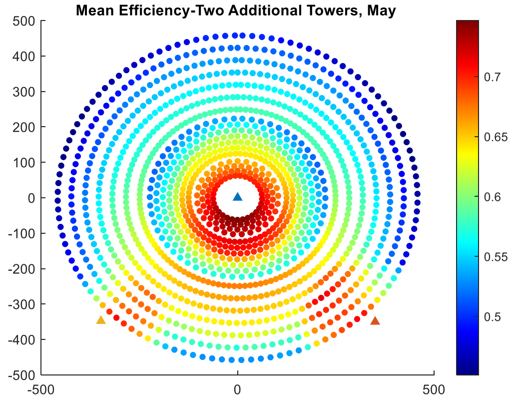
Mean Efficiency-Two Additional Towers, May

(i)

(j)

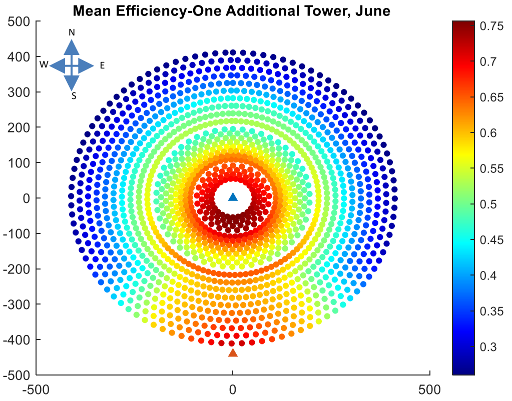
Mean Efficiency-One Additional Tower, June

(k)

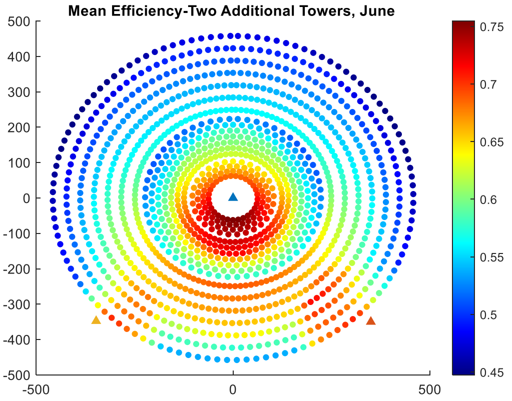
Mean Efficiency-Two Additional Towers, June

(l)

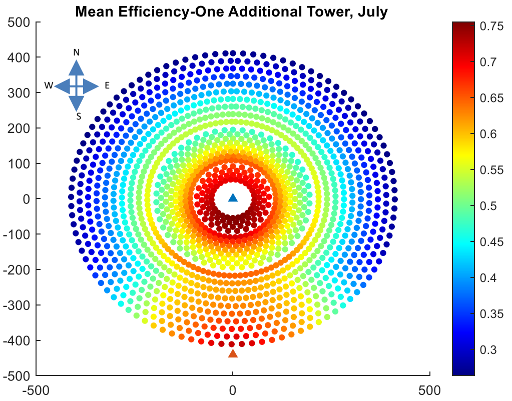
Mean Efficiency-One Additional Tower, July

(m)

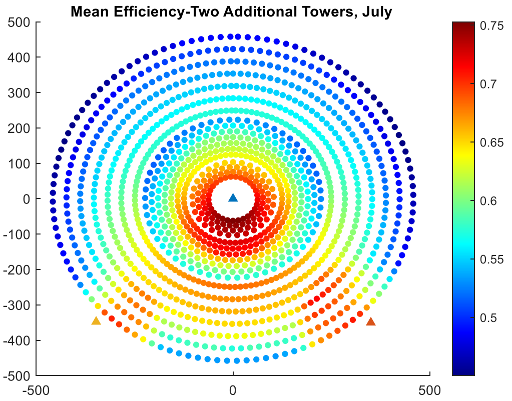
Mean Efficiency-Two Additional Towers, July

(n)

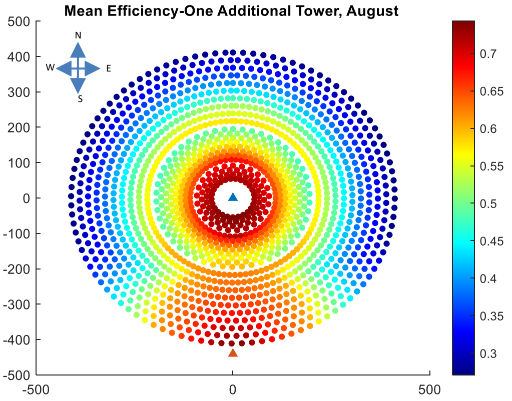
Mean Efficiency-One Additional Tower, August

(o)

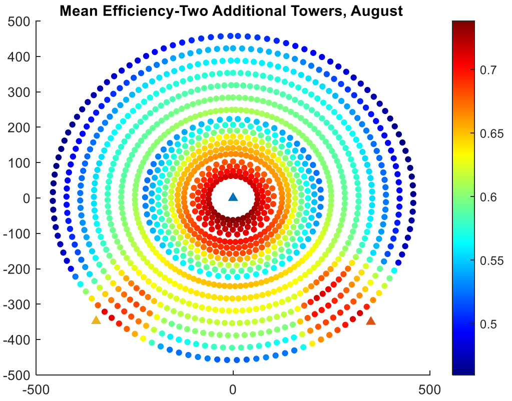
Mean Efficiency-Two Additional Towers, August

(p)

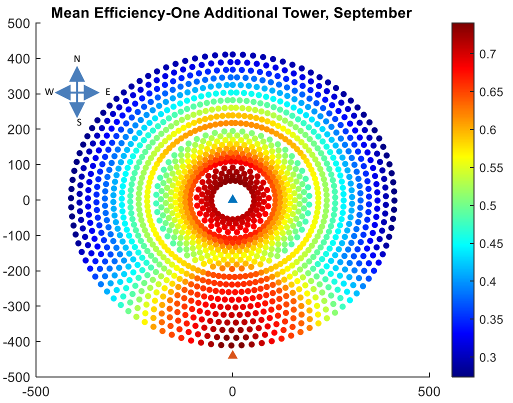
Mean Efficiency-One Additional Tower, September
N
W
E
S
500
400
300
200
100
0
-100
-200
-300
-400
-500
-500
0
500
0.7
0.65
0.6
0.55
0.5
0.45
0.4
0.35
0.3

(q)

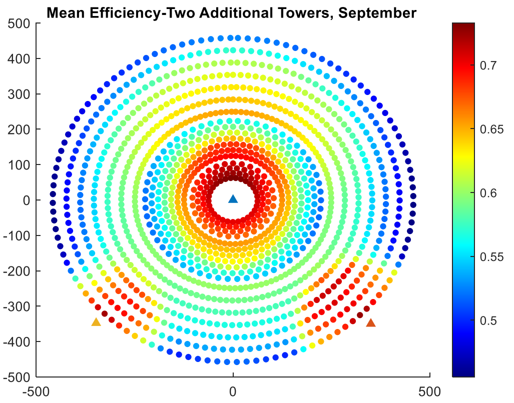
Mean Efficiency-Two Additional Towers, September
500
400
300
200
100
0
-100
-200
-300
-400
-500
-500
0
500
0.7
0.65
0.6
0.55
0.5

(r)

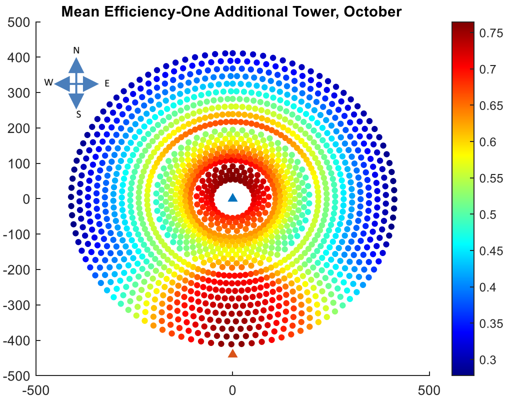
Mean Efficiency-One Additional Tower, October
N
W
E
S
500
400
300
200
100
0
-100
-200
-300
-400
-500
-500
0
500
0.75
0.7
0.65
0.6
0.55
0.5
0.45
0.4
0.35
0.3

(s)

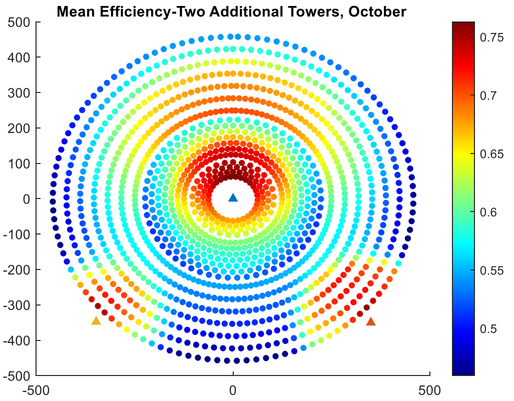
Mean Efficiency-Two Additional Towers, October
500
400
300
200
100
0
-100
-200
-300
-400
-500
-500
0
500
0.75
0.7
0.65
0.6
0.55
0.5

(t)

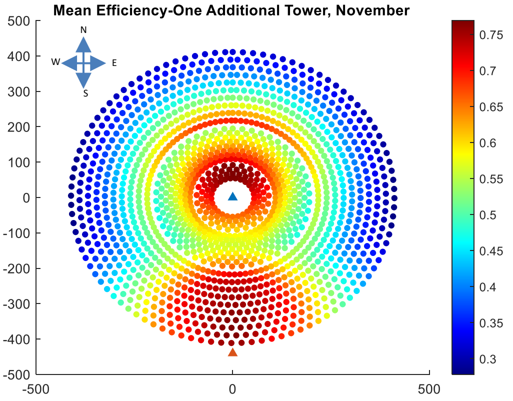
Mean Efficiency-One Additional Tower, November
N
W
E
S
500
400
300
200
100
0
-100
-200
-300
-400
-500
-500
0
500
0.75
0.7
0.65
0.6
0.55
0.5
0.45
0.4
0.35
0.3

(u)

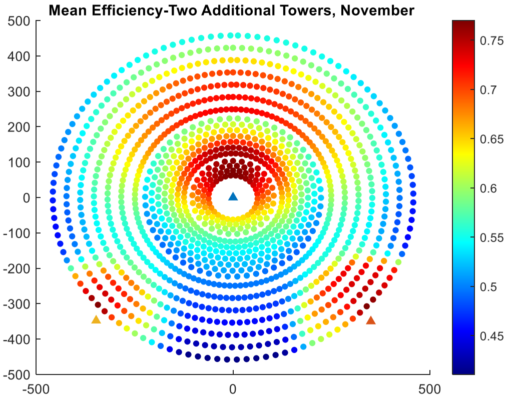
Mean Efficiency-Two Additional Towers, November
500
400
300
200
100
0
-100
-200
-300
-400
-500
-500
0
500
0.75
0.7
0.65
0.6
0.55
0.5
0.45

(v)

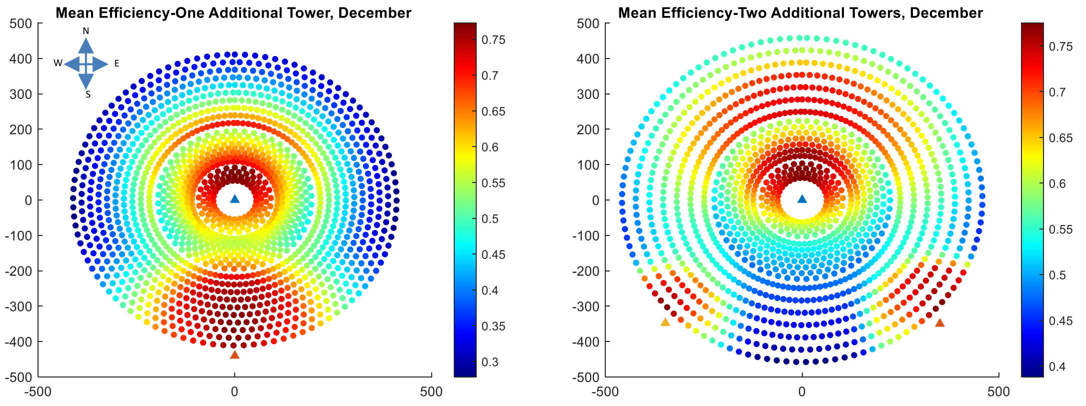

(w) (x)

Figure C-1 Mean annual efficiency field layout in a representative day of the month for a 50MWth conventional field. a-x) January to December

C.2 Optimised Multi-Tower Field Results

Here, the results from the optimised one and two auxiliary tower multi-tower field are shown in Table C1 and C2 respectively.

Table C-1 Multi-Tower Optimised Field-One Auxiliary Tower

Multi-Tower Optimised Field-One Auxiliary Tower					
Power (MWth)	**Number of Heliostats**	**Heliostat Area (m²)**	**Reflective Surface Area (m²)**	**Field Efficiency (%)**	**LCOH ($/kWht)**
25.00	779.00	79.91	62,249.89	65.68%	0.0667
50.00	1,500.00	93.99	140,987.00	58.79%	0.0574
100.00	4,687.00	65.90	308,873.30	56.90%	0.0492
150.00	5,152.00	106.53	548,842.56	55.57%	0.0478
200.00	7,504.00	91.32	685,265.28	55.01%	0.0457
300.00	11,629.00	85.12	989,860.48	53.96%	0.0442
400.00	14,916.00	97.13	1,448,791.08	52.11%	0.0426
500.00	17,595.00	98.31	1,729,764.45	50.53%	0.0433
600.00	26,304.00	87.00	2,288,448.00	49.89%	0.0438

Table C-2 Multi-Tower Optimised Field-Two Auxiliary Tower

Multi-Tower Optimised Field-Two Auxiliary Tower					
Power (MWth)	**Number of Heliostats**	**Heliostat Area (m²)**	**Reflective Surface Area (m²)**	**Field Efficiency (%)**	**LCOH ($/kWht)**
25.00	946.00	58.12	54,981.99	68.72%	0.0801
50.00	1,334.00	91.57	122,154.38	62.89%	0.0574
100.00	4,140.00	69.74	288,714.49	60.44%	0.0538
150.00	4,882.00	88.43	431,715.26	58.44%	0.0527
200.00	6,190.00	85.32	528,130.80	57.84%	0.0500
300.00	10,242.00	95.32	976,267.44	55.87%	0.0484
400.00	15,194.00	91.97	1,397,392.18	54.76%	0.0470
500.00	18,708.00	90.86	1,699,808.88	53.45%	0.0479
600.00	23,739.00	94.65	2,246,896.35	52.05%	0.0488

Appendix D Additional Tower with Subfield Configuration

Here, additional results from the Additional Tower with Subfield configuration are shown.

D.1 One Auxiliary Tower with Subfield Configuration

In Figure D1, additional results from the 50MWth ATS field are shown.

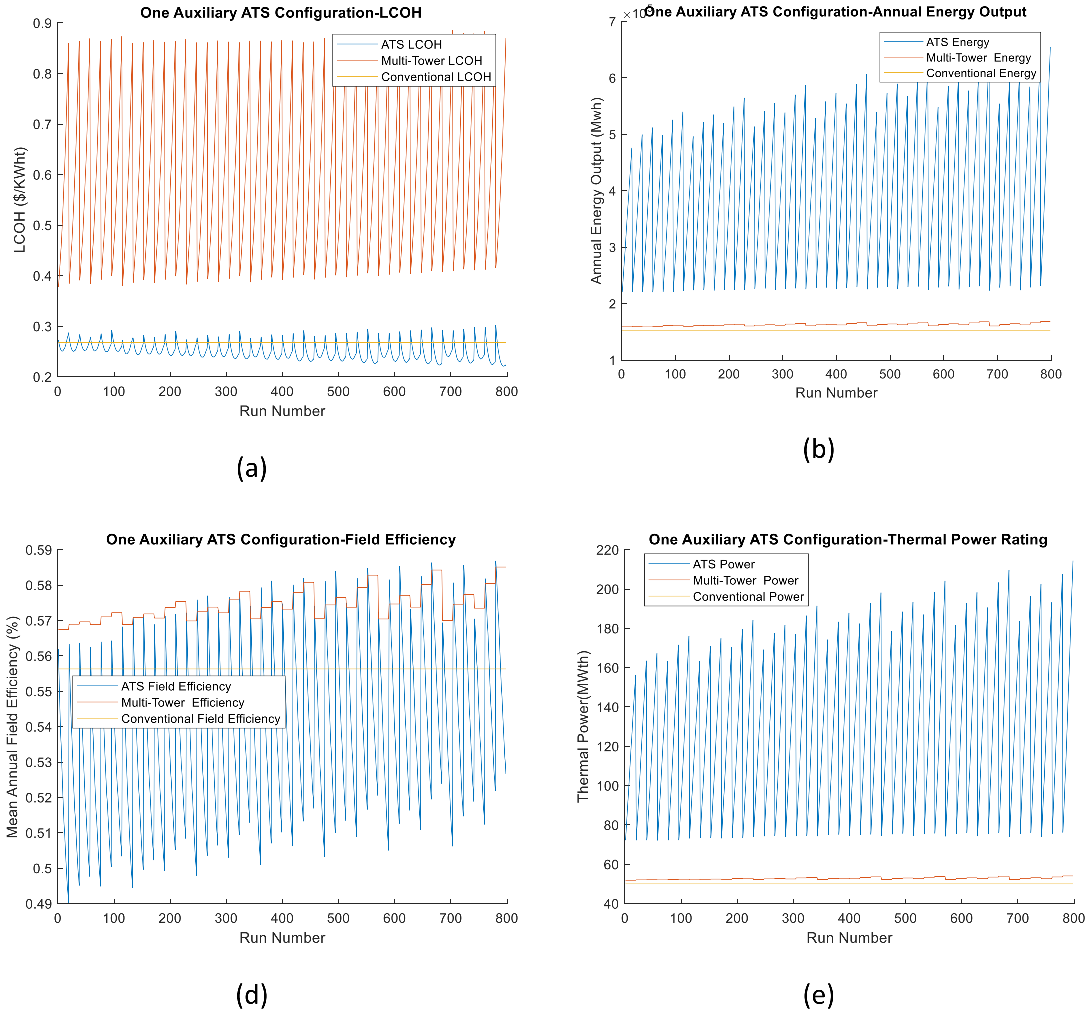

(a)

(b)

(d)

(e)

Figure D-1 Results from 50MWth One ATS configuration showing the a) LCOH b) Annual Energy Output c) Field Efficiency d) Thermal Field Output Power

From Figure D1 a-d, each figure denotes the results from ATS configuration, multi-tower field (an auxiliary tower alone in the field) and conventional field for LCOH, annual energy output and thermal power at receiver respectively under the different combination of design variables highlighted in Table 5-5. A clear increase in the efficiency, thermal energy output and thermal power rating is witnessed in the ATS configuration. The LCOH however can be seen to increase here under different thermal field powers.

Table D-1 Results at different thermal powers for the one ATS configuration

50MWth One ATS Field

Total Field Thermal Power (MWth)	Optimum Levelized Cost of Heat ($/MWht)	Mean Annual Field Efficiency (%)	Total Heliostats	Total Field Reflective Surface Area (m²)
50.00	0.0472	54.80%	1,600.00	152,272.00
75.11	0.0479	56.70%	2,215.00	210,801.55
90.02	0.0460	55.98%	2,740.00	260,765.80
99.90	0.0450	55.87%	2,964.00	282,083.88
121.94	0.0440	54.80%	3,784.00	360,123.28
131.00	0.0436	54.58%	4,090.00	389,245.30
140.00	0.0434	54.46%	4,416.00	420,270.72
149.57	0.0431	54.31%	4,762.00	453,199.54
160.61	0.0432	53.43%	5,411.00	514,964.87
170.05	0.0438	52.35%	6,233.00	593,194.61
191.07	0.0445	51.45%	7,616.00	724,814.72

100MWth One ATS Field

Total Field Thermal Power (MWth)	Optimum Levelized Cost of Heat ($/MWht)	Mean Annual Field Efficiency (%)	Total Heliostats	Total Field Reflective Surface Area (m²)
100.00	0.0445	53.14%	3,990.00	326,501.70
129.84	0.0448	54.85%	4,890.00	400,148.70
139.92	0.0445	54.01%	5,310.00	434,517.30
149.03	0.0441	53.25%	5,740.00	469,704.20
160.01	0.0437	53.01%	6,015.00	492,207.45
174.76	0.0434	52.62%	6,625.00	542,123.75
199.73	0.0431	52.21%	7,980.00	653,003.40
209.76	0.0432	52.19%	8,390.00	686,553.70

150MWth One ATS Field

Total Field Thermal Power (MWth)	Optimum Levelized Cost of Heat ($/MWht)	Mean Annual Field Efficiency (%)	Total Heliostats	Total Field Reflective Surface Area (m²)
150.00	0.0428	52.50%	5,720.00	463,377.20
173.85	0.0435	54.27%	6,440.00	612,894.80
200.09	0.0430	55.14%	7,215.00	686,651.55
210.90	0.0426	53.86%	7,745.00	737,091.65
219.96	0.0425	53.74%	8,040.00	765,166.80
230.92	0.0425	53.45%	8,690.00	827,027.30
240.62	0.0421	53.05%	8,950.00	851,771.50

250.19	0.0420	53.03%	9,320.00	886,984.40
268.91	0.0421	51.65%	10,550.00	1,004,043.50
289.13	0.0423	50.92%	11,830.00	1,125,861.10

200MWth One ATS Field

Total Field Thermal Power (MWth)	Optimum Levelized Cost of Heat ($/MWht)	Mean Annual Field Efficiency (%)	Total Heliostats	Total Field Reflective Surface Area (m²)
200.00	0.0425	48.52%	4,968.00	566,928.29
229.81	0.0435	53.65%	5,868.00	669,632.69
251.91	0.0431	53.94%	6,718.00	766,631.29
280.27	0.0425	56.65%	6,718.00	766,631.29
303.54	0.0421	55.30%	7,938.00	905,852.81
320.12	0.0418	55.05%	7,938.00	905,852.81
370.55	0.0420	54.63%	9,368.00	1,069,038.69

300MWth One ATS Field

Total Field Thermal Power (MWth)	Optimum Levelized Cost of Heat ($/MWht)	Mean Annual Field Efficiency (%)	Total Heliostats	Total Field Reflective Surface Area (m²)
300.00	0.0425	48.52%	14240	1,013,460.80
320.11	0.0455	54.27%	14520	1,033,388.40
347.21	0.0442	55.14%	15560	1,107,405.20
370.25	0.0426	53.88%	16560	1,178,575.20
398.33	0.0421	53.86%	17840	1,269,672.80
417.18	0.0421	52.75%	19520	1,389,238.40
450.20	0.0423	52.05%	21380	1,521,614.60

400MWth One ATS Field

Total Field Thermal Power (MWth)	Optimum Levelized Cost of Heat ($/MWht)	Mean Annual Field Efficiency (%)	Total Heliostats	Total Field Reflective Surface Area (m²)
400.00	0.0434	47.76%	16,128.00	1,473,615.36
419.03	0.0443	48.34%	17,005.00	1,553,746.85
451.06	0.0437	48.49%	17,448.00	1,594,223.76
471.13	0.0435	45.99%	18,448.00	1,685,593.76
502.05	0.0429	45.29%	19,728.00	1,802,547.36
519.39	0.0426	47.17%	19,728.00	1,802,547.36
548.03	0.0428	45.39%	21,408.00	1,956,048.96

500MWth One ATS Field

Total Field Thermal Power (MWth)	Optimum Levelized Cost of Heat ($/MWht)	Mean Annual Field Efficiency (%)	Total Heliostats	Total Field Reflective Surface Area (m²)
500.00	0.0442	45.9%	18,816.00	1,775,854.08
520.01	0.0449	52.6%	19,146.00	1,806,999.48
560.32	0.0442	51.7%	20,136.00	1,900,435.68

579.78	0.0438	50.0%	20,841.00	1,966,973.58
600.39	0.0435	48.2%	21,786.00	2,056,162.68
619.55	0.0433	47.0%	22,806.00	2,152,430.28
653.70	0.0429	46.3%	24,096.00	2,274,180.48
681.35	0.0432	45.9%	26,153.00	2,468,320.14

D.2 Two Auxiliary Tower with Subfield Configuration

In Figure D2, additional results from the 50MWth Two ATS field are shown.

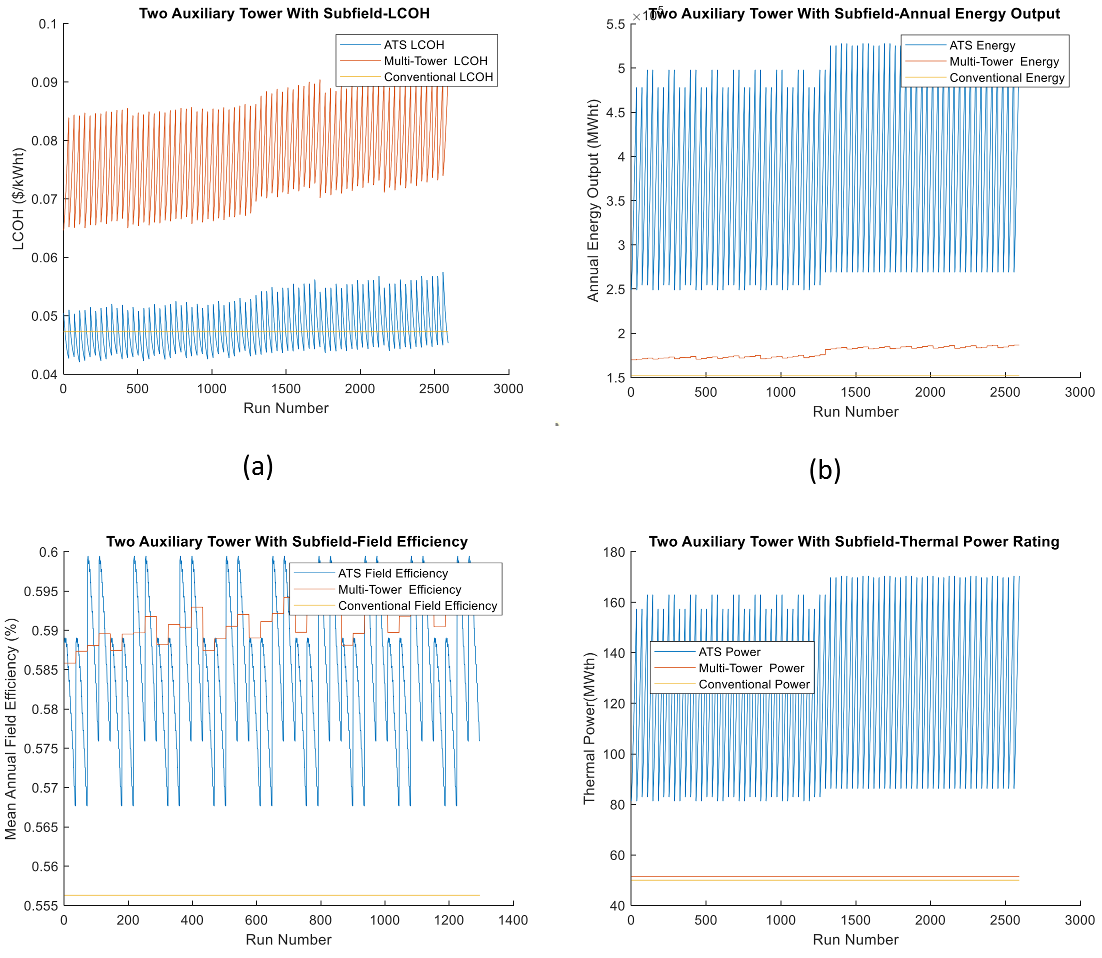

(a) (b)

(d) (e)

Figure D-2 Results from 50MWth two ATS configuration showing the a) LCOH b) Annual Energy Output c) Field Efficiency d) Thermal Field Output Power

From Figure D2 a-d, each figure denotes the results from ATS configuration, multi-tower field (two auxiliary towers alone in the field) and conventional field for LCOH, annual energy output and thermal power at receiver respectively under the different combination of design variables highlighted in Table 5-6. An even higher increase in the efficiency, thermal energy output and thermal power rating is witnessed in the two ATS configuration when compared to both the tow

ATS setup and conventional field. The gain recorded is not however enough to overturn the LCOH in the 50MWth HRC.

Table D-2 Results at different thermal powers for the Two ATS configuration

50MWth Two ATS Field

Total Field Thermal Power (MWth)	Optimum Levelized Cost of Heat ($/MWht)	Mean Annual Field Efficiency (%)	Total Heliostats	Total Field Reflective Surface Area (m²)
50.0000	0.0472	54.80%	1,600.00	152,272.00
89.5044	0.0499	59.83%	2,416.00	229,930.72
99.5494	0.0475	58.94%	2,720.00	258,862.40
120.2533	0.0456	58.63%	3,232.00	307,589.44
141.1023	0.0438	58.42%	3,840.00	365,452.80
158.9688	0.0431	58.38%	4,328.00	411,895.76
170.4871	0.0431	56.52%	5,100.00	485,367.00

100MWth Two ATS Field

Total Field Thermal Power (MWth)	Optimum Levelized Cost of Heat ($/MWht)	Mean Annual Field Efficiency (%)	Total Heliostats	Total Field Reflective Surface Area (m²)
100.00	0.0445	53.14%	3,990.00	326,501.70
120.58	0.0475	56.15%	4,476.00	366,271.08
149.57	0.0455	57.93%	5,220.00	427,152.60
160.07	0.0442	56.63%	5,622.00	460,048.26
180.37	0.0432	56.24%	6,190.00	506,527.70
190.20	0.0427	55.50%	6,718.00	549,733.94
215.53	0.0417	55.03%	7,440.00	608,815.20
261.73	0.0412	54.82%	9,260.00	757,745.80
298.33	0.0419	52.61%	11,970.00	979,505.10

200MWth Two ATS Field

Total Field Thermal Power (MWth)	Optimum Levelized Cost of Heat ($/MWht)	Mean Annual Field Efficiency (%)	Total Heliostats	Total Field Reflective Surface Area (m²)
200.00	0.04	48.52%	4,968.00	566,928.29
229.59	0.04	59.88%	5,454.00	622,388.66
261.14	0.04	58.74%	6,198.00	707,290.97
281.72	0.04	58.06%	6,600.00	753,165.60
329.11	0.04	57.03%	8,418.00	960,628.49
370.28	0.04	56.62%	9,072.00	1,035,260.35

390.78	0.04	56.60%	9,608.00	1,096,426.53
429.70	0.04	55.89%	10908	1,244,777.33
485.35	0.04	55.04%	12948	1,477,573.97
505.53	0.04	54.73%	13768	1,571,149.09

300MWth Two ATS Field

Total Field Thermal Power (MWth)	Optimum Levelized Cost of Heat ($/MWht)	Mean Annual Field Efficiency (%)	Total Heliostats	Total Field Reflective Surface Area (m²)
300.00	0.0425	48.52%	14,240.00	202,777,600.00
324.36	0.0450	54.14%	14,726.00	209,698,240.00
346.96	0.0437	53.94%	15,470.00	220,292,800.00
388.23	0.0426	53.31%	15,872.00	226,017,280.00
405.56	0.0422	51.89%	16,968.00	241,624,320.00
442.47	0.0418	51.34%	17,690.00	251,905,600.00
505.46	0.0404	49.48%	22,144.00	315,330,560.00
571.34	0.0400	49.63%	23,120.00	329,228,800.00
601.57	0.0404	48.72%	24,388.00	347,285,120.00

500MWth One Two Field

Total Field Thermal Power (MWth)	Optimum Levelized Cost of Heat ($/MWht)	Mean Annual Field Efficiency (%)	Total Heliostats	Total Field Reflective Surface Area (m²)
500.00	0.0442	45.9%	18,816.00	1,775,854.08
532.02	0.0457	53.31%	19,266.00	1,818,325.08
592.26	0.0443	51.58%	20,830.00	1,965,935.40
630.78	0.0437	50.47%	22,032.00	2,079,380.16
675.69	0.0435	49.74%	23,514.00	2,219,251.32
701.51	0.0433	49.28%	24,448.00	2,307,402.24
761.06	0.0428	47.82%	27,240.00	2,570,911.20
814.59	0.0425	47.68%	28,964.00	2,733,622.32
894.71	0.0426	47.02%	32,616.00	3,078,298.08

Appendix E Heliostat Repositioning Configuration

Here, additional results from the Heliostat Repositioning Configuration (HRC) with one and two auxiliary towers are shown.

E.1 One Auxiliary Tower Heliostat Repositioning Configuration

In Figure E1 a-e, additional results from the 50MWth HRC field are shown.

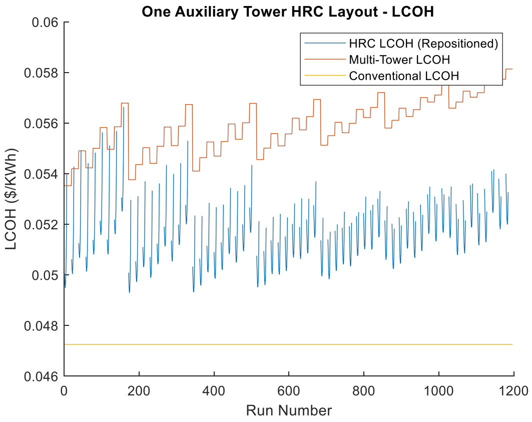
One Auxiliary Tower HRC Layout - LCOH

(a)

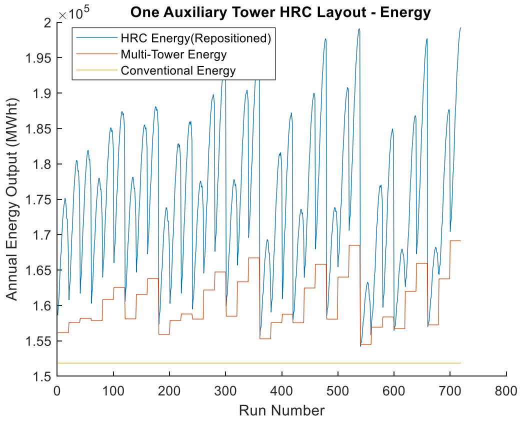
One Auxiliary Tower HRC Layout - Energy

(b)

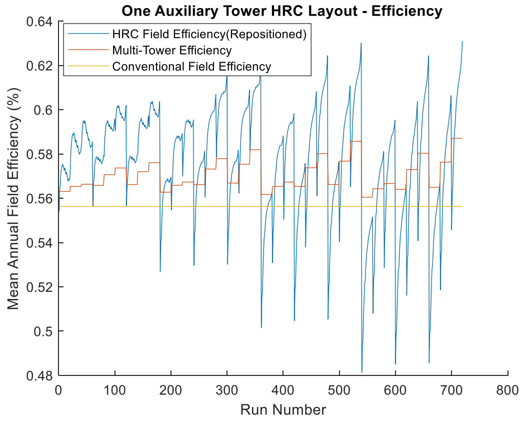
One Auxiliary Tower HRC Layout - Efficiency

(d)

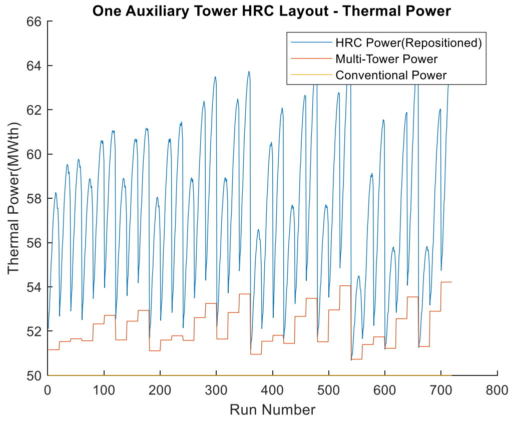
One Auxiliary Tower HRC Layout - Thermal Power

(e)

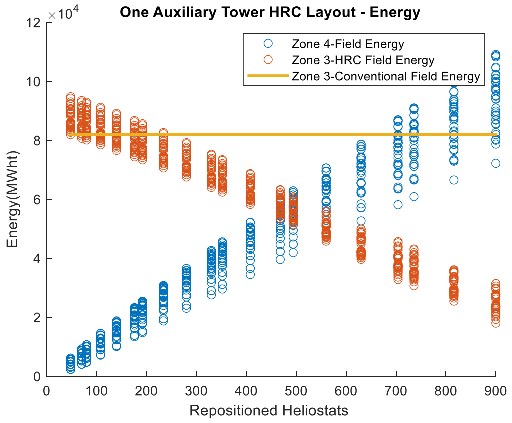

(e)

Figure E-1 Results from 50MWth one auxiliary tower HRC showing the a) LCOH b) Annual Energy Output c) Field Efficiency d) Thermal Field Output Power e) Zone 3 and 4 Energy Output

From Figure E1 a-d, each figure denotes the results from HRC configuration, multi-tower field (an auxiliary tower alone in the field) and conventional field for LCOH, annual energy output and thermal power at receiver respectively under the different combination of design variables highlighted in Table 5-7. A clear increase in the efficiency, thermal energy output and thermal power rating is witnessed in the HRC configuration. The gain recorded is not however enough to overturn the LCOH in the 50MWth HRC. In Figure E1-d, the field efficiency only improves for specific combination of design variables and at a certain number of repositioned heliostats.

In Figure E1-e, the field energy output from Zone 3 in the main-field and Zone 4 from the subfield can be seen. As heliostats are taken out from Zone 3, the efficiency increases (as only the most efficiency heliostats are left out) but the energy output from the Zone reduce due to fewer number of heliostats. On the other hand, in the subfield, an increase in the energy output is witnessed.

E.2 Two Auxiliary Towers Heliostat Repositioning Configuration

In Figure E2, additional results from the 50MWth two auxiliary towers HRC field are shown.

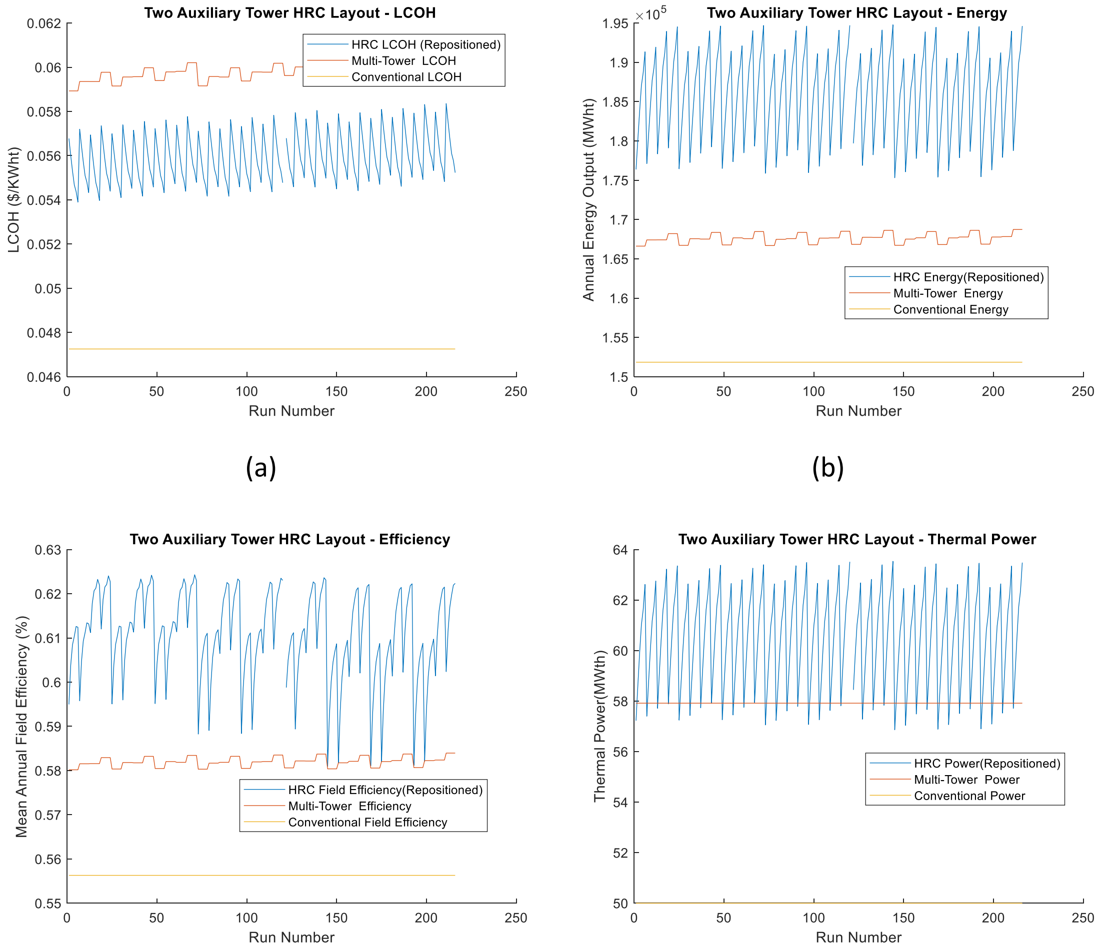

(a) (b)

(d) (e)

Figure E 2 Results from 50MWth two auxiliary towers HRC showing the a) LCOH b) Annual Energy Output c) Field Efficiency d) Thermal Field Power

From Figure E2 a-d, each figure denotes the results from HRC configuration, multi-tower field (two auxiliary towers only in the field) and conventional field for LCOH, annual energy output and thermal power at receiver respectively under the different combination of design variables highlighted in Table 5-7. An even higher increase in the efficiency, thermal energy output and thermal power rating is witnessed in the two-auxiliary tower HRC configuration when compared to both the one auxiliary tower HRC and conventional field. The gain recorded is not however enough to overturn the LCOH in the 50MWth HRC.

Appendix F Gemasolar Field

Here, additional results from the Gemasolar field case study are shown.

F.1 Gemasolar Field Model: Optical Efficiency Loss Factors

The field layout showing the optical efficiency loss factors for the replicated Gemasolar field model is shown in Figure F1.

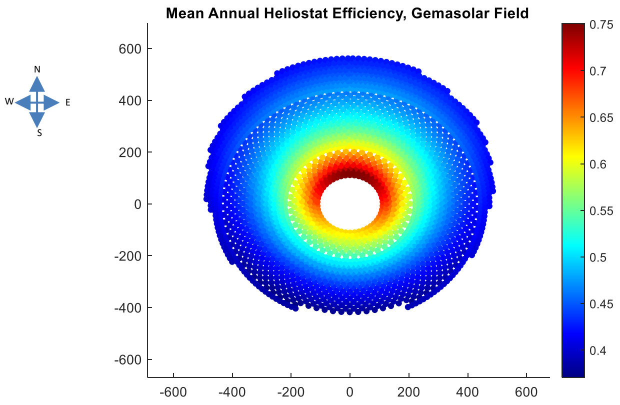

(a)

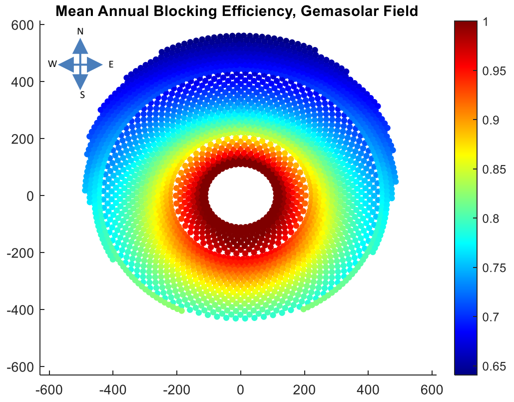

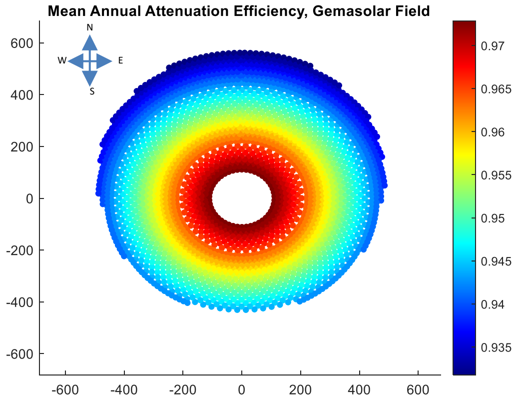

(b)

(c)

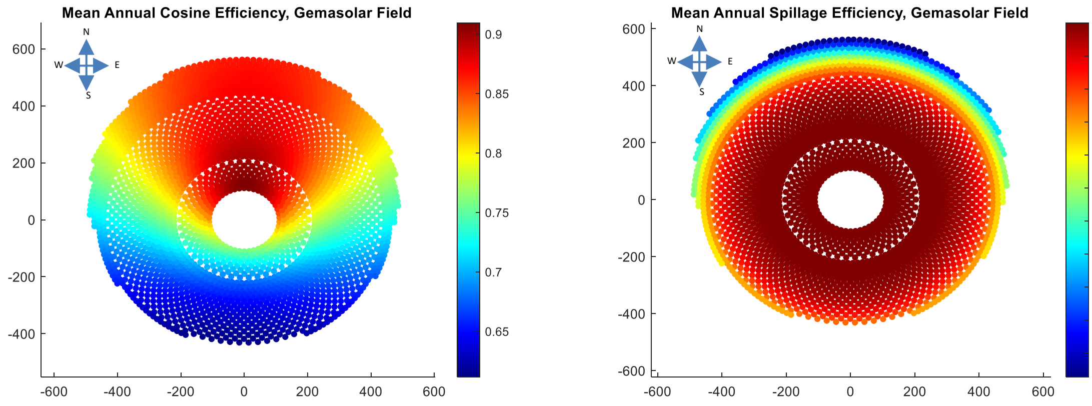

(d) (e)

Figure F-1 Gemasolar field model layout showing a) mean annual efficiency, b) blocking loss, c) attenuation loss, d) cosine loss, and e) spillage loss respectively

F.1.1 Monthly Energy and Efficiency Output

In Figure F2a & b, the month on month variation of the total energy output and mean efficiency values for both the conventional field and the multi-tower field is shown.

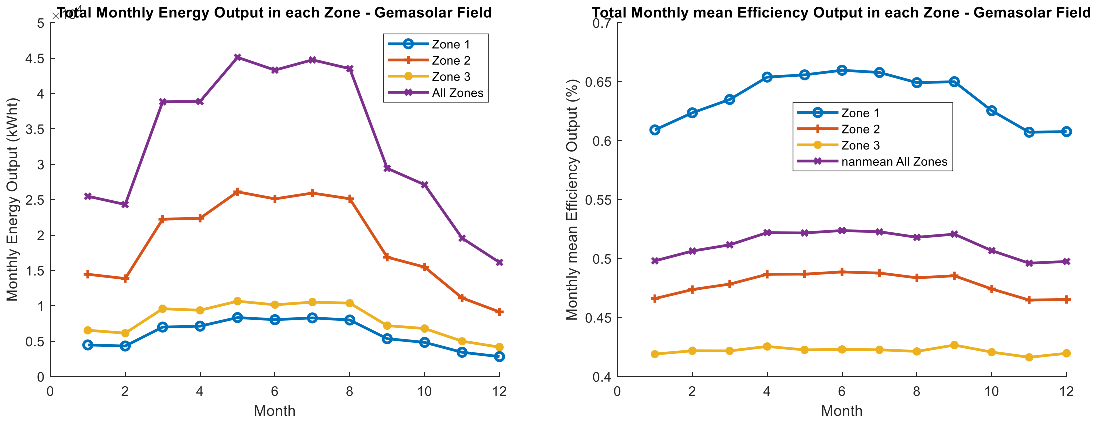

(a) (b)

Figure F-2 Gemasolar Field, Total monthly energy output b) Gemasolar Field, Total monthly mean efficiency.

F.2 Multi-Tower Gemasolar Field Remodelling

Here, the Gemasolar field is remodelled into a multi-tower field by adding an auxiliary tower and optimizing the field in order to achieve the same thermal power. The layout of the field showing the mean annual efficiency of this remodelled field is shown in Figure F-3.

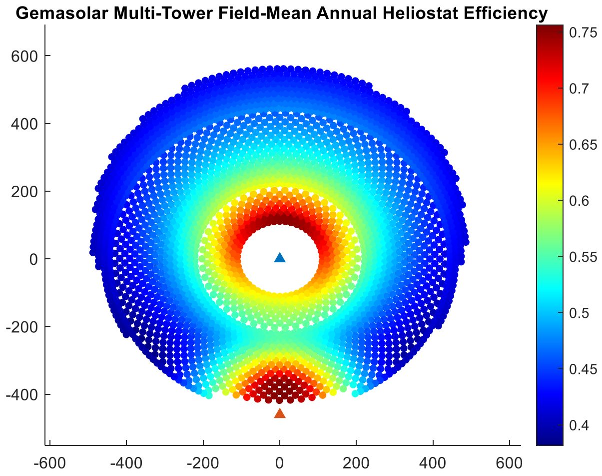

Figure F-3 Multi-Tower Gemasolar Field

In Table F1, the results from the developed Gemasolar field and remodelled multi-tower field.

Table F-1 Results showing conventional Gemasolar field and multi-tower field

Parameter	Conventional Field	Multi-tower Field
Levelized Cost of Heat ($/kWht)	0.0449	0.0491
Field Power (MWth)	120.68	120.90
Mean Annual Efficiency (%)	51.22	52.55
Reflective Surface Area (m^2)	305,401.90	293,487
Number of Heliostats	2,650	2,540
Annual Energy (MWht)	396,453.21	408,878.54
System Cost ($)	97,025,168.28	117,055,559.70

The results from Table F1 shows an ample increment in the annual energy and efficiency of the reconfigured Gemasolar field over the conventional Gemasolar field. This thus led to an LCOH value which could not break even with conventional Gemasolar field.

In the subsequent sections, HRC and ATS configurations are applied in the multi-tower Gemasolar field.

F.2.1 Multi-Tower Gemasolar Field - Heliostat Repositioning Configuration

Here, the HRC is applied on the developed and remodelled Gemasolar field.

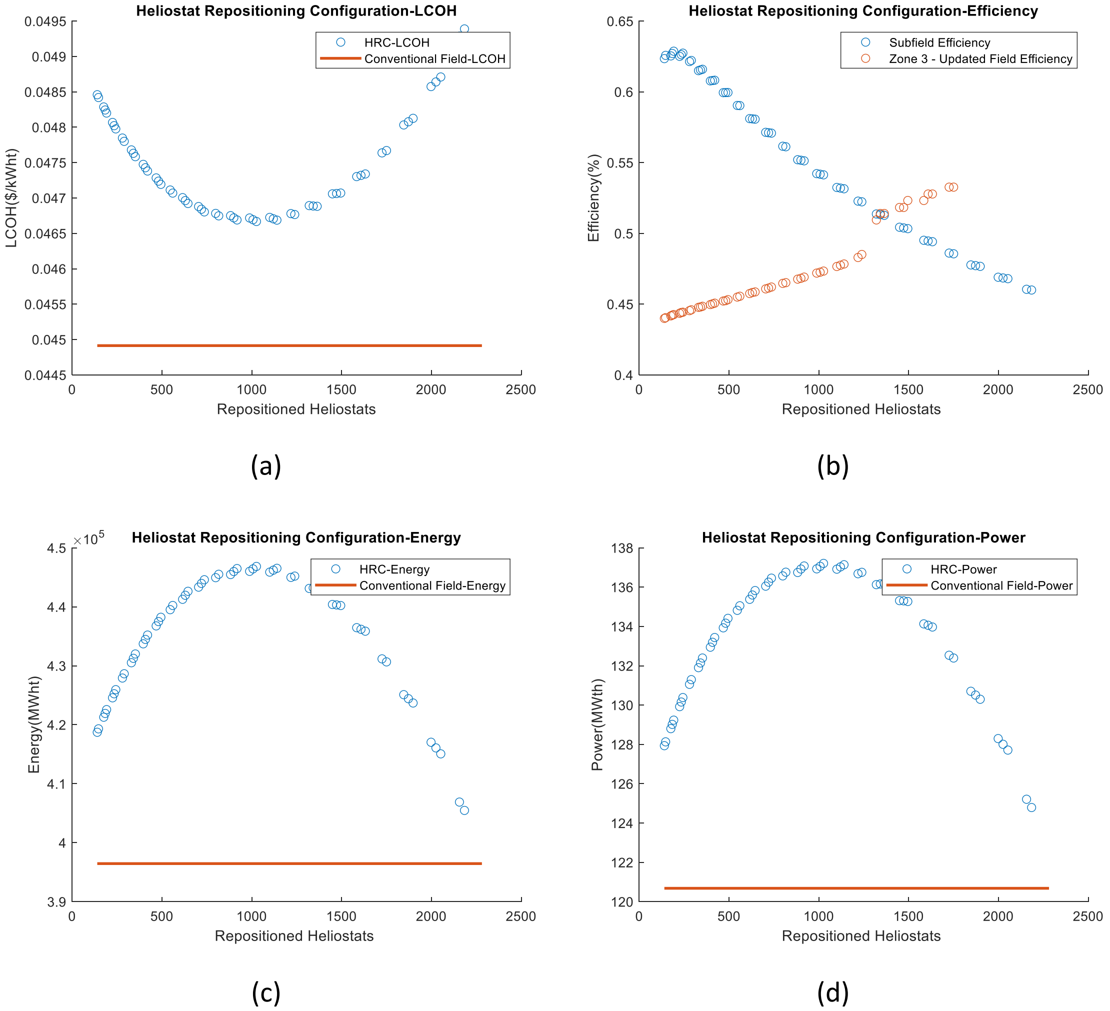

Figure F-4 Results from the remodelled Gemasolar with HRC applied showing a) LCOH b) Field Efficiency c) Annual Energy Output d) Thermal Field Output Power

The effects of the repositioning are clearly outlined in Figure F4. Similar to all HRC configuration previously outlined, a reduction in the LCOH is witnessed (Figure F4a) with the optimum value at 0.047$/kWht. Energy and thermal power, from Figure F4c and d all peak at the optimum point when 1,026 heliostats have been repositioned. In Figure F4b, the effect of the configuration in the subfield and in Zone 3 can be seen. With more heliostats in the subfield, the advantages in repositioning progressively becomes weaker. Despite all the merits from the configuration, the optimum LCOH could not equal nor surpass the conventional Gemasolar LCOH.

F.2.2 Multi-Tower Gemasolar Field – Auxiliary Tower with Subfield

Here, the ATS configuration is applied on the developed and remodelled Gemasolar field.

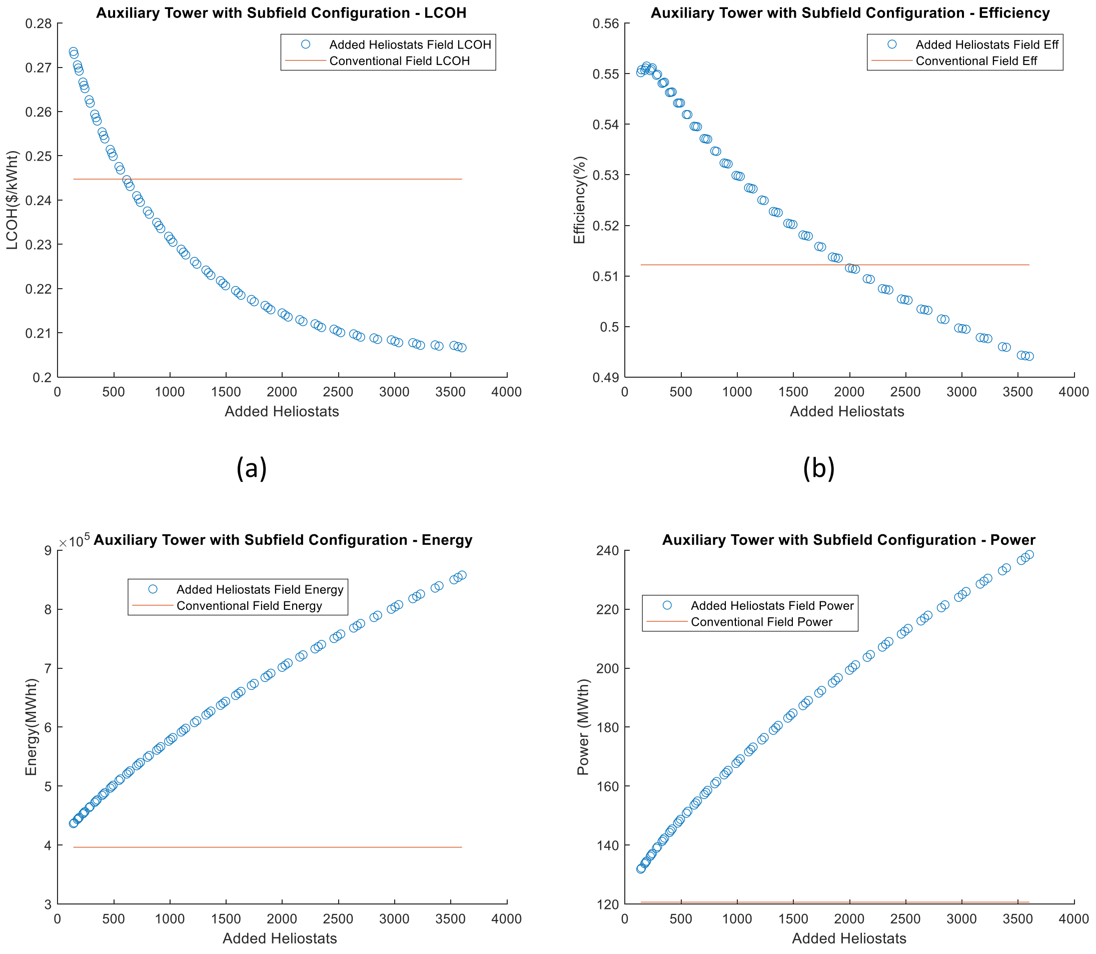

(a) (b)

(c) (d)

Figure F 5 Results from the remodelled Gemasolar with ATS configuration applied showing a) LCOH b) Field Efficiency c) Annual Energy Output d) Thermal Field Output Power

The results from F5 shows a progressive increase in the thermal energy and power in the configuration (Figure F5c and d). The trend slightly begins to dip due the continual reduction in the efficiency (Figure Fb) primarily as a result of the subfield taking in too many heliostats. The continual reduction in the efficiency is reflected in the LCOH (Figure F5a). The LCOH can be seen to outdo the initial conventional field LCOH from the 615th added heliostat. However, it should be noted that at this point the field thermal output power is at 154MWth, 34MWth higher than the initial field's value. Thus, in this configuration, the supplementary energy attained must be able to surpass a conventional field of that value before comparison can be appropriately made.

From the two configurations observed: ATS and HRC, it can be seen that the field improvement strategies perform better when the auxiliary tower is optimised from a conventional field rather than applying directly to an optimised multi-tower field as seen here. At an optimum 160MWth thermal for example, the additional energy in the configuration from Chapter 6.2 (Figure 6-7) computes to 537,406.60MWht while in the configuration applied directly to an optimised multi-tower field, the energy equates to 520,561.02MWht. A difference of 17,000MWht.The LCOH on the hand, equates to 0.0440$/kWht in the former and 0.0449$/kWht in the latter.